Dissertation

submitted to the

Combined Faculties of the Natural Sciences and Mathematics

of the Ruperto-Carola-University of Heidelberg. Germany

for the degree of

Doctor of Natural Sciences

Put forward by

Hagen Thilo Meyer

born in: Quedlinburg, Germany

Oral examination: December 20, 2012

The progenitors of early-type dwarf galaxies in the Virgo cluster

Referees: Priv.-Doz. Dr. Thorsten Lisker
Prof. Dr. Volker Springel

Zusammenfassung

In der vorliegenden Doktorarbeit untersuche ich die möglichen Vorgänger von elliptischen Zwerggalaxien im Virgo Galaxienhaufen. Zur Analyse der Galaxien des späten morphologischen Typs wurde ein Breitband-Datensatz in den u, g, r, i und z Filtern des Sloan Digital Sky Survey benutzt. Die photometrischen und strukturellen Eigenschaften (z.B. Helligkeit und Radius) der einzelnen morphologischen Unterklassen wurden mit einem bestehenden Datensatz von elliptischen Zwerggalaxien verglichen, um mögliche evolutionäre Verbindungen zu untersuchen. Innerhalb des Datensatzes zeigen Galaxien vom Typ der *blauen kompakten Zwerge* — bei vorheriger Entfernung des Einflusses der Sternentstehungskomponente — eine bemerkenswerte Ähnlichkeit mit den elliptischen Zwerggalaxien. Diese Übereinstimmung bezüglich der photometrischen Eigenschaften könnte auf eine mögliche evolutionäre Verbindung hindeuten.

Die Resultate der Photometrie des gesamten Datensatzes wurden als Eingabewerte für einen Evolutionssynthese-Modelle benutzt, mit dem die ungestörte und gestörte zeitliche Entwicklung der photometrischen Parameter der Galaxien simuliert wurden. Durch den Vergleich der Modellergebnisse mit den Beobachtungsdaten heutiger elliptischer Zwerggalaxien bin ich in der Lage, die möglichen Vorgängertypen auf bestimmte morphologische Unterklassen einzugrenzen.

Innerhalb dieser Doktorarbeit konnte ich zeigen, dass neben den heutigen *blauen kompakten Zwerggalaxien*, auch die zukünftigen photometrischen Eigenschaften von späten Spiralgalaxien des Typs Sd und Sm sehr gut mit denen heutiger elliptischer Zwerggalaxien übereinstimmen.

Abstract

In the here presented thesis, I investigate the possible progenitors of elliptical dwarf galaxies in the Virgo galaxy cluster. For the analysis of the galaxies of the late morphological type, a broadband data set in the u, g, r, i and z filters of the Sloan Digital Sky Survey was used. The photometric and structural properties (e.g. luminosity and radius) of the single morphological subclasses was compared with an existing data set of elliptical dwarf galaxies to explore the possible evolutionary connections. Within the sample, galaxies of the type *blue compact dwarf* — if the contribution of the starburst component is removed — show a remarkably good similarity to the elliptical dwarf galaxies. This agreement in the photometric properties could point to a possible evolutionary connection.

The results of the photometry of the entire sample were used as input parameters for an evolutionary synthesis code, which simulates the undisturbed and disturbed evolution of the photometric parameters of the galaxies. By comparing the results of the simulation with the ones of the observations of today's elliptical dwarf galaxies, I am able to restrict the possible progenitors to certain morphological subclasses.

In the course of this thesis, I was able to show that apart from *blue compact dwarf galaxies*, also the prospective photometric properties of late-type spirals of the type Sd and Sm are in good agreement with today's elliptical dwarf galaxies.

Declaration

This thesis contains no material that has been accepted for the award of any other degree or diploma.

Hagen Thilo Meyer

Contents

Chapter 1 Introduction

1.1 Galaxies

Since thousand of years humans are fascinated by the starry sky. Apart from the twinkling stars a milky band was apparent in the sky, which was therefore called the “Milky Way” or in grecian “Galaxy”. With the emerge of the telescope in the 17th century it was Galileo Galilei who first pointed it to the nightly sky and discovered the famous moons of the planet Jupiter, which in turn revolutionised our understanding of the Universe. But he also pointed his telescope to the milky band in the sky and discovered that it actually consists of thousands and thousands of stars.

Centuries after the discoveries of Galilei our view of the Milky Way has changed from an accumulation of stars on a sphere to an disc-like object with a spacial extension. However, the real physical extent of the Galaxy was under debate until the beginning of the last century and found its highlight in “Great Debate”. Within the Great Debate it was devotedly discussed whether objects like the Andromeda nebula are objects *within* our own Galaxy or if they are other galaxies *far away*. With the measurement of the distance of variable stars within the Andromeda nebula (M31) by Edwin Hubble (e.g. Hubble, 1922, 1929) it became clear that M31 is far away from our Galaxy and is indeed another galaxy in the Universe. Thus, there is not only our own Galaxy, which forms the Universe, but there are other objects like the Galaxy. Other examples of galaxies in our neighbourhood are the Small and Large Magellanic Clouds (SMC and LMC), which are even visible with the naked eye. Figure 1.1 shows images of M31, LMC and SMC at visible wavelength.

Thus, starting from this we have to ask what actually is a galaxy? A naive answer to the question would be that galaxies are a vast number of stars in a limited volume.

However, detailed studies over the last decades reveal a more complicated view

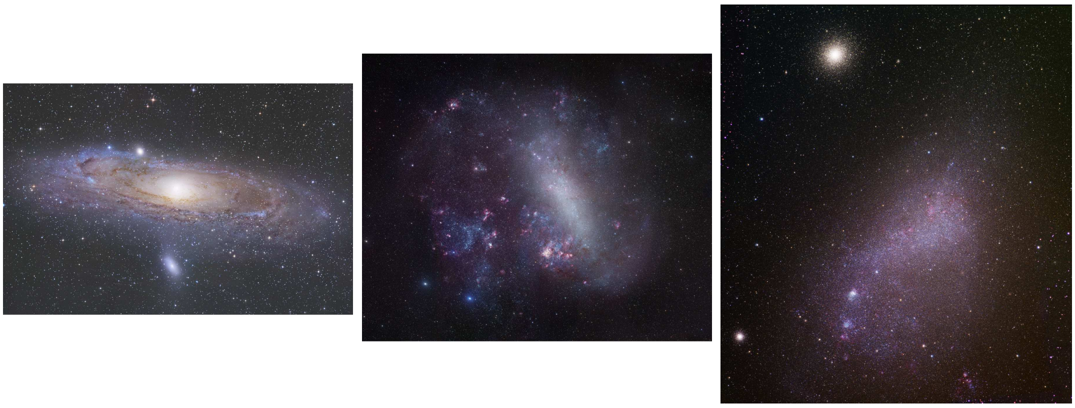

Figure 1.1: Optical images of the Andromeda Nebula (left), LMC (middle) and SMC (right) (Credit: R. Gendler (left and middle); J. Hambsch and R.Gendler (right)).

of galaxies. First of all, galaxies do not only contain stars, but huge amounts of other ingredients. One ingredient in galaxies is gas in different phases and different abundance. A part of these gas clouds represents the birth place of new born stars and are therefore called star forming regions. One of the prominent representative of a gas cloud in our Galaxy is the Orion Nebula, also visible with the naked eye. In galaxies we found atomic gas as well as molecular gas. As we will see in this thesis, gas plays an important role on how a galaxy is classified today and how it would evolve with time.

In the last century the movement of the stars in galaxies was investigated and the outcome of these studies provided a remarkable result. The stars of a galaxies do not move as they should in the sense of the classical Keplerian physics, where an object nearby the centre of gravity moves faster than an object at larger distance, given by the following formula:

$$\mathrm{V} \sim \frac{1}{\sqrt{R}} \tag{1.1}$$

where V is the velocity of the object and R is the radius from the centre of gravity (e.g. Binney and Tremaine, 2008). Moreover, stars at the outer rim of some special kind of galaxy move almost with the same velocity as stars at intermediate distance (Rubin and Ford, 1970). To overcome this problem a large amount of invisible matter, which is only measurable through its gravitational influence, was introduced and was called “Dark Matter” (DM). As we will see, DM is one of the key parameters in the description of the Universe and the formation of galaxies.

Other ingredients of galaxies are for example dust and of course the stars. Dust has only a minor contribution to the total mass of a galaxy, however it has the ability to change the appearance of a galaxy due to absorption and scattering of the star light.
The mass range of galaxies spans several orders of magnitudes from several million solar masses ($M_\odot$) up to 10^{12} $M_\odot$ for the most massive ones (Willman et al., 2006; Misgeld and Hilker, 2011). Since the total mass of a galaxy is not easy to measure, it is common to use the luminosity of the galaxies instead of the mass. In astronomy the luminosity is often expressed in terms of magnitude m, which is defined as

$$m = -2.5 \cdot \log(f/f_0) \tag{1.2}$$

where f is the measured flux of the object and f_0 is the flux of a reference object (e.g. the star Vega).
Looking at images of galaxies one immediately realises that galaxies do not form a uniform class of objects, but show a large variety in morphology from galaxies with a rather smooth appearance to galaxies with an obvious spiral structure. In the framework of the famous study by Hubble (1926) the galaxies were classified regarding their morphology, starting with smooth elliptical galaxies with different degrees of flattening to the prominent spiral galaxies (see Fig. 1.2). The class of elliptical galaxies is also called "early-type" galaxies (ETGs), which are characterised by relatively red optical colours and almost no sign of star formation. On the other hand there are the spirals, which are also called "late-type" galaxies. Galaxies in the transition between ellipticals and spirals are called lenticular galaxies (S0 galaxies) and are associated to the early-type galaxies, too. It has to be pointed out that the terms "early-types" and "late-types" do not give any hint to the stage of evolution of the galaxies, moreover the light of late-type galaxies is dominated by young massive stars, while the light of early-type galaxies is dominated by an old stellar population.
Hubble furthermore subdivided the spiral galaxies into the groups of spirals with and without a stellar bar, which is denoted by a capital "B" in the morphological class - like SBa in Fig. 1.2. These two groups of spirals are then further classified regarding the pitch angle, which describes the opening angle of the spiral arms and the ratio of the size of the central component (the bulge) to the size of the surrounding disc. Apart from morphological differences to the ETGs, spiral galaxies also differ to ETGs in the ability to form new stars. The stellar disc of spiral galaxies is a location of enhanced star formation. As already mentioned, stars are formed in gas clouds, therefore the disc of spiral galaxies must contain gas to fuel the star formation. To determine the amount of stars formed within a unit time - the star formation rate (SFR) - different

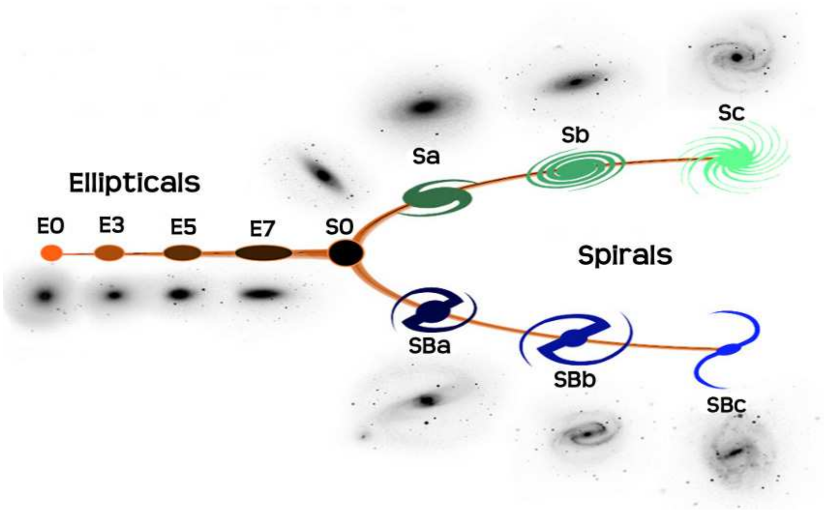

Figure 1.2: The Hubble Tuning Fork. (Credit: NASA & ESA (adapted by R. Kotulla))

star formation laws are used. The simplest law uses a power law correlation between the surface density of the gas and the SFR (Schmidt, 1959; Kennicutt, 1998). Although the light of the young and massive stars in the spiral arms dominates the total light of the galaxy at the visible wavelength, the contribution of these stars is less to the total mass of the galaxy. The majority of the total mass of the disc of spiral galaxies comes from an older stellar population.

It was soon realised that some galaxies do not belong to any of the above described classes of ellipticals and spirals, respectively. Among these are faint galaxies with an irregular shape, which are therefore classified as "irregular galaxies". With the improvement of observational techniques it became clear that large and bright elliptical and spiral galaxies of the Hubble sequence are a minority. Most of the galaxies, which are observed today, are faint dwarf galaxies, making the bulk of the galaxy population (Phillipps et al., 1998; Trentham and Hodgkin, 2002). This overabundance of dwarf galaxies makes the study of them even more interestingly and necessary.

The dwarf galaxy population on its own can also be subdivided in almost the same manner as the bright ellipticals and spirals. At first glance early-type dwarf galaxies (ETDGs) - like their massive counterparts - have a smooth appearance and relatively red colours. However, studies by e.g. Sandage and Binggeli (1984), Jerjen et al. (2000), Lisker et al. (2007) and others revealed several subclasses with disc- and spiral-features, central nuclei and central star formation, thus making our view of dwarf galaxies more complicated.

Another group of the dwarf galaxies are the late-type dwarfs. In contrast to ETDs these galaxies significantly form new stars and may show a high order of distortion. In the class of the late-type dwarf galaxies one finds the “dwarf irregular galaxies” (dIs) and the “Blue Compact Dwarfs” (BCDs). The particular class of “Blue Compact Dwarfs” (BCDs) was first described in the early work of e.g. Zwicky (1965) and Searle and Sargent (1972) and their physical properties are still under debate. First believed to be very young objects with primordial chemical composition, Loose (1985) showed that they are composed of two components. One component exhibits a phase of very strong star formation, producing very massive and young stars, while the other component consists of an old stellar population. Therefore the BCDs cannot be young galaxies, making them even more interesting due to their particularly low chemical abundance, which is originally more common for young galaxies in the early Universe (Izotov et al., 1999b).

The difference between dIs and BCDs is commonly given by a higher SFR, compact optical size and higher surface brightness of the BCDs compared to dI galaxies (Thuan and Martin, 1981). However, there is no well defined limit for the division, resulting in the presence of transition types. Furthermore, the problem of a not well defined limit is not only valid in case of late-type dwarfs, but between late-types and early-type dwarf galaxies as well (Dellenbusch et al., 2008).

In general, the magnitude is used to divide galaxies into dwarf and giant galaxies. The limit, where a galaxy is a dwarf or a giant, is relatively arbitrary set to e.g. $M_B = -18$ mag (e.g. Thuan and Martin, 1981; Mo et al., 2010)[1], indicating the absolute magnitude in the blue filter at 4360 Å. However, this limiting magnitude holds some problems, since there are overlap regions between low-luminosity spirals and dwarf galaxies. Furthermore, when applying this limit one also has to care about the distance of the galaxy, which is needed to calculate the absolute magnitude. Thus, measuring a wrong distance, may shift a gigantic galaxy into the regime of the dwarfs, even though the physical properties may be very different.

This problem of defining the dwarf- and non-dwarf galaxies is still not solved and an actual matter of discussion among the scientific community.

[1] Even more confusing: Ferguson and Binggeli (1994) used a limit of $M_B = -16$ mag, but also $M_B = -18$ mag, to define dwarf elliptical galaxies.

1.2 Galaxy clusters and the transformation of galaxies

As we saw in the last section, there is a wealth of galaxies with very different properties. Surveys of large areas in the sky found that galaxies are not homogeneous distributed in the sky, but that there are regions with a high galaxy density (ρ) and regions with a lower ρ. The regions with a lower ρ and low number of galaxies are called "the field", whereas regions with a high ρ and high frequency of galaxies are called "clusters" and "groups". In a galaxy cluster there are thousands of galaxies in a volume of a few megaparsec[2] and prominent examples are the Perseus-, Coma- and Virgo cluster. The difference between groups and clusters is not well defined.

As shown by many studies over the last decades, galaxy clusters do not just contain galaxies. Zwicky (1937) showed by the study of the movement of galaxies in the Coma cluster that galaxy clusters need additional non-visible mass to be stable. He was the first who introduced the term "Dark Matter". Apart from galaxies and DM one also finds gas in the cluster, which is called intra cluster medium (ICM). As we will see in this thesis, this gas plays an important role in the evolution of the galaxies in the dense environment of a cluster.

In this thesis I will focus on the Virgo galaxy cluster, which has a distance of 16.52 Mpc (Mei et al., 2007) and a mean velocity of about 1200 km/s (Binggeli et al., 1987). The Virgo cluster is also the nearest galaxy cluster to our Galaxy, therefore detailed investigations and surveys exist (e.g. Sandage and Binggeli, 1984; Sandage et al., 1985; Binggeli et al., 1985; Côté et al., 2004; Fritz and Hevics Collaboration, 2011). In the early study of Binggeli et al. (1985) there were 2096 galaxies listed in the Virgo Cluster Catalog (VCC) and 388 of them are in the focus of my study.

It was first noted by Oemler (1974) and Dressler (1980) that the distribution of galaxy types in a galaxy cluster is not homogeneous. In the local Universe the fraction of early-type to late-type galaxies is lower in the inner regions of a galaxy cluster and vice versa for the outer region. This behaviour is called the morphology-density relation (Postman and Geller, 1984; Whitmore et al., 1993; Goto et al., 2003). Naturally the question arises why do we have this morphology-density relation and what drives the evolution of galaxies?

There are several mechanisms acting on a late-type galaxy, which are able to transform it. Some of them are internal others are external mechanisms and the influence depends on several parameters, for instance the mass and velocity of the galaxy and the density

[2]parsec (pc) = $3.09 \cdot 10^{16}$ m (Jones and Lambourne, 2004).

of the ICM within the galaxy cluster.

One of the internal mechanisms, which is able to influence a galaxy, is caused by the natural evolution of the stars within a galaxy. Due to stellar evolution, the lifetime of stars is limited and depends on the initial mass and chemical composition of the single star. A star like the sun has a lifetime of about 10 Gyr on the main sequence, while the lifetime is getting shorter with increasing mass and/or decreasing fraction of heavy elements (Sparke and Gallagher, 2000). Massive stars with masses about 100 $M_\odot$ will live only for several million years. In their final stage they will end up in a super nova (SN) explosion, releasing a huge amount of energy into the galaxy and the gas within. Due to the shallow gravitational potential, less massive galaxies are more effected by the feedback of the SNe than the massive ones. In extreme cases, parts the gas of the late-type galaxy can be "blown out" by the simultaneous SNe explosions in a star forming region, resulting a galactic wind (Dekel and Silk, 1986; Izotov et al., 1996; Heckman et al., 2001).

There are also external forces acting on late-type galaxies which fall into a cluster. When the galaxy enters the cluster, the ISM of the galaxy interacts with the hot ICM of the cluster, resulting in the removal of the galaxy's ISM (van Zee et al., 2004; Boselli et al., 2008). In case of the removal of the gas, which is located in the envelope of the galaxies, the star formation does not stop immediately but decreases slowly until the gas is consumed (Larson et al., 1980). This scenario is also called starvation and strangulation, respectively.

On the other hand, when almost all gas is removed from the in-falling late-type galaxy, the star formation will decrease on very short time scales. This process is called ram pressure stripping (RPS, Gunn and Gott, 1972; Farouki and Shapiro, 1981). Figure 1.3 shows an observational example for a galaxy in the Virgo cluster, which loses its gas due to RPS (Kenney et al., 2004). It is also visible in the figure that the stellar component is not influenced by the RPS event. However, the effect of ram pressure on spiral galaxies and their star formation is still debated. Gavazzi et al. (1995) and Fujita and Nagashima (1999) argued that ram pressure can also induce new star formation in galaxy, entering the cluster for the first time, by compressing the gas, which is left over in the galaxy.

Starvation and RPS are processes that occur in galaxy clusters, but they are not limited to the inner dense core of cluster. Tonnesen et al. (2007) showed that they also play an important role even up to a distance of a virial radius, which has a value of 1.5 Mpc in

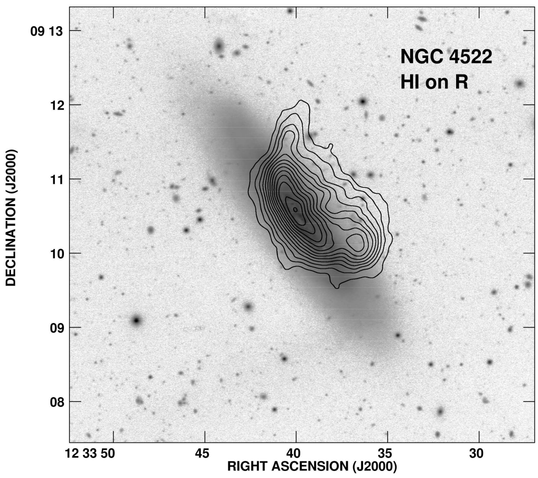

Figure 1.3: Combined image (R-band and HI) of NGC-4522 taken from Kenney et al. (2004). The HI gas was observed at radio wavelength and is over-plotted via a contour map.

case of the Virgo cluster (McLaughlin, 1999).
Another process, which influences the evolution of galaxies in a cluster, is galaxy harassment (Farouki and Shapiro, 1981; Moore et al., 1996; Mastropietro et al., 2005). In the harassment scenario high-speed encounters between cluster galaxies occur and in contrast to RPS and starvation, also the stellar component of the galaxy are affected. As a result, disc galaxies will lose a fraction of their stars and the remaining stars will be heated up, which thickens the stellar disc.
In summary, all the above described processes act on late-type galaxies, which fall into a galaxy cluster and result in a morphological transformation. This transformation will change the present-day appearance of the late-type galaxies. But the question is, how will the morphology change - to objects looking like today's dwarf elliptical galaxies or something completely different? At present day the question is not fully answered and there are also arguments against the evolution from late-types to dwarf ellipticals due to differences in their chemical composition (e.g. Grebel et al., 2003).
Therefore, the questions about the evolution of galaxies in clusters or groups, but also in isolation, is still controversially discussed among the community and there is no commonly accepted consensus in this field. To bring the discussion forward and shed more light on the evolution of galaxies, it is crucial to investigate all the transformation effects, but also the initial conditions, which are set by the currently observed galaxies.

1.3 The observation of galaxies

To investigate the properties of galaxies and galaxy clusters, informations from the light distributions of the objects are necessary. The Sloan Digital Sky Survey (SDSS, Adelman-McCarthy et al., 2007) provides a wealth of digital informations of the Virgo galaxy cluster. The SDSS uses a 2.5 m telescope (left panel of Fig. 1.4) and is located at Apache Point Observatory in New Mexico, USA (York et al., 2000; Gunn et al., 2006). To collect the light of the galaxies, the SDSS uses a 120 mega pixel CCD camera with a field of view of 1.5 square degree. The camera consists of 30 chips assembled in 6 columns with 5 filters (u,g,r,i and z) per column (right panel of Fig.1.4) and a pixel scale of 0.396 arcsec (Gunn et al., 1998). The filter characteristics[3] are shown in Fig. 1.5, and the informations of the central wavelength and the "Full Width Half Maximum" (FWHM) are summarised in Tab. 1.1.
The SDSS observed the astronomical objects in drift-scan-mode, which enables the observation in each single filter at almost the same time. Therefore, one obtains a precise photometry for the objects. The exposure time in each filter amounts to 54 s.
Due to the observation of the galaxies with the same telescope and the same observational technique, we are in the excellent situation to investigate the structural parameters and the evolutionary connections of the late-type and early-type galaxies of the Virgo galaxy cluster based on a very homogeneous sample.

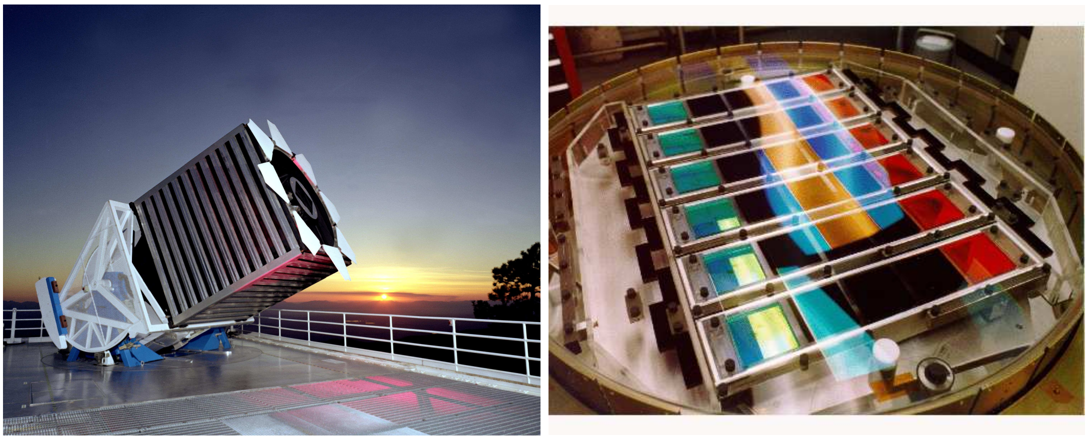

Figure 1.4: The 2.5 m telescope (left) and the CCD-camera of the SDSS (right; both images from www.SDSS.org).

[3] Intensities in Fig. 1.5 are given in arbitrary units.

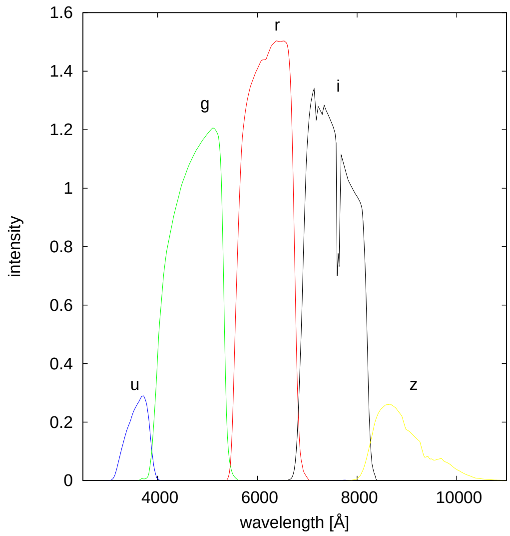

Figure 1.5: Filter characteristic of the SDSS camera.

Table 1.1: Filter characteristic of the SDSS camera.

Filter	Central wavelength [Å]	FWHM [Å]
u	3540	570
g	4770	1370
r	6230	1370
i	7630	1530
z	9130	950

1.4 Thesis outline

In Chapter 2 the structural properties of Blue Compact Dwarf galaxies (BCDs) are studied in more detail, by decomposing the contribution of the star burst region and the old stellar population of the underlying host galaxy. The results of this analysis will be used for the discussion of the possible evolutionary connections between star forming dwarfs and early-type dwarf galaxies.

In Chapter 3 the entire late-type population of the Virgo galaxy cluster is investigated and the structural properties are derived. The results of the different morphological types will be compared with each other in the derived parameter-space and, if necessary, single galaxies will be reclassified to a new morphological class.

The results of the late-type galaxies will be the foundation of Chapter 4, where the structural parameters will be used to model the time evolution of the galaxies by the means of evolutionary synthesis models of GALEV. The outcome of these analyses will shed more light on the long debated possible evolutionary links between late-type and early-type galaxies.

Chapter 2 What will blue compact dwarf galaxies evolve into?

Blue compact dwarf galaxies are objects with particular interesting properties due to their compact optical sizes, extreme star formation rates and low metallicities, which were therefore first believed to be young systems. With the improvement of the observational techniques, it was soon realised that there is an underlying component, consisting of old stars, which in turn raises the question whether these systems are really young. To investigate the underlying component of the blue compact dwarfs, the contribution of the starburst regions has to be subtracted from the total optical luminosity. The properties of this underlying component are in the focus of the following chapter. Furthermore, the derived results of the underlying components are compared to a sample of early-type galaxies within the Virgo cluster. This study sheds light on the possible evolutionary connections between the starbursting blue compact dwarfs and the "red and dead" early-type dwarf galaxies.

This study will be published together with Thorsten Lisker, Joachim Janz and Polychronis Papaderos.

2.1 Introduction

Galaxy clusters like the Virgo cluster are characterised by a large variety in galaxy morphology. This morphological variety depends on the local galaxy density, it therefore shows a clear trend with the cluster centric radius R_{CC}. The dependence of the morphology on R_{CC} was first studied by Dressler (1980) and confirmed by many subsequent studies (e.g. Binggeli et al., 1990; Jerjen, 2012). At small R_{CC} the dominant galaxy types are early-type galaxies (ETGs): elliptical (E) and lenticular (S0), normal and nucleated dwarf ellipticals (dEs and N,dEs, respectively), dwarf lenticular (dS0), and dwarf spheroidal (dSph) galaxies, spanning a range from high to low luminosities. Traditionally, ETGs are associated with a smooth, regular appearance, with no signs of star formation. However, among the dEs is a particular class of galaxies with relatively blue cores, which indicate recent or still ongoing star formation at very low star formation rates (SFRs) (e.g. Lisker et al., 2006a).

Studies of ETGs showed that they are dominated by an old stellar population, resulting in relatively red colours. These properties indicated that ETGs are the oldest galaxy population in galaxy clusters. On the other hand, dynamically young galaxy clusters (e.g. the Virgo galaxy cluster) also contain late-type galaxies, which, in contrast to the ETGs, are located at larger R_{CC}. In its low-luminosity end this group is composed of star forming (SF) dwarf galaxies like blue compact dwarfs (BCDs) and dwarf irregulars (dIs) with properties strikingly different than those of ETGs. As shown by Vilchez (1995), the Hβ equivalent width (EW) of late-type galaxies in the Virgo cluster increases with increasing R_{CC}, echoing the strong impact of the cluster environment on galaxy evolution.

Tempting questions in this respect are i) how could this morphology-density relation be explained, ii) which mechanisms are responsible for the gradual transformation of late-type galaxies into ETGs as R_{CC} decreases, and iii) are the descendants of today's late-type galaxies objects like ETGs in the Virgo cluster. In the literature several mechanisms have been proposed as drivers of galaxy transformations within the dense cluster environment, most notably *ram pressure stripping* (Gunn and Gott, 1972), *tidal stirring* (Mayer et al., 2001) and *harassment* (Moore et al., 1996; Mastropietro et al., 2005), all of which have in common the removal of gas (see e.g. Hensler, 2012, for a recent review).

Dwarf galaxies with a low central stellar density $\rho_\star$, such as dIs, are expected to be particularly prone to gas removal as they plunge into the hot intracluster medium (ICM), whereas high-$\rho_\star$ systems such as BCDs (cf. e.g. Papaderos et al., 1996b) might be able to retain some fraction of their gaseous reservoir down to a lower R_{CC}. But how would these dwarfish late-type galaxies in the cluster periphery look like after some billion years, once their gas content has been removed, in the course of one or several passages through the dense ICM core, and their ensuing long passive photometric evolution? Addressing this question is fundamental to the understanding of the morphological diversity of the dwarf galaxy population in clusters. Another issue of special interest is, what impact has the initial contact of late-type dwarfs with the cluster periphery on their SF activity and whether, for certain conditions, starbursts can be ignited, transforming them into BCDs. If so, then how do these cluster-BCDs differ from the main population of field BCDs in their recent star formation history (SFH) and the morphological and metric properties of their SF component?

BCDs are low-luminosity galaxies ($M_B > -18$ mag) with a compact optical appearance and blue integral colours (Thuan and Martin, 1981). Many studies over the past decades have shown that BCDs are metal deficient with a median oxygen abundance $12 + \log(O/H) \sim 8.0$ (e.g. Kunth and Östlin, 2000) and a small percentage of systems with a gas-phase metallicity as low as $7.0 \lesssim 12 + \log(O/H) \lesssim 7.6$ (Searle and Sargent, 1972; Izotov et al., 1999a; Kunth and Östlin, 2000; Kniazev et al., 2004; Papaderos et al., 2008). These systems (XBCDs) are therefore the best nearby analogues of young low-mass galaxies in the early Universe (see e.g. the discussion in Papaderos et al., 2008). Apart from their low metallicity, BCDs also exhibit strong bursts of star formation, which are fed by a relatively large amount of gas (Thuan and Martin, 1981; Staveley-Smith et al., 1992; van Zee et al., 1998). Various arguments suggest, in line with evolutionary synthesis models, that starbursts in BCDs do not last longer than a few 10^7 yr (Thuan, 1991; Krüger et al., 1995; Mas-Hesse and Kunth, 1999; Thornley et al., 2000) and have to be separated by long (~1 Gyr) quiescent phases. Dwarf irregulars, on the other hand, are characterised by prolonged low-level star formation over time scales of 450 Myr up to 1.3 Gyr, as shown by, e.g., McQuinn et al. (2010b, see also Skillman et al. (2012) for a review) through colour-magnitude diagram (CMD) studies of 20 of these systems.

The seminal study by Loose and Thuan (1985) has shown that BCDs are composed of two main stellar components. The first one displays the region of the ongoing star formation where young OB-stars are rapidly formed, it therefore has a low M/L-ratio. Due to the simultaneous formation of new massive stars in the starburst and their death within several Myr, metal-enriched galactic winds resulting from multiple supernovae explosions are expected to influence the chemical evolution of BCDs. However, studies have shown that in most cases starburst-driven feedback is insufficient for the expulsion of the entire ISM from a BCD (e.g. Silich and Tenorio-Tagle, 1998; Ferrara and Tolstoy, 2000; Tajiri and Kamaya, 2002; Recchi and Hensler, 2006).

The starburst component contributes, on average, ~50% of the optical emission of a BCD and, in some cases, up to 90% (Papaderos et al., 1996b; Noeske, 1999;

Cairós et al., 2001b; Amorín et al., 2009). Quite importantly, in several XBCDs[1] nebular emission has been determined to be extraordinarily intense (EW ~ 1600 – 2000Å) and to contribute 30–50% of their total optical luminosity (Papaderos et al., 1998, 2002), in line with theoretical predictions for young starbursts (e.g. Krüger et al., 1995).

The second component of BCDs is dominated by an old population of M and K stars. This component is referred to in the following as the *host galaxy* or *low-surface brightness (LSB)*[2] component and is characterised by a high M/L-ratio. Various studies indicate that the LSB-component dominates the baryonic-, and in some cases even the virial mass of BCDs within their Holmberg radius[3], it therefore has to have a significant influence on the gas collapse characteristics and the starburst activity in these systems (e.g. Papaderos et al., 1996a; Östlin et al., 1999; Lelli et al., 2012).

According to Loose and Thuan (1986) BCDs can be classified in four main classes, based on the morphology of their SF- and LSB-component. Table 2.1 summarises the different morphological types of BCDs. Nuclear-elliptical (nE) and irregular-elliptical (iE) BCDs, both characterised by an extended circular or elliptical LSB-component, dominate the BCD population (~90%). Irregular (iI) BCDs comprise about 10% of local BCD population. Interestingly, their *cometary* (iI,C) subclass (see e.g. Noeske et al., 2000, for two nearby examples) is remarkably common among XBCDs (Papaderos et al., 2008), a fact pointing to a connection between gas-phase metallicity, morphology and evolutionary status. This is also indirectly suggested by the large frequency of cometary galaxies (also referred as tadpoles) among comparatively unevolved high-z galaxies (e.g. Elmegreen and Elmegreen, 2010). Whereas, the galaxies VCC-0802 and VCC-0274 are the most characteristic examples of the iI,C class in the Virgo cluster, a closer inspection of the VCC catalogue reveals several more such candidates. It is probable that the cometary morphology in cluster-BCDs has a different origin than in more isolated systems. Cometary morphology in field XBCDs has been proposed to result from unidirectional sequential SF activity with a typical velocity of the sound speed in the warm ISM (~20 km/sec, Papaderos et al., 1998,

---

[1]The X indicates the *extreme* properties of these BCDs.

[2]Note: The LSB-component of BCDs should not be mixed up with the galaxy type commonly called "Low Surface Brightness galaxies". To the contrary, a high central surface brightness ($\mu_0(B)$ <22 mag/arcsec^2) has been found to be a characteristic property of the LSB host of BCDs (Papaderos et al., 1996a; Gil de Paz and Madore, 2005) implying a much higher central mass density than in dIs, and the more so, in dSphs and genuine ($\mu_0 \geq 23.5$ mag/arcsec^2) LSB galaxies.

[3]The Holmberg radius defines the radius, where μ(B) = 26.5 mag/arcsec^2.

2008). This scenario is supported by stellar age gradients along the “comets tail” (e.g. Guseva et al., 2003). In the cluster periphery, however, cometary morphology may arise from extranuclear star formation that is triggered through the interaction with the ICM (see Hensler, 2012, for a recent comprehensive review), as, e.g. the impressive cases of two SFDGs in Abell 1367 (Gavazzi et al., 2001) demonstrate.

Apart from the classification scheme of Loose and Thuan (1986), there are also other proposed schemes in the literature based on photometric and/or spectroscopic properties of the BCDs (e.g. Salzer et al. (1989), Sung et al. (2002), Telles et al. (1997) and Cairós et al. (2001a)). In the study presented here, will shall use the classification schema by Loose and Thuan (1986).

The evolution of star forming dwarf galaxies (SFDGs) like BCDs to “red and dead” early-type galaxies is still under debate and there is no satisfying answer right as yet. Early studies by Thuan (1985) and Davies and Phillipps (1988) introduced the possible evolution of dIs into BCDs in several bursts and finally, after reaching a higher metallicity and the depletion of gas, the fading into dEs. Thuan (1985) concluded that the metallicities of BCDs and dEs are very different and that only periods of 3-10 bursts over the Hubble time could be able to produce the metallicity range of dEs. The study of Marquart et al. (2007) on the BCD He 2-10 showed that the stars in this galaxy have random motions and show signatures of a merger. They concluded that, due to the velocity dispersion of the stars, in the future this BCD may evolve into a nucleated dE. In comparison to this, the simulations of Bekki (2008) showed that dwarf-dwarf mergers are able to produce BCDs, but the further evolution of these BCDs into dEs with no gas is ruled out due to the extended gas discs of the simulated BCDs.

In contrast to BCDs, the early-type dwarf galaxies (ETDGs) show almost no evidence for ongoing SF. However, several studies e.g. by Vigroux et al. (1984), Gu et al. (2006) or Lisker et al. (2006a) found dEs with blue colours (so called dE(bc)s) in their central region. The study by Lisker et al. (2006a) of 476 dEs in the Virgo cluster has disclosed 23 dEs with central blue colours, indicating recent or ongoing SF. Since the debate of the evolutionary connection of ETDGs and BCDs is still ongoing, it is worth to compare the structural properties of these two types of galaxies (BCDs vs. ETDGs) and in particular the properties of the dE(bc)s (BCDs vs. dE(bc)s).

The goal of this study is to shed light on two questions. First, whether BCDs in the periphery of galaxy clusters share similar structural properties with field BCDs and, secondly, whether the former can evolve into dEs after the cessation of their starburst. Neither question has been previously addressed in the literature.

Table 2.1: Different subtypes of BCDs according to the morphology of the starburst- and LSB-component.

Subtype	Description
nE	nuclear star forming region and
	elliptical LSB-component (~20%)
iE	irregular star forming region(s)
	and elliptical LSB-component (~70%)
iI	irregular star forming region(s)
	and LSB-component (~10%)
iI,C	iI with cometary shape
i0	no detected LSB-component (very rare)

This paper is structured as follows: Section 2 presents our sample of cluster BCDs and the classification criteria used. In Section 3 we discuss the method used to derive surface brightness profiles (SBPs) and their decomposition into the luminosity contribution from the starburst and the underlying LSB-component. Several examples of our decomposition methodology and an initial discussion of the derived structural properties are given in Section 4, and in Section 5 we present a comparative study of the structural properties of our BCD sample with field BCDs, dIs and dEs. Our results and conclusions are summarised in Section 6.

2.2 Sample selection and data reduction

2.2.1 Sample selection

Our sample is based on the Virgo Cluster Catalog (VCC) by Binggeli et al. (1985), which includes galaxies of all types within the Virgo cluster area. Due to incomplete velocity information for the VCC galaxies, the VCC includes certain and possible cluster members (updated by Binggeli et al., 1993), apart from background galaxies. Since new velocities have become available in the meantime, largely due to the Sloan Digital Sky Survey (SDSS, Adelman-McCarthy et al., 2007), the membership was revised by one of us (T.Lisker, see appendix of Weinmann et al. 2011) using the NASA/IPAC Extragalactic Database (NED). If a galaxy is listed as certain or possible member in the VCC, but has a velocity above 3500 km/s, it is considered as a background galaxy. We do not change possible to certain members or vice versa.

For our study we take into account both certain and possible members to a magnitude limit of $m_B \leq 18.0$ mag, to which the VCC was found to be complete (Binggeli et al., 1985). When applying a constant distance modulus of $m - M = 31.09$ mag (d = 16.5 Mpc; Mei et al., 2007) to all galaxies, this corresponds to an absolute magnitude limit of $M_B < -13.09$ mag.
Within these limits, the VCC contains 57 galaxies which have the term “BCD” included in their morphological type, 38 of them with BCD as the only or primary class (Tab. 2.2.2). Among the galaxies listed as “unknown” in the VCC, a visual inspection of the SDSS images[4] suggests a reclassification of VCC-0429 and VCC-1713 to the transition type “Im / BCD”, and of VCC-1411 to a possible “BCD?”, thus adding up to 60 galaxies, and 39 with BCD as primary class. Since the VCC photographic plates were more sensitive in the blue, it needs to be kept in mind that this could have partly influenced the classification, as any underlying red stellar population would appear less prominent in the blue. Therefore, we treat the 39 galaxies with primary class BCD as the primary working sample for our analysis. The remaining 21 galaxies with uncertain morphological classification, but still possibly being a BCD, are treated as a separate sample, which will be compared to the BCDs in Section 2.4.8.

2.2.2 SDSS data

To analyse the Virgo BCDs we have used the SDSS Data Release Five (DR 5) in u, g, r, i and z band with an effective exposure time of 54 s. Due to insufficient sky subtraction of the SDSS pipeline for nearby galaxies of large apparent size, we used the sky-subtracted images of Lisker et al. (2007), using DR5 data. All images were flux calibrated and corrected for Galactic extinction following Schlegel et al. (1998). Five of the 39 BCDs are not covered by the SDSS DR5 and one BCD is excluded because of a nearby other galaxy (VCC-1944). Figure 2.1 shows the distribution of the remaining 33 BCDs within the Virgo cluster. The position of M87 is marked with a black cross.
To avoid contamination by other sources than the galaxy itself, one has to remove these sources very carefully. This was done for the BCD sample by replacing for instance the flux of a star by the median flux of its environment.
For the analysis of the sample of dEs, dE(bc)s and dIs we follow the method described in Lisker et al. (2007) and Janz and Lisker (2008). The parameters of the additional sample are measured within an elliptical aperture of two Petrosian radii (Petrosian,

[4]Using the online Image List Tool of the SDSS, http://skyserver.sdss3.org/dr8/en/tools/chart/list.asp.

Table 2.2: Galaxies that were initially classified according to their morphology as "BCD" or "uncertain BCD". In the VCC a ":" indicates a weak uncertainty in the morphological classification of the galaxy, whereas a "?" points to a strong uncertainty. Roman numerals are the luminosity class of the galaxy regarding the original catalogue by Sandage and Binggeli (1984).

Amount	Type
38	"BCD", "BCD?", "BCD:","BCD or merger"
10	"Im / BCD", "Im III / BCD", "Im III / BCD:"
	"Im III / BCD?", "Im III,pec / BCD"
3	"Spec / BCD", "Spec,N / BCD"
3	"Sm III / BCD", "SBm III / BCD"
1	"dS? / BCD?"
1	"Sd / BCD?"
1	"dS0 or BCD"
2	"unknown" → "Im / BCD"
1	"unknown" → "BCD?"

1976) and objects, which do not belong to the galaxy were masked out. The effective radius was measured via:

$$\mathrm{R_{eff}} = \mathrm{a_{hl}} \cdot \sqrt{(b/a)}, \tag{2.1}$$

with the semi-major axis half-light radius $\mathrm{a_{hl}}$ and the axis radio (b/a).

2.3 Surface photometry and decomposition

BCDs consist of a starburst (SB) component embedded within a more extended stellar LSB-component of older stars (see Section 2.1). The luminosity contribution of the starburst amounts, on average, to ~ 50% of the *B* band emission, and in some extreme cases reaches up to ~ 90% (Papaderos et al., 1996b; Noeske, 1999; Salzer and Norten, 1999; Amorín et al., 2009). On the other hand, the starburst component is almost negligible, in terms of its fraction by *mass*, as its M/L ratio is several times lower than that of the LSB-component. An adequate separation of its emission via 1D or 2D decomposition is clearly necessary for isolating the emission and studying the structural properties of the host galaxy. Indeed, the composite SBP of a BCD holds prior to decomposition little insight into the photometric structure. For example, Papaderos et al. (1996b) have pointed out that the SBP of a nE BCD can closely

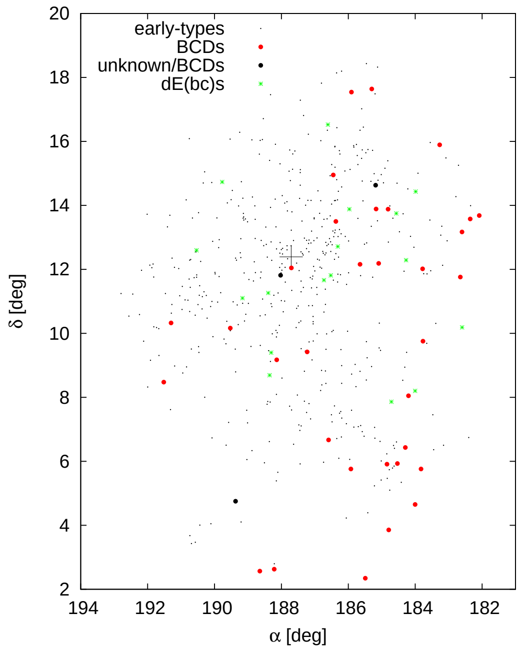

Figure 2.1: Map of the Virgo cluster. Red symbols refer to BCDs, big black dots to galaxies of the class “unknown”, small black dots to early-type galaxies, green asterisks to dE(bc)s and the black cross to M87.

resemble the $R^{1/4}$ SBP of a massive elliptical, whereas a typical feature of the SBPs of iE BCDs is an extended *plateau*, which can be fitted by a Sérsic law with an exponent of $2.5 \lesssim \eta \lesssim 4$, and resembling the bulge of S0 galaxies. Similarly the effective radius R_{eff}, a quantity commonly used in studies of high-z galaxies, can vary by up to a factor $\sim$3, depending on the starburst luminosity fraction (cf. e.g. Papaderos et al., 2006).
For galaxies with a smooth appearance like elliptical galaxies the easiest way to obtain SBPs is to use elliptical apertures and sum up the enclosed flux. Due to the irregular morphology of BCDs, however, such an approach is impractical, on the one hand because the choice of the ’galaxy center’ is subjective and wavelength-dependent (thus SBPs and radial colour profiles are not easily reproducible), and, on the other hand, because SBPs derived in this way show, in the case of iE- and iI-BCDs, discontinuous jumps. In some cases, the latter can significantly affect the intensity profile of the LSB-component, thereby biasing studies of the photometric structure of BCDs. 2D axis-symmetric models to BCDs other than those falling into the nE class also yield systematic residuals, unless one carefully masks out and avoids fitting of the SF-component, as was done in e.g. Amorín et al. (2009).

Therefore, we applied method iv) of Papaderos et al. (2002), which was also used by Noeske et al. (2006) under the name LAZY. This method, which has as input a set of co-aligned multi-band images of the same pixel scale (SDSS: 0.396 arcsec/pix) and point spread function (psf), does not require a choicse for the 'centre' of a galaxy. In our study, an average FWHM of the psf of 4 pix (1.584 arcsec) was applied to smooth the input images with a Gaussian convolution kernel. From these co-aligned images a S/N weighted average image (called reference frame) is created, which is used to calculate a mask for each intensity interval ΔI within the range I_{min} to I_{max}. Pixels outside the intensity interval of $I - \Delta I \leq F \leq I$ are set to zero, while pixels within the interval are given full consideration (set to unity). In the next step, each mask is multiplied by all input images (ugriz-band) and the flux is measured within each irregular mask. The corresponding photometric radius R^* is calculated as:

$$R^* = \left(\frac{A_I + A_{I-\Delta I}}{2\pi}\right)^{1/2}. \tag{2.2}$$

In Equation 2.2, $(A_I + A_{I-\Delta I})$ are the areas with intensities above I and $I - \Delta I$. In the case of multiple SF regions the R^* derived in this way corresponds to the sum of their area, a concept which translates into a monotonous increase of radius with decreasing intensity threshold.

A validity check of Lazy can be found in Section 2.3.6, where the SBPs of dEs are compared for different methods of profile derivation.

2.3.1 LSB-component: exponential model

To distinguish the SB- from the LSB-component we use (g-i)-colour profiles. At smaller R^* the (g-i)-colour profile is due to the superposition of the contribution of the young SB population and the old population of the LSB-component, which results in relatively blue values. At larger R^* the contribution of the SB-component vanishes and the old LSB-component dominates, which results in relatively constant red colours. The radius beyond which the colour index levels off to a red, nearly constant value is referred to as *transition radius* R_{tr} (Papaderos et al., 1996b; Cairós et al., 2003; Noeske et al., 2003). We used this characteristic radius to define the minimum R^* for fitting an exponential law of the form

$$I_{LSB}(R^*) = I_{LSB,0} \exp\left[-(R^*/\alpha)\right], \tag{2.3}$$

to the LSB-component. In units of mag arcsec^{-2} Equation 2.3 reads as

$$\mu_{LSB}(R^*) = \mu_{LSB,0} + 1.086\,(R^*/\alpha), \tag{2.4}$$

where $I_{LSB,0}$ and $\mu_{LSB,0}$ are the central intensity and central surface brightness of the LSB-component, and α is its exponential scale length.

2.3.2 LSB-component: inner flattening

In some cases the extrapolation of the exponential fit to R^*=0 arcsec exceeds the intensity observed at intermediate and small radii. This implies that the exponential law is not applicable in the central part of the LSB-component and must flatten to a central surface brightness that is lower than the extrapolated value $\mu_{LSB,0}$ of the fit for $R^* \geq R_{tr}$. This kind of perfectly exponential SBPs with a flat core were noticed by Binggeli and Cameron (1991) who have called them type V. Papaderos et al. (1996b) introduced a modified exponential law to approximate such profiles, motivated by two considerations: First, a Sérsic law with a shape parameter $\eta \lesssim 0.5$ cannot fit type V SBPs without producing systematic residuals (see Noeske et al., 2003, for a detailed discussion of this subject). Secondly, as shown by radiation transfer models by Papaderos et al. (1996b), a Sérsic law with $\eta \lesssim 0.5$ implies an extended 'hole' in the intrinsic luminosity density of a spheric-symmetric emitter, if radiation isotropy, and a uniform M/L ratio and intrinsic extinction are assumed. As these authors considered the evacuation of the dwarf galaxy centres to be improbable, they introduced an intensity profile for which the intrinsic luminosity density increases monotonously with decreasing radius (for small flattening parameters at least; see below) and has a finite central value. This modified exponential fitting law (**modexp**) has the form

$$I_{LSB}(R^*) = I_{LSB,0}\ \exp\left(-\frac{R^*}{\alpha}\right)[1 - q \cdot\ \exp(-P_3(R^*))], \tag{2.5}$$

where

$$P_3(R^*) = \left(\frac{R^*}{b\alpha}\right)^3 + \left(\frac{R^*}{\alpha} \cdot \frac{1-q}{q}\right), \tag{2.6}$$

with the typical ratio b/q being of the order of three (Papaderos et al., 1999 and Papaderos and Östlin, 2011). b is a measure of the radial extent of the central core in units of the exponential scale length α and $q = \frac{\Delta I}{I_{LSB,0}}$ describes the attenuation of the **modexp** fit, as compared to the central intensity $I_{LSB,0}$ predicted by the pure exponential fitting law. A parameter of $(b, q) = (2.40\ , 0.80)$ corresponds to a flattening of the central intensity for a pure exponential LSB-component of 20% and a core radius of 2.4 α. Due to the poor knowledge of the structure of the LSB-component in its central part it is not clear at the moment which parameter combination of (b,q) satisfactorily describes the original shape. Therefore, the choice of (b,q) is not a straightforward task

and has to rely on plausibility considerations (cf. Noeske et al., 2003). In this study a flattening toward smaller radii was only applied when $\mu_{\mathrm{LSB},0}$ exceeds the LSB+SB central surface brightness $\mu_{\mathrm{tot},0}$, and the spectrum shows clear signs of star formation.
For a detailed discussion about the advantage of using flattening formula instead of Sérsic fits we refer to the study of Noeske et al. (2003) and Cairós et al. (2003). By using a parameter of $(b, q) = (2.40, 0.80)$ the resulting magnitude of the LSB-component is increased by 0.48 mag and μ_0 is reduced by 1.747 mag/arcsec^2. Since the magnitude difference of 0.48 mag is applied to all filter bands, the colours of the LSB-components are not affected.
The SBP of the galaxy VCC-0641 exemplifies the central flattening of the exponential LSB-component (see Fig. 2.5 and Section 2.4.1).
The mean effective surface brightness $\langle\mu\rangle_{\mathrm{eff}}$ of the LSB-component was calculated by:

$$\langle\mu\rangle_{\mathrm{eff,LSB}} = \mathrm{m}_{\mathrm{LSB}} + 2.5\log\left(2\pi\,\mathrm{R}^2_{\mathrm{eff,LSB}}\right). \tag{2.7}$$

The effective radius $\mathrm{R}_{\mathrm{eff,LSB}}$ of the LSB-component was determined by the integration of the exponential or flattened SBP to the radius within which one half of the total flux is enclosed.

2.3.3 LSB-component: outer tail

The inspection of the SBPs of our BCD sample reveals that in most cases the exponential slope of the LSB-component shows a slight flattening for large radii, corresponding to very faint surface brightness levels ($\mu \gtrsim 27$ mag/arcsec2). This is illustrated in Fig. 2.2 for one galaxy, and is also clearly visible in Fig. 2.5 for VCC-1744 for a radius R > 15 arcsec. We note that such a flattening has been reported in the outskirts of some BCDs, e.g. II Zw 71 and Mrk 178, and it contributes for no more than ~3% of the total luminosity (Papaderos et al., 2001, 2002).
Due to this additional flux contribution from the outermost luminosity component, it is possible that the $\mathrm{R}_{\mathrm{eff}}$ is slightly increased, even though this effect is likely marginal. To check the influence of the tail on the $\mathrm{R}_{\mathrm{eff}}$, the LSB-component was integrated for an exponential slope until $\mathrm{R}_{\mathrm{tail}}$ and then for $\mathrm{R} > \mathrm{R}_{\mathrm{tail}}$ with the observed tail (the LSB+tail-profile). The radius where the observed SBP of the LSB-component deviates from a pure exponential slope is called tail-radius $\mathrm{R}_{\mathrm{tail}}$. This tail-radius $\mathrm{R}_{\mathrm{tail}}$ is located in Fig. 2.5 for VCC-1744 at a radius R > 15 arcsec. If necessary, a flattening of the SBP towards smaller radii was applied too.
In Fig. 2.2 one can see an example of an SBP with a tail.

From the integration of the LSB+tail-profile one can also obtain the Petrosian radius where the η – function[5] reaches $\eta = 0.2$ (Blanton et al., 2001; Yasuda et al., 2001). For reasons of homogeneity all parameters are derived within two Petrosian radii of the LSB+tail-profile. The tail of the BCDs may be caused by nearby bright stars or galaxies, which increase the local sky. LAZY, just like all surface photometry codes, is very sensitive on the quality of sky subtraction, and objective selection and removal of areas with enhanced sky level adjacent to a galaxy is difficult, and may introduce additional uncertainties. To overcome this problem the parameters of the LSB-components were derived within R_{tail} and subsequently corrected for the missing flux. The latter was estimated by integrating the SDSS images in each filter in the interval of $[R_{tail} : R_{2Petrosian}]$ using elliptical apertures and the masking program SExtractor (Bertin and Arnouts, 1996). This analysis resulted in a correction value δX of the magnitude and R_{eff}, respectively. The final parameter X was corrected by the following equation:

$$X_{corrected} = X\,(\leq R_{tail}) + \delta X. \tag{2.8}$$

Using this correction all photometrical and structural parameters were derived within two Petrosian radii (Petrosian, 1976; Graham and Driver, 2005) with $\eta(R_{Petrosian}) = 0.2$ using the combined SBP of the LSB-component. This combined LSB-profile accounts for additional flux at very low surface brightness level. For the diagrams and tables of this work, all value were corrected for the tail with the above described technique.

2.3.4 Starburst component

The SBPs of BCDs display at small photometric radii a luminosity excess that is due to emission from the SF regions. However, this central peak in SBPs does not necessarily imply that all SB regions are centrally confined to the BCD host, given that LAZY automatically ascribes the smallest R^* to the brightest region in a galaxy. Besides a central, nearly Gaussian luminosity peak, reflecting the emission of the brightest SB region (if available), the SBPs of BCDs display at small to intermediate radii the *plateau* feature mentioned in Section 3. The plateau can be approximated (see e.g. Papaderos et al., 1996b) by the Sérsic law (Sérsic, 1968):

$$I_P(R^*) = I_{P,0}\, \exp\left[-(R^*/\beta)^{\eta}\right], \tag{2.9}$$

with the scale length β and the Sérsic index η.

[5]Please do not mix up η of the Sérsic law with the η of the η – function.

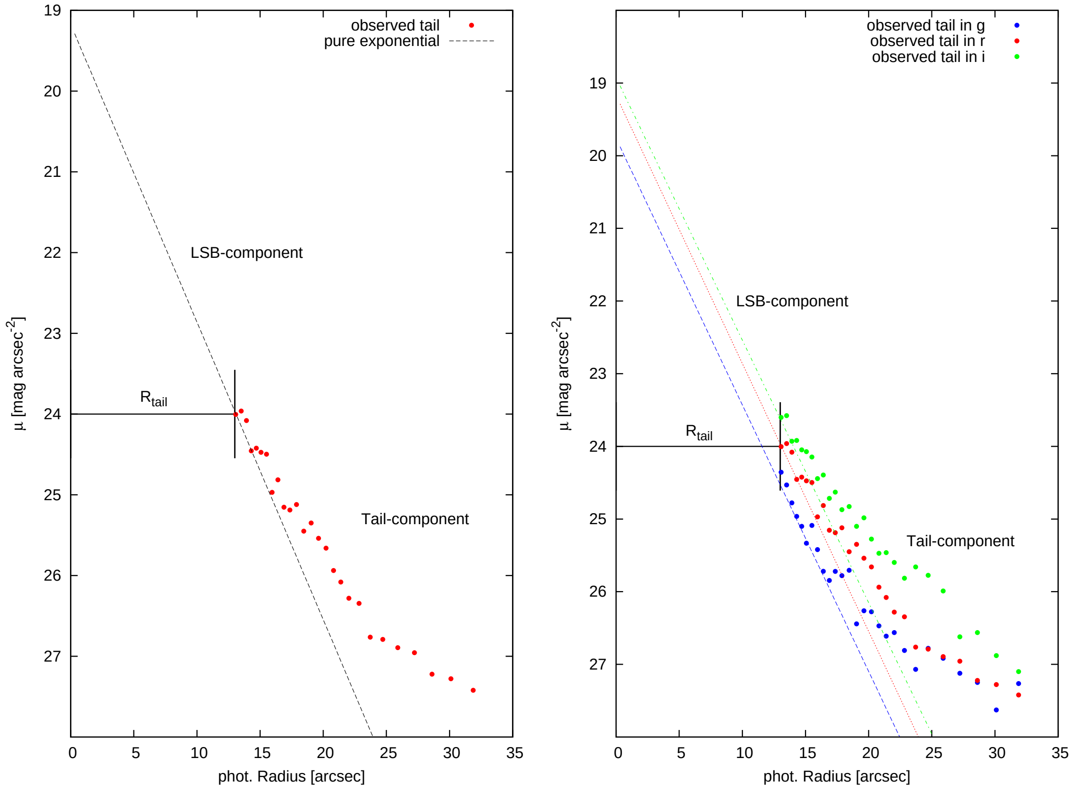

Figure 2.2: SBP of a BCD. Left panel: Line corresponds to an exponential fit to the LSB-component and the red data points show the outer tail in r-band. Right panel: same, but for the g,r and i-filters. Obvious are the outer tails of the profiles at low surface brightness levels. The horizontal bars indicate the radius at which the profile deviates from a pure exponential fit.

The corresponding surface brightness reads:

$$\mu_{\mathrm{P}}(\mathrm{R}^*) = \mu_{\mathrm{P},0} + 1.086\,[(\mathrm{R}^*/\beta)^{\eta}]. \tag{2.10}$$

Even in the case of a flatting of the SBP towards smaller photometric radii, a weak starburst is assumed and superposed on the LSB component.

2.3.5 Determination of the apparent axis ratio

To derive the apparent axis ratio b/a $= 1 - \epsilon$ - where a and b are the semi-major and semi-minor axis, respectively and ϵ is the ellipticity of the LSB-component - we used the IRAF task *ellipse* (Jedrzejewski, 1987). The axis ratio b/a was measured at a radius of one Petrosian radius (Petrosian, 1976) with an elliptical annulus. The

Petrosian radius was measured for the entire BCD without any decomposition into star burst and LSB-component. We choose the one Petrosian radius to avoid disturbances due to the star forming inner regions of the BCDs. The axis ratio was determined by the co-added optical gri-image of the BCD, without taking into account the flattening of the LSB-component. Since the flattening is only important for the inner part of the LSB-component the axis ratio at larger radii is not effected and therefore no special algorithm was applied.

2.3.6 Additional tests: comparison of SBPs for different methods

To check the validity of the code LAZY, we compare the results of LAZY with IRAF/ellipse for two dwarf elliptical galaxies. Since the light distribution in dEs is a smooth function, both methods should provide the same results. Figure 2.3 shows the comparison of both methods for two example dEs from the Virgo cluster (VCC-0218 and VCC-0916). As one can see, both method indeed produce almost the same SBPs. To obtain the magnitude and the effective radius of the galaxies, the SBP were integrated over the entire range of radius. The results of the integration are shown in Tab. 2.3.

Table 2.3: Comparison between LAZY and IRAF/ellipse.

VCC	$m_{ellipse}$ [mag]	m_{LAZY} [mag]	$R_{eff,ellipse}$ [arcsec]	$R_{eff,LAZY}$ [arcsec]
0218	14.13	14.02	12.80	13.48
0916	14.81	14.83	5.33	5.249

Additionally, values of the total SBP, where no decomposition was applied, of the two BCDs are displayed in Tab. 2.4. The SBPs were integrated by using three different methods, namely a profile integration using the program python, LAZY and AMOR. For these two example galaxies, one can see that the results are in good agreement. However, LAZY seems to produces slightly larger effective radii.

2.4 Results

2.4.1 Decomposition examples

In this section we discuss in more detail our analysis methodology on the basis of three illustrative examples. The upper panels of Fig. 2.4 show the co-added gri-SDSS

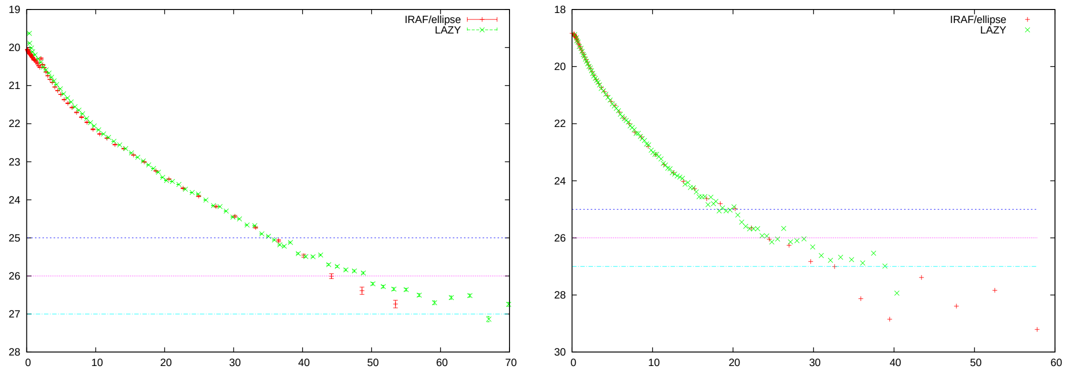

Figure 2.3: SBPs of two dEs from the early-type sample of Janz and Lisker (2008); Janz and Lisker (2009), derived with LAZY (green) and IRAF/ellipse (red data points), respectively. Left: VCC-0219; Right: VCC-0916.

Table 2.4: Comparison between python-, LAZY- and Amor-integration. “expo” corresponds to an exponential fit to the LSB-component.

VCC	m_{python} [mag]	m_{LAZY} [mag]	m_{Amor} [mag]	$R_{eff,python}$ [arcsec]	$R_{eff,LAZY}$ [arcsec]	$R_{eff,Amor}$ [arcsec]
0001	14.76	14.73	14.73	4.59	4.84	4.53
0024	14.82	14.80	14.88	4.49	4.77	4.23
0001 (expo)	14.86	14.86	-	5.04	5.03	-
0024 (expo)	15.08	15.08	-	5.30	5.28	-

images of these three galaxies. VCC-1744 (left) shows a very strong star forming region, which is off-centred. On the other hand, the star forming regions in VCC-0130 are spread over the entire galaxy, resulting in an irregular LSB-component. This is also visible in the contour map of the galaxy (middle right panel). VCC-0641 also shows star formation spread over a large fraction of its surface with one dominant SF knot, which is off-centered. The SDSS spectrum of VCC-1744 shows very strong emission lines, as typical for BCDs. VCC-0130 and VCC-0641 also show emission lines and a rising blue continuum in their spectra, even though these emission lines are not as strong as in the case of VCC-1744. Figure 2.5 shows the results of our decomposition analysis of these three BCDs. The upper panels of Fig. 2.5 show the SBPs in the r band and the lower panels show the colour profiles. The colour profiles for the galaxies do not cover the same range in photometric radius as the SBPs because the S/N in the outskirts of the LSB-component become lower, resulting in a large variation in

the colours. VCC-1744 on the left hand side of Fig. 2.5 is an example for a galaxy with an exponential LSB-component. By extrapolating its slope to $R^* = 0$ arcsec one obtains a central surface brightness of $\mu_{0,\mathrm{LSB}} = 21.61$ mag/arcsec^2. At $\mu =$ 25 mag/arcsec^2 the size of the SB- and LSB-component amounts $R^*_{\mathrm{SB}_{25}} = 2.4$ arcsec and $R^*_{\mathrm{LSB}_{25}} = 11.6$ arcsec, respectively. The transition radius - where the colours are getting roughly constant, or the slope of the colour-profile changes - was found to be $R_{\mathrm{trans}} \approx 4$ arcsec. This can be seen in the colour profile in the lower left panel in Fig. 2.5. At smaller radii ($R^* < 4$ arcsec) the colours became bluer, due to the strong star forming region. The SBPs of the galaxy VCC-0130 (middle) and VCC-0641 (left) of Fig. 2.5 show that a pure exponential approximation of the LSB-component would overestimate the central surface brightness of the LSB-component ($\mu_{0,\mathrm{LSB}}$). Therefore, we assume a central flattening with a flattening parameter of (b,q) = (2.4,0.8) and obtain $\mu_{0,\mathrm{LSB,flat}} = 22.13$ mag/arcsec^2 for VCC-0130 and $\mu_{0,\mathrm{LSB,flat}} =$ 21.95 mag/arcsec^2 for VCC-0641. Furthermore, looking at the central upper panel of Fig. 2.4, one can see that the optical image of VCC-0130 shows several star forming regions, which further justify the application of the **modexp** fitting function.
The colour profile of VCC-0130 shows a very flat form with no hint of a strong star formation, but with the informations from the optical image and the spectrum it is evident that the BCD hosts significant SF activity, a fact again motivating the application of **modexp**. On the other hand, the colour profile of VCC-0641 shows redder colours at larger radii, indicating a change of the stellar population from its SF component towards its LSB-component. Another aspect, which is apparent from the colour profile of VCC-0641, is some ambiguity in the classification of BCDs: the starburst component is offset from the centre indicating an irregular starburst. The LSB-component has an elliptical shape, but with some distortion, thus it is possible to classify it both as iI or iE.

2.4.2 Comparison of integral photometric properties with those of the LSB-components

The structural and colour properties of the BCDs are illustrated in Fig. 2.6 for the entire galaxies, and in Figs. 2.7 through 2.9 for the LSB-components only. Table 6.2 summarises the results of our analysis. For every single BCD the results for the total BCD and the underlying LSB-component are given (column [5] to [12]). The membership (ms) to the Virgo cluster was adapted from Binggeli et al. (1985) and Binggeli et al. (1993) with an update by T. Lisker (see Lisker et al. (2006a)

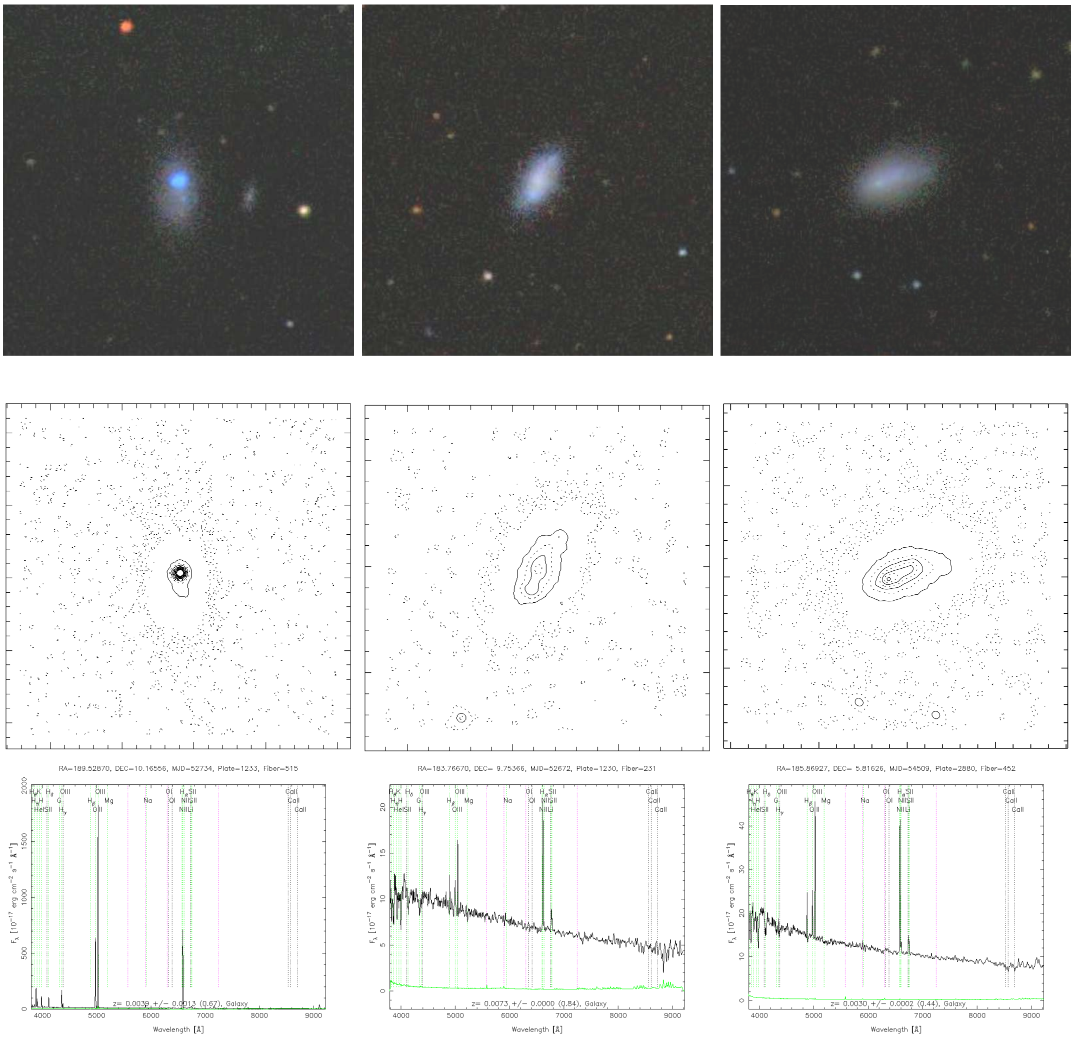

Figure 2.4: Co-added gri-SDSS images (upper), contour-maps (middle) and spectra (lower) of VCC-1744 (left panel), VCC-0130 (middle panel) and VCC-0641 (right panel).

and references therein) with recent values from the literature (column [2]). The classification criteria of the LSB-component (column [3]) are given according to Tab. 2.1. Column [4] indicates whether a flattening towards smaller radii was applied (see Section 2.3 for more details). Column [14] shows the total absolute magnitude of the entire BCD when applying the distance given by the GOLDMine data base. The differences between a distance of 16.52 Mpc and the GOLDMine distance are discussed in detail in Section 2.5.2.

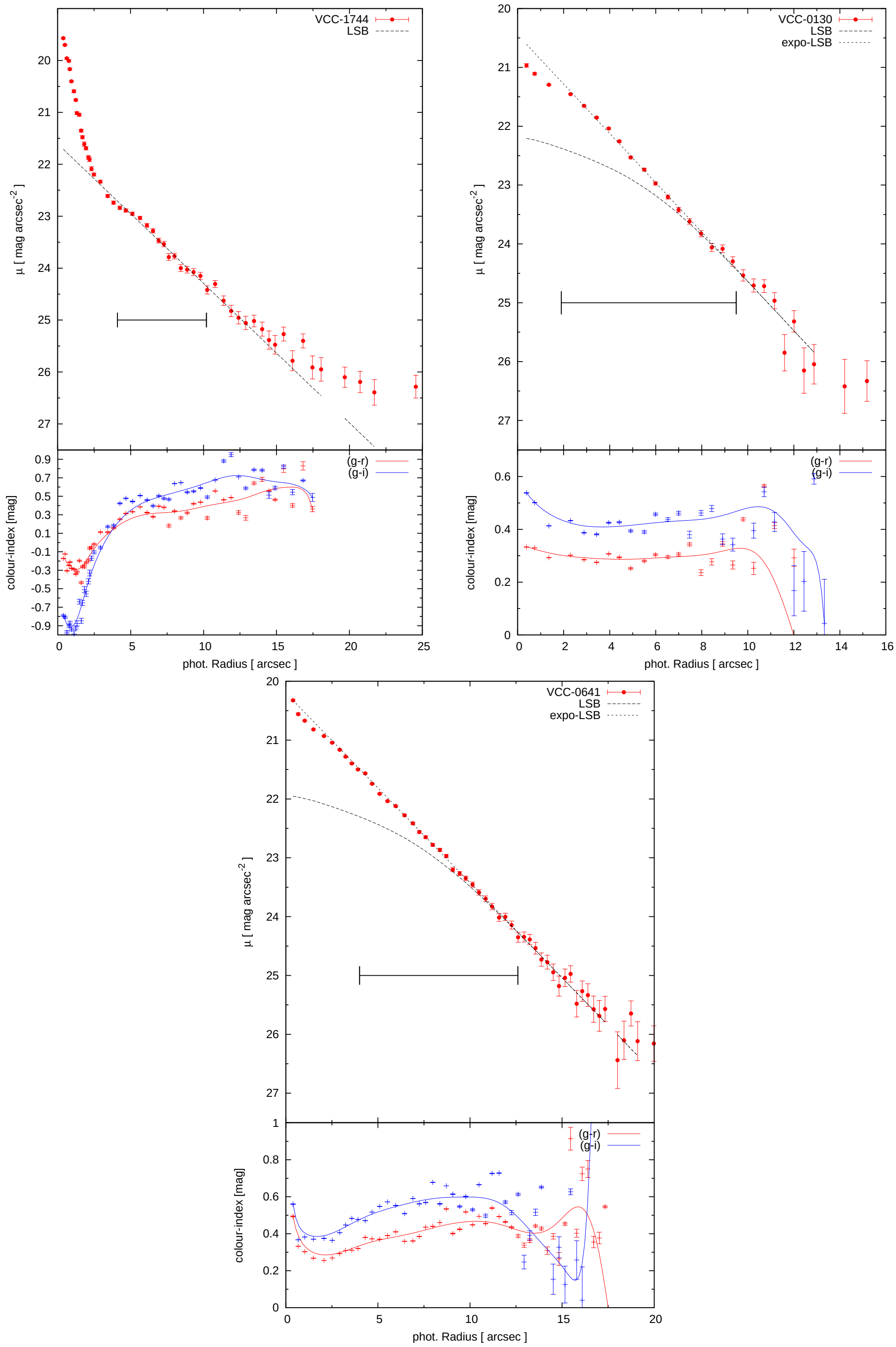

Figure 2.5: Upper panels: SBPs (up) and colour profiles (down) of galaxy VCC-1744 (left) and VCC-0130 (right) in the r-band. Lower panel: same for VCC-0641. In the case of VCC-1744 a pure exponential law was assumed to fit the LSB-component, while for VCC-0130 and VCC-0641 a profile flattening towards smaller radii was assumed.

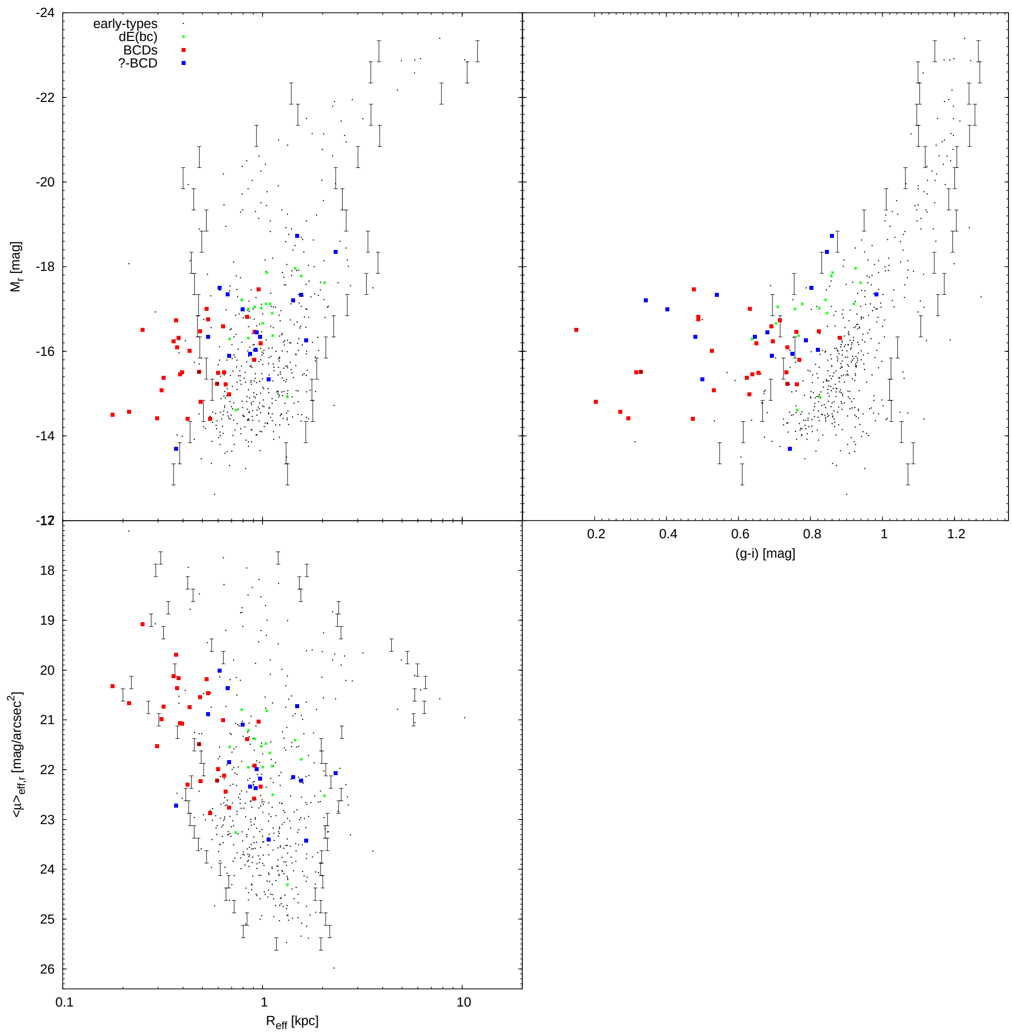

Figure 2.6: The $\mathrm{M_r} - \mathrm{r_{eff}} - \langle\mu\rangle_{\mathrm{eff}}$-plane of BCDs and ETGs. No decomposition into starburst and LSB-component was applied. Red squares represent the BCDs. Black dots represent the sample of early-type galaxies taken from Janz and Lisker (2008); Janz and Lisker (2009), and green asterisks are dE(bc)s from Lisker et al. (2006a). The 2σ deviations of the ETGs is displayed by the vertical bars. Blue squares are possible BCDs, but with an uncertain morphological classification.

Table 2.5: Derived structural parameters of the BCDs and their LSB-components.

VCC [1]	ms [2]	LSB [3]	Flattening [4]	$(g-i)_{tot}$ [5]	$(g-i)_{LSB}$ [6]	$M_{tot,r}$ [7]	$M_{LSB,r}$ [8]	$R_{eff,tot,r}$[kpc] [9]	$R_{eff,LSB,r}$[kpc] [10]	$\langle\mu\rangle_{eff,tot,r}$ [11]	$\langle\mu\rangle_{eff,LSB,r}$ [12]	D [Mpc] [13]	$M_{tot,r}$ [14]
0001	2	nE	0	0.881	0.873	-16.32	-16.27	0.38	0.39	20.16	20.30	32.0	-17.75
0010	1	iE??	0	0.735	0.754	-16.09	-15.87	0.37	0.42	20.36	20.84	32.0	-17.52
0022	1	nE	0	0.638	0.734	-15.45	-15.30	0.39	0.42	21.07	21.42	32.0	-16.89
0024*	2	nE	0	0.695	0.765	-16.24	-16.01	0.36	0.42	20.12	20.69	32.0	-17.68
0074	1	nE	1	0.736	0.765	-15.23	-15.23	0.59	0.57	22.22	22.12	17.0	-15.30
0130	1	iI	1	0.417	0.400	-14.65	-14.73	0.36	0.35	21.73	21.60	17.0	-14.72
0144	2	iE	0	0.149	0.249	-16.51	-15.97	0.25	0.34	19.08	20.26	32.0	-17.94
0172	1	iI	0	0.489	0.743	-16.82	-16.30	0.84	1.07	21.38	22.42	32.0	-18.25
0207	1	iI	0	0.271	0.215	-14.57	-14.19	0.21	0.26	20.67	21.50	32.0	-16.01
0223	1	nE?	0	0.623	0.758	-15.37	-15.01	0.32	0.41	20.74	21.63	32.0	-16.81
0274	1	iI	0	0.473	0.622	-14.40	-14.34	0.55	0.60	22.87	23.13	32.0	-15.84
0324	1	i?	0	0.476	0.630	-17.46	-17.25	0.96	1.17	21.03	21.68	17.0	-17.52
0334*	2	iE	0	0.526	0.698	-16.02	-15.72	0.43	0.54	20.74	21.53	17.0	-16.08
0340*	1	nE	0	0.632	0.753	-17.00	-16.46	0.52	0.68	20.18	21.28	32.0	-18.43
0410	2	nI	0	0.294	0.460	-14.42	-14.31	0.30	0.31	21.53	21.70	17.0	-14.48
0428	2	iI	0	-0.049	0.164	-14.41	-14.32	0.42	0.44	22.30	22.47	17.0	-14.47
0429	1	iI/nI	0	0.630	0.883	-15.16	-14.95	0.79	0.98	22.92	23.60	17.0	-15.23

continued

VCC [1]	ms [2]	LSB [3]	Flattening [4]	$(g-i)_{tot}$ [5]	$(g-i)_{LSB}$ [6]	$M_{tot,r}$ [7]	$M_{LSB,r}$ [8]	$R_{eff,tot,r}$[kpc] [9]	$R_{eff,LSB,r}$[kpc] [10]	$\langle\mu\rangle_{eff,tot,r}$ [11]	$\langle\mu\rangle_{eff,LSB,r}$ [12]	D [Mpc] [13]	$M_{tot,r}$ [14]
0459	2	iI	0	0.489	0.636	-16.75	-16.20	0.53	0.67	20.47	21.51	17.0	-16.81
0513	1	iI	0	0.823	0.770	-16.48	-16.51	0.49	0.56	20.55	20.83	17.0	-16.54
0562	2	iI	0	0.316	0.399	-15.50	-15.45	0.64	0.53	22.12	21.76	17.0	-15.56
0641	2	iI	1	0.329	0.406	-15.51	-15.54	0.48	0.46	21.49	21.37	23.0	-16.23
0802	2	iI,C	0	0.630	0.726	-14.98	-14.96	0.68	0.68	22.76	22.79	17.0	-15.05
0841*	2	iE	0	0.761	0.853	-16.46	-16.19	0.91	1.14	21.92	22.67	17.0	-16.53
0890*	1	iE?	0	0.531	0.819	-15.07	-14.81	0.31	0.39	20.98	21.72	23.0	-15.79
1141	2	nE	0	0.733	0.738	-15.50	-15.34	0.40	0.46	21.08	21.57	23.0	-16.22
1313	2	iI	0	-0.263	0.058	-14.50	-13.66	0.18	0.26	20.33	22.03	17.0	-14.56
1411	2	iE	0	0.650	0.768	-16.19	-16.20	0.98	1.09	22.34	22.58	17.0	-16.25
1437*	2	nE	0	0.715	0.801	-16.74	-16.40	0.37	0.50	19.69	20.70	17.0	-16.80
1459	1	iE?	0	0.762	0.820	-15.22	-15.21	0.65	0.72	22.44	22.67	17.0	-15.28
1572	1	iE	0	0.769	0.914	-15.79	-15.57	0.91	1.06	22.58	23.14	17.0	-15.86
1713	1	iI	1	0.599	0.750	-15.71	-15.70	0.79	0.89	22.37	22.64	17.0	-15.77
1744	2	nI,C	0	0.204	0.598	-14.80	-14.59	0.49	0.60	22.23	22.87	17.0	-14.87
2015	1	nE?	0	0.655	0.771	-15.49	-15.36	0.60	0.66	21.99	22.33	17.0	-15.55
2033*	2	iE	0	0.691	0.826	-16.59	-16.17	0.63	0.84	21.01	22.04	17.0	-16.65

Derived structural parameters of the BCDs and their LSB-components.

Notes. [1]: VCC-numbers marked with "*" were also discussed in Lisker et al. (2006a); [2]: membership (ms) of the BCDs regarding the VCC; [3]: detailed classification of the LSB-component (see Tab. 2.1); [4] flattening: 1= flattening was applied; [13]: GOLDMine distance; [14]: magnitude with GOLDMine distance.

2.4.3 Colour-magnitude diagrams

Figure 2.7 shows the colour-magnitude diagram (CMD) of the LSB-components (red squares) of our BCD sample. Galaxies with a profile flattening toward smaller radii are indicated with a black cross and the corresponding change in the magnitude is described by a vector. As mentioned in Section 2.3 the profile flattening parameters (b,q) are uncertain, therefore, the vector is to be regarded as an aid to the eye, pointing to the locus of the diagram where the true values are expected to be. The criteria for the profile flattening were only fulfilled for three BCDs (VCC-0074, VCC-0130 and VCC-0641).

Blue squares show the results for galaxies with an uncertain morphological classification (see also Section 2.4.8). Additionally, we plot with black dots the CMD of ETGs within the Virgo cluster (Janz and Lisker, 2009). Horizontal bars indicate the 2σ deviations of the early-types within a magnitude bin of $\Delta M_r = 1$ mag (vertical length of the bars). The green asterisks correspond to dEs with a blue core in the centre, taken from Lisker et al. (2006a). On average the LSB-components of BCDs are still bluer compared to the ETG population in the Virgo cluster. The LSB-components of the BCDs show a large spread in (g-i)-colours of about 1.2 mag, in contrast to the dEs with a colour range of 0.96 mag. On the other hand, there is one extremely blue BCD (VCC-1313), which can be found at $(g-i)_{LSB} \approx 0.03$ mag. Such an extremely blue $(g-i)_{LSB}$-colour can naturally arise from extended nebular emission, as is the case for the XBCDs SBS 0335-052 E (Papaderos et al., 1998) and I Zw 18 (Papaderos et al., 2002). Extended nebular emission could diminish morphological asymmetries, and due to its nearly exponential drop-off for large radii, it can easily be mistaken for a stellar disc in distant, poorly resolved starburst galaxies (Papaderos et al., 2002; Papaderos and Östlin, 2012). Therefore, some caution is in order when the data of VCC-1313 are interpreted.

Looking at Fig. 2.7, one can see that the dE(bc)s are slightly offset from the Virgo dEs on the CMD plot, showing bluer colours with an average (g-i)-colour of $\langle g-i \rangle = 0.81$ mag. It looks as if dE(bc)s are the brighter extension of the LSB-components of BCDs. There are two low luminous dE(bc)s (VCC-0674 and VCC-0901) with $M_r > -15$ mag. These two galaxies have a low S/N and therefore their derived properties should be regarded with some caution.

Lisker et al. (2006a) included in their study an additional sample of galaxies that also includes BCDs of our here presented study. These galaxies from Lisker et al. (2006a) are marked in Tab. 6.2 with a "*". Due to the sample selection, all BCDs in the sample of Lisker et al. (2006a) show regular elliptical isophotes, corresponding to the nE type. To gain a deeper insight on the structure of the BCDs we also classify the shape of the starburst region and of the LSB-component based on the classification schema of Loose and Thuan (1986). These subtypes of the BCDs are also shown in Tab. 6.2. Calculating the average (g-i)-colours of the different subtypes of BCDs one finds the tendency that BCDs with regular LSB-components (nE or iE) are redder than irregular shaped LSB-components (see Tab. 2.6). The right hand side of Fig. 2.7 shows the same CMD but additionally the Virgo dwarf irregulars (dIs)[6] are plotted. No obvious separation between BCDs or dIs can be found, since they almost cover the same region in the CMD. However, the dIs tend to have redder colours at fainter magnitudes, with colours comparable to the ETGs or even redder. The upper right panel of Fig. 2.6 shows for comparison the same CMD, but there the total values of the entire BCDs are used.

Table 2.6: Average values of different dE- and LSB-types.

Subtype	$\langle g - i \rangle$	σ	$\langle M_r \rangle$	σ	$\langle R_{eff,r} \rangle$ [kpc]	σ	$\left\langle \langle \mu \rangle_{eff,r} \right\rangle$	σ
dE(bc)	0.814	0.084	-16.81	0.93	1.10	0.34	21.89	0.88
BCDs (total)	0.535	0.243	-15.68	0.82	0.53	0.22	21.36	0.98
BCDs (LSB)	0.647	0.217	-15.49	0.80	0.61	0.26	21.84	0.90
nE (LSB)	0.760	0.051	-15.64	0.55	0.55	0.14	21.56	0.79
iE (LSB)	0.711	0.213	-15.81	0.49	0.68	0.33	21.70	1.17
iI (LSB)	0.521	0.264	-15.14	0.89	0.60	0.26	22.13	0.79

Notes. The averages were determined for colours of $(g - i) > 0$ mag to avoid extremely blue BCDs, which could be contaminated by strong nebular emission. σ corresponds to the standard deviation of the mean.

2.4.4 Sizes of BCDs

Figure 2.8 shows the effective radius R_{eff} vs. the mean effective surface brightness $\langle \mu \rangle_{eff,r}$ in r-band of the LSB-components and ETGs. The meaning of the symbols is the same as in Section 3.3.2. From Fig. 2.8 one can see that the LSB-components of the BCDs occupy a region at the edge of the 2σ area of the ETGs. With decreasing $\langle \mu \rangle_{eff,r}$ the LSB-components tend to become more compact than the ETGs. When

[6]Note that the *dIs* of our sample and the *Ims* of the VCC are handled as the same morphological class of dwarf irregular galaxies and we therefore use both notations.

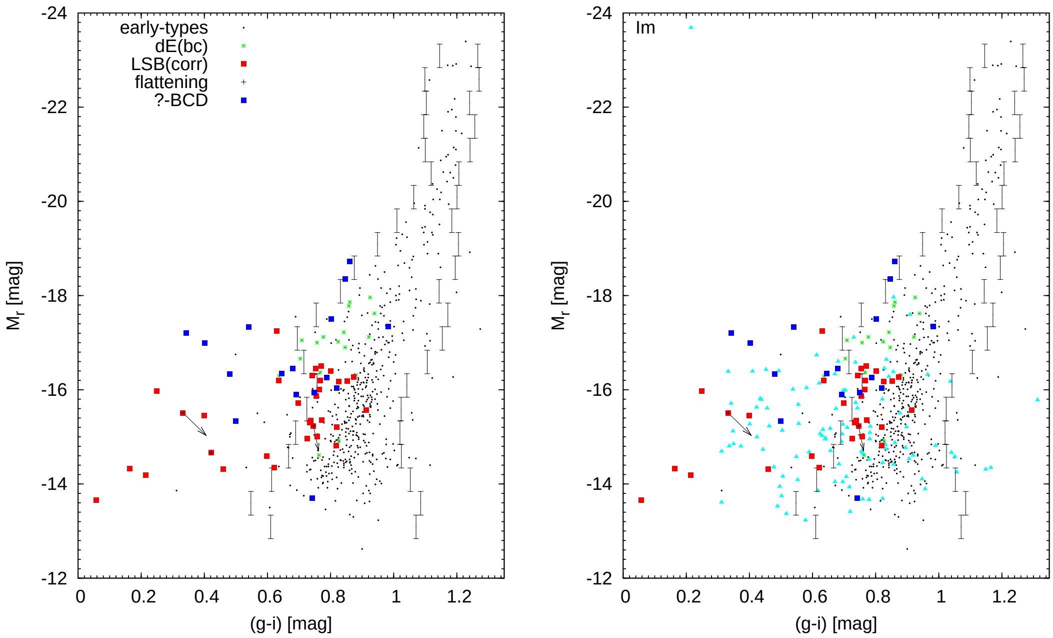

Figure 2.7: Left: CMD of the LSB-components of our BCDs and for comparison the early-type galaxies of the Virgo cluster are plotted, too. Red squares correspond to values of the LSB-components, where black crosses show LSB-components with inner profile flattening. The notation "LSB(corr)" indicates that the parameters of the LSB-components are corrected for the outer tail (see Section 2.3.3). The black vectors display the change of the parameters when an inner profile flatting is applied. Right: same CMD, but additionally plotted are the dIs (cyan triangles).

applying a profile flattening to the LSB-components regarding the criterion described in Section 2.3, one can see that the resulting values are well within the 2σ area of the ETGs. Nevertheless, the LSB-components of the BCDs are still very compact compared to all dEs, but still they cover the same region as the most compact dEs. This supports also the early findings of Drinkwater and Hardy (1991) on a small sample of Virgo BCDs (also see Section 2.5.5). Table 2.6 summarises the average values of the different subtypes of dwarf galaxies. Since nE-BCDs have similarities to the dE(bc)s it could have been expected that their sizes are comparable. However, we find that the nE-BCDs are significantly more compact. In summary, even with the subdivision of the BCDs, the LSB-components tend to be more compact than the dEs. Regarding the average of $\langle\mu\rangle_{\mathrm{eff},r}$ there are no significant differences between the BCD subtypes.
The right hand side of Figs. 2.8 and 2.9 shows additionally the results of the dI galaxies. In both diagrams one finds a clear separation between the LSB-components and dIs

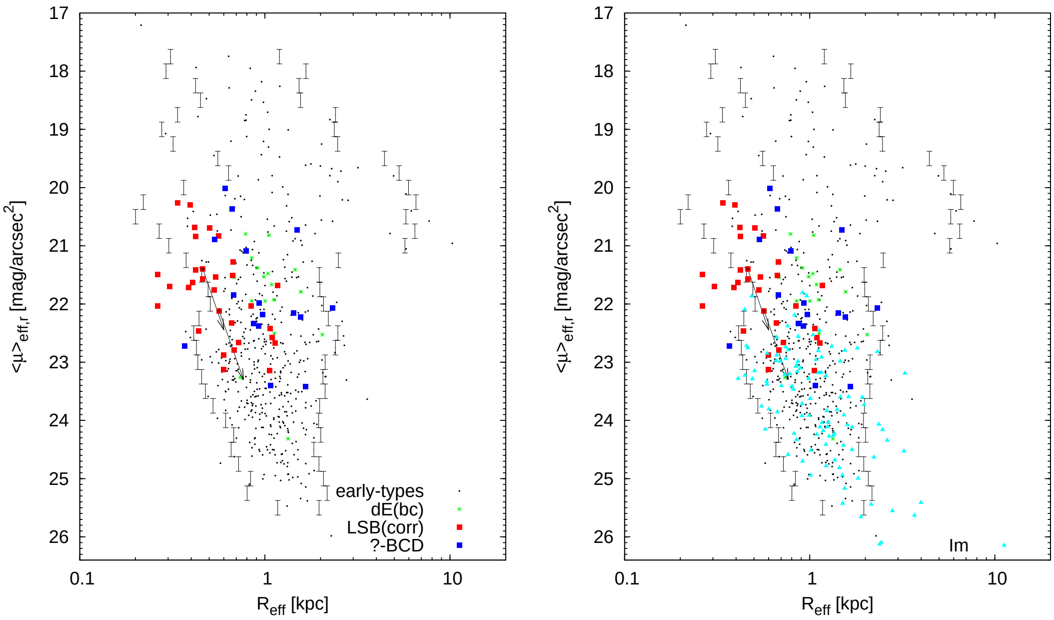

Figure 2.8: Effective radius R_{eff} vs. mean effective surface brightness $\langle\mu\rangle_{eff,r}$. Symbols are the same as in Fig. 2.7.

with a transition region, where both types can be found. Two BCDs (VCC-0274 and VCC-1572) are in the main region of the dIs. A detailed inspection of the gri-image and spectrum of VCC-1572 shows a diffuse galaxy and a spectrum without strong emission lines but a rising blue continuum. Therefore, VCC-1572 could be interpreted as a galaxy in a post-starburst phase, or simply as a misclassified dI. In contrast to VCC-1572, the galaxy VCC-0274 shows in the gri-image a clearly separated starburst region and the spectrum also shows strong emission lines. To summarise, at a given R_{eff} the LSB-components of BCDs tend to be brighter and have a higher $\langle\mu\rangle_{eff,r}$. As in Fig. 2.8, the LSB-components in Fig. 2.9 tend to be more compact at a given magnitude than the ETGs. Comparing the LSB-components and the dE(bc)s one may conclude that dE(bc)s are the linear extension of the LSB-components toward larger R_{eff} and brighter magnitude. To illustrate this we overlay linear fits to the LSB-components (red-line) and dE(bc)s (green lines) in Fig. 2.9.

Figure 3.19 shows mean surface brightness $\langle\mu\rangle_{eff,r}$ as a function of the absolute magnitude M_r for the LSB-components of the Virgo cluster on the left hand side and additionally plotted are the dIs on the right panel. The BCDs and the dIs are separated from each other in this diagram, but they share the same location as the dEs. There are seven LSB-components, which are outside the 2σ deviation of the dEs.

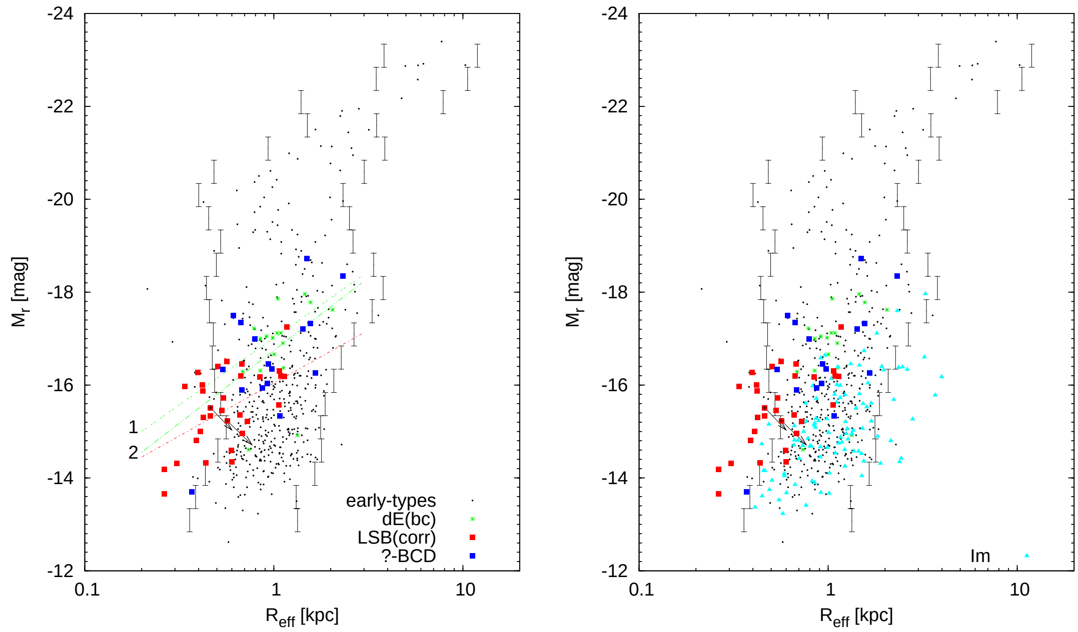

Figure 2.9: Effective radius R_{eff} vs. absolute magnitude M_r in r-band. Symbols are the same as in Fig. 2.7. Red dashed line shows a fit to the LSB-components and the green lines fits to the dE(bc)s (line 1: fit without the two faint galaxies with $M_r > -15$ mag; line 2: fit with the two faint galaxies).

2.4.5 Properties of the starburst regions

Figure 2.11 shows the concentration index (CI) of our BCD sample. The concentration index, according to the definition of Papaderos et al. (1996b) (hereafter P96b), describes the relative isophotal area of the SF-component compared to that of the LSB-component, both defined at $\mu(B) = 25$ mag/arcsec^2. This definition differs from the commonly used logarithmic ratio of the radii encircling, e.g. 20% and 80% of the total luminosity, which primarily measures the (passband dependent) luminosity fraction from the SB. Especially for studies of higher-z starburst galaxies, the CI can be a useful supplement to the CAS quantitative morphology scheme, as it has the advantage of being less sensitive to k corrections and cosmological dimming. CI is defined as

$$\mathrm{CI} = 1 - \left(\frac{\mathrm{P}_{25}}{\mathrm{E}_{25}}\right)^2, \tag{2.11}$$

where P_{25} and E_{25} denote the isophotal radius of the SB- and LSB-component at an extinction-corrected surface brightness level of $\mu_B = 25$ mag/arcsec^2. P96b have used the CI to quantify the morphological variation from nE- towards iE-BCDs, which

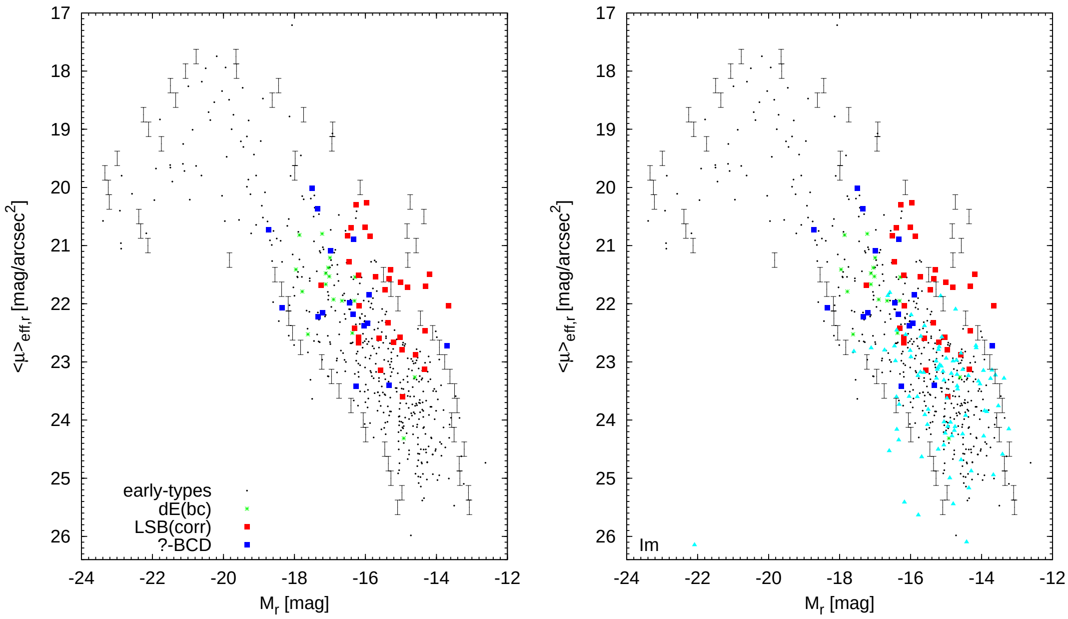

Figure 2.10: Absolute magnitude M_r vs. mean effective surface brightness $\langle\mu\rangle_{\mathrm{eff,r}}$ in r-band. Symbols are the same as in Fig. 2.7.

show a high and low CI, respectively. They also pointed out that interacting BCDs systematically deviate from the CI vs. M_B sequence delineated by relatively isolated ones.

The horizontal lines in the figure represent the different regimes of CI. CI $>$ 0.8 corresponds to a centrally concentrated starburst, as in the case for nE-BCDs, whereas iE-BCDs are typically characterised by a CI $\leq$ 0.7. In BCDs exhibiting a nearly galaxy-wide SF activity (i0 type), hence the LSB-component is almost invisible at the surface brightness cutoff of μ_B = 25 mag/arcsec^2, the CI drops to $<$ 0.5. Over their whole magnitude range, BCDs in the Virgo cluster tend to have a CI larger than CI $>$ 0.65, with an average value of $\langle\mathrm{CI}\rangle = 0.9$ ($\sigma = 0.06$) without accounting for the inner flattening and $\langle\mathrm{CI}\rangle = 0.8$ ($\sigma = 0.12$) when a **modexp** fit is applied to their LSB-component. In contrast to the sample of field BCDs studied by Papaderos et al. (1996a) we do not find any trend of CI with absolute r-band magnitude, a fact which may provide a hint to the influence of the cluster environment on the spatial distribution of SF activities in dwarf galaxies. Looking at Fig. 2.11, one also realises that BCDs with central flattening tend to have a CI $<$ 0.8. This finding is to be expected, given that an extended central core in the LSB-component would imply a larger luminosity fraction and spatial extent for the SF-component. Since the star formation in dE(bc)s is located within the central region of the galaxy, the CI of the dE(bc)s must have a value of CI > 0.8, thereby similar to the majority of the Virgo BCDs.

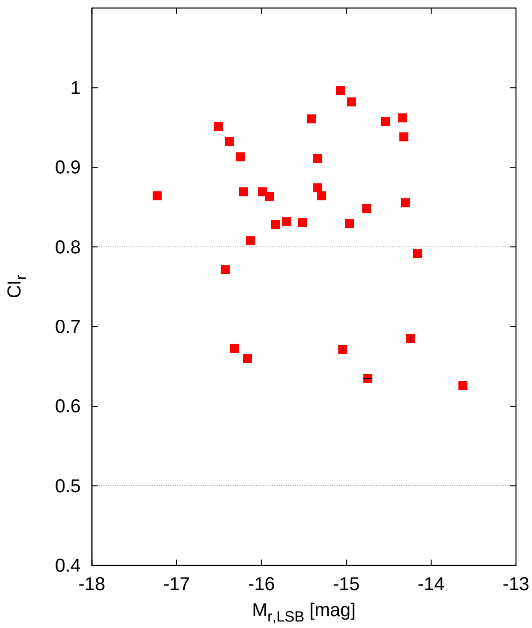

Figure 2.11: Absolute magnitude M_r vs. concentration index CI in r-band. Symbols are the same as in Fig. 2.7.

2.4.6 Apparent axis ratio of the LSB-component

Figure 2.12 shows the number distribution of the axis ratio of the LSB-components in the r-band and additionally the distribution of Virgo dIs, dEs and dE(bc)s. The LSB-components have an average axis ratio of $\langle b/a \rangle_{\mathrm{LSB}} = 0.64 \pm 0.2$. We found that the average axis ratio of our BCD sample is slightly smaller than that for dEs from Janz and Lisker (2009) (hereafter JL09) with an average value of $\langle b/a \rangle_{\mathrm{dE}} = 0.70 \pm 0.18$, implying that BCDs are slightly flatter than dEs. This is in agreement with the results for BCDs by Sung et al. (1998), who found $\langle b/a \rangle_{\mathrm{BCD,Sung}} = 0.67$, which is even closer to the dE value. Interestingly, there is no difference between the axis ratio of the LSB-components and dE(bc)s ($\langle b/a \rangle_{\mathrm{dE(bc)}} = 0.63 \pm 0.2$). In Fig. 2.13 the axis ratio is plotted versus the r-band magnitude of the LSB-components and compared against the dE sample of JL09. One can see that BCDs cover the same area like the dEs.

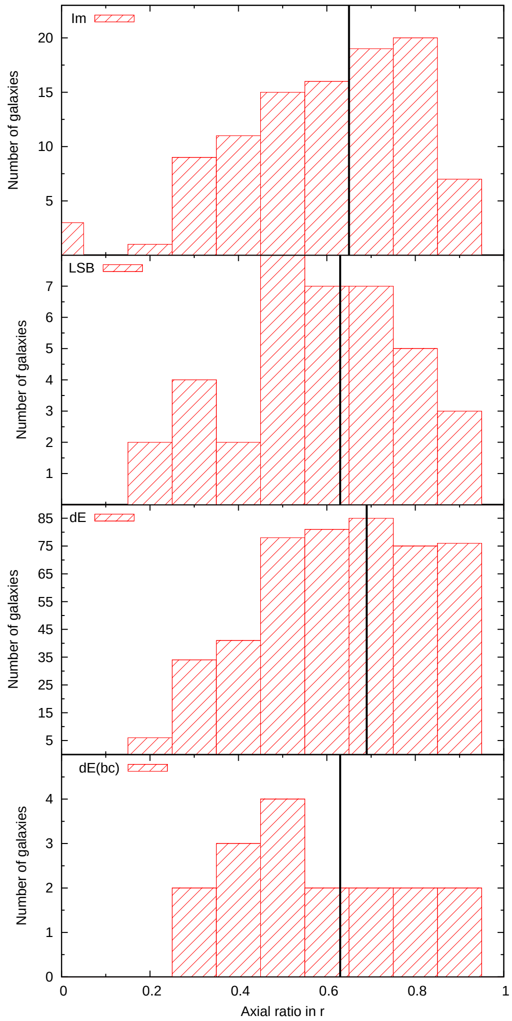

Figure 2.12: Number distribution of Virgo cluster dwarf galaxies. The dEs also include the dE(bc)s, which are additionally plotted in the lower panel. The upper panels show the number distributions of the axial ratios of the LSB-components and dIs.

2.4.7 Colour gradients within BCDs

A large gradient in the colour profile indicates a change in the stellar population of the galaxy. Studies by Clemens et al. (2011) and Peletier et al. (2012) on early-type dwarf galaxies in the infrared showed that they do not have constant colour profiles. Therefore, in respect to the possible evolutionary connection between BCDs and dEs, a constant colour profile is not peremptory (especially in case of the dE(bc)). However, these studies observed in the IR, which makes a comparison to optical data difficult. In another study by Koleva et al. (2011) about gradients in early-type dwarf galaxies

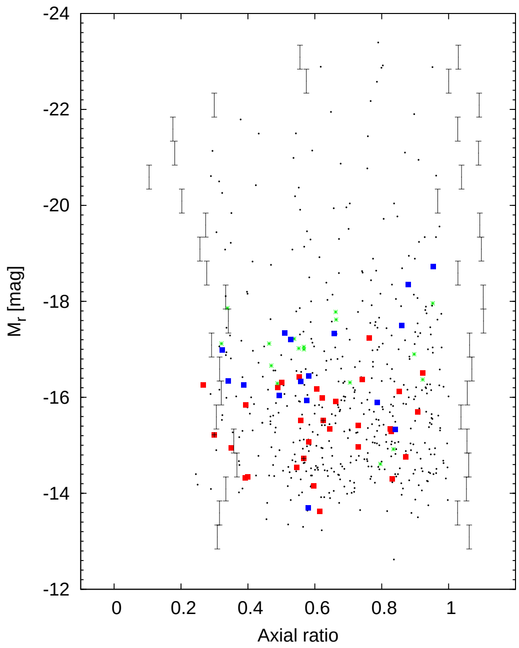

Figure 2.13: Axial ratio b/a vs. absolute magnitude M_r in r of the LSB-components and ETGs. Symbols are the same as in Fig. 2.7.

using long-slit spectroscopy, they pointed out that dEs with gradients are may be the progenitors of BCDs with low angular momentum. Table 2.8 shows the colour gradients of the LSB-components. The gradients were measured by the difference of the colours at a radius of $r < 1/8\ R_{eff}$ and at $r = 2\ R_{eff}$. The colour of the LSB-component at the inner radius of $r < 1/8\ R_{eff}$ - which is probably within the seeing of most of the cases - depends strongly on the fitting of the LSB-component. Therefore, the following analysis serves as a first-order approximation.

The average difference of the (g-i)-colours at $r < 1/8\ R_{eff}$ (following Peletier et al., 2012) and at $r = 2\ R_{eff}$ of all LSB-components amounts for $\langle\Delta(g-i)\rangle = 0.26$ mag. To compare the colour gradients of the LSB-components to the ones of the dEs and dE(bc)s, additionally the colour at $r = 1\ R_{eff}$ was measured for all three classes. The dEs have an almost constant (g-i)-colour profile $\langle\Delta(g-i)\rangle_{dE} = 0.01$ mag, while the dE(bc)s (due to the blue colour excess in the centre) show a slightly gradient $\langle\Delta(g-i)\rangle_{dE} = 0.03$ mag. The LSB-components have an average gradient for $r = 1\ R_{eff}$ to $r = 2\ R_{eff}$ of $\langle\Delta(g-i)\rangle_{LSB} = 0.14$ mag, therefore, the (g-i)-colour profile clearly differs from the early-type galaxies. However, for simplification the flattening of the SBPs of the BCDs was not taken into account, what would slightly decrease

$\langle\Delta(g-i)\rangle_{LSB}$. To obtain an almost flat (g-i)-colour profile for the LSB-components of the BCDs, the composition of the stellar population has to change. The change in the colour profile would also influence the effective radius of the LSB-components in the way that it became larger, bringing them even more into the regime of the dEs.

But how is the effective radius influenced in detail when the colour gradients in the BCDs almost vanish? To investigate the influence on R_{eff}, the BCD VCC-0274 was used as an example. Since the r-band was used as the reference band in our study, the (g-r)-colours were used instead of (g-i). The difference of the innermost (g-r)-colour to the colour of the LSB-component at r = 2 R_{eff} amounts for $\Delta(g-i)_{LSB} = 0.178$ mag. Assuming that the LSB-component has constant (g-r)-colours, the innermost colour has to be increased by 0.26 mag and μ_0 has to be increased, too. With this information we were able to construct the new SBP and integrate it to obtain the new effective radius. In case of VCC-0274, the effective radius change from R_{eff} = 0.599 kpc to R_{eff} = 0.602 kpc. Thus, the influence on the effective radius due to a change of the colour gradient is minor (see Tab. 2.7).

The (g-i)-colour profiles of the LSB-components are shown in Fig. 2.14 and the averages of the different morphological types are summarised in Tab. 2.7.

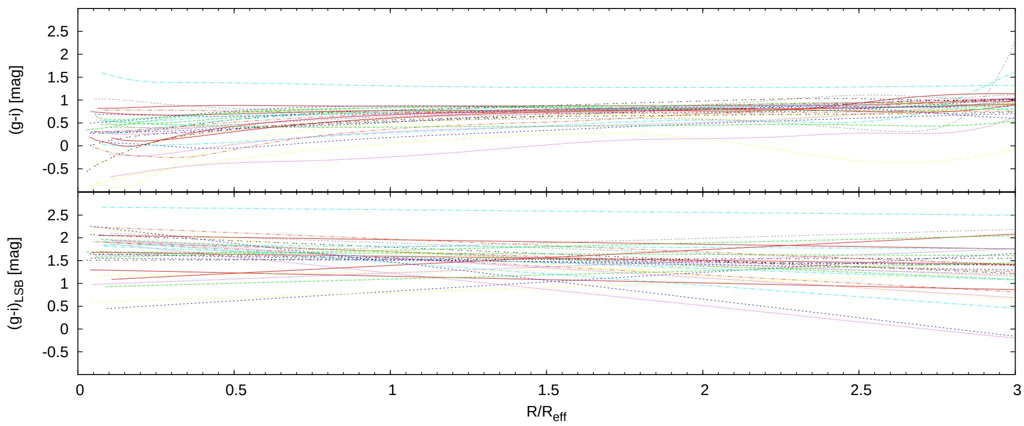

Figure 2.14: Radial colour profiles of the BCDs without decomposition (upper panel) and of the LSB-components (lower panel). The colour profiles are normalised to the effective radii of the LSB-components.

Figure 2.15 shows the colour gradients of the Virgo galaxies as a function of their magnitude. The scatter for the dEs became larger with increasing magnitude, but on average it is almost zero. This scatter is reasonable, since with increasing magnitude

Table 2.7: Average (g-i)-colour gradients of the different morphological types.

Type	$\langle\Delta(g-i)\rangle$	Radius range
BCD	0.26	$r/R_{eff} = 1/8$ to $r/R_{eff} = 2$
LSB	0.14	$r/R_{eff} = 1$ to $r/R_{eff} = 2$
dE	0.01	$r/R_{eff} = 1$ to $r/R_{eff} = 2$
dE(bc)	0.03	$r/R_{eff} = 1$ to $r/R_{eff} = 2$

also the S/N decreases. The same behaviour like for the dEs can be observed for the LSB-components with much larger scatter. In case of the LSB-components, this scatter cannot be explained by the S/N, since the scatter is present at all magnitudes. Without accounting for the fainter dE(bc)s with $M_r > -15$ mag, the dE(bc)s show an increase of the colour gradient for fainter magnitudes.

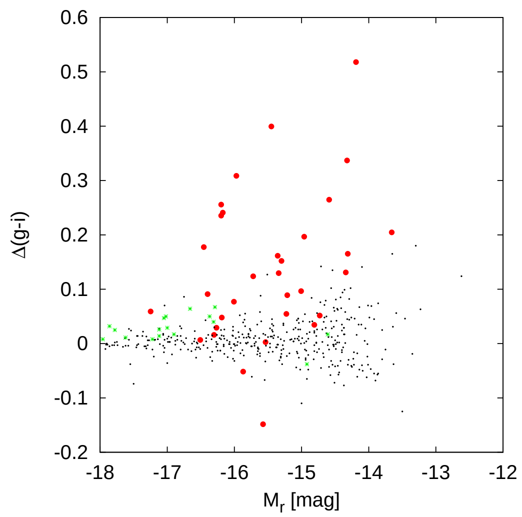

Figure 2.15: (g-i)-colour gradient as a function of the absolute r-band magnitude for the LSB-components (red dots), dEs (black dots) and dE(bc)s (green asterisks).

2.4.8 Where are galaxies with uncertain morphological classification?

In the classification scheme of the VCC one also finds 19 galaxies with an uncertain morphological classification like ”Im / BCD“. In Tab. 2.9 these uncertain types are summarised. Using the above described parameter-space ($M_r - (g-i)_{LSB} - R_{eff} - \langle\mu\rangle_{eff}$) of the BCDs, we are able to conclude whether these galaxies truly share the same parameter-space like the BCDs or not. If a galaxy occupies the same region in the parameter-space, then one can conclude that this galaxy is probably a BCD. In a first step, we compared the derived parameters of irregular (dI) galaxies with that of BCDs. By inspecting the properties of these types in the parameter-space, we found that VCC-1374 clearly falls within the same parameter-space like the other BCDs.

For the galaxies VCC-0309 and VCC-2037, we found that most of the parameters are in the same region where irregular galaxies are located. For the rest of the galaxies a clear distinction between BCDs and dIs is not possible, because they are located in the overlap zone between these two dwarf galaxy classes.

There are three galaxies initially classified as “Sm / BCD” and “SBm / BCD”, respectively. VCC-1356 is located in the same parameter-space as the BCDs. VCC-1725 and VCC-1791 do not show a clear membership or separation from the BCDs.

The galaxy VCC-0281 was taken from JL09 and was classified as “dS?/BCD?” with strong morphological uncertainties. It was also described by Lisker et al. (2006a) as a dE(bc). In the $(g-i)-M_r$-plane, VCC-0281 occupies the same region like the BCDs, however, this is not the case with regard to the other two planes ($R_{eff} - M_r - \langle\mu\rangle_{eff}$).

Regarding their classification, VCC-0213 (“dS?/BCD?”) and VCC-1955 (“Spec/BCD”) show features of spiral structure. Indeed, looking at the co-added SDSS gri-images one can find these spiral structures. The spiral structure is clearly visible when applying unsharp masks (see Lisker et al. (2006b) and Lisker et al. (2006a) for detailed description). In the classification scheme by Sung et al. (2002), they reported of “spiral structures with compact off-centred core” for the “Postmerger BCDS”. But, to the knowledge of the authors, there is no detailed study about BCDs with spiral structure visible at optical wavelengths. Only HI observations of BCDs by van Zee et al. (2001) reveal rotation in BCDs, but the optical morphology of the used sample has smooth, symmetrical isophotes. In the CMD of Fig. 2.7, galaxy VCC-0213 and VCC-1955 are located at the brighter and redder end of the BCD regime. In Fig. 2.8, VCC-0213 has almost the same parameters like the BCDs. The effective radius of VCC-1955 is too large compared to the other BCDs. In Fig. 2.9, VCC-0213 is again in the regime of the BCDs, albeit it is at the boundary of the parameter-space populated by BCDs. VCC-1955 shows too large values for both parameters. Using all these informations, it is possible that VCC-0213 is a BCD with obvious optical spiral structure. Nevertheless, the red core of VCC-0213 contradicts the classification of a BCD. The spiral structure, together with the red core (may be a bulge?), might hint to a spiral galaxy with a larger distance than the one of the GOLDMine data base of D=17.0 Mpc. To investigate this issue it is worth to analyse the spectrum of the galaxy. The spectrum of VCC-0213 gives a redshift of z=-0.0006 (blue shifted), with a corresponding heliocentric recessional velocity regarding GOLDMine of $v_{helio} = -165$ km/s, which indeed locates VCC-0213 at a distance of 17 Mpc (see Fig. 2.17). The upper left panel of Fig. 2.16 shows the co-added SDSS gri-image of galaxy VCC-0213 and the residual image in the upper right panel. The lower panel of Fig. 2.16 shows the residual flux-conserving unsharp mask image of VCC-0213 (cf. Papaderos and Östlin, 2012), which shows the colours of the spiral structure. Interestingly, the colour distribution of the spiral structures is not homogeneous, but shows a gradient from left to right.

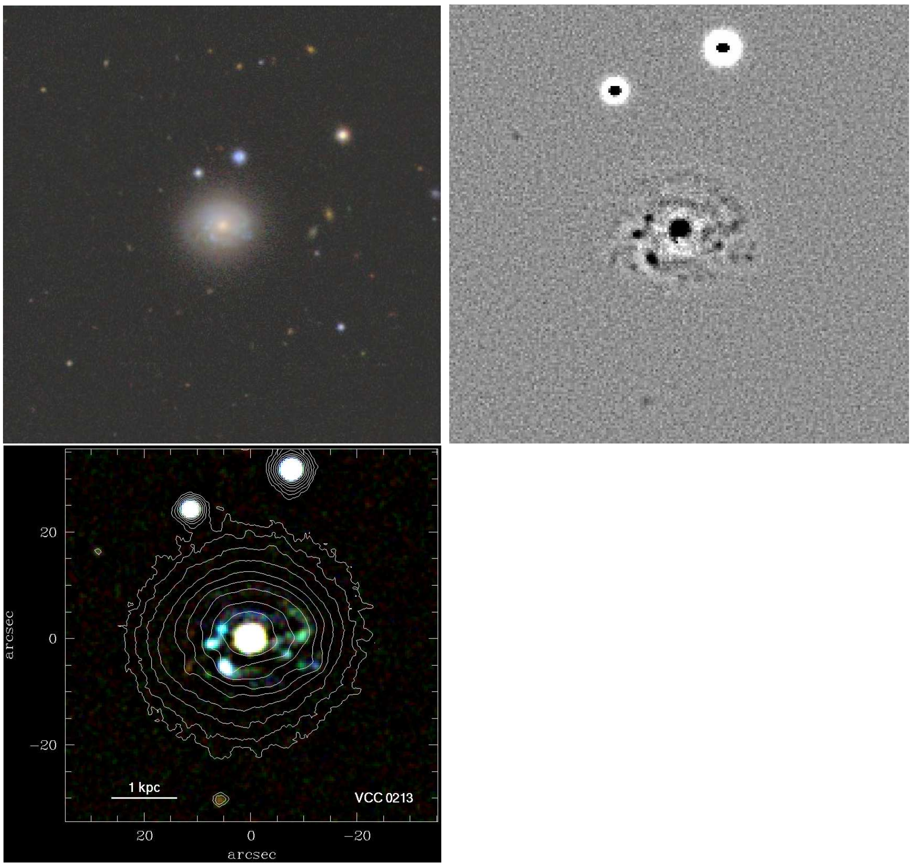

Figure 2.16: Top: co-added SDSS gri-image (left) and zoomed residual image using a two pixel kernel (right) of the galaxy VCC-0213. Bottom: flux-conserved and combined unsharp mask image of VCC-0213.

At first glance the galaxy VCC-0655 (Spec/BCD) seems to be too bright compared to the BCDs. Additionally, its R_{eff} is too large. The gri-image displays several SF regions in the central part of the galaxy, which are surrounded by a redder stellar host. This is typical for BCDs and furthermore VCC-0655 has some similarities to the BCD Mrk-

86. The sample of BCDs in Papaderos et al. (2008) also shows a large spread in radius from very compact objects up to object with $R_{eff} \gtrapprox 1$ kpc (see also Section 2.5.4). Thus, it cannot be ruled out that VCC-0655 is a BCD.

The galaxy VCC-0135 (Spec/BCD) covers almost the same region in the R_{eff}-M_{tot}-$\langle\mu\rangle_{eff}$ as the other BCDs. However, its (g-i)-colours are too red. The gri-image shows a galaxy with red core, comparable to VCC-0123, but there is no obvious spiral structure visible. The spectrum shows strong emission lines and indeed a detailed inspection of the "core-region" reveals a blue structure, which is located in the region of the SDSS spectroscopic fibre. With this information about VCC-0123, we go along with the former classification, but indicate the new classification with a strong uncertainty regarding the BCD class ("Spec/BCD?").

The analysis of the two unknown galaxies ("?" in Tab. 2.9) shows that the properties of VCC-0429 and VCC-1713 have more similarities to the dIs. This is also supported by the optical images of VCC-0429 and VCC-1713. Therefore, these two galaxies should be classified as a transition type (BCD/dI).

Table 2.8: Colour gradients of the BCDs.

VCC	Δ(g – i)	Δ(g – r)	Δ(i – z)	Δ(u – g)	$R_{eff,r}$ [kpc]	$R_{eff,r,nograd}$ [kpc]
0001	0.052	-0.018	-0.240	-0.172	0.395	0.401
0010	-0.100	-0.117	-0.145	-0.338	0.422	0.451
0022	0.300	0.132	-0.103	-0.584	0.423	0.464
0024	0.147	0.025	0.035	-0.589	0.419	0.452
0074	0.101	0.141	0.499	-0.304	0.566	0.597
0130	0.093	0.042	-0.133	0.309	0.355	0.351
0144	0.564	0.322	0.106	0.466	0.339	0.396
0172	0.030	-0.003	-0.293	-0.096	1.068	1.146
0207	0.903	0.305	0.658	-1.177	0.263	0.293
0223	0.178	0.162	0.184	-0.610	0.408	0.472
0274	0.249	0.178	0.546	-1.261	0.599	0.602
0324	0.112	0.036	0.271	-0.006	1.171	1.227
0334	0.233	0.009	0.247	-0.537	0.542	0.566
0340	0.331	0.061	0.271	-0.584	0.675	0.760
0410	0.306	0.292	1.424	-1.195	0.306	0.344
0428	0.609	-0.517	-0.766	0.956	0.438	0.418
0459	0.439	0.215	-0.298	-0.779	0.669	0.717
0513	0.012	-0.084	-0.119	0.463	0.563	0.553
0562	0.749	0.371	1.224	-1.081	0.532	0.565
0641	0.005	0.151	0.162	-0.489	0.462	0.474
0802	0.364	0.188	-0.369	-0.467	0.683	0.762
0841	0.096	-0.031	0.043	-0.021	1.135	1.235
0890	0.067	-0.019	-0.167	0.779	0.388	0.381
1141	0.246	0.054	0.143	-0.275	0.462	0.463
1313	0.384	1.164	1.842	-2.629	0.264	0.308
1411	0.484	0.135	0.368	-1.530	1.092	1.053
1437	0.170	0.051	-0.185	-0.103	0.504	0.560
1459	0.169	0.054	-0.533	0.301	0.723	0.628
1572	-0.284	-0.252	1.056	-1.482	1.061	1.008
1744	0.496	0.231	-0.199	-0.056	0.597	0.579
2015	0.317	0.243	0.133	0.263	0.660	0.706
2033	0.453	0.077	-0.401	-0.243	0.842	0.856

Table 2.9: Uncertain morphological classifications.

VCC	Type	$M_{tot,r}$	$R_{eff,r}$[kpc]	$\langle\mu\rangle_{eff,r}$	(g – i)
0135	Spec / BCD	-17.34	0.67	20.36	0.98
0213	dS? / BCD?	-17.50	0.61	20.01	0.80
0281*	dS0 or BCD	-16.37	1.13	22.50	0.77
0309	Im / BCD	-15.33	1.07	23.41	0.50
0429	?	-15.10	0.73	22.81	0.65
0446	Im / BCD:	-15.94	0.87	22.34	0.75
0655	Spec,N: / BCD	-18.73	1.49	20.73	0.86
0737**	Sd / BCD?	-	-	-	-
0848**	ImIIIpec / BCD	-	-	-	-
1179	ImIII / BCD	-16.34	0.97	22.18	0.64
1356	SmIII / BCD	-16.34	0.54	20.89	0.48
1374	ImIII / BCD	-16.99	0.79	21.09	0.40
1427	Im / BCD:	-16.45	0.93	21.98	0.68
1713	?	-15.66	0.75	22.30	0.56
1725	SmIII / BCD	-17.33	1.56	22.22	0.54
1791	SBmIII / BCD	-17.20	1.43	22.15	0.34
1804	ImIII / BCD	-16.04	0.92	22.37	0.82
1955	Spec / BCD	-18.35	2.33	22.07	0.85
1960	ImIII / BCD?	-13.70	0.37	22.73	0.74
2007	ImIII / BCD:	-15.89	0.68	21.85	0.69
2037	ImIII / BCD	-16.26	1.66	23.42	0.79

Notes. * from JL09; ** not covered by SDSS

2.5 Discussion

2.5.1 Difference between certain and possible cluster member BCDs

From Tab. 2.10 it is apparent that various photometric parameters of certain Virgo BCDs and cluster-member candidates are identical within $\sim 1\sigma$. Therefore, in the following discussion no differentiation based on Virgo membership was applied, even though photometric quantities in Tab. 2.10 are listed separately.
To avoid contamination due to extreme outliers, the average values were determined within the colour interval (g – i) > 0 mag (see Section 2.7 for explanation).

Table 2.10: Comparison of the BCDs regarding their membership to Virgo.

Parameter	Certain	σ	Possible	σ
$\langle M_r \rangle$ [mag]	-15.488	0.835	-15.489	0.783
$\langle g - i \rangle$ [mag]	0.589	0.254	0.696	0.172
$\langle R_{\mathrm{eff,r}} \rangle$ [kpc]	0.569	0.251	0.650	0.275
$\langle \mu \rangle_{\mathrm{eff,r}}$ [mag/arcsec^2]	21.697	0.843	21.963	0.950

2.5.2 Distance dependence of the results

The GOLDMine data base provides the distances of the BCDs, which can be found in column [13] in Tab. 6.2. Table 2.5.2 shows the different distances and the resulting errors if one assumes a distance of d = 16.52 Mpc (m-M=31.09) instead of the GOLDMine value. $\alpha(R_{\mathrm{eff}})$ corresponds to the factor, about which R_{eff} [kpc] changes due to different distances. Additionally, the spacial location within the Virgo cluster of the corresponding distances are given (Gavazzi et al., 1999, hereafter G99). The distances of different substructures of Virgo in Tab. 2.5.2 were derived by using the Tully-Fisher relation (Tully and Fisher, 1977) for a sample of spiral galaxies and the Fundamental Plane (Djorgovski and Davis, 1987; Dressler et al., 1987) for the E/S0 in the study of G99. G99 found three separate regions in their Figs. 4 and 5 (velocity (v_{LG})[7] versus the distance of the galaxies), which in turn define the distances of the substructures. However, since the allocation of the BCDs to the different substructures of the Virgo cluster only depends on the projected location of the galaxies, the GOLDMine distances can not be taken for granted. For instance, the column depth

[7] v_{LG} defines the velocities of the galaxies with respect to the local group (LG) and was calculated via $v_{LG} = v_{helio} + 220$ km/s.

of the different substructures in Virgo is not taken into account.
Additionally, it needs to be pointed out that the finite extent of the cluster causes a natural scatter in the distance. As an example, galaxy VCC-1313 has the smallest cluster centric distance to M87, but it also has the bluest (g-i)-colours within the sample. Therefore, VCC-1313 could fall into the Virgo cluster from a larger de-projected cluster centric radius in the fore- or background of the cluster. Such affects are not accounted for by the GOLDMine data base.

Table 2.11: GOLDMine distances of the different Virgo clouds. Δm and $\alpha(R_{eff})$ indicate the variation of the corresponding parameters if the GOLDMine distance is used instead of a constant distance of 16.52 Mpc.

Distance [Mpc]	Location in Virgo cluster	Δm [mag] to d=16.52 Mpc	$\alpha(R_{eff})$ to d=16.52 Mpc
17	E-, N-, S-cloud, A-cluster	0.06	1.04
23	B-cluster	0.72	1.40
32	M-, W-cloud	1.44	1.95

Figure 2.17 shows the distance in Mpc of the Virgo BCDs against the velocity given by GOLDMine (see also Fig. 5 in G99). Regarding G99 galaxies with $v_{LG} > 1900$ km/s belong to the M or W cloud with a distance of 32 Mpc. As one can see, four BCDs (VCC-0022, VCC-0024, VCC-0274 and VCC-0340) have a GOLDMine distance of 32 Mpc, but do not have velocities of $v_{LG} > 1900$ km/s. Therefore, we do not assume a distance of 32 Mpc, but instead a distance of 16.52 Mpc. These galaxies are displayed by green squares in Fig. 2.18. For all other BCDs the GOLDMine distances are adopted.
Figure 2.18 shows the $(M_r - R_{eff} - \langle\mu_{eff}\rangle)$-plots of the analysed galaxies with the GOLDMine distances. Interestingly, there are only three LSB-components of the BCDs that do not fall into the ETG's 2σ-plane and these BCDs are classified as "iI" and "nI". One of these three BCDs also needs a profile flattening of the LSB-component, bringing it even more into the 2σ-plane.
In the $M_r - R_{eff}$-diagram, there are two other BCDs outside the 2σ-deviation of the dEs, where the velocity criterion is not fulfilled. The comparison of the late-type dwarfs (BCD(-LSB) and dI) and the early-type dwarfs reveals another interesting result. The LSB-components of the BCDs and the dI galaxies form a continuous sequence, which has the same location as the early-type dwarf galaxies. This is consistent with the hypothesis that, once star formation in Virgo BCDs has ceased, their

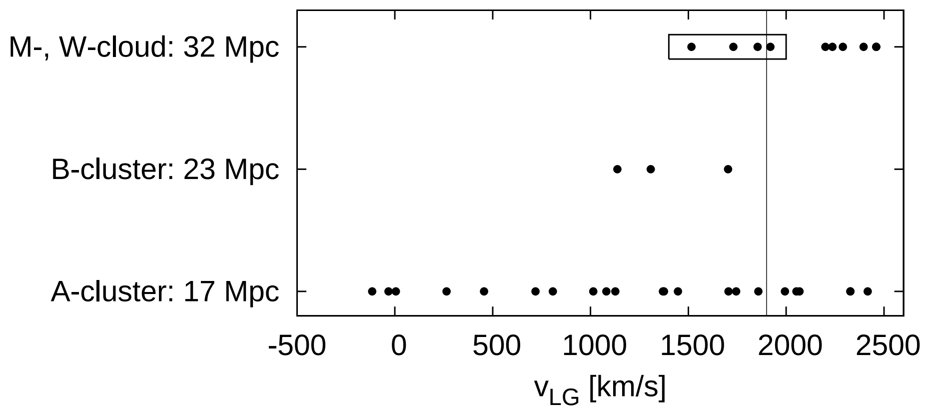

Figure 2.17: GOLDMine distance vs. the velocity of the Virgo BCDs. The vertical solid line at v_{LG} = 1900 km/s corresponds to the limit from which galaxies belong to the M and W cloud regarding Gavazzi et al. (1999). The four BCDs in the box are below or slightly above this velocity limit, but have a GOLDMine distance of 32 Mpc.

descendants could evolve into dEs. Additionally, Virgo dIs could form the progenitor population of dEs with the largest effective radii. Clearly, one has to keep in mind that R_{eff} is not a particularly sensitive discriminator between SBPs of substantially different shapes, consequently the alignment of all dwarf galaxy types along a common sequence on the $M_r - R_{eff}$ diagram is unsurprising. Moreover, it should be pointed out that these findings are critically dependent on the distance of the galaxies. As seen in Figs. 2.8 and 2.9, there are more BCDs outside the 2σ deviation when a constant distance of 16.52 Mpc is adopted.

2.5.3 Comparison between BCDs and the inner components of dEs

A recent study by Janz et al. (2012) investigated the different components of ~70 dEs in the Virgo cluster in H-band in the range of $-19 \le M_r \le -16$ mag. As mentioned before, dEs do not form a homogeneous class of objects, but show disc features and inner components, which were modelled with GALFIT 3.0 (Peng et al., 2010) in the study of Janz et al. (2012). Apart from the H-band, also r-band profiles of the dEs were analysed, thus, we are able to compare the inner components of the dEs with our sample. Figure 2.19 shows the results of our study of the LSB-components and the results for the different components of the dEs.

Interestingly, the inner components of dEs and the LSB-components cover a very sim-

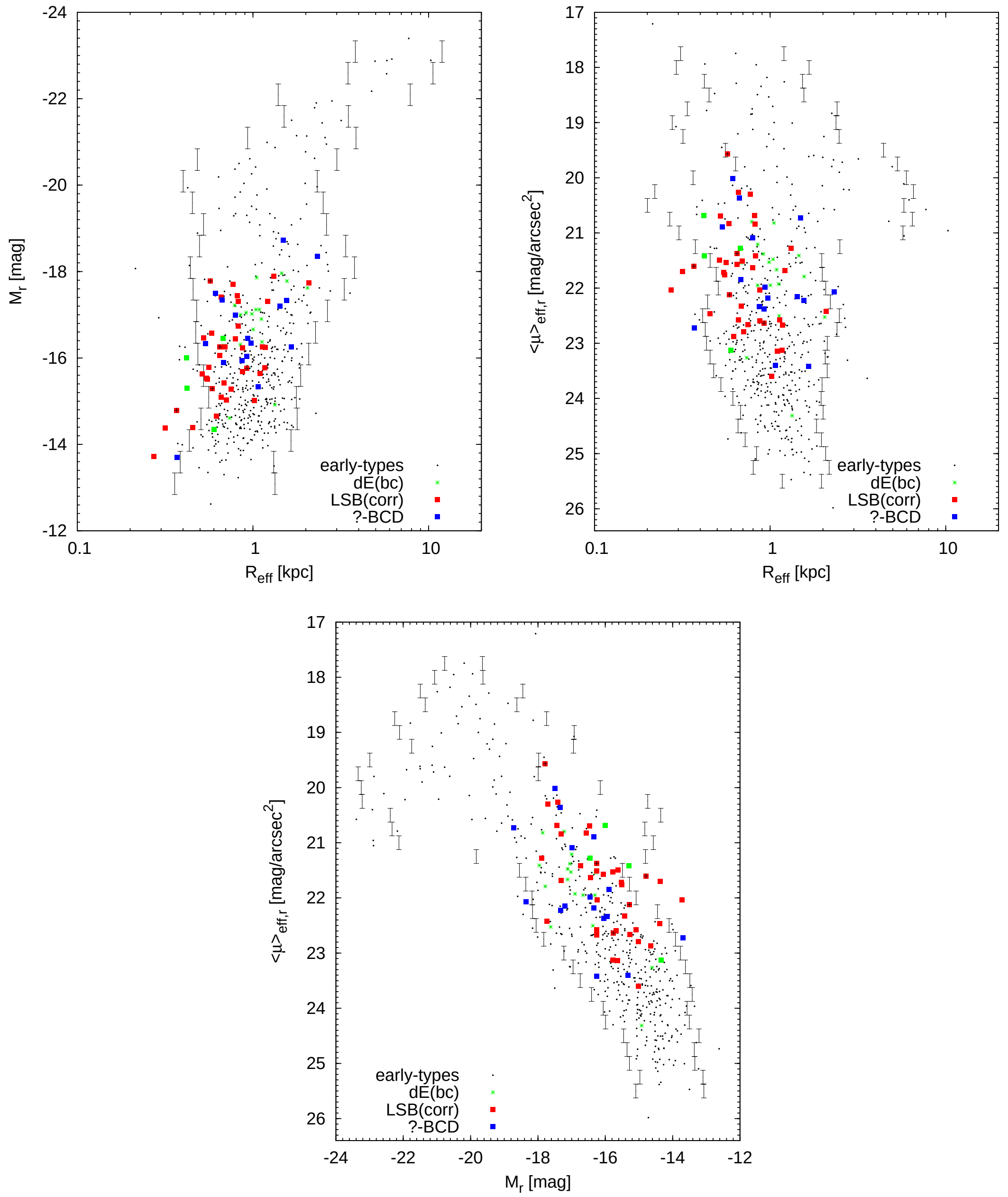

Figure 2.18: Same as Figs. 2.8, 2.9 and 3.19, but instead of a constant distance of 16.52 Mpc, the distances given by the GOLDMine data base are used for the LSB-components. Green squares correspond to BCDs with a GOLDMine distance of 32 Mpc, but with velocity $v_{LG} \lesssim 1900$ km/s. Therefore, a distance of 16.52 Mpc was applied.

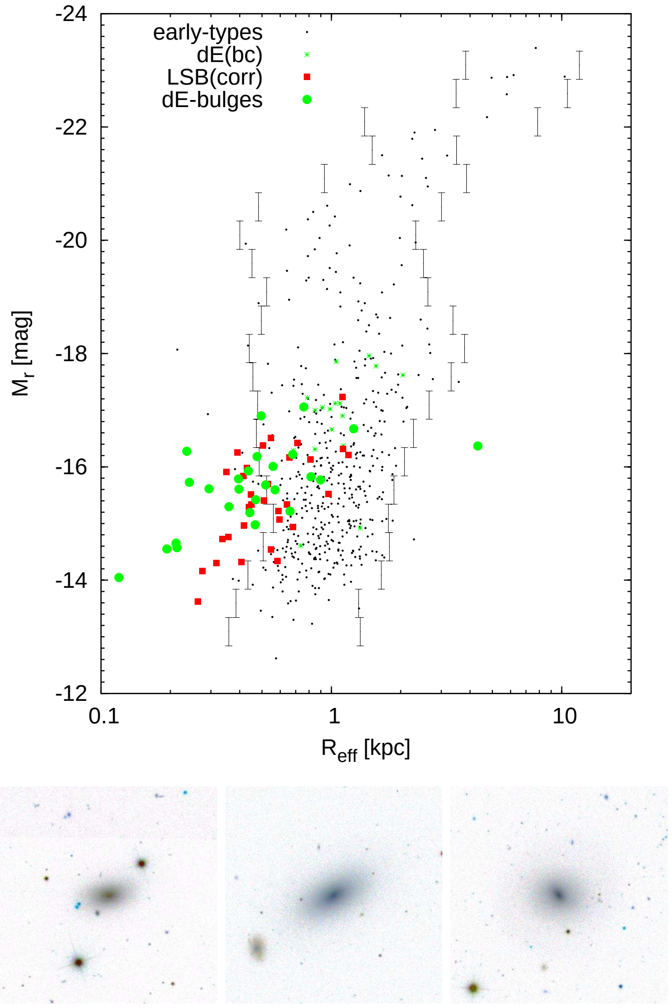

Figure 2.19: Same as Fig. 2.9, but additionally the inner components of dEs are shown. Lower panels show the inverted SDSS images of three example dEs, which inner components cover the region of $0.3 < R_{eff} < 0.7$ kpc and $-14.4 > M_r > -16.4$ mag. This parameter region corresponds to the bulk of the LSB-components.

ilar region in the $R_{eff} - M_r$-parameter-space. The physical reason for this coincidence is not clear at the moment and it is also not clear if there are any connections between the inner components of dEs and LSB-components of BCDs. One should also keep in mind that the inner components of dEs are accompanied by outer (disc) components. While the outer tails of some BCDs qualify as an equivalent outer component, for most of them these are not as prominent (or even not detected) as in the multicomponent dEs. This reflects again the fact that the LSB-components, even with the outer tails, only overlap with the more compact ~half of the dEs. Therefore, if the similarity to the inner components of dEs had an evolutionary meaning, LSB-components would have to form a surrounding disc to look like present day dEs.

2.5.4 Comparison with other BCDs

Table 2.12 shows the results of a sample of BCDs from Papaderos et al. (2008) (hereafter P08) from the SDSS. Values of the LSB-component of this study were transformed into an effective radius using the formula of Graham and Driver (2005). All given values of P08 were measured in the SDSS g-band, therefore, R_{eff} for the r-filter was calculated with the following approximation:

$$R_{eff,r} = \frac{1}{0.95} \cdot R_{eff,g}.$$

As one can see, the effective radii of the P08 sample are also very compact with an average of $\left\langle R_{eff,g} \right\rangle = 0.62$ kpc, but with a large scatter.

Table 2.12: Galaxies from the study of Papaderos et al. (2008).

Galaxy	$m_{tot,g}$	$M_{tot,g}$	$\mu_{0,g}$	$\mu_{e,g}$	$\langle\mu\rangle_{e,g}$	$R_{eff,g}$ [arcsec]	D [Mpc]	$R_{eff,g}$ [kpc]	$R_{eff,r}$ [kpc]
J0133+1342	17.9	-15.0	22.1	34.7	23.22	4.63	37.8	0.85	0.89
J1044+0353	17.2	-16.3	19.9	35.3	21.02	2.32	51.2	0.58	0.61
J1201+0211	17.4	-13.3	22.2	32.5	23.32	6.10	14.0	0.41	0.44
J1414-0208	18.1	-13.7	21.6	33.6	22.72	3.35	23.0	0.37	0.39
J2230-0006	17.0	-15.0	19.8	33.8	20.92	2.43	24.9	0.29	0.31
J2302+0049	18.6	-17.0	20.8	37.4	21.92	1.84	134.6	1.20	1.26

However, there are also other examples of BCDs, having a very extended LSB-component. One example of these BCDs is Markarian 86 (Mrk-86). The SBP of Mrk-86 is shown in Fig. 2.20. The derived effective radius at an assumed distance of 7.0 Mpc amounts for $R_{eff,R} = 0.94$ kpc (regarding Graham's formula and with values from Papaderos et al., 1996b) in the Johnson-filter system or $R_{eff,r} = 1.2$ kpc (from profile integration) in r of SDSS. Compared to the Virgo BCDs, even these extended BCDs are in the same radius range. Interestingly, Mrk-86 has a very red LSB-colour of (g-i)=0.92 mag. Together with $R_{eff,R}$, $M_{tot,g} = -17.06$ mag and $\langle\mu\rangle_{eff,LSB} = 20.98$ mag/arcsec^2, it occupies the same region as the dE(bc) population of Virgo.

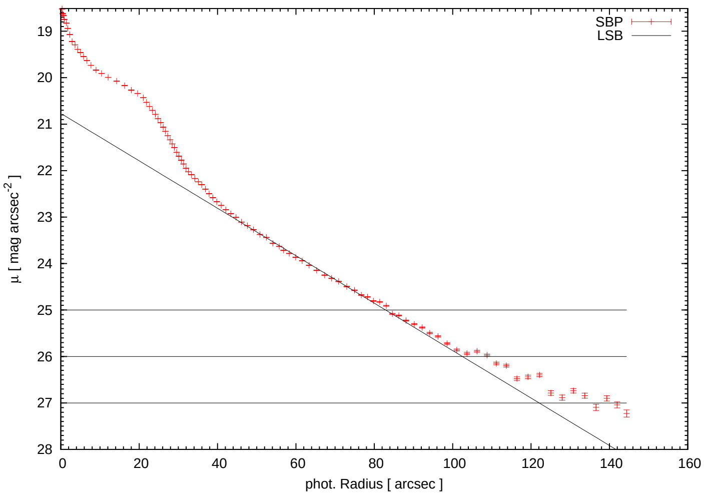

Figure 2.20: The SBP of the BCD Mrk-86, which is not located in the Virgo cluster.

Since the BCDs of our study are located in the region of the Virgo cluster, one may ask whether they are some special kind of BCD and deviate from other (field) BCDs. To investigate this question a large sample of emission-line galaxies in arbitrary environments (unpublished study by H. T. Meyer, R. Kotulla, P. Papaderos, Y. Izotov, N.G. Guseva and K.J. Fricke) was used. The galaxies were spectroscopically selected, therefore, also non-dwarfish galaxies are included in the initial sample. To include only star forming dwarf galaxies, a g-band magnitude cutoff of $M_{cutoff} = -18.0$ mag was applied and the resulting sample is called the *second sample*. To all star forming galaxies of this sample the same photometric analysis (derivation of SBPs and decomposition) was applied, thus the derived parameters of both samples can be compared. The CMD of the LSB-components of the Virgo BCDs and the SFDGs of the second sample is shown in Fig. 2.21. The LSB-components of the Virgo BCDs tend to be more reddish compared the other LSB-components of the second sample. This could be a hint to the influence of the denser cluster environment on the Virgo BCDs, making them redder due to e.g. the removal of gas. In the other two diagrams of Fig. 2.21, no obvious differences between these two samples can be found. Nevertheless, the SFDGs of the second sample tend to have larger effective radii than the BCDs of Virgo, which is may caused by selection effects. It also has to be pointed out that the sample of Virgo BCDs is small, making a comparison quite difficult. Therefore, an increase of the sample size of *cluster* BCDs (e.g. Perseus-, Coma-, Fornax cluster) would be desirable for future investigations.

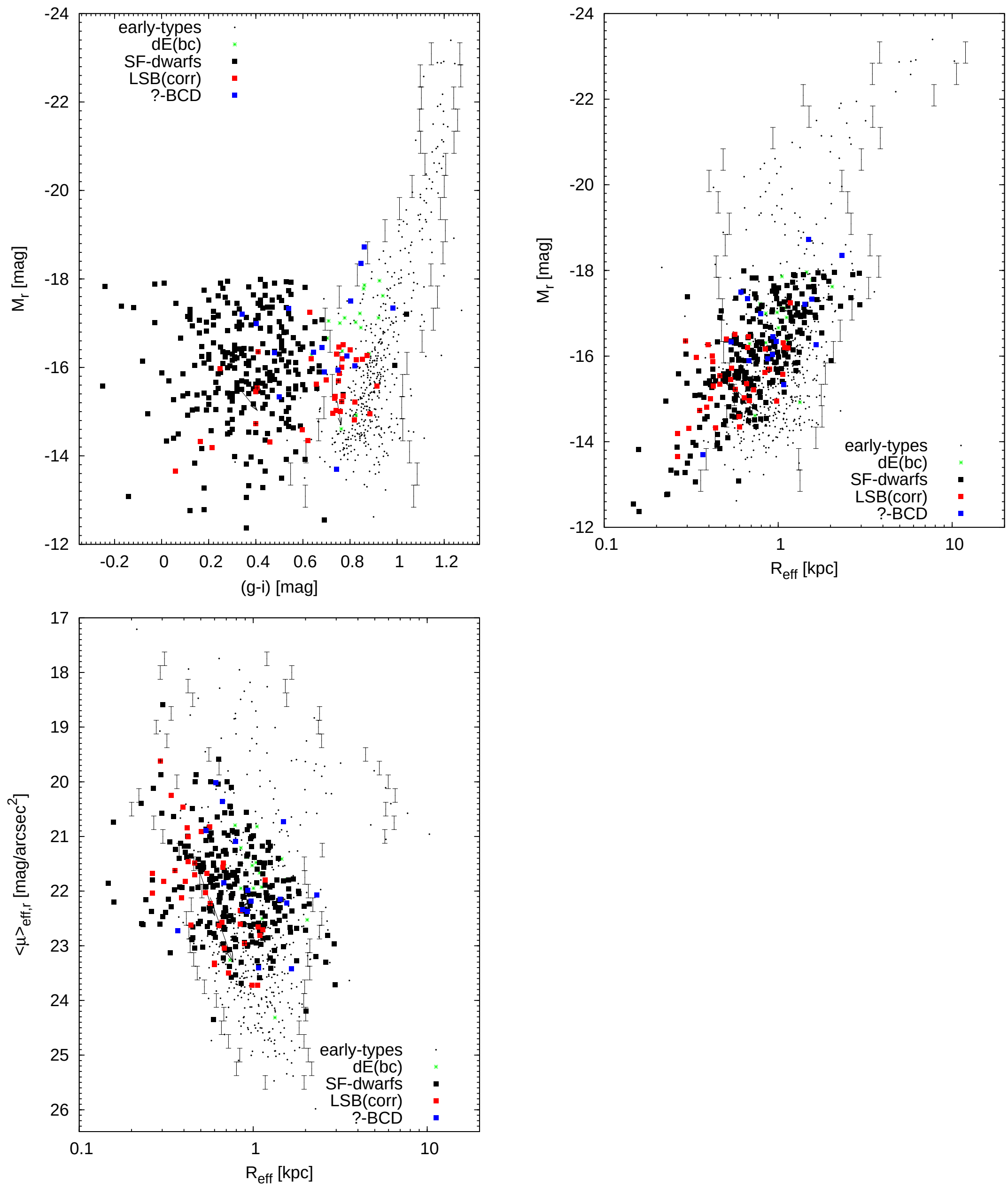

Figure 2.21: Parameter-space of the LSB-components of our Virgo BCDs and a comparison sample of SFDGs in arbitrary environments. The black squares corresponds to the second sample of SFDGs, while the other galaxy types are colour code as in the previous figures of this chapter.

2.5.5 Evolutionary connection between different dwarf galaxies in galaxy clusters

Various observational and theoretical lines of evidence suggest that the evolutionary pathways of late-type dwarfs in a cluster environment have to significantly differ from those in the field. Even in the cluster periphery, late-type dwarfs have undergone interaction with the hot ICM and other nearby galaxies since a few hundreds of Myr, a time span on the order of their dynamical timescale. Starbursts transforming late-type dwarfs plunging into the ICM into BCDs, may have a different origin than starbursts in the general population of field BCDs. Consequently, one should be cautious when comparing structural and integral photometric properties (e.g. colour, burst parameter, effective radius, concentration index) of cluster-BCDs with literature data for normal BCDs. Various mechanisms for starburst ignition shortly in initial stages of the interaction of a dwarf with the ICM can be envisaged, for example triggered gas collapse by the external ICM pressure (as opposed to gas collapse driven by self-gravity), or strong dissipation and gas cooling in large-scale shocks, followed by collective star formation. For such reasons, it is not even for sure that the compact structure of the LSB-component – a typical, if not the most distinctive characteristic of field BCDs – has to be common in systems classified as BCDs in galaxy clusters. For example, external agents (see above) could ignite a BCD-typical starburst in a genuine (that is, relatively diffuse) dI. Alternatively, an externally triggered destabilisation and inflow of gas could eventually lead to an adiabatic contraction of the LSB-component (Papaderos et al., 1996a), and the opposite may happens after complete removal of the dwarf gas halo, as it sinks deeper within the hostile ICM environment. As our understanding of the early interaction of late-type dwarfs in the cluster environment is still poor, it would be speculative to generalise conclusions drawn from our Virgo BCD sample to the BCD population as a whole. Still, the discussion below is instructive in its own right, because it concentrates on a complete and well-selected sample of cluster-BCDs and probable candidates, thereby minimising contamination of the trends found for field BCDs.

The evolutionary scenario of Davies and Phillipps (1988) describes how a dwarf irregular galaxy can ignite a starburst and become a BCD due to in-falling gas from a surrounding reservoir.

After several starburst (BCD) phases and non-starbursting dI-phases, the galaxy evolves to a passive dE galaxy. If the latter evolutionary sequence was possible at present epochs, and specifically in the outskirts of the Virgo cluster, BCDs and dEs should have a similar structure.

Observational studies of BCDs by Drinkwater and Hardy (1991)[8] and Papaderos et al. (1996a) showed that BCDs are very compact objects compared to the dEs. They concluded that only the most compacted dEs may be related to the BCDs. An even more extreme conclusion is reached by Drinkwater et al. (1996), who state that "no blue star-forming progenitors of dE galaxies" exist in the Virgo cluster down to an absolute *B*-magnitude of $M_B \approx -14$ mag. At first view, these findings seem to be supported by our photometric measurements for the galaxies' entire light: Fig. 2.6 (top left panel) shows that the majority of BCDs are more compact than even the 2σ-range of dEs at a given magnitude.

However, if the gas reservoir that is immediately available to a BCD's starburst region is limited, thus restricting the starburst phase to durations of some 10^8 yrs or less (Thuan, 1991; Thornley et al., 2000), a population of non-starbursting counterparts must exist *within the same spatial volume*. Assuming a velocity of 1000 km/s, a BCD could only move some 100 kpc during the starburst phase, i.e. some tenths of the Virgo cluster's virial radius — which means that the outskirts of the Virgo cluster should hold many non-starbursting counterparts to BCDs. How do these look like?

To investigate this, we determined the structural properties of the underlying LSB-component of the Virgo BCDs, i.e. without the contribution of the starburst region. The results already show much more overlap with the dEs in the parameter-space of structure and also colour (see Figs. 2.7, 2.8 and 2.9). When we also take into account the different distances of the various parts of the Virgo region, the LSB-components turn out to fit remarkably well to the dE population with small effective radii (Fig. 2.18). The left side of Fig. 2.22 shows a collection of such dEs that fall within the locus of the LSB-components: these may look like the future "red and dead" descendants of BCDs. Average dEs are shown on the right side for comparison.

As for the few objects that remain more compact than the dEs, none of them actually has a clearly *red* LSB-component (Fig. 2.23). Judging from their measured values and their images, only VCC-1313 (probably also VCC-0410) seems to follow the literal meaning of the term "blue compact dwarf", while most of the other BCDs rather have the appearance of a dE or dI with additional starburst. The non-detection of a red LSB-component down to low surface brightness levels for some "extreme" BCDs was already reported by Drinkwater and Hardy (1991): two BCDs in their

[8]It should be pointed out that the findings of Drinkwater and Hardy (1991) particular based on a sample of the most compact BCDs in Virgo.

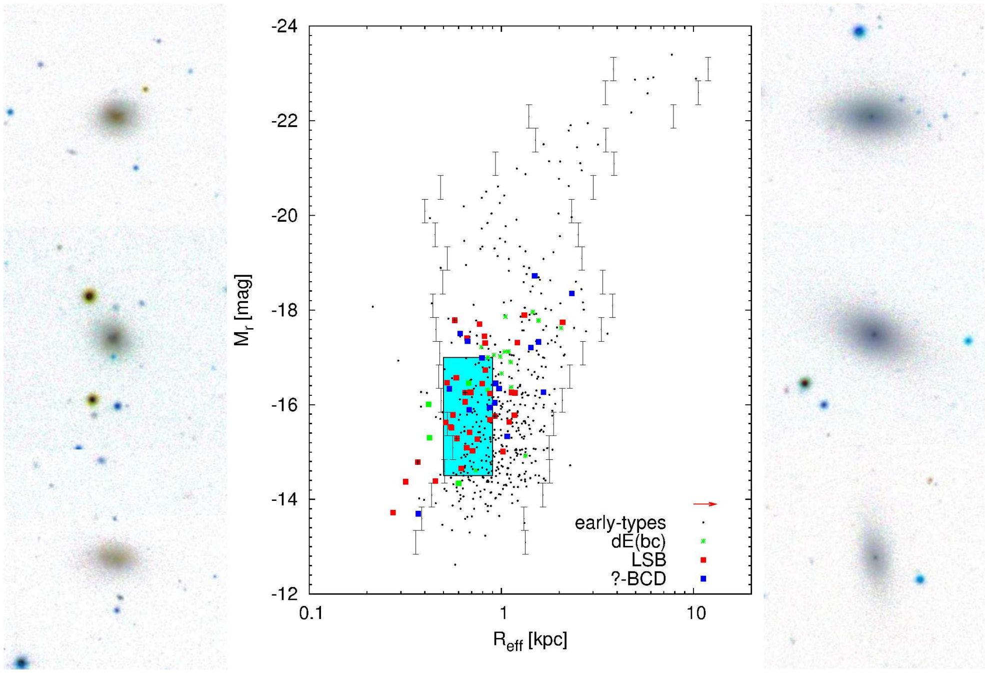

Figure 2.22: Possible descendants of BCDs in the Virgo cluster. The figure in the middle shows the $R_{eff} - M_r$ diagram of the analysed galaxies with the GOLDMine distances, and the blueish box displays the locus of the LSB-components. The three example BCDs on the left (from top to bottom: VCC-0022, VCC-1141 and VCC-1623) are selected in the parameter-interval of $0.5 < R_{eff} < 0.9$ kpc, $-17.0 < M_r < -14.5$ mag and $21.0 < \langle\mu\rangle_{eff,r} < 23.0$ mag/arcsec^2. The three dEs on the right hand side are randomly selected in the same parameter-interval (from top to bottom: VCC-0178, VCC-1308 and VCC-1980). All images have the same scale (x-edge length is 100 arcsec and 7.95 kpc for a distance of 16.52 Mpc).

study had no surrounding low-surface-brightness envelopes detected to a limit of μ(V) = 27 mag/arcsec^2, which therefore would be classified as i0-BCDs. For all of these, the Next Generation Virgo Cluster Survey (NGVS, Ferrarese et al., 2012) will provide unprecedented insight into their outer structure and older stellar population, if existent.

Are dEs the only morphological type that qualifies as non-starbursting counterparts of BCDs? Figure 2.24 shows the number distribution of galaxies in the outer region of the Virgo cluster that fall in the same parameter-space of magnitude and mean surface brightness as the LSB-components of the BCDs[9], displayed separately for blue and

[9]Results of uncertain morphological types are taken from Section 2.4.8.

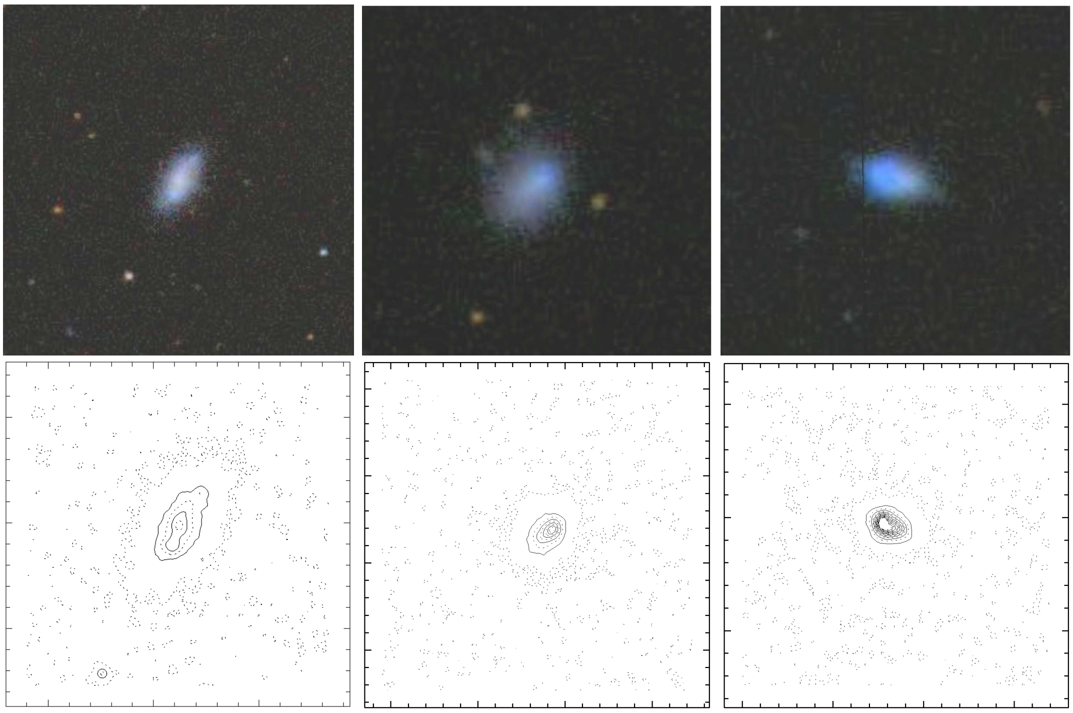

Figure 2.23: BCDs that are more compact than the dEs and are outside the 2σ deviation in Fig. 2.18. The upper panels show the co-added gri-SDSS images and the lower panels show the contour maps of the BCDs. From left to right: VCC-0130, VCC-0410 and VCC-1313.

red ($g - i > 0.7$) galaxies. Only for blue galaxies (left panel), late-type spirals and especially irregular galaxies form a population of significant size compared to the dEs. However, the majority of the LSB-components of BCDs is already in the red colour regime (right panel), where the dEs clearly outnumber all other galaxy types.

Vaduvescu et al. (2006) concluded that "BCDs and dIs are similar structurally", which is in conflict with our results (see Figs. 2.8 and 2.9). We measure dIs to be systematically more extended than the LSB-components of BCDs at a given magnitude, hence only a small fraction of the dIs would qualify as non-starbursting BCDs. Vaduvescu et al. fitted structural parameter relations to dIs and claimed consistency of the BCDs with these relations. Their Figs. 4 and 5 show large scatter among their BCD sample, with at least half of the BCDs lying clearly at smaller radii than the dI relations. Among the five BCDs that lie significantly above the dI relation, the three largest ones have been classified as ambiguous types between Sm, dI and BCD in the VCC, and appear closer to Sm/dI by visual inspection of SDSS colour

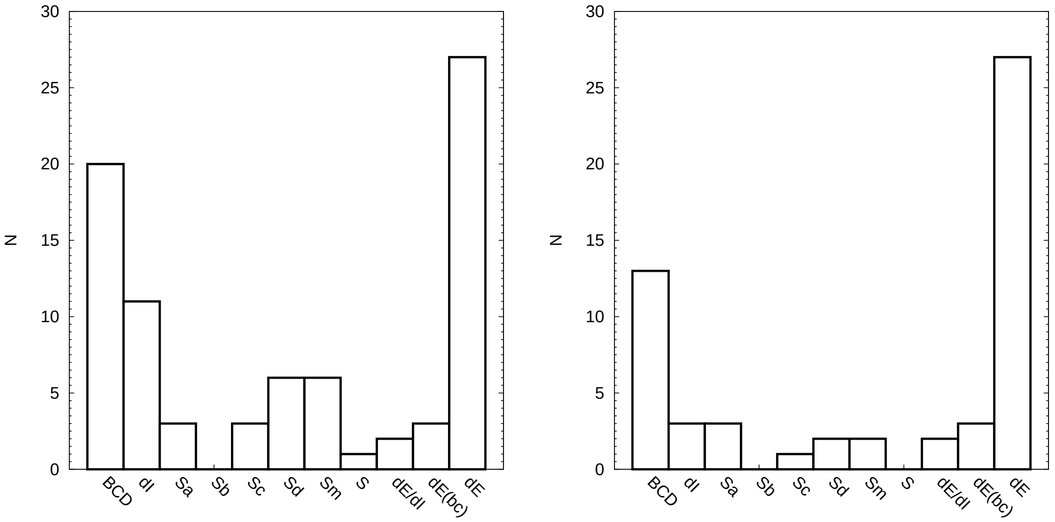

Figure 2.24: Late-type and early-type galaxies in the outer region of Virgo ($D_{M87} > 0.6$ Mpc). In the left panel a cutoff of $M_r < -18$ mag and $\langle\mu_r\rangle_{eff,r} > 23$ mag/arsec^2 was applied to restrict the parameter region to the locus of most of the LSB-components. The same cutoffs were used in the right panel but with an additionally colour cutoff of $(g - i) > 0.7$ mag. The histogram of the dEs also includes the dE(bc)s. The morphological types are taken from the VCC.

images. This may provide an explanation for the discrepant findings.

In summary, *if* the starbursts of the BCDs are relatively short, then many of the dEs in the Virgo outskirts with similar magnitudes must be the non-starbursting counterparts to the BCDs. Unless we are witnessing all BCDs in their very last starburst phase, which seems unlikely, this unavoidably means that *a number of dEs must be able to re-ignite a starburst*. Interestingly, a recent paper by Hallenbeck et al. (2012) finds gas in Virgo dEs and furthermore studies by Gu et al. (2006) and Lisker et al. (2006a) find dEs with blue cores, indicating recent or ongoing star formation. At first glance, one may speculate that these type are related with each other. However, we find that the dE(bc)s are on average less compact and brighter than the LSB-components of the BCDs (see Figs. 2.8 and 2.9).

To gain a deeper insight into the connections of BCDs and dEs, a large HI survey of both populations is worthwhile and may also change our view from “red and dead” dEs to more complex systems. This “increase” of complexity already started with several studies of dEs with spiral feature, discs or blue cores (e.g. Jerjen et al., 2000; Lisker et al., 2006b; Hallenbeck et al., 2012), and the improvement of observational techniques (e.g. E-ELT[10], JWST[11]) and new surveys (e.g. NGVS[12]) will push this complexity even further. Of course, this is also true for the BCDs, where new observations will probably reveal new substructure in the SB-regions as well as in the underlying LSB-component — e.g. i0-BCDs, where no LSB-component is detected until now.

[10] European Extremely Large Telescope (e.g. Kissler-Patig et al., 2009)
[11] James Webb Space Telescope (e.g. Gardner et al., 2006)
[12] Next Generation Virgo Cluster Survey (e.g. Ferrarese et al., 2012)

Chapter 3 The structural properties of late-type galaxies in the Virgo cluster

In this chapter, the structural parameters of the late-type galaxy population of the Virgo cluster are analysed. Furthermore, the distribution of the galaxies within the Virgo cluster and the dependence of the morphology according to the distance to M87 is investigated. Finally, the entire photometric and structural informations of the galaxies are used to review and update the initial classifications. To study the possible evolutionary connections between late- and early-type dwarf galaxies, the properties of these two groups are compared.
Together with the results of the BCDs and dIs from the previous chapter, the results of this chapter form the foundation for the investigation of the evolution with time of the late-type galaxies.

The results of this study were partly presented in Meyer and Lisker (2011) and throughout several conference contributions.

3.1 Introduction

Galaxies in the Virgo cluster, but also in other regions in the Universe, show a large variety in morphology, ranging from almost featureless galaxies to galaxies with impressing spiral structures. Moreover, galaxies show a diversity in colours, from relatively red to blue colours. The former class of galaxies with their smooth shape and red colours are called early-type galaxies (ETGs), while the latter are called late-type galaxies. The terms “early” and “late” do not give any hint to the evolutionary state of the galaxies and are mostly used for historical reasons. For instance, early-type galaxies are dominated by an old stellar population, while the luminosity of the late-type galaxies is dominated by young and massive stars (e.g. Sparke and Gallagher, 2000).

ETGs show a large spread in magnitude, ranging from a r-band magnitude of $M_r = -13$ mag for the most faintest ones of up to $M_r = -23$ mag for the brightest ETGs in the sample of this thesis. This means that the faintest ETG differs from the most luminous one by a factor of 10^4! The gigantic ETGs are also the largest galaxies in diameter of the entire morphological sequence, while the dwarfish ellipticals are the most frequently observed galaxy type.

As mentioned above, a first inspection of the optical images of ETGs show galaxies that are characterised by a smooth appearance and relatively red colours. However, studies of ETGs show that there are several subclasses with centrally concentrated star formation (Lisker et al., 2006a), disc features or spiral arms (Jerjen et al., 2000; Lisker et al., 2006b, 2007). These initially believed to be simple systems, are thus much more complicated.

Apart from the ETGs, there is another population of galaxies with bluer colours at a given magnitude. One of the representative of this morphological class shows prominent and striking spiral arms. These galaxies also show a large range in morphology ranging from Sa to Sm galaxies and are called spiral galaxies.

Looking at optical images of spiral galaxies, one realises that Sa galaxies have an inner dense region, which is most prominent in the class of Sa galaxies, and is called the *bulge*[1]. The stars in the bulge have random motions and the colours are generally red. From Sa to Sc galaxies the bulge became less prominent and vanished for the late-type spirals of type Sd and Sm. To characterise the importance of the bulge, the bulge-to-disc (B/D) ratio was introduced, which describes the ratio of the light contribution of the bulge to the one of the disc (Sandage, 1961; Graham and Worley, 2008). Bulge dominated systems like Sa galaxies have $B/D \sim 0.3$, while later types like Sc have $B/D \sim 0.05$ (Mo et al., 2010).

The dust in spiral galaxies is found to be located in a layer, which is very thin and has a spatial extend comparable to the stellar population (Xilouris et al., 1999). The extinction due to dust is also responsible to influence the colours of galaxies. Since dust extinction depends on the observed wavelength in way that the influence in the infrared is less than in UV, galaxies appear to be redder in the presence of dust. Therefore, the colours of a dust dominated galaxy do not represent the light distribution of the current

[1] Also the bulges show a variety in morphology: classical, boxy and peanut bulges (e.g. Athanassoula, 2005).

stellar population. Due to the distribution of the dust in a layer, the inclination angle also plays an important role. Galaxies that are observed face-on are less influenced by dust extinction than edge-on galaxies (Cunow, 1999).

Along the sequence of late-type galaxies the gas mass fraction varies strongly. McGaugh and de Blok (1997) showed that the gas mass fraction is a function of the central surface brightness μ_0 and the colour of the disc in a way that galaxies with a high surface brightness and red colours have a lower gas mass fraction. That means, the gas mass fraction of Sa galaxies is lower compared to late spirals. The different phases of the gas are also used as a tracer e.g. for the star formation rate (SFR) and metallicity (Z) and it was found that the SFR and Z are not homogeneous over the entire galaxy. For instance, observations and simulations of Virgo spirals reveal negative metallicity gradients (Magrini et al., 2011; Roediger et al., 2011).

The informations about the SFR of spiral galaxies are obtained from observation in Hα, which are available for many spiral galaxies in the Virgo cluster. Koopmann and Kenney (2004) found a reduction of the SFR in the outer part of the discs of Virgo spirals compared to field spirals of the same morphological type. Since the SFRs in the inner parts of the cluster spirals and field spirals are similar, they concluded that the reduction of the SFR is due the truncation of the disc in the dense cluster environment when the galaxies fall into the cluster. Comparing the late-type population of a cluster to the one in the field, it was shown that both populations differ from each other. For instance, the global SFR differs between galaxies in a cluster and galaxies in the field, what points to a transformation of galaxies, which enters the cluster. Indeed, Tully and Shaya (1984) showed by models that spiral galaxies just entered the Virgo cluster within several Gyr. A more detailed review of the differences of field and cluster galaxies is presented by Boselli and Gavazzi (2006).

Looking at the number distribution of luminous objects[2], spiral galaxies are the most frequently observed morphological type, but not the most luminous compared to the giant ellipticals. In the Virgo cluster, the faintest spiral galaxies of type Sm differ from the brightest Sc by a factor ~ 600 in luminosity.

It has to be pointed out that in early times galaxies of type Sd-Sm-Im were initially classified as an irregular class of Irr I and Irr II. Later, de Vaucouleurs (1974) introduced the classes of Sd, Sm and Im[3]. The “m” in Sm and Im is an abbreviation for Magellanic and indicates the similarities of these type to the Magellanic clouds (see

[2]Objects with brighter magnitudes than the dwarf galaxies.

[3]Please note that the classes of dI and Im will treated equally in this study.

also Fig. 1.1 of Chapter 1).
Galaxies which do not belong to any of the above mentioned classes are then classified as irregular galaxies.
Looking at all the different morphological types in the Virgo cluster, but also in other clusters, it was realised that the spatial distribution of the galaxies is not homogeneous. Furthermore, studies showed that the fraction of blue (late-type) to red (early-type) galaxies is a function of the distance of the galaxy to the centre of the cluster, which is called the morphology-density relation (Dressler, 1980). Thus, the galaxies will change their appearance when moving through the dense cluster environment. For instance, Conselice et al. (2001) showed that several early-type dwarf galaxies are not an old cluster population, but originated from in-falling field galaxies and therefore (parts) of the dEs are not formed in-situ. But the question is, which morphological type is able to form an early-type dwarf galaxy? To answer this question, it is crucial to investigate the structural parameters of both, early- and late-type galaxies, and after that, the evolution with time of these parameters by the means of models and simulations.
In this chapter we analyse the photometric and structural properties of the Virgo late-type galaxy population. The results of this chapter will serve as input parameters for the evolutionary synthesis models of GALEV in Chapter 4. The GALEV-code models the time evolution of the galaxies, and will be therefore the foundation of our investigation of possible connections between early- and late-type galaxies.

3.2 The sample and data reduction

3.2.1 Sample selection

Using the Virgo Cluster Catalog (VCC) by Binggeli et al. (1985) we selected all late-type galaxies within the Virgo cluster up to magnitude of $m_B \leq 18.0$ mag, where the VCC was found to be complete. This magnitude cutoff hence ensures that there is no bias due to undetected galaxies with a low surface brightness.
Applying a distance modulus of $m - M = 31.09$ mag (according to a distance of $D = 16.5$ Mpc; Mei et al., 2007; Blakeslee et al., 2009) this magnitude limit corresponds to an absolute magnitude of $M_B \leq -13.09$ mag.
To cover the entire morphological sequence from early-type to late-type galaxies within the Virgo cluster, we supplement the results from Janz and Lisker (2008); Janz and Lisker (2009) on ETGs.

To decide whether a galaxy belongs to the Virgo cluster or is located in the background, a heliospheric velocity criterium of $-730 \leq v_{helio} \leq 2990$ km/s was used (see appendix of Weinmann et al., 2011). All galaxies in this velocity range are treated as certain members. However, there are also galaxies with morphologies similar to Virgo galaxies but without any velocity information. These galaxies are handled as possible members. The original VCC was updated by Dr. T. Lisker using new velocities using the NASA/IPAC Extragalactic Database (NED) or SDSS (see Lisker et al., 2006b, and references therein).
Figure 3.1 shows the velocities and the corresponding distances of our sample taken from the GOLDMine data base (Gavazzi et al., 2003)[4]. Vertical lines correspond to the above mentioned velocity limits. There is one galaxy (VCC-0323) with a slightly larger velocity of $v_{helio} = 3002$ km/s, which is also included in the analysis[5]. Galaxies

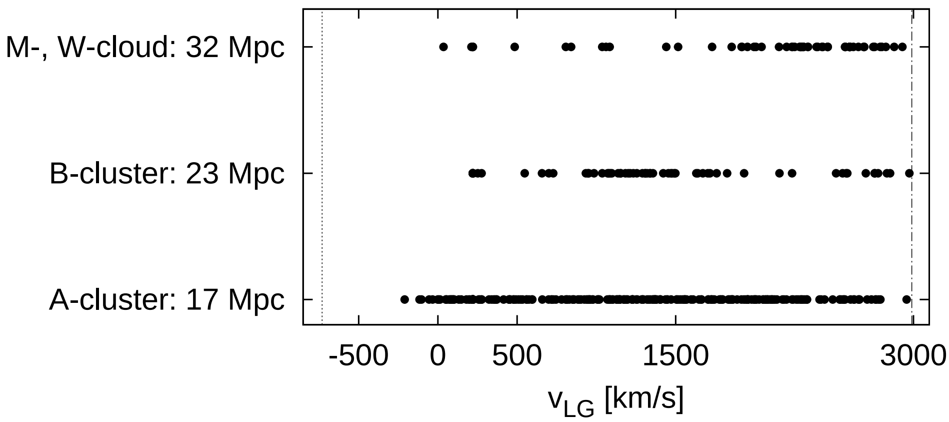

Figure 3.1: Velocities of the sample galaxies vs.their assumed distances. The heliocentric recessional velocities v_{helio} are taken from the GOLDMine data base, as well as the informations about the distances. To compare the velocities with the study of Gavazzi et al. (1999), which used velocities with respect to the local group (LG), we transformed v_{helio} into v_{LG} via $v_{LG} = v_{helio} + 220$ km/s.

with nearby bright foreground or background objects and mergers were also removed from the sample, since an accurate analysis of the photometric properties would not be possible. There are several galaxies that are not or only partly covered by SDSS.

[4]Web-page of the GOLDMine data base: http://goldmine.mib.infn.it/

[5]In an updated version of the GOLDMine data base (check: 04.10.2012), VCC-0323 has a velocity of $v_{helio} = 2756$ km/s.

These galaxies were removed from the analysis as well.
The complete sample of late-type galaxies consists of 388 galaxies and a summary of the sample with all derived parameters can be found in Tab. 6.2 of the appendix.

3.2.2 Remarks on the distances

During our analysis, we realised that some galaxies were listed as Virgo members, but do not fulfil the above mentioned velocity criterium. In the past, the membership was first determined only by morphology without available distance measurements. With new velocity data from SDSS and other observations, the GOLDMine data were updated and the new velocities were added. It turns out that in some cases the GOLDMine data base has used the wrong spectral informations from the SDSS, as illustrated in Fig. 3.2. The left panel of Fig. 3.2 shows VCC-0703 which is classified as dI (GOLDMine: Im), with a spectral derived distance of 95 Mpc. The cyan square indicates the location of the SDSS fibre, which was used to determine the distance. It is obvious that the spectrum used to derive the redshift, is that of the wrong galaxy and therefore also the distance is not the one of VCC-0703.
Another example of an issue with GOLDMine is VCC-0574 (D_{GOLDMine} = 307 Mpc), which is shown in the right panel of Fig. 3.2. In this case the situation is even worse. The coordinates of the dI VCC-0574 point to the galaxy with the cyan square, which clearly is not of type dI. Furthermore, there is a very faint galaxy in the north of the galaxy, which has the right morphological properties of a dI[6]. Moreover, it is also possible that the galaxy with the cyan square is a distant disc galaxy. Thus, it is very uncertain which galaxy actually is VCC-0574.

3.2.3 Classification

As a starting point we used the VCC classification of Binggeli et al. (1985). This step is important to obtain a first overview for the location of the different morphological types within the parameter-space of the derived photometric properties. In the course of this section the classification is reviewed and if necessary the galaxies are re-reclassified. One possible reason for a misclassification can be the usage of photometric plates from the Las Campanas survey. Figure 3.4 shows images of VCC-0979 from three different observations. On the left hand side of Fig. 3.4 the original photometric plate of the Las Campanas survey is shown, while the middle and right panels show the gri-

[6] For a better contrast we recommend the digital version of this thesis.

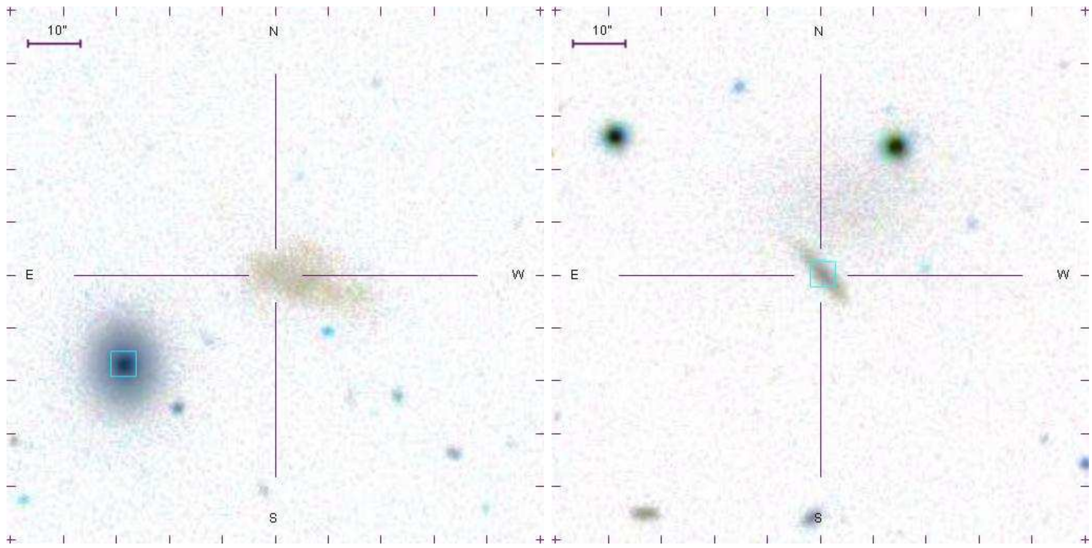

Figure 3.2: Wrong identified distances in GOLDMine due to inaccurate determination of the SDSS fibres. Left: VCC-0702; Right: VCC-0574.

SDSS and Hubble Space Telescope (HST) (WFPC2-F606W filter at 5957Å) image, respectively. Using the photometric plate, VCC-0979 was classified as Sa galaxy in the original work of Binggeli et al. (1985). However, the images of SDSS and HST show significantly more details and reveal possible ongoing or recent star formation in the centre of the galaxy, as well as dust lanes. Thus, with upcoming new, deeper and more detailed observations the morphological types of the galaxies will need to be revised once again.

Figure 3.3 shows the number distribution of the different classes of the late-type galaxies in the sample for the classification by Binggeli et al. (1985) and additionally the new classes after the revision of this study. Additionally plotted is the distribution of possible members of the Virgo cluster relative to the total amount of galaxies. As expected dwarf irregular galaxies (dIs) are the main class of late-type galaxies in the Virgo cluster with 95 galaxies. Compared to the dIs, the BCDs are less abundant with a total amount of 37 galaxies.

Within the class of spiral galaxies, the Sc galaxies are by far the most numerous class (83 galaxies), followed by the Sa (35 galaxies). The other spiral classes of Sb (18), Sd (21) and Sm (26) are represented in roughly equal numbers. In the class of galaxies with an unknown morphology, almost all galaxies were reclassified as part of this study. For completeness sake, we also include spiral galaxies of the type Sa, despite knowing that Sa galaxies, due to their large bulge, are not able to transform into early-type

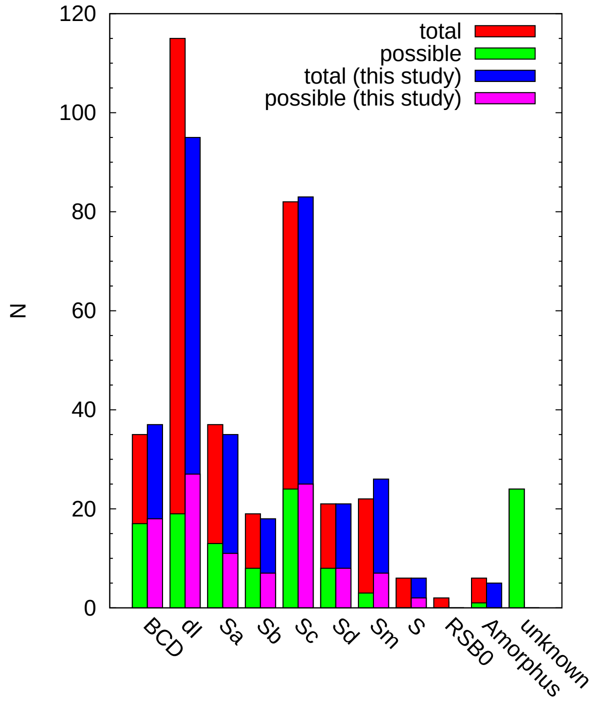

Figure 3.3: Number distribution of the different classes of the Virgo cluster. In each class the left bar corresponds to the classification of Binggeli et al. (1985) and the right one to the revision of our study.

dwarf galaxies. For the same reason of completeness, we also include two galaxies (VCC-0654 and VCC-1883) classified as "RSB0", which are S0 galaxies with a ring structure.
The group of star forming dwarf galaxies (BCDs and dIs) was already subject of the previous Chapter 2.

3.2.4 Data reduction

To analyse the optical properties of the late-type galaxy population of the Virgo cluster, we use the ugriz photometry with an effective exposure time of 54 s per filter (Gunn et al., 1998; Smith et al., 2002) from the Sloan Digital Sky Survey (SDSS) Data Release Five (DR5, Adelman-McCarthy et al., 2007). Since the SDSS does not point to each single galaxy, but operates in drift scan mode, the galaxies are not always covered by a single CCD image, which makes an alignment of several images necessary. Due to the high precision of the astrometry (Pier et al., 2003) the necessary alignment can

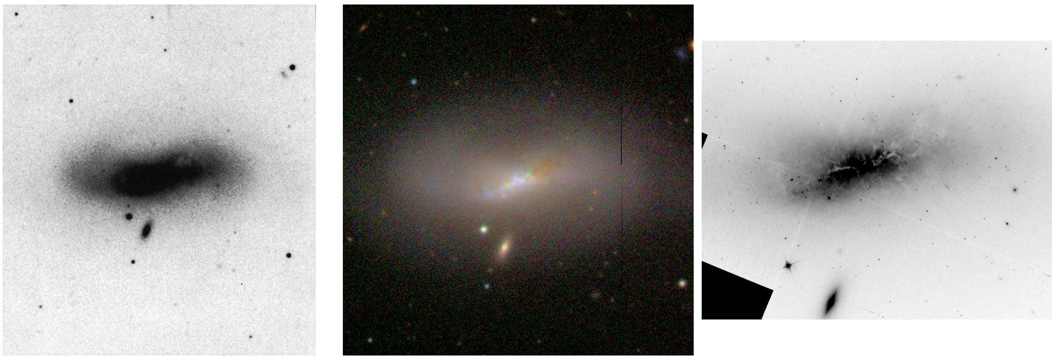

Figure 3.4: VCC-0979 observed with different telescopes. Left: photographic plate from the Las Campanas survey; Middle: gri-SDSS image; Right: HST image (WFPC2-F606W at 5957 Å).

be done automatically.
The SDSS pipeline provides measurements of the sky brightness, which turn out to be insufficient for our purpose. Therefore, we used the method of Lisker et al. (2007) for accurate sky subtraction. To determine the sky flux of the images, in a first step masks of all objects were created using the software SExtractor (Bertin and Arnouts, 1996). To avoid additional contamination of the sky due to too small masks, the masks were "blown up" through a gaussian kernel using the astronomical software package IRAF[7] (Tody, 1993). To increase the S/N, the g, r and i images were co-added to a single image and in combination with the "blown up" mask a new mask was created, which was finally applied to the images in different filters to obtain the accurate sky values. As shown by Lisker et al. (2007) the sky is not constant over the entire image. To account for this non-constant sky, the above mentioned mask was applied to the images and the sky was determined within overlapping boxes of the size 201 x 201 pixels. This results in a master sky image of each filter that was finally subtracted from the images.
The sky-subtracted SDSS images were finally flux calibrated by using the information from the SDSS, and Galactic extinction was corrected by using the equation given by Schlegel et al. (1998). The zero point offsets of the u and z filter were also corrected (Oke and Gunn, 1983) with:

$$\begin{aligned} u_{AB} &= u_{SDSS} - 0.04 \text{ mag} \\ z_{AB} &= z_{SDSS} + 0.02 \text{ mag}. \end{aligned} \tag{3.1}$$

[7]http://iraf.noao.edu/

All the above mentioned data reduction steps were done automatically with the program *virgocam*, which was provided by T. Lisker.
The error of the fluxes Δf in each filter x (x=u, g, r, i, z) was calculated by the formula given in Lisker et al. (2008):

$$\Delta f_x = f_x \cdot \left(\left(\frac{\sigma \cdot \sqrt{N_{pix}}}{f_x} \right)^2 + 2 \cdot \left(\frac{0.002 \cdot \sigma \cdot N_{pix}}{f_x} \right)^2 + \left(10^{0.4 \cdot \Delta\varphi} - 1\right)^2 + \Theta \cdot \left(10^{0.4 \cdot 0.02} - 1\right)^2 \right)^{0.5} \tag{3.2}$$

with

$$\Theta = \begin{cases} 0, & \text{for g,r,i and z} \\ 1, & \text{for u} \end{cases} \tag{3.3}$$

and

$$\Delta\varphi = \begin{cases} 0.02, & \text{for g,r and i} \\ 0.03, & \text{for u and z} \end{cases} \tag{3.4}$$

In Equation 3.2 N_{pix}, is the number of pixels within the aperture, f_x the measured flux and σ the noise level per pixel. $\Delta\varphi$ accounts for the uncertainties of the photometric calibration in the different filters. The last term in the formula accounts for the red leak in the u-band, resulting in an uncertainty of 0.02 mag. Equation 3.2 also includes the uncertainties regarding the determination of the Petrosian radius (see next Section 3.2.5). It was estimated that the error of the Petrosian determination has the same order as the sky uncertainties (Lisker et al., 2008).
With the propagation of uncertainty the errors of the colours were calculated. The following equation shows the error of the (g-i)-colour, which is the main colour index used in this study:

$$\Delta(g - i) = -2.5 \cdot \log \left(1 - \sqrt{\left(\frac{\Delta f_g}{f_g} \right)^2 + \left(\frac{\Delta f_i}{f_i} \right)^2} \right) \tag{3.5}$$

with the measured fluxes f_g, f_i and the corresponding errors of Equation 3.2.

3.2.5 Data analysis

In the course of our data analysis, it was realised that the centre coordinates, given by the VCC, are inaccurate for some galaxies. Therefore, we determine the centre

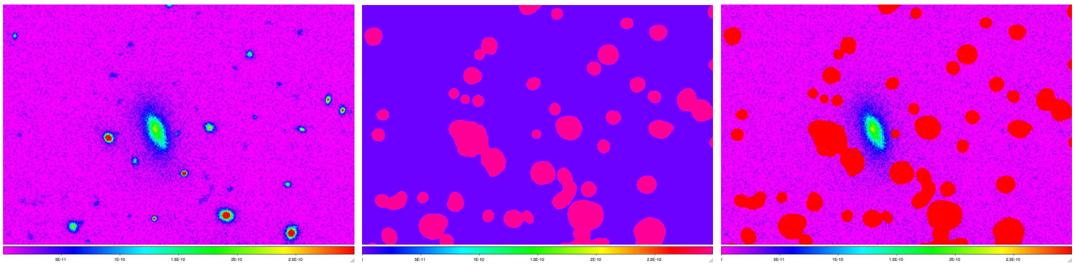

Figure 3.5: Reduction of VCC-0030. Left: gri-SDSS image in false colours; Middle: corresponding mask for the image; Right: Combination of image and mask.

coordinates for the entire sample using the IRAF task *ellipse* (Jedrzejewski, 1987). This was done in several steps starting with an initial rough eye approach of the centre. With these centre coordinates a first determination of the Petrosian semi-major axis a_p (Petrosian, 1976) for an elliptical aperture (Lotz et al., 2004), using the co-added SDSS gri-image of the galaxy, was performed by the program *AMOR* of T. Lisker. The derived parameters (x_0,y_0, ϵ_0 and $a_{p,0}$) of this run were used as starting conditions for IRAF/ellipse with a fixed a_p. This analysis yielded the new centre coordinates (x_c,y_c), ellipticity (ϵ) and position angle (p.a.) for each galaxy. Using these parameters, the Petrosian radius was determined again and in the last step the IRAF parameters (x_c, y_c, ϵ and p.a.) were fixed and the final Petrosian radius was determined within the co-added gri-image. The derived parameters of the gri-image are used for all filters in the same manner and were used to measure the total flux and the half-light semi-major axis a_{hl} within $2a_p$ aperture for all five SDSS filters.

To avoid flux contamination by sources other than the galaxy, the above mentioned masks were used as a first approximation. To analyse the galaxy, the region around the relevant galaxy has to be unmasked, resulting in an image where all objects, except the sky and galaxy, are masked out. Small scale objects on top of the galaxy, which do not belong to the galaxy (e.g. stars), are not masked by the first mask. Therefore, these objects were visually inspected and are masked by hand. The left panel of Fig. 3.5 shows, in false colours, the image of VCC-0030, with the corresponding mask in the middle. The combination of the image and the mask is shown in the right panel of the figure.

With the final set of x_c, y_c, ϵ, p.a. and a_{hl}, we are able to perform our analysis within an aperture of $2a_p$, yielding all relevant parameters, including the semi-major half light radius a_{hl} in units of pixels. To obtain the effective radius R_{eff} in arcsec, the semi-major half light radius a_{hl} has to be transformed via:

$$\mathrm{R_{eff}} = 0.396\,\frac{\mathrm{arcsec}}{\mathrm{pixel}} \cdot \mathrm{a_{hl}} \cdot \sqrt{b/a}, \tag{3.6}$$

with the axis ratio (b/a) and the SDSS pixel scale of $0.396\frac{\mathrm{arcsec}}{\mathrm{pixel}}$.
To convert $\mathrm{R_{eff}}$ from arcsec into parsec the following conversion was used

$$\mathrm{R_{eff}[pc]} = \mathrm{R_{eff}[arcsec]} \cdot \tan\left(\frac{1}{3600} \cdot \frac{\pi}{180}\right) \cdot \mathrm{D[pc]}, \tag{3.7}$$

with the distance D of the object in parsec. In case of the Virgo cluster a constant distance of D=16.5 Mpc was assumed (Mei et al., 2007).
The mean effective surface brightness $\langle\mu\rangle_{\mathrm{eff}}$ of the galaxies was calculated by

$$\langle\mu\rangle_{\mathrm{eff}} = \mathrm{m} + 2.5\log\left(2\pi\mathrm{R_{eff}^2}\right), \tag{3.8}$$

with the apparent magnitude m and $\mathrm{R_{eff}}$ in units of arcsec.
Since the above described parameters differ from filter to filter, it is reasonable to choose a reference band. If not stated otherwise, the r-band was used as the reference filter.

3.3 Results

In this section we present the results of the analysis of the late-type galaxy population within the Virgo cluster. In the first part, the spatial distribution of the galaxy within the Virgo cluster is described. In the second part of this section, the photometric properties of the sample are presented and furthermore the results are compared for different approaches for the distances. Finally, the morphological classes of the VCC are reviewed and if necessary the galaxies are reclassified by using all the informations of the following analysis.

3.3.1 Distribution within the Virgo cluster

The distribution of the galaxies within the Virgo cluster is shown in Fig. 3.6, which is divided into two panels for reasons of clearness. The position of M87 is marked with a black cross and defines the assumed centre of the Virgo cluster at a position of $\alpha = 187.705907$ deg and $\delta = 12.3911409$ deg (α = 12h 30min 49.4s; δ = 12d 23min 28.0s). Additionally, the sample of early-type galaxies from the study of Janz and Lisker (2008) is plotted as small black data points. Particular in the case of the spirals in the right hand side of Fig. 3.6, one can see a clustering of the morphological types into different clouds, which was already reported by the early studies of de Vaucouleurs (1961), Binggeli et al. (1985) and Binggeli et al. (1993). These clouds were also mentioned in the BCD Section 2 (see Tab. 2.5.2). Figure 3.7 shows the original map from Gavazzi et al. (1999) with the subdivision of the cluster into different regions. The coordinates of the galaxies correspond to the equinox of J1950, in contrast to the coordinates of this study with an equinox of J2000.

Comparing the distribution of the Virgo galaxies with the study of Gavazzi et al. (1999), the galaxies can be associated with the different clouds and sub-clusters. The distance of each galaxy within GOLDMine is based on the location within these cluster regions, thus a galaxy in the A-cluster has a distance of D=17 Mpc, whereas a galaxy in the M-cloud has a distance of D=32 Mpc. These distances will be from particular interest in the Sections 3.4.2 and 3.4.3, where we also discuss the implications of assigning distances this way.

With the exact centres of the galaxies it is possible to measure the projected distance to M87. The distances of the galaxies to M87 are calculated with

$$R_{CC}[\text{degree}] = \sqrt{\left(\alpha_{M87} - \alpha_{galaxy}\right)^2 + \left(\delta_{M87} - \delta_{galaxy}\right)^2}. \quad (3.9)$$

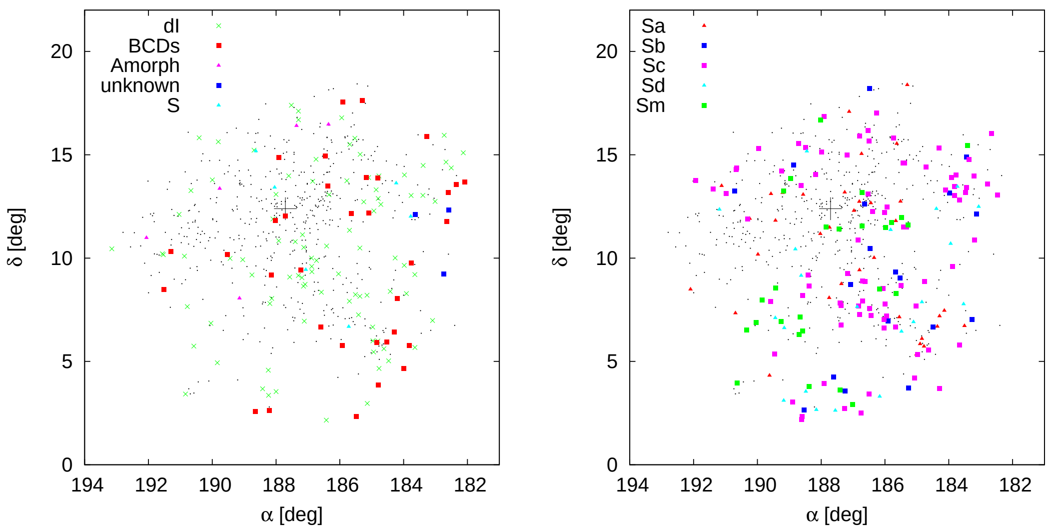

Figure 3.6: The distribution of late-type galaxies in the Virgo cluster. For comparison the early-type galaxies (black dots) are plotted too. Different sub-regions of the cluster are visible and can be compared with Fig. 3.7.

This radius is also called the cluster centric radius R_{CC}.
Figure 3.8 shows the number distribution of the different types as a function of the distance to M87. R_{CC} was normalised to a virial radius of $R_{Virial} = 1.5$ Mpc (McLaughlin, 1999).
As seen in Fig. 3.8, dIs have a relative mean distance to M87 of $\left\langle \frac{R_{CC}}{R_{Virial}} \right\rangle = 0.88 \pm 0.44$ with a small increase at $\frac{R_{CC}}{R_{Virial}} = 1.5$. Compared to the dIs, the BCDs are further out at $\left\langle \frac{R_{CC}}{R_{Virial}} \right\rangle = 0.99 \pm 0.49$, with two peaks in the number distribution at $\frac{R_{CC}}{R_{Virial}} = 0.6$ and $\frac{R_{CC}}{R_{Virial}} = 1.1$.
Due to the limited number of galaxies of the morphological type unknown, Amorphous and S, the statistic is quite poor. However, they all show a similar distribution of the cluster centric radius with an average of $\frac{R_{CC}}{R_{Virial}} \approx 0.75$.
Looking at the spiral galaxies in the right panel of Fig. 3.8, one can see that the most abundant type are the Sc galaxies, which are located at $\left\langle \frac{R_{CC}}{R_{Virial}} \right\rangle = 0.91 \pm 0.41$. The distribution of the Sa galaxies shows two peaks at $\frac{R_{CC}}{R_{Virial}} \approx 0.4$ and $\frac{R_{CC}}{R_{Virial}} \approx 1.25$, respectively. The Sb and Sc galaxies show a quite broad distribution with the Sb galaxies peaking at $\frac{R_{CC}}{R_{Virial}} = 0.75$. The morphological type of the Sm galaxies are also located in a small distance to M87 and show a broad distribution from $0 \leq \frac{R_{CC}}{R_{Virial}} \lessapprox 2$.
Table 3.1 shows the average radii from M87 for the different morphological types. It was found that galaxies of type S have the smallest distance to the centre, while Sd

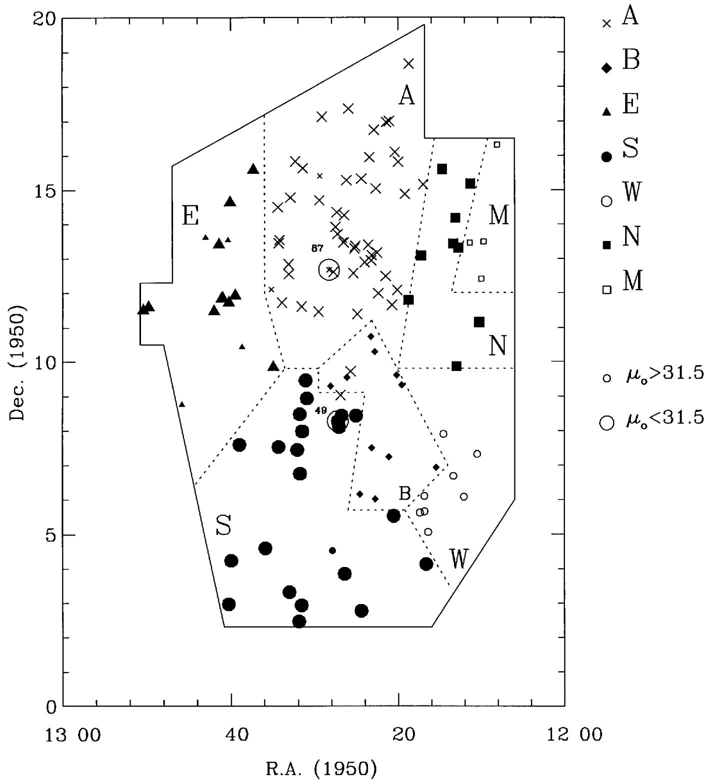

Figure 3.7: Map of the Virgo cluster, taken from Gavazzi et al. (1999), showing the different regions of the cluster. The position of M87 is indicated by a circle with superscript number 87. Large capitals label the region within the Virgo cluster and the size of the symbols corresponds to the distance modulus μ_0 of the galaxies.

galaxies have the largest distance, as expected from the morphology-density relation.

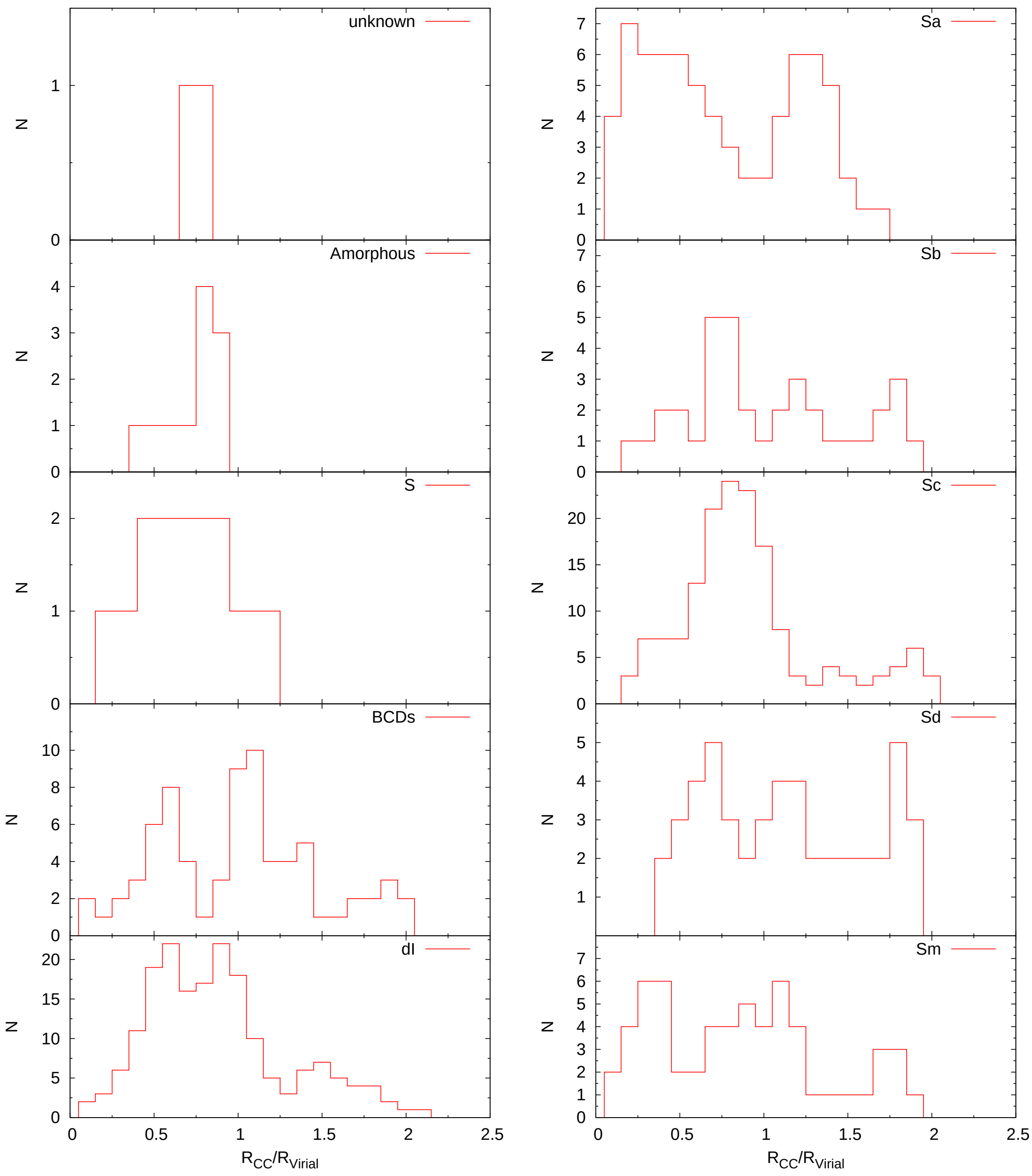

Figure 3.8: Number distribution of different galaxy types regarding the cluster centric radius R_{CC}, which is normalised to a virial radius of $R_{virial} = 1.5$ Mpc and a step size of 0.2 R_{virial}. Note: the scale of the y-axis changed with the different morphological types.

Table 3.1: Average radii R_{CC} to M87 normalised to a virial radius of R_{virial} = 1.5 Mpc.

Type	$\langle R_{CC}/R_{virial} \rangle$	σ
Sa	0.76	0.46
Sb	1.01	0.49
Sc	0.91	0.41
Sd	1.08	0.49
Sm	0.86	0.51
S	0.67	0.31
Amorph	0.76	0.19
BCDs	0.99	0.49
dI	0.88	0.42

3.3.2 Photometric properties

In this section we present the results of our analysis. For a first approach, we will assume a constant distance of D=16.5 Mpc, and later on discussing the variation of the derived parameters if we instead use the distances from the GOLDMine data base. In Section 3.4.3, galaxies that are conspicuous in the diagrams are discussed in more detail.

Figures 3.9 to 3.19 show the results of late-type galaxies in the colour-magnitude diagram (CMD) and in the $R_{eff} - M_r - \langle\mu\rangle_{eff}$-plane (together *the* parameter-space). For a first approach, we use the galaxy types of the VCC and the first revision of T. Lisker in the diagrams. Therefore, the given average values correspond to the revised version of the VCC by T. Lisker. Later on, the galaxy types are reclassified if their location within the $(g - i) - M_r - R_{eff} - \langle\mu\rangle_{eff}$ parameter-space does not fit to the bulk of the single galaxy types.

Parameters of BCDs are taken from Chapter 2 and are corrected for the flux of the starburst region. As in the previous plots, we show the results from Janz and Lisker (2008); Janz and Lisker (2009) for a sample of ETGs in the Virgo cluster as black data points. The vertical bars in the diagrams correspond to the 2σ deviation of the ETG sample within a magnitude bin of $\Delta M_r = 0.5$ mag or $\Delta \langle\mu\rangle_{eff,r} = 0.5$ mag/arcsec^2. Green asterisks correspond to ETGs with a blue core (dE(bc)), which are characterised by ongoing or recent star formation(Lisker et al., 2006a).

In Tab. 6.2 of the appendix, the results of the analysis are summarised. The membership (ms) to the Virgo cluster was adapted from Binggeli et al. (1985) and was updated by T. Lisker with recent values from the literature (column [2]).

In the following we discuss the properties of each morphological galaxy type, as well as potential outliers in the diagrams.

Sa

Galaxies classified as Sa are located in the region of $0.53 < (g - i) < 1.23$ mag, $-21.91 < M_r < -15.11$ mag, $0.61 < R_{eff} < 5.26$ kpc and $18.91 < \langle\mu\rangle_{eff,r} < 23.70$ mag/arcsec^2 in the $(g - i) - M_r - R_{eff} - \langle\mu\rangle_{eff}$ parameter-space in Fig. 3.9 to 3.19.

Calculating the mean values of all parameters reveal a mean colour of $\langle(g - i)\rangle = 1.05 \pm 0.14$ mag, a magnitude of $\langle M_r\rangle = -19.39 \pm 1.48$ mag, an effective radius of $\langle R_{eff}\rangle = 2.04 \pm 1.07$ kpc and $\langle\langle\mu\rangle\rangle_{eff,r} = 20.43 \pm 0.96$ mag/arcsec^2 (see Fig. 3.25). All quoted errors for the average values represent the 1σ deviations.

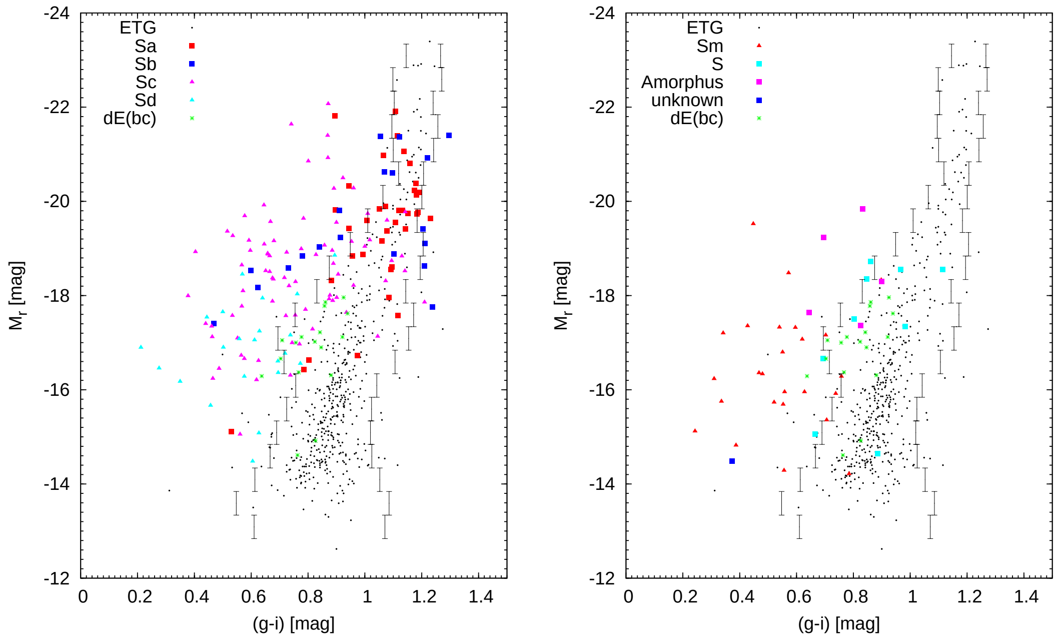

Figure 3.9: Colour-magnitude diagrams of late- and early-type galaxies in the Virgo cluster. Black dots show the ETG sample of Janz and Lisker (2008); Janz and Lisker (2009). The vertical bars correspond to the 2σ deviation within a magnitude bin of 0.5 mag. For clearness the CMD is divided into two parts. Left panel: CMD with spirals (Sa-Sd); Right panel: same CMD for Sm, SB, Amorphous, S and unknown galaxies. The CMD of the BCDs and the dIs can be found in Chapter 2.

At first glance one realises galaxies in the region between $1.1 < (g-i) < 1.5$ mag and $-20.0 < M_r < -17.2$ mag on the left hand side of Fig. 3.9 which are slightly redder than the population of ETGs. One may speculate that these galaxies are inclined ones. However, a detailed inspection of the co-added gri-SDSS images of the Sa galaxies in this region showed that there is no general trend of being edge-on. In this case it is worth to investigate the shifts of the magnitude[8] introduced by different distance approaches, what will be done in Section 3.4.3.
Sa galaxies have an average axis ratio of $\langle (b/a) \rangle = 0.56 \pm 0.20$ with a broad distribution from almost circular galaxies with $(b/a) \approx 1$ down to $(b/a) \approx 0.2$, indicating very elliptical shapes (Fig. 3.10). Assuming that face-on Sa galaxies are almost round with an axis ratio of $(b/a) \approx 1$ and also assuming that they are very thin in the z-direction, it became clear that several Sa galaxies of the sample have to be inclined.

[8]The colours are not affected by different distances, since we are still at redshifts close to zero.

With increasing inclination angle the path length through the disc increases and in turn increasing the dust reddening. Therefore, also the magnitude and the corresponding colours are influenced. From this we conclude that the intrinsic colour distribution, corrected for inclination, is somewhat bluer than the observed one.

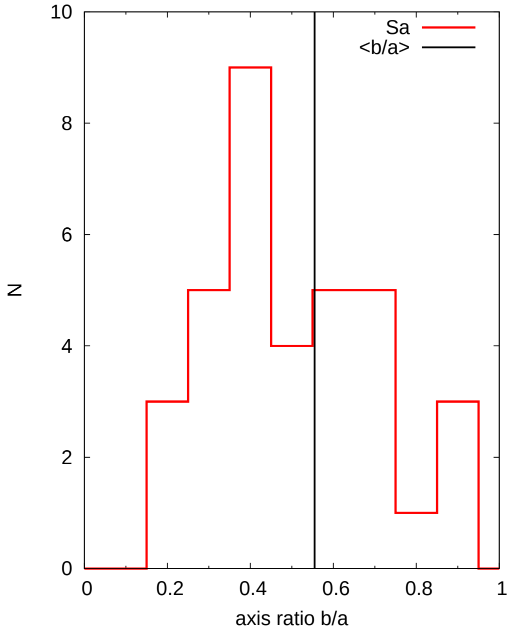

Figure 3.10: Histogram of the axis ratio of Sa galaxies. The mean axis ratio is indicated by the black line and amounts $\langle (b/a) \rangle = 0.56 \pm 0.20$.

Sb

In the region of $0.47 < (g - i) < 1.3$ mag, $-21.40 < M_r < -17.41$ mag, $0.76 < R_{eff} < 5.3$ kpc and $18.78 < \langle\mu\rangle_{eff,r} < 22.38$ mag/arcsec^2 of Figs. 3.9 to 3.19 the Sb galaxies are located. Looking at the CMD in Fig. 3.9, one finds Sb galaxies in the region of $(g - i) > 1.0$ mag and $M_r > -20.0$ mag, which are, from a visual inspection, invariably inclined galaxies. Except for the galaxies in this region, the other Sb galaxies follow an almost linear correlation in the way that with increasing colours the galaxies getting brighter. In the $R_{eff} - \langle\mu\rangle_{eff,r}$-diagram of Fig. 3.18, we found that Sc galaxies with a larger effective radius are also brighter.

No obvious outliers can be found, except for VCC-0267, which has a slightly lower $\langle\mu\rangle_{eff,r}$ compared to the other Sb galaxies in Fig. 3.12 and 3.19.

The following average values and 1σ deviations were calculated for the Sb galaxies: $\langle(g-i)\rangle = 0.98 \pm 0.25$ mag, $\langle M_r \rangle = -19.46 \pm 1.25$ mag, $\langle R_{eff} \rangle = 2.13 \pm 1.24$ kpc and $\left\langle \langle\mu\rangle_{eff,r} \right\rangle = 20.42 \pm 0.88$ mag/arcsec^2. The average axis ratio was measured to $\langle(b/a)\rangle = 0.55 \pm 0.23$. However, Fig. 3.11 shows a double peak in the histogram at $(b/a) = 0.2$ for highly inclined Sb galaxies and at $(b/a) = 0.7$. This double-peak distribution may be explained by the inclination angles. A face-on spiral is easily classified according its bulge-disc ratio and pitch-angle of the spiral arms. However, these features became less obvious in case of increasing inclination.

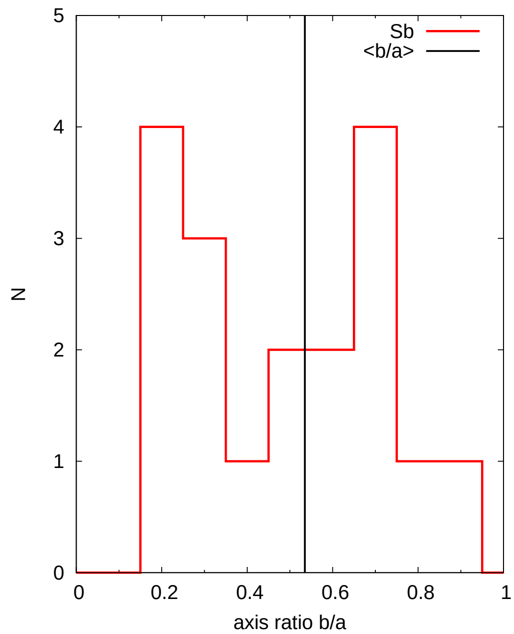

Figure 3.11: Same as Fig. 3.10, but for the Sb galaxies. $\langle(b/a)\rangle = 0.55 \pm 0.23$.

Sc

In Figs. 3.9 to 3.19 the region of $0.39 < (g-i) < 1.21$ mag, $-22.07 < M_r < -15.05$ mag, $0.67 < R_{eff} < 7.62$ kpc and $19.72 < \langle\mu\rangle_{eff,r} < 23.16$ mag/arcsec^2 is populated with Sc-type galaxies.
Inclined Sc galaxies can be found in the region of $(g-i) > 1.0$ mag and $M_r > -19.0$ mag. The rest of the Sc galaxies covers a region in the CMD from $0.39 < (g-i) < 1.2$ mag and $-22.0 < M_r < -16.0$ mag, with one outlier (VCC-0989) at (g-i) = 0.56 mag and $M_r = -15.05$ mag, which will be discussed in Section 3.4.3.
Calculating the mean values of all parameters reveal: $\langle(g-i)\rangle = 0.76 \pm 0.20$ mag, $\langle M_r \rangle = -18.51 \pm 1.31$ mag, $\langle R_{eff} \rangle = 1.97 \pm 1.26$ kpc and $\left\langle \langle\mu\rangle_{eff,r} \right\rangle = 21.20 \pm 0.80$

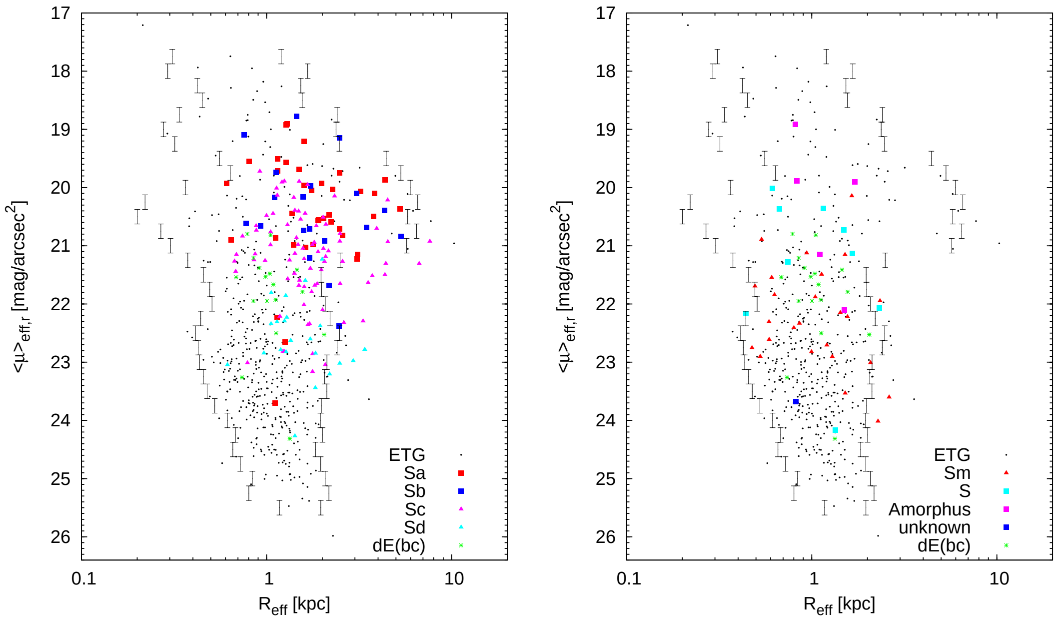

Figure 3.12: Effective radius R_{eff} vs. the mean effective surface brightness $\langle\mu\rangle_{eff,r}$ in r-band. Left panel: spirals (Sa-Sd); Right panel: same for Sm, SB, Amorphous, S and unknown galaxies.

mag/arcsec^2.

Like the Sb galaxies, also the Sc's show double peak in the histogram for the axis ratio (Fig. 3.13). However, the region between the two peaks is small and thus may disappears when different bin sizes and steps were applied. The average axis ratio over the entire range in the histogram of the Sc galaxies is $\langle(b/a)\rangle = 0.54 \pm 0.25$.

Sd

Galaxies classified as Sd galaxies are located in the region of $0.21 < (g-i) < 0.89$ mag, $-18.86 < M_r < -14.48$ mag, $0.62 < R_{eff} < 3.39$ kpc and $21.23 < \langle\mu\rangle_{eff,r} < 24.27$ mag /arcsec^2.

Compared to the Sc galaxies, the Sd galaxies in Fig. 3.9 have bluer (g-i)-colours with a minimum at $(g-i) = 0.21$ mag. At a given (g-i)-colour of $(g-i) \approx 0.62$ mag two galaxies have relatively faint magnitudes ($M_r > -15.1$ mag) compared to the other Sc galaxies at the same (g-i)-colour. These two galaxies are VCC-0132 and VCC-1605 and are also conspicuous in Figs. 3.18 to 3.19, particular VCC-1605 stands out with a very small R_{eff} compared to the other Sc galaxies.

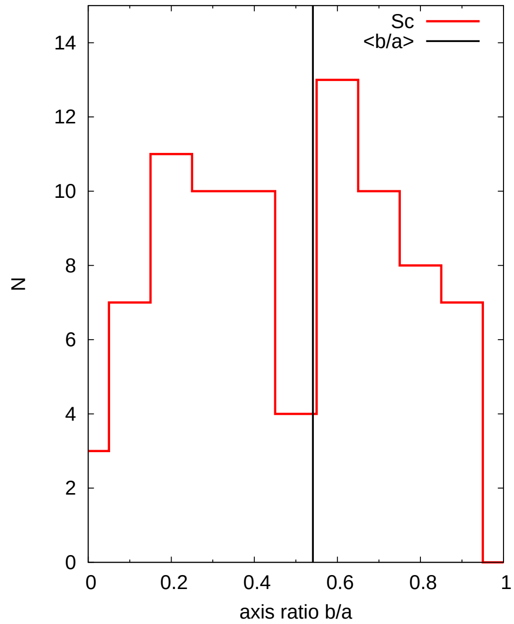

Figure 3.13: Same as Fig. 3.10, but for the Sc galaxies. $\langle(b/a)\rangle = 0.54 \pm 0.25$.

The Sd galaxies have an average (g-i)-colour of $\langle(g-i)\rangle = 0.58\pm 0.17$ mag, $\langle M_r\rangle =$ -16.88 ± 1.03 mag, $\langle R_{eff}\rangle = 1.66\pm 0.68$ kpc and $\left\langle\langle\mu\rangle_{eff,r}\right\rangle = 22.61\pm 0.66$ mag/arcsec^2. Figure 3.14 shows the histogram of the distribution of the axis ratio (b/a), with an average of $\langle(b/a)\rangle = 0.59 \pm 0.29$. The axis ratio has a broad distribution with one peak at (b/a)=0.8.

Sm

In the right panels of Figs. 3.9 to 3.19, we show the results of the Sm galaxies. The Sm galaxies cover a region in the parameter-space of $0.24 < (g-i) < 0.90$ mag, $-19.52 < M_r < -14.22$ mag, $0.48 < R_{eff} < 2.62$ kpc and $20.14 < \langle\mu\rangle_{eff,r} < 24.02$ mag/arcsec^2. There are three galaxies (VCC-1554, VCC-1575 and VCC-1686) which are conspicuous in the diagrams. However, only VCC-1554 shows obvious differences from the rest of the Sm population, while the other two galaxies are at the “boundaries” of the Sm distribution. The “boundaries” are described by the margins of the bulk of the population in the parameter-space.

Averaging all Sm galaxies we obtain: $\langle(g-i)\rangle = 0.55\pm 0.14$ mag, $\langle M_r\rangle = -16.42\pm 1.30$ mag, $\langle R_{eff}\rangle = 1.21\pm 0.64$ kpc and $\left\langle\langle\mu\rangle_{eff,r}\right\rangle = 22.24\pm 0.90$ mag/arcsec^2. The average axis ratio is $\langle(b/a)\rangle = 0.54 \pm 0.14$ and the distribution for the entire Sm

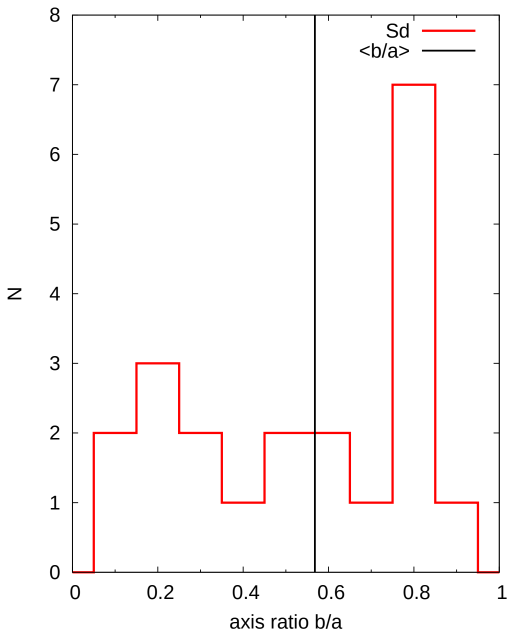

Figure 3.14: Same as Fig. 3.10, but for the Sd galaxies. $\langle(b/a)\rangle = 0.59 \pm 0.29$.

sample can be found in Fig. 3.15.

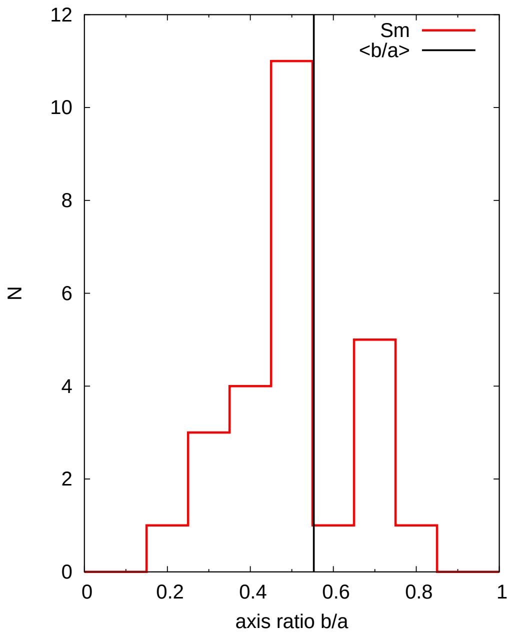

Figure 3.15: Same as Fig. 3.10, but for the Sm galaxies. $\langle(b/a)\rangle = 0.54 \pm 0.14$.

Unknown

Most of the initially "unknown" galaxies were reclassified by T. Lisker as irregular galaxies. To check this reclassification, all "unknowns" from the original VCC are used and were checked again in the parameter-space.
Galaxies classified as "unknown" in the VCC cover almost the same region in the CMD as the dIs, therefore, the revision by T. Lisker seems plausible. However, in the case of VCC-0020 it is not easy to decide which galaxy was classified in the initial VCC. In the image of the VCC-0020 there are three galaxies close together. The most prominent one has blue colours and could be classified as dI regarding its morphology, while the others have too red colours. The coordinates, given by GOLDMine for VCC-0020, point exactly to a galaxy which is relatively red. Due to the insufficient coordinates, we cannot confirm its VCC classification, and therefore VCC-0020 should not be taken into account for the remaining analysis.
After the first revision by T. Lisker, there is only one galaxy left over in the class of the "unknown" galaxies. This galaxy (VCC-0113) has very similar properties in the parameter-space as the BCDs in Figs. 3.9 and 3.18. However, the surface brightness is too low compared to the BCDs and LSB-components (see Figs. 3.12 and 3.19). Furthermore, the optical SDSS image of VCC-0113 shows some possible hints for interaction, noticeable by an extended halo with some kinds of loops or shells.

S

The class of "S" galaxies has be introduced for galaxies, showing a spiral structure but which cannot be associated with a special subtype (e.g. Sa or Sm). Looking at the class of "S" galaxies, one realises that they cover a range in magnitude of $\Delta M_r = 3$ mag and $\Delta \langle\mu\rangle_{\mathrm{eff,r}} = 4$ mag/arcsec^2, locating them in the regime of both giants and dwarfs.
Figure 3.9 shows two galaxies (VCC-0135 and VCC-0213), which are offset from the rest with a magnitude $M_r > -16$ mag and were already discussed in Section 2.4.8. They will also be discussed in Section 3.4.3. Averaging over the entire parameter-space yields a (g-i)-colour of $\langle(g-i)\rangle = 0.87 \pm 0.14$ mag, $\langle M_r\rangle = -17.26 \pm 1.53$ mag, $\langle R_{\mathrm{eff}}\rangle = 1.18 \pm 0.62$ kpc and $\left\langle\langle\mu\rangle_{\mathrm{eff,r}}\right\rangle = 21.36 \pm 1.29$ mag/arcsec^2.
The distribution of the axis ratio is shown in Fig. 3.16. It has a discrete distribution with several peaks and an average axis ratio of $\langle(b/a)\rangle = 0.57 \pm 0.27$. However, this finding should be handled with care, since there are only a few galaxies in this morphological class, resulting a poor statistic.

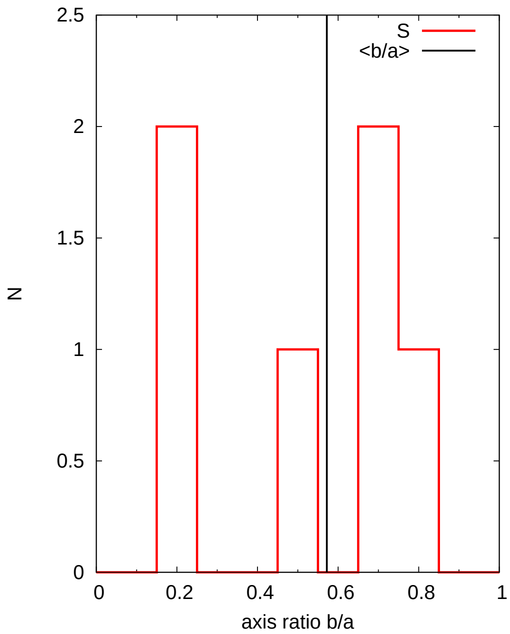

Figure 3.16: Same as Fig. 3.10, but for the S galaxies. $\langle (b/a) \rangle = 0.57 \pm 0.27$.

Amorphous

First introduced by Sandage and Brucato (1979), the Amorphous galaxies are "a redefinition of the standard Irr II type"[9]. Here the group of Irr I galaxies shows some hints of spiral arms (or more commonly: a organised structure), while the Irr II galaxies do not show any organised structure (Carroll and Ostlie, 2006). Thus, one would expect galaxies with irregularities. However, the gri-images of the Amorphous galaxies show discy galaxies with a wide range in colour. Comparing the classification of the original VCC and the data from GOLDMine also shows differences. Four out of five Amorphous galaxies are classified as "unknown" in GOLDMine and one galaxy (VCC-1675) is classified as "Pec". The classification of GOLDMine may be the better choice, since the amorphous class is somewhat loosely defined.

In Figs. 3.9 to 3.19, the Amorphous galaxies can be found in the region of 0.65 $<$ $(g-i) <$ 0.90 mag, -19.84 $< M_r <$ -17.34 mag, 0.82 $<$ $R_{eff} <$ 1.7 kpc and 18.92 $< \langle \mu \rangle_{eff,r} <$ 22.10 mag/arcsec^2 with average values of: $\langle (g-i) \rangle = 0.78 \pm 0.11$ mag, $\langle M_r \rangle = -18.48 \pm 1.05$ mag, $\langle R_{eff} \rangle = 1.21 \pm 0.41$ kpc, $\left\langle \langle \mu \rangle_{eff,r} \right\rangle = 20.39 \pm 1.24$ mag/arcsec^2 and $\langle (b/a) \rangle = 0.52 \pm 0.07$. The histogram of (b/a) is shown in Fig. 3.17 and has a very narrow distribution around the average, partly due to the small amount

[9]Citation from Sandage and Brucato (1979).

of galaxies with this classification.

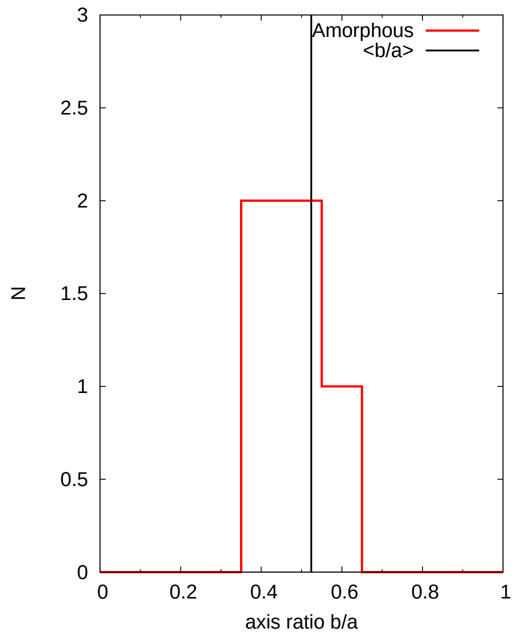

Figure 3.17: Same as Fig. 3.10, but for the Amorphous galaxies. $\langle (b/a) \rangle = 0.52 \pm 0.07$.

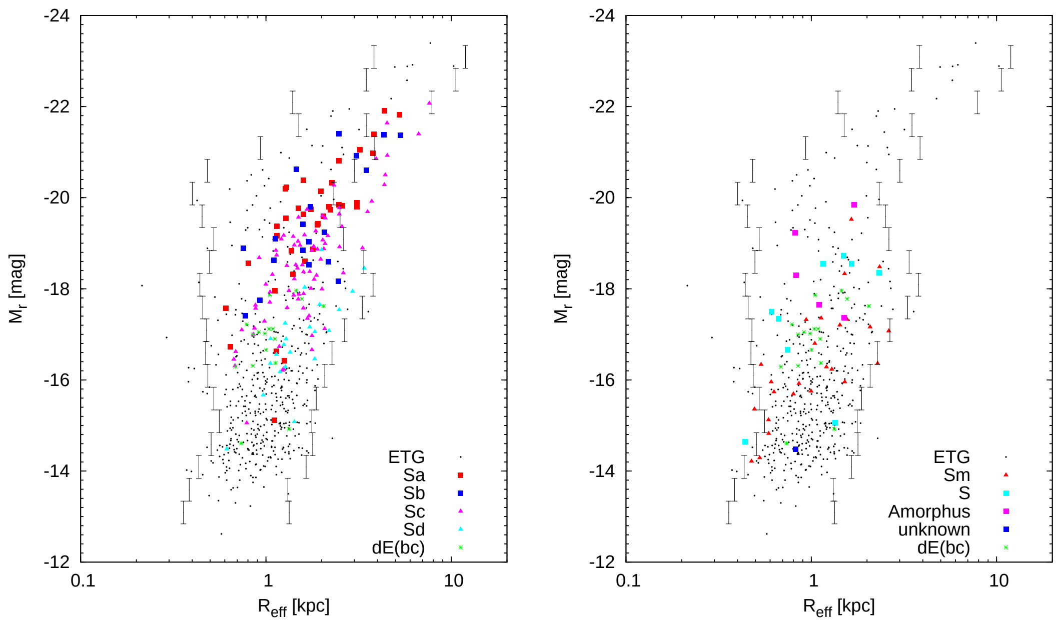

Figure 3.18: Effective radius R_{eff} vs. absolute magnitude M_r in r-band. Left panel: spirals (Sa-Sd); Right panel: same for Sm, SB, Amorphous, S and unknown galaxies.

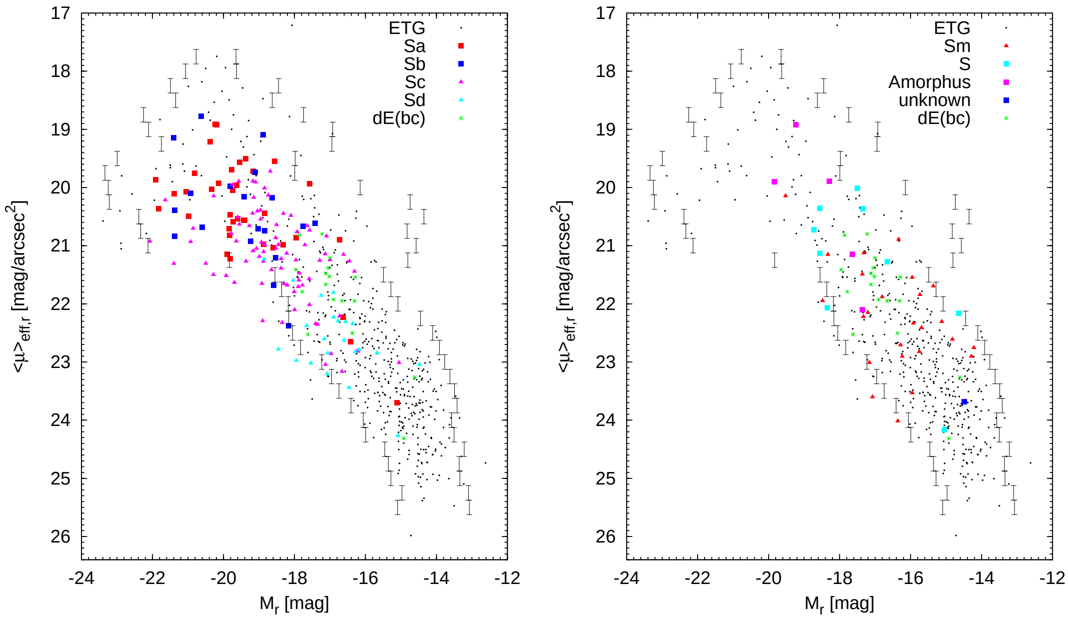

Figure 3.19: Absolute magnitude M_r vs. the mean effective surface brightness $\langle\mu\rangle_{\mathrm{eff,r}}$ in r-band. Left panel: spirals (Sa-Sd); Right panel: same for Sm, SB, Amorphous, S and unknown galaxies.

3.3.3 Colour-colour diagrams

Since all galaxies were analysed in all SDSS filter bands from u to z, also other colour informations are available. Figures 3.20, 3.21 and 3.22 for example, show the distance independent colour-colour diagram of all galaxies in our sample. Used colours are the (u-g)-colour, which is most sensitive to the age due to the UV flux of the young stellar population and the (i-z)-colour, most sensitive to the metallicity.
In the sample of ETGs, there are some galaxies that are relatively offset from the rest of the ETG population. This pertains to VCC-1039 and VCC-1719 with an (i-z)-colour of 0.84 mag and 1.15 mag, respectively. In the (u-g)-colours, VCC-0091 is offset from the rest with an (u-g)-colour of (u-g)=3.25 mag. In the figures a cutoff at (u-g)=2.5 mag and (i-z)=0.6 mag was applied, thus the above mentioned galaxies are not visible in the diagrams.
In Fig. 3.20, the Sa to Sd galaxies are displayed and additionally the ETGs are plotted (black dots). Among the Sa galaxies there are three galaxies which are very conspicuous in the diagram with colours of $(u - g) < 1.25$ mag and $(i - z) < 0.04$ mag, corresponding to VCC-0015, VCC-1358 and VCC-1933. The rest of the Sa galaxies have colours of $(u - g) > 1.3$ mag and $(i - z) > 0.1$ mag
One of the Sc galaxy (VCC-0865) has a very red (i-z)-colour of $(i - z) = 0.25$ mag compared to the other Sc galaxies. The other Sc galaxies have at given (u-g)-colours redder (i-z)-colour compared to the ETGs, but cover almost the same range in the (u-g)-colours of the ETGs.
In the class of the Sd galaxies, there is one galaxy (VCC-0132) that totally offset from the rest with extreme (i-z)-colours of $(i - z) = -0.48$ mag, which is only reached by the dIs.
The Sm galaxies are displayed in Fig. 3.21 and are found at (u-g)-colours of (i-z)$<$ 1.24 mag, with a large spread in the (i-z)-colours.
The loosely classified S galaxies, have the same coverage as the Sb and Sc galaxies. Furthermore, looking at the distribution of the Sb galaxies in Fig. 3.20, one can find a kind of underrepresentation of Sb galaxies between $1.25 < (u - g) < 1.45$ mag and $(i - z) < 0.16$ mag, which is filled by three of the S galaxy (Fig. 3.21), while the other S galaxies cover the same region as the Sb galaxies. However, this is only a weak indication to the exact morphological type of the S galaxies, since the same colours do not necessarily mean that the galaxies have the same morphology (structure). One of the S galaxies (VCC-0320) can be found at $(u - g) = -1.38$ mag and $(i - z) = -0.39$ mag. Among the spiral galaxies only the Sb galaxies have comparable red (i-z)-colours, what

could be therefore again hint to the exact morphological type.
The only “unknown” galaxy (VCC-0113) is located at (u-g)=-0.82 mag and (i-z)=-0.46 mag, which is only reached by the dI galaxies (cf. Fig. 3.22).
The colour-colour diagram of the BCDs and dIs is shown in Fig. 3.22. In contrast to the analysis of Chapter 2, the BCDs are not divided into the contribution of the starburst and LSB-component, due to the low S/N of the z-filter, what would be resulted in large photometric errors. Therefore, we use the total colours of the BCDs, instead of the colours of the LSB-component. The dIs show a large scatter in the colour-colour diagram and together with the BCDs, they tend to have redder (i-z)-colours at a given (u-g)-colour than the bulk of the dEs. However, also the dEs show a larger scatter in the diagram.

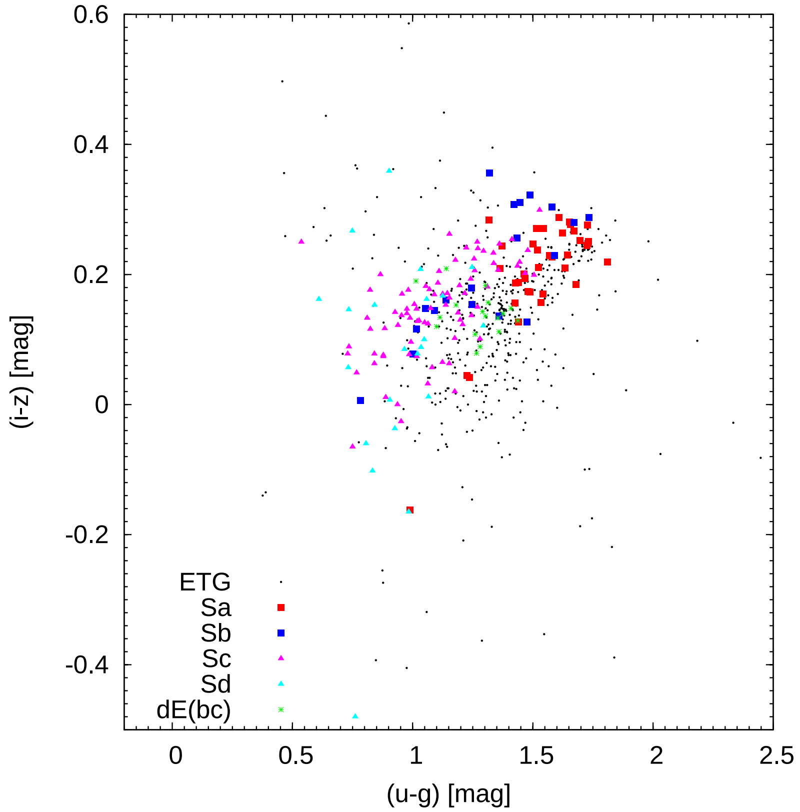

Figure 3.20: Colour-colour diagram of the late-type sample. Displayed are the spirals and the ETGs.

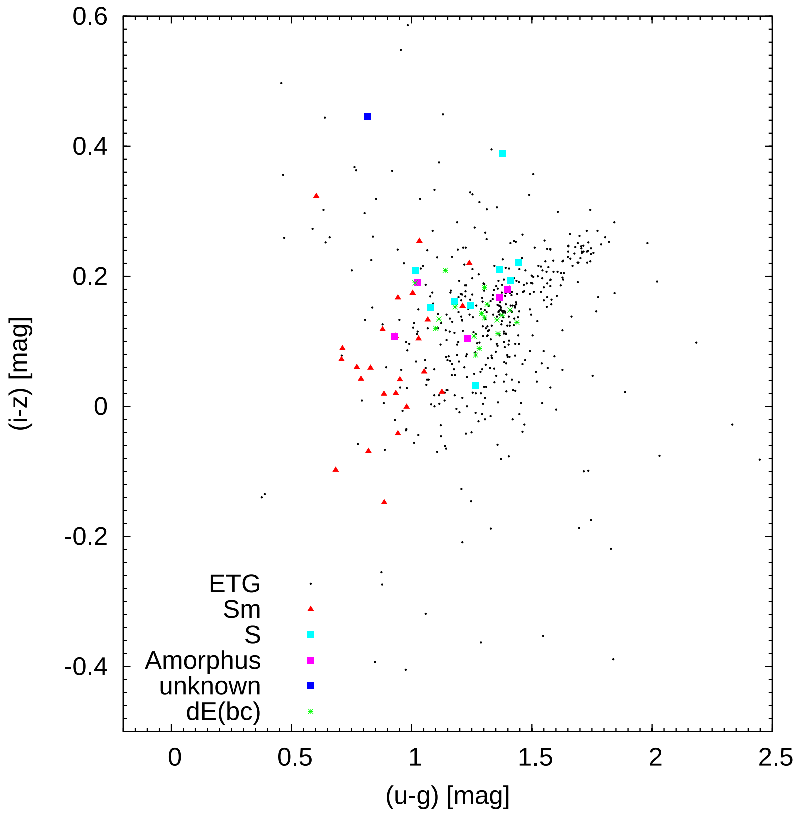

Figure 3.21: Same as Fig. 3.20, but for the Sm, S Amorphous and unknown galaxies.

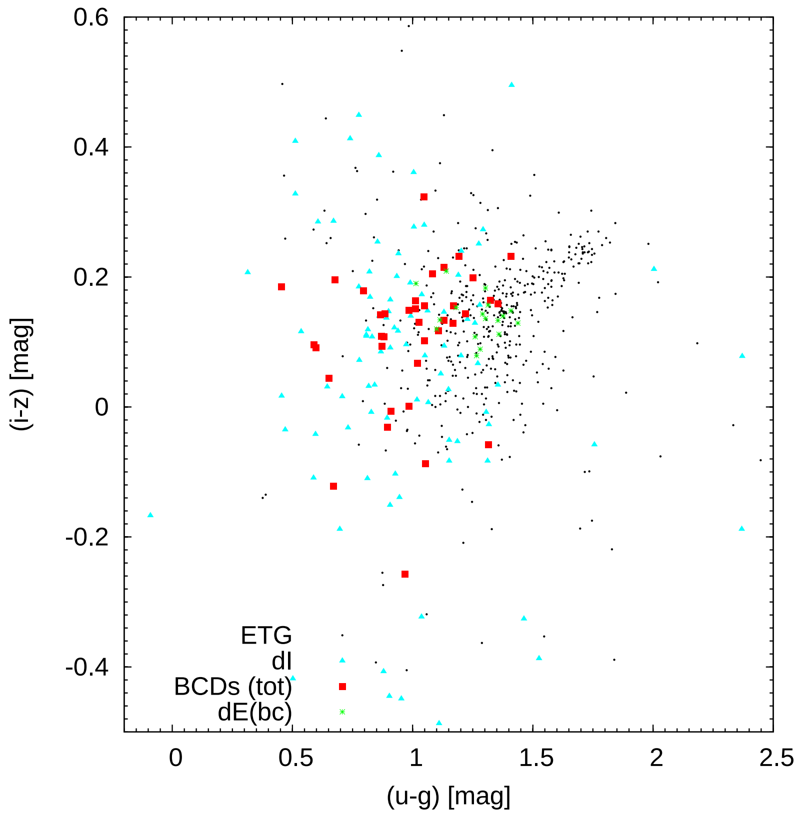

Figure 3.22: Same as Fig. 3.20, but for the BCDs and dIs. For the BCDs the total values are used, since the S/N of the LSB-component in z is too low.

3.3.4 The luminosity function

The luminosity function (LF) describes the number of galaxies dN per magnitude bin dM. LF can be approximated by an analytical function, given by Schechter (1976):

$$\mathrm{N(M)dM} = \phi^* \cdot 10^{-0.4(\alpha+1)\mathrm{M}} \cdot \mathrm{e}^{10^{\left(0.4(\mathrm{M}^*-\mathrm{M})\right)}}\mathrm{dM} \tag{3.10}$$

with the free parameters of the slope α, the normalisation ϕ^* and the characteristic magnitude M^*.

Figure 3.23 shows the LF of the early-type and late-type population of the Virgo cluster in the range of -22.0 to -13.0 mag with a bin width of 0.5 mag. Errors were estimated by

$$\Delta N(M) = \sqrt{N(M)}. \tag{3.11}$$

The black squares correspond to the overall LF of the entire Virgo cluster population. The green asterisks and red triangles indicate the distribution of the late-type and early-type galaxies, respectively. The solid line corresponds to the overall LF using Equation 3.10. The error weighted fit was performed with a non-linear least-square Marquardt-Levenberg algorithm. The slope α was found to be

$$\alpha = -1.27 \pm 0.02 \tag{3.12}$$

and the characteristic magnitude has a value of

$$\mathrm{M}_\mathrm{r}^* = -21.58 \pm 0.25 \text{ mag.} \tag{3.13}$$

Additional to the Schechter-function, also a linear fit (straight line in Fig. 3.23) to the data in the interval $-14.4 \leq \mathrm{M_r} \leq 19.0$ mag was applied, with a slope of

$$\alpha_{\mathrm{lin}} = -1.30 \pm 0.10. \tag{3.14}$$

The slopes α and α_{lin} are in good agreement with Rines and Geller (2008) also using SDSS r-band data and it is also in good agreement with Blanton et al. (2001) for their sample of 11275 galaxies from the SDSS. However, our values of α are slightly lower compared to other studies of the Virgo cluster by Trentham and Hodgkin (2002) and Sabatini et al. (2003), who found a slope of $\alpha \approx -1.6$ in the B-band. The SDSS analysis of Krywult (2009) on Abell clusters with richness classes (Abell et al., 1989) of $\mathrm{R} \geq 2$ (rich cluster) and $\mathrm{R} \leq 1$ (poor cluster) found quite different results. In the g-band they obtained slopes of Schechter-function fits of $\alpha = -0.70$, and even lower

values ($\alpha \approx 0.55$) for the other SDSS filters for the Abell rich clusters.
Trentham and Hodgkin (2002) investigated in their study whether the parameters of the LF depend on the used filter. Therefore, all five filters are used to derive the parameters of the LF and the results of the analysis are shown in Tab. 3.2. The results of α for the different filters show quite small deviations. When taken the errors of α into account, the differences are negligible.
The data of this thesis were partly used in Lieder et al. (2012) to determine the LF of the Virgo core region. A transformation of our r-band data to the V-band magnitude, using the method of Jester et al. (2005), and a linear fit to the Lieder et al. (2012) sample in the interval -18.0 $\leq M_V \leq$ -13.0 mag reveals a slope of $\alpha = -1.50 \pm 0.05$. Similar to the studies of Trentham and Hodgkin (2002) and Sabatini et al. (2003), this slope is steeper than ours.

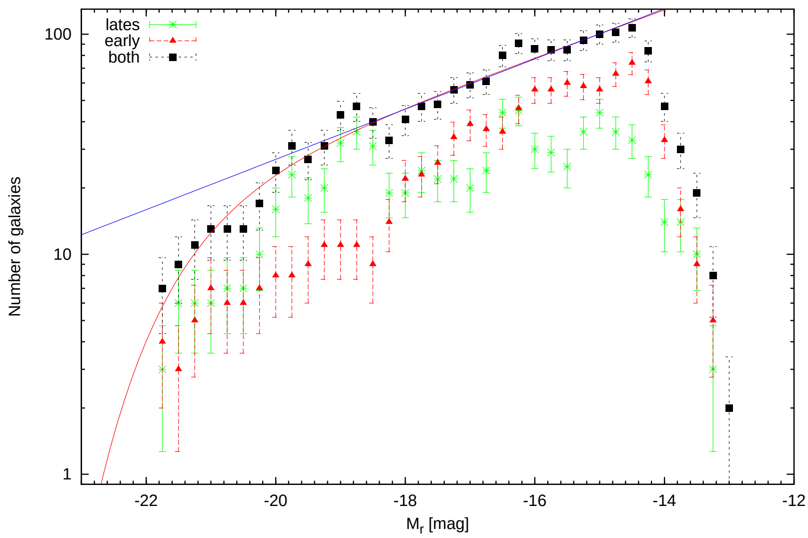

Figure 3.23: Luminosity function of Virgo galaxies. Plotted are late-type, early-type galaxies on its own (green and red symbols) and the total LF. The red line corresponds to a Schechter-function and the blue line to a linear fit in the interval $-14.4 \leq M_r \leq 19.0$ mag.

Figure 3.24 shows the same LF, but subdivided into the contribution of the different morphological types, using a bin size of 0.25 mag. In both panels of Fig. 3.24 the distribution of the ETGs and dE(bc)s is shown with a different y-scale compared to the other panels. The ETGs show a gradually increase of the LF with a turnover at

Table 3.2: Parameters of the LF for different filters.

Filter	α	$\Delta\alpha$	M^*	ΔM^*
u	-1.371	0.091	-20.049	0.519
g	-1.337	0.037	-21.593	0.299
r	-1.297	0.037	-22.023	0.324
i	-1.276	0.028	-22.367	0.265
z	-1.295	0.027	-22.863	0.374

$M_r \approx -14$ mag.

The Sd and Sm galaxies have a relative similar distribution, even though the Sm galaxies are less abundant. Among the spirals, the Sc galaxies have the broadest distribution from almost $M_r = -23$ mag down to $M_r = -15$ mag. The bulk of the Sc galaxies can be found around a magnitude of $M_r = -19$ mag. As already mentioned in Section 3.3.2, Sa galaxies show a large range in magnitude, what is also visible in Fig. 3.24 with a similar range like the Sc galaxies. Inspecting the star forming dwarfs in this figure, one realises that the BCDs have a narrower distribution than the dIs. There are dIs with slightly higher magnitudes than the BCDs, but there are also dIs with lower magnitudes. The LFs of the loosely classified "S" galaxies, together with the unknown and Amorphous galaxies, suffer from the poor number of galaxies within these morphological classes. Therefore, any interpretation has to be handled with care. Also obvious in Fig. 3.24 is the overlap between regions of generally classified dwarfs and spiral galaxies. For instance, the spiral types of Sd and Sm share a large overlap region with the BCDs and dIs, which makes a simple magnitude division in dwarf and non-dwarfs questionable.

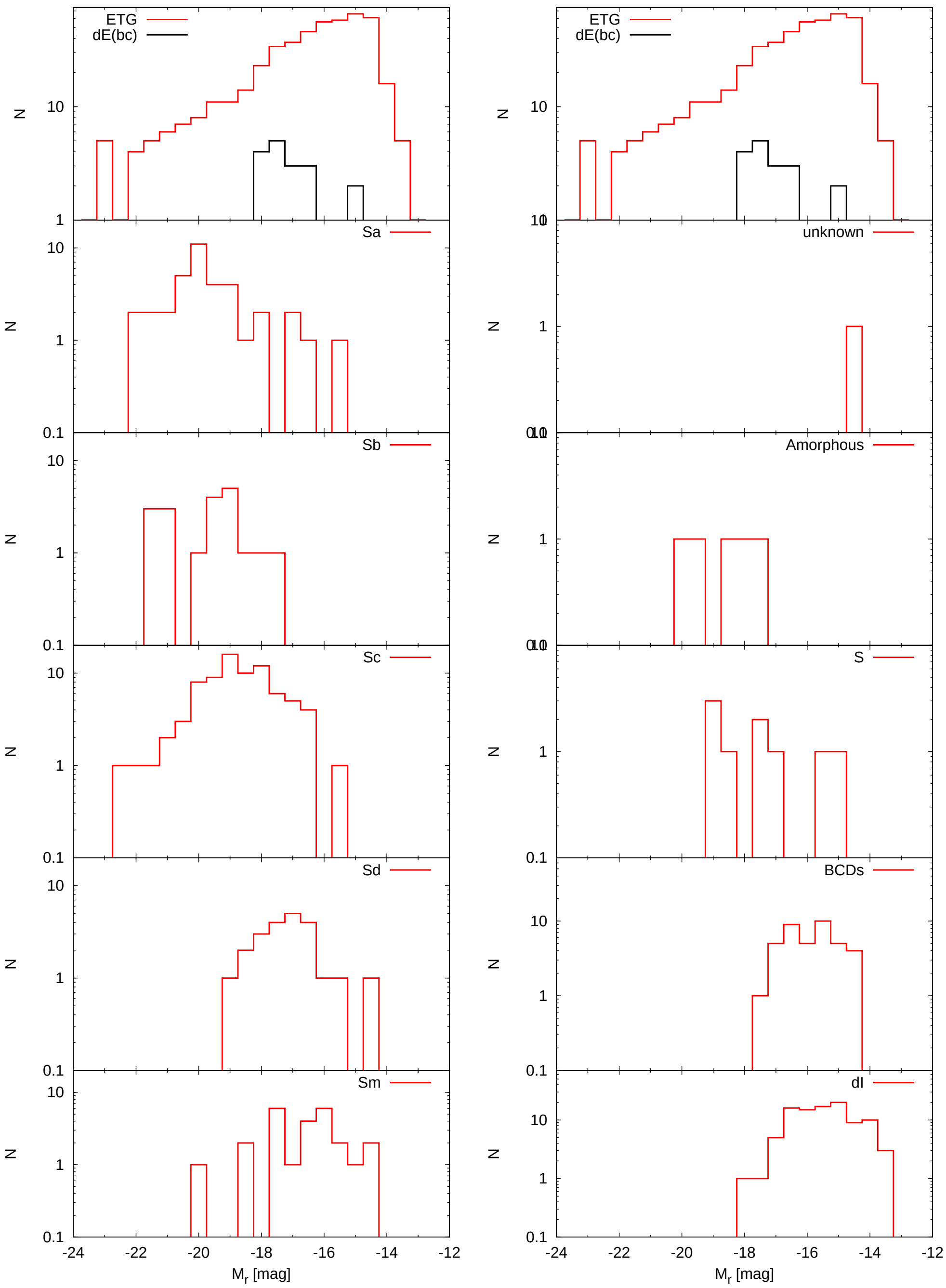

Figure 3.24: Luminosity functions of the different morphological types. Note: the plots of the ETGs and dE(bc)s have different y-scales than the other plots.

3.4 Discussion

3.4.1 Comparison of the different types

The following Figs. 3.25 and 3.26 show the averages and the 1σ deviation of the derived parameters of the different morphological types. The derived parameters of our galaxies are given for every morphological type of the original VCC (red bars) and of the revision by T. Lisker (red bars). Additionally to the late-type galaxies, the averages of the complete ETG population are given as well. Furthermore, the sample of ETGs is subdivided into the contribution of the dEs ($M_r < -18$ mag) and the dE(bc)s .

The difference between the VCC and the revision are minor for the magnitude M_r, (g – i)-colours and $\langle\mu\rangle_{eff,r}$. However, the differences for R_{eff} and the axis ratio (b/a) are more prominent, especially for the Sb and Sd galaxies.

In the next step, the morphological types are compared with each other. The parameters of the Sa and Sb galaxies do not show a large deviation from each other, while they differ from the other spirals of the type Sc, Sd and Sm. The Sd and Sm galaxies also show similarities in M_r and (g – i). However, the Sd galaxies have on average a larger R_{eff} and a lower $\langle\mu\rangle_{eff,r}$ compared to the Sm galaxies.

The unknown galaxies of the original VCC show a similar behaviour like the dIs, which again supports the reclassification of most of them to the morphological class of the dIs by T. Lisker. Owing to the fact that the revision only contains one unknown galaxy, no error bars are given in the diagrams.

Since the main aim of this study is to find the possible progenitors of the early-type dwarf galaxies, it is worth to compare the derived parameters of today's late-type galaxies with the ones of the dEs. To obtain a more sophisticated insight into the possible connections, we will also study the photometric evolution of the late-type population by means of evolutionary synthesis models in Chapter 4.

One of the main findings of Chapter 2 was that the LSB-components of the BCDs and the compact dEs cover almost the same region in the $M_r - R_{eff} - \langle\mu\rangle_{eff,r}$-plane, what can also be seen in Figs. 3.25 and 3.26. It is also obvious that the LSB-components are on average bluer and more compact than the dEs. However, the effective radius in units of kpc of the LSB-components is also influenced by the different distance approaches, what will be discussed in more detail in Section 3.4.2.

Comparing the results of the other morphological types with the ETGs, one can see obvious differences, but also some similarities. However, when comparing the averages one should also keep in mind the 1σ deviation of the results.

As expected, the averaged parameters of the Sa and Sb galaxies significantly differ from the ones of the dEs. On average the magnitude M_r and mean surface brightness $\langle\mu\rangle_{\mathrm{eff,r}}$ of the Sa and Sb galaxies are too high and the effective radius R_{eff} is too large compared to the ETGs. Looking at Fig. 3.9, it is visible that most of the spiral galaxies at a given (g-i)-colour are brighter than the ETGs. Furthermore, due to the active star formation of the spiral galaxies, expectedly they have bluer colours than the ETGs. In Figs. 3.12 and 3.19 the spirals within a 2σ deviation cover the same region as the ETGs. Galaxies with $M_r < -20$ mag are slightly fainter with increasing radius compared to the ETGs in Fig. 3.18.

As already seen in Fig. 3.24, there is no clear separation between the dwarf galaxies and spirals. This motivates to ask what really defines a dwarf galaxy? The definition by a certain magnitude holds overlaps with spirals as well as in surface brightness and effective radius.

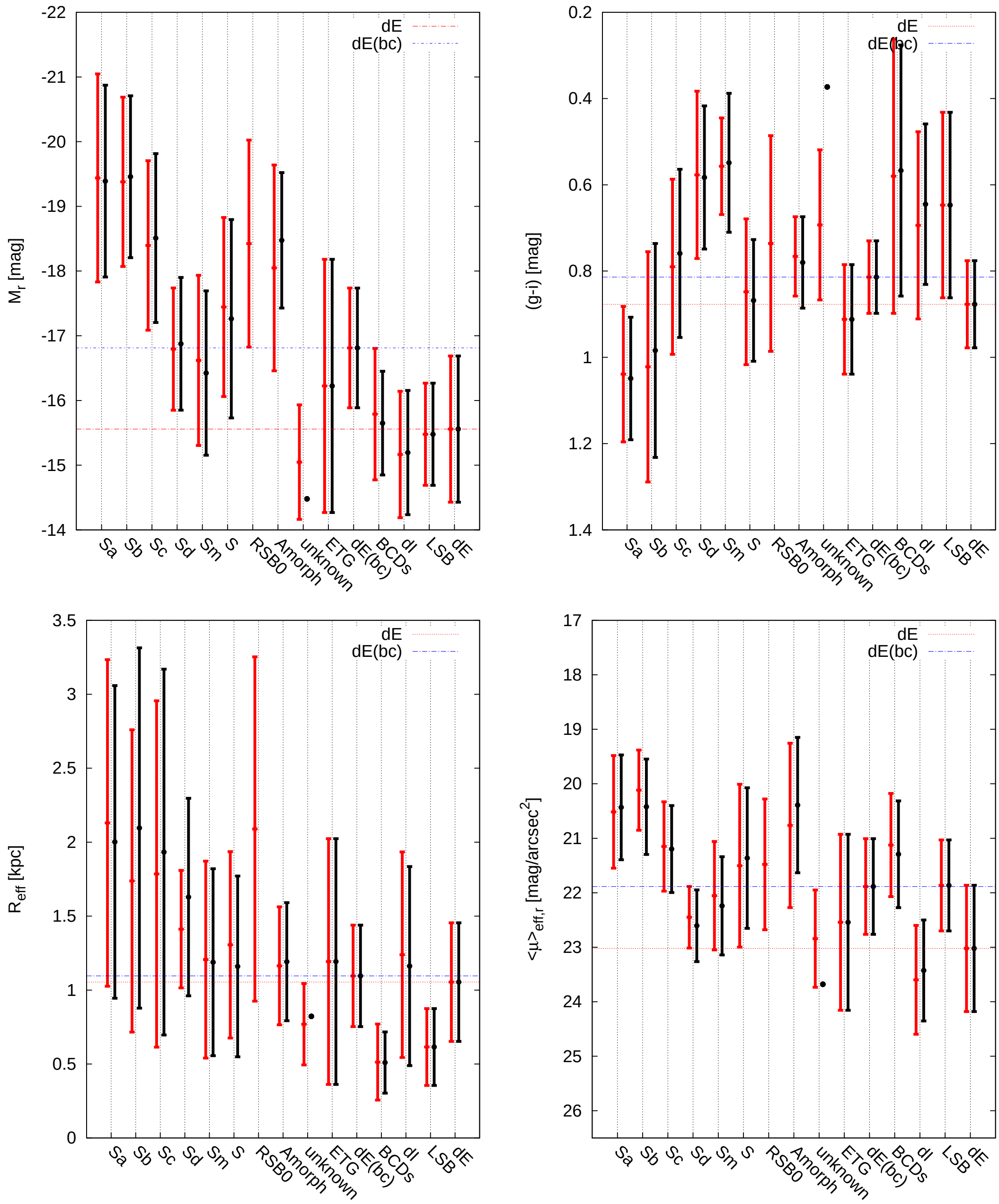

Figure 3.25: Distribution of the averaged results of the late-type galaxies in the Virgo cluster. The red bars correspond to the morphological types derived by the initial VCC, while the black bars show the results for the morphological types classified by T. Lisker. Additionally shown are the results of the early-type galaxies. The horizontal red and blue lines indicate the averages of the dEs and dE(bc)s, respectively.

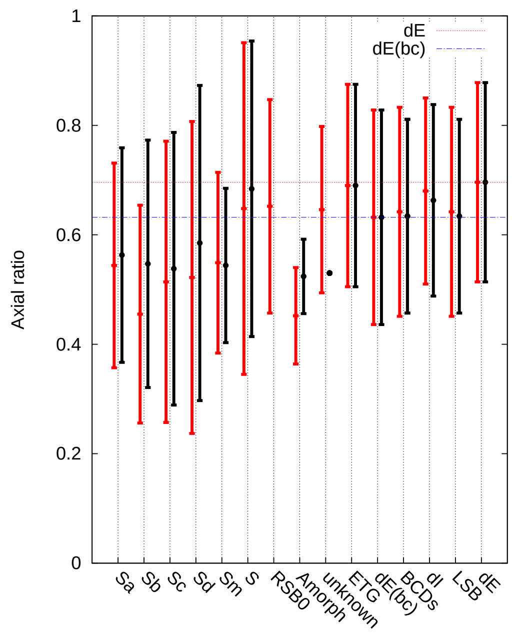

Figure 3.26: Same as Fig. 3.25, but for the axis ratio b/a.

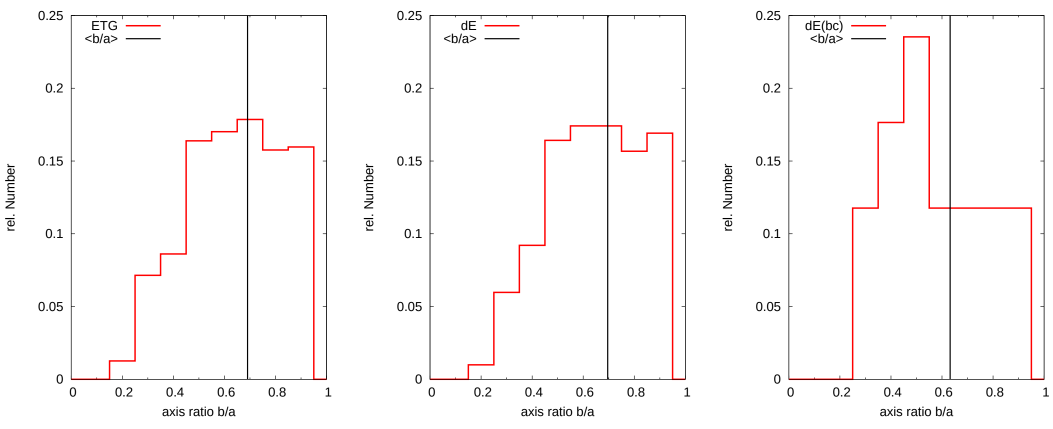

Figure 3.27: Normalised distribution of the axis ratio for the ETGs, dEs and dE(bc)s of the sample of Janz and Lisker (2008); Janz and Lisker (2009) with corresponding averages of $\langle(b/a)\rangle_{\mathrm{ETG}} = 0.69 \pm 0.19$, $\langle(b/a)\rangle_{\mathrm{dE}} = 0.70 \pm 0.18$ and $\langle(b/a)\rangle_{\mathrm{dE(bc)}} = 0.63 \pm 0.2$.

3.4.2 Application of the GOLDMine distance

For all the above showed plots a constant distance of 16.5 Mpc was applied. Since the GOLDMine data base also provides the distances according to the different clouds of the Virgo cluster (see Figs. 3.6 and 3.7), it is worth to compare our results with the different distance estimates. It has to be pointed out that these cloud distances based on Tully-Fisher distance measurements (Tully and Fisher, 1977) of a small sample of spiral galaxies (Gavazzi et al., 1999), therefore, the estimated distance of each galaxy within a cloud based on a small number statistic. Furthermore, galaxies of a certain right-ascension and declination may be associated with e.g. the B-cluster with a distance of 23 Mpc, but in reality the galaxy is located in the periphery of the A-cluster with a distance of 17 Mpc. Therefore, also the different distances of the galaxies in the cloud should be handle with care.

It was realised through the analysis that some galaxies have distances which are well behind the Virgo cluster. To minimise the distortion of the averaged values due to background galaxies, galaxies with a distance of $D > 32$ Mpc are excluded from the calculation of the averages. Figures 3.28 to 3.31 show the same diagrams as Figs. 3.9, 3.18, 3.12 and 3.19, but now with the corresponding GOLDMine distances[10]. A summary of the shifts due of the distance depended parameters can be found in Fig. 3.32, which shows the averaged values of R_{eff} and M_r derived with the GOLDMine distances. Since only the effective radius in kpc and the apparent magnitude are a function of the distance, the other parameters do not change and the averaged values can be taken from Figs. 3.25 and 3.26. The red bars in the histograms correspond to the morphological type, which have been reclassified by T. Lisker. The black bars show the same morphological types, but with the application of the GOLDMine distances. The green bars display the averages of the morphological types, which are reclassified by this study and additionally the GOLDMine distance was used (see next Section 3.4.3). All spiral galaxies and the dIs become brighter and larger in R_{eff}, if one uses the GOLDMine distances. The difference between the magnitudes is about $\Delta M_r \approx 0.5$ mag and $\Delta R_{eff} \approx 0.4$ kpc for the effective radii. This magnitude difference gets smaller within the spiral types from Sa to Sm. In case of the Sm galaxies, the difference is only $\Delta M_r \approx 0.15$ mag.

[10]The GOLDMine distances were only applied to the late-type galaxies and not to the early-types.

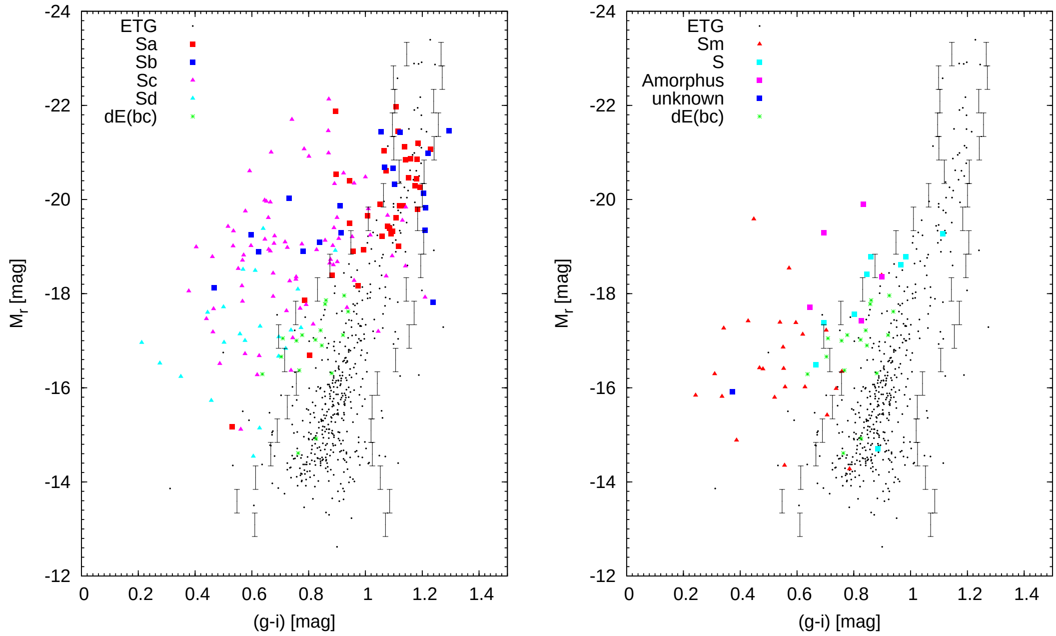

Figure 3.28: Colour-magnitude diagrams of late- and early-type galaxies in the Virgo cluster. Black dots show the ETG sample of Janz and Lisker (2008); Janz and Lisker (2009), where the vertical bars correspond to the 2σ deviation within a magnitude bin of 0.5 mag. For clearness the CMD is dived into two parts. Left panel: CMD with spirals (Sa-Sd); Right panel: same CMD for Sm, SB, Amorphous, S and unknown galaxies. To calculate the distance of the galaxies values from the GOLDmine data base are used.

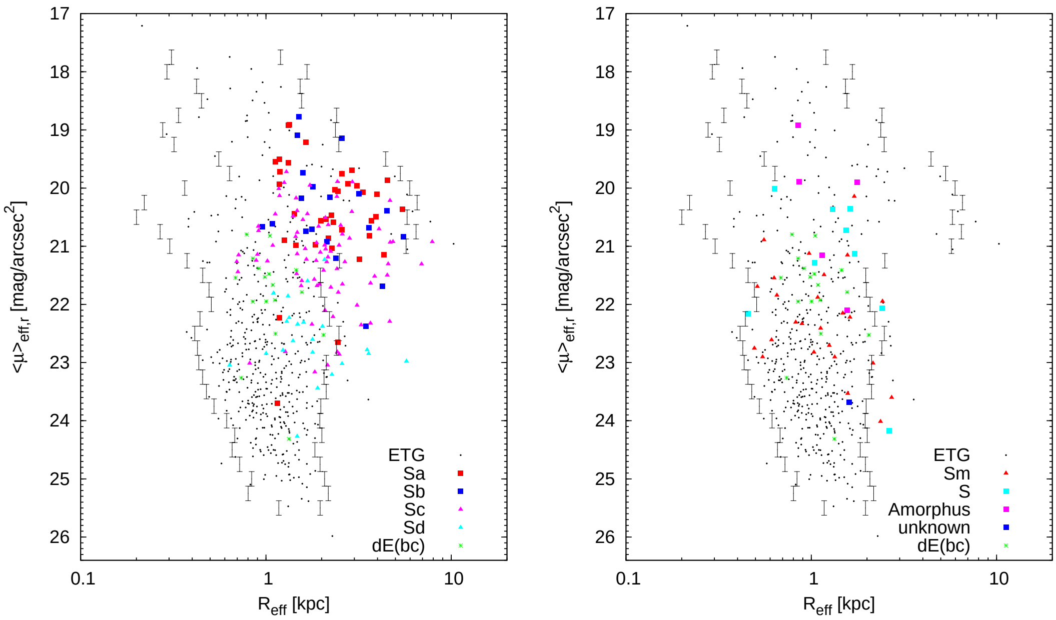

Figure 3.29: Same as Fig. 3.28, but for the effective radius $R_{\rm eff}$ vs. the mean effective surface brightness $\langle\mu\rangle_{\rm eff,r}$ in r-band.

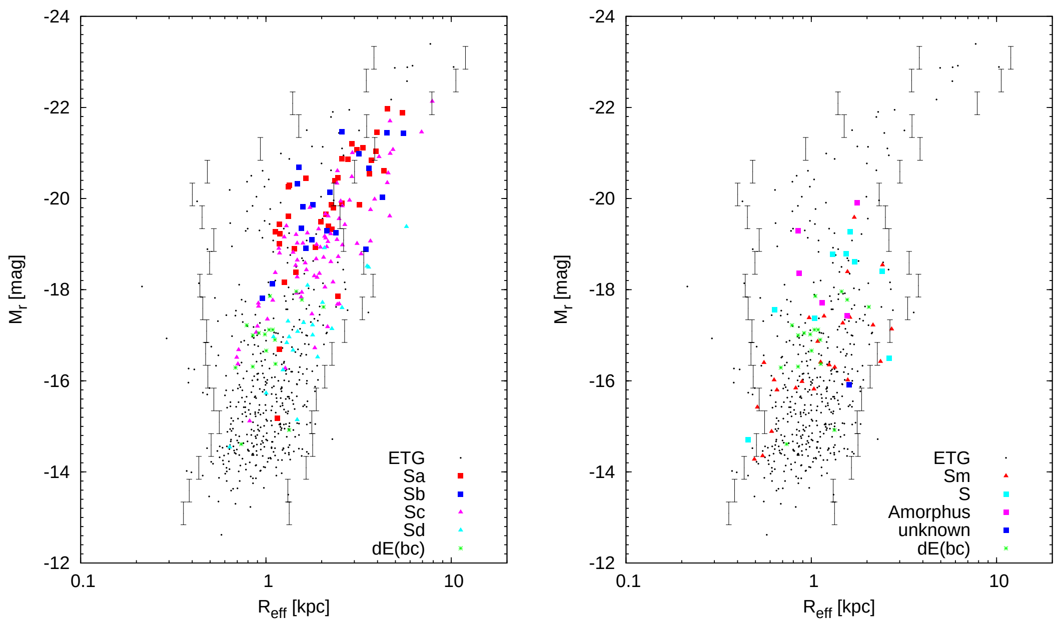

Figure 3.30: Same as Fig. 3.28, but for the effective radius $R_{\rm eff}$ vs. absolute magnitude M_r in r-band.

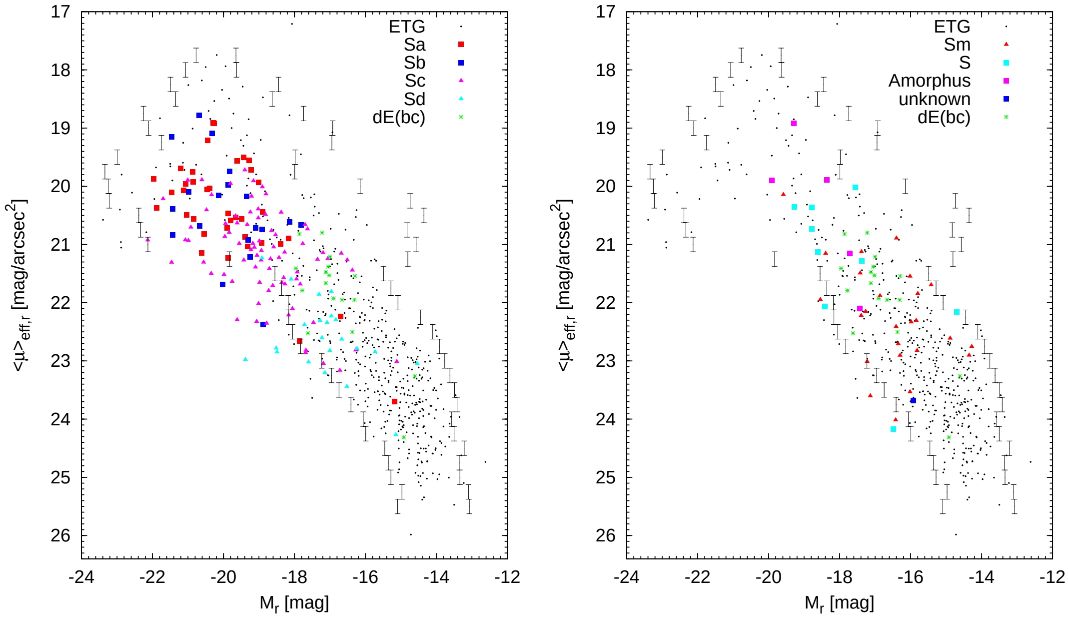

Figure 3.31: Same as Fig. 3.28, but for the absolute magnitude M_r vs.mean effective surface brightness $\langle\mu\rangle_{\rm eff,r}$ in r-band.

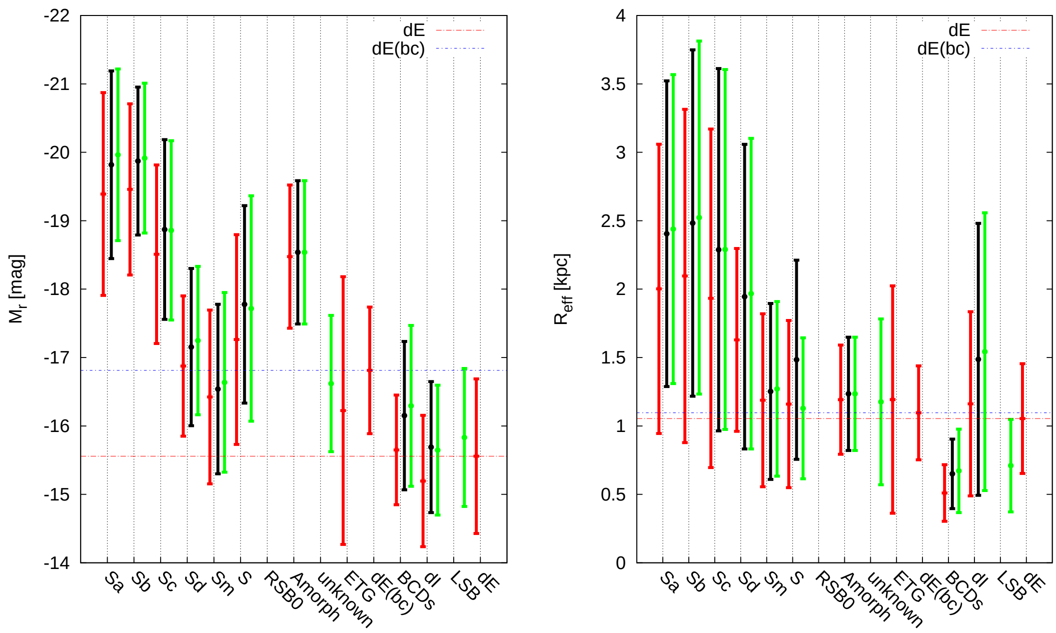

Figure 3.32: Histograms of late-types with the GOLDMine distance. The red and black bars correspond to the initial classification by T. Lisker and the values if one uses the GOLDMine distances, respectively. The green bar shows the averages using the new classification of Section 3.4.3 and additionally the GOLDMine distance instead of a constant distance of D=16.52 Mpc.

3.4.3 Reclassification

Using the informations of all derived parameters, we are able to check the initial classification of the VCC and the revision by T. Lisker. The reclassified galaxies with the old types from the VCC and the corresponding new types will be summarised in Tab. 3.3. Galaxies classified as a mixed type of BCDs like "Im/BCD" were already discussed in Chapter 2.4.8, but are also listed.

In the class of Sa galaxies, there are three galaxies which are offset from the rest of this type, having a lower surface brightness, fainter magnitude and bluer (g-i)-colour. VCC-1933 has the lowest surface brightness, bluest (g-i)-colour and faintest magnitude, what would point to a misclassification in the VCC. Indeed, the GOLDMine data base classifies VCC-1933 as a Sm galaxy. However, with our findings in the parameter-space it is also possible to classify VCC-1933 as a dwarf irregular (dI) galaxy. The gri-image from SDSS in the right panel of Fig. 3.33 shows a galaxy with a possible spiral structure, but it could also interpreted as features of interaction. Therefore, the class of GOLDMine is used, but with a strong uncertainty.

The two other galaxies (VCC-0015 and VCC-1358) have properties of the morphological types of the Sc's and Sd's, therefore, they should be classified as Scd (with more weight to Sd). Moreover, the gri-image of VCC-0015 (left panel of Fig. 3.33) does not show a prominent bulge, what would be typical for Sa galaxies, reinforcing a misclassification. However, when applying the distances of the GOLDMine data base the magnitude of VCC-0015 would be shifted to the regime of the other Sa galaxies. Interestingly, the SDSS image of VCC-1358 (middle panel of Fig. 3.33) shows a galaxy without any spiral structure, but with a blue core in the centre of the galaxy. The optical image has similarities to dE(bc)s and indeed does the location of VCC-1358 fit to the one of the dE(bc)s in the entire parameter-space. Even with the distance of GOLDMine, there is no shift in the parameter-space, since it is stated with 17 Mpc. Therefore, VCC-1358 is reclassified as a dE(bc). The VCC classifies VCC-0989 as a "Sc or Im" and the GOLDMine data base as "Sc (dSc)". Using our recent results, we would classify VCC-0898 as a dI galaxy, since $\langle\mu\rangle_{\mathrm{eff,r}}$ at a given $R_{\mathrm{eff,r}}$ is quite low compared to the other Sc galaxies. Without deep observation, the GOLDMine class of a dSc could not be ruled out, but the optical image in the left panel of Fig. 3.34 does not give any hint of a spiral structure, which would confirm the irregular class "dI". Three galaxies are conspicuous in the Sd class (VCC-0132, VCC-1605 and VCC-1685). All three galaxies are classified in the VCC and GOLDMine as Sd and SBd, respectively. Comparing the results of the galaxies with other types, VCC-0132 and VCC-1605

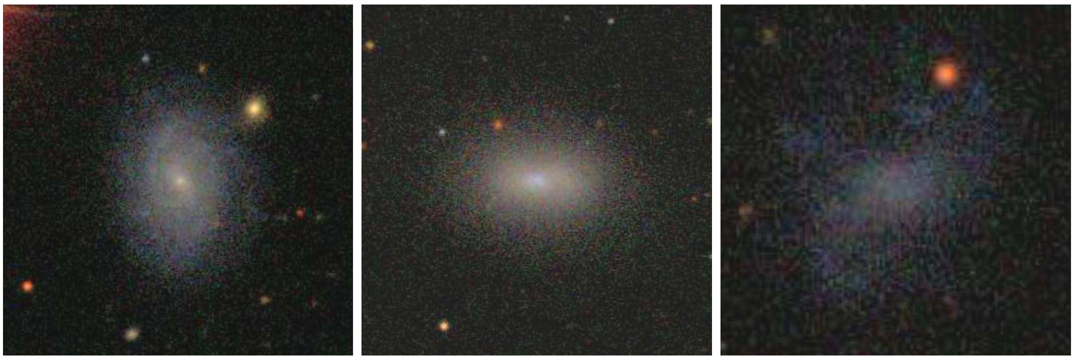

Figure 3.33: Galaxies initially classified as Sa, but not belonging to the parameter-space of Sa galaxies (from left to right: VCC-0015, VCC-1358 and VCC-1933).

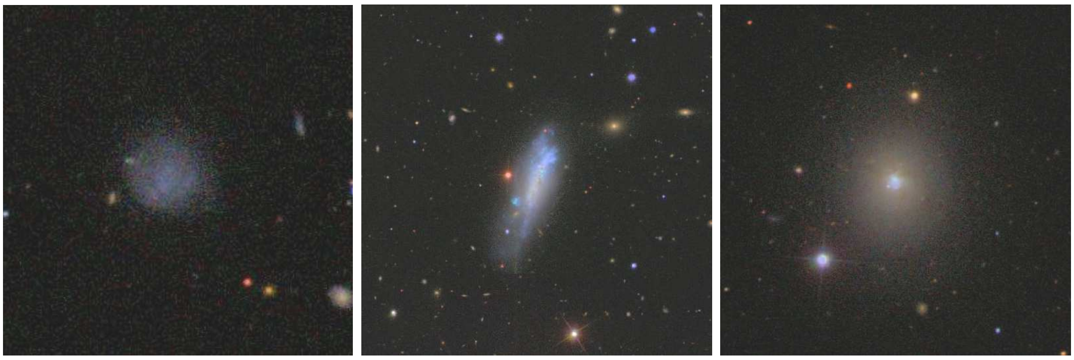

Figure 3.34: Left: Galaxy VCC-0989 was initially classified as Sc (dSc), which could be reclassified as a dI; Middle: The very puzzling galaxy VCC-1664, which could not be associate to any late-type class; Right: VCC-1955, possibly a dE(bc).

share the same parameter-space like dI galaxies. VCC-1685 also has properties in common with the dIs, but also with the Sm galaxies. The optical image of VCC-0132 (left in Fig. 3.35) shows a faint galaxy with no obvious spiral structure, except for a faint loop in the south, supporting the galaxy class of "dI:", with a minor uncertainty. Furthermore, in the colour-colour-diagram in Fig. 3.20, the (i-z)-colours of VCC-0132 are only reached by far by the dIs.

The images of VCC-1605 (middle) and VCC-1685 (right panel of Fig. 3.35) reveal inclined galaxies. Therefore, the classification of the Sd type cannot be ruled out. There are several galaxies classified as "S" or "S (dS)" in the sample. VCC-0213 and VCC-1955 were already discussed in Chapter 2, concluding that VCC-0213 could be a BCD with a spiral structure regarding its parameter-space, but nevertheless there are uncertainties regarding the classification.

Figure 3.35: Galaxies initially classified as Sd, but not belonging to the parameter-space of Sd galaxies (from left to right: VCC-0132, VCC-1605 and VCC-1685).

VCC-1574 is classified as a “S” in the VCC and as “?” (unknown) in GOLDMine. Cross-checking the redshift with SDSS reveals z = 0.0756, bringing it well behind the Virgo cluster. However, in the GOLDMine data base a velocity of v_{hel} = 639 km/s is given. This value based on HI measurements from Gavazzi et al. (2006) (their Table 3). The optical image shows a galaxy with obvious spiral structure, but with the applied distance it is rather small for a typical spiral galaxy. Therefore, we are not able to give any new information regarding the classification, but VCC-1574 is marked with a “:”, indicating the uncertainties in the classification.

As VCC-1358, also VCC-1955 covers almost the same parameter-space as the dE(bc)s and it was also included in the additional sample of Lisker et al. (2006a). The SDSS image of VCC-1955 is shown in the right panel of Fig. 3.34. The centre of the galaxy has blue colours and the surrounding disc does not show any feature of spiral structure. Therefore, VCC-1955 was reclassified to a dE(bc).

The parameter-space of VCC-0320, which is classified as a “S(dS)” in GOLDMine, shows all structural properties of the dI sample at a distance of D=16.5 Mpc. Regarding the GOLDMine data base, VCC-0320 has a distance of D=32 Mpc, making an allocation to the dIs still possible, but also shifting it into the region of the late spirals in the $M_r - R_{eff}$-plane. Despite to the other late spirals, VCC-0320 has a remarkable low $\langle\mu\rangle_{eff,r}$, which would confirm the classification as a dI.

Another galaxy classified as “S (dS)” is VCC-1086. In the optical image (left panel of Fig. 3.36), one can see that it is strongly inclined and with the informations from the structural parameters we are able to conclude that VCC-1086 is not a dwarf spiral, since it has a too bright magnitude and a too high surface brightness compared to the other star forming dwarfs of the sample. However, due to the inclination it is not

possible to determine the exact type.
Within the class of the Sm galaxies, there is one galaxy that is offset from the other Sm galaxies. This offset for VCC-1554 is visible in the entire parameter-space. The visual inspection of the gri-image in the right panel of Fig. 3.34, reveals a galaxy with extended star forming regions, a bar-like structure and an irregular morphology. Nevertheless, it has a very high surface brightness and a magnitude assimilable to early spirals. Thus, in the parameter-space VCC-1554 is not a Sm galaxy, but it is also not an early spiral regarding its optical morphology. Due to the above mentioned problems a reclassification is not easily possible and we just mark the galaxy with a “pec” to indicate the peculiarity of this galaxy. In the morphological class of the

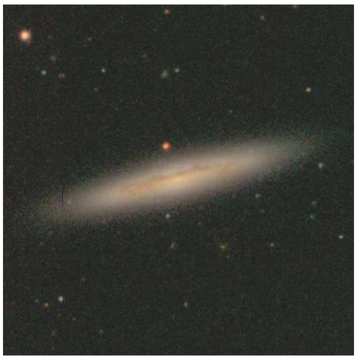

Figure 3.36: The “S (dS)” galaxy VCC-1086.

“unknown”, eight galaxies are in the region of the dIs, thus they were reclassified as ”dI” by T. Lisker. There is one galaxy among these eight “unknowns”, which optical image (middle panel of Fig. 3.37) shows a galaxy with an obvious starburst region. The comparison with the BCDs reveals that the *total* parameters of VCC-0237 do only fit to the parameters of the LSB-components, therefore, an allocation to the BCDs would not be sensible and the class of “Im/BCD:” was used.
In the parameter-space, VCC-0031 has in common all properties with the BCDs. However, the optical image shows a red core in the centre of the galaxy. To check the parameters of VCC-0031, it was analysed as a BCD. A fit to the outer exponential component of the surface brightness profile would require an inner flatting of the surface brightness profile and the (g-i)-colour profile also does not have the typical slope as the other BCDs. Therefore, VCC-0031 is still classified as “unknown”.
There is one formally classified unknown, which shares the same properties as the BCDs (right panel of Fig. 3.37). Therefore, VCC-1411 is reclassified as a BCD and was analysed and included in the BCD sample of Chapter 2.

Four other unknown galaxies are classified as transition types between dI and BCDs, indicated by “dI/BCD” and were already discussed in Chapter 2.
The only unknown galaxy left over after the revision of T. Lisker, corresponds to VCC-0113. Using the informations from the (u-g)-(i-z)-diagram, it became clear that only the dIs share the same location in Fig. 3.21. In the parameter-space it also resides in the same region as the dIs. Thus, VCC-0113 can be reclassified as a dI, however, with some uncertainties due to the visible loops in the optical image of Fig. 3.37 (left).
Figures 3.32 and 3.26 show the averaged results of each morphological class. The first

Figure 3.37: Galaxies initially classified as unknown (from left to right: VCC-0113, VCC-0237 and VCC-1411).

bar (red) indicates the average from the VCC and the second bar (black) the averaged values using the classes after the reclassification *and* application of the GOLDMine distances. As seen in the figures, the influence to the parameters is minor but visible.

Table 3.3: The reclassification of the VCC galaxies.

VCC	VCC – type	GOLDMine	New class
0015	Sa	Sa	Scd?
0020	unknown	unknown	dI
0030	unknown	unknown	dI
0085	unknown	unknown	dI
0113	unknown	unknown	dI:
0132	Sd	Sd	dI:
0135	Spec/BCD	S/BCD	Spec/BCD?
0213	Sd?/BCD?	S/BCD	S/BCD
0237	unknown	unknown	dI/BCD:

continued

VCC	VCC – type	GOLDMine	New class
0247	unknown	unknown	dI
0309	Im/BCD	Im/BCD	dI
0320	S	Sc(dS)	dI:
0379	unknown	unknown	dI
0429	unknown	unknown	dI/BCD
0446	Im/BCD	Im/BCD	Im/BCD
0488	unknown	unknown	dI
0596	Sc?	Sc(dS)	Sc
0655	Spec,N:/BCD	S/BCD	BCD: (Mrk-86 like)
0737	Sd/BCD?	S/BCD	-
0848	ImIIIpec/BCD	Im/BCD	-
0989	Sc	Sc (dS)	dI
1086	S	S (dS)	S
1179	ImIII/BCD	Im/BCD	dI/BCD
1237	unknown	unknown	dI/BCD
1358	Sa	Sa	dE(bc)
1374	ImIII/BCD	Im/BCD	BCD
1411	unknown	Pec	BCD
1427	Im/BCD:	Im/BCD	dI/BCD
1515	unknown	unknown	dI
1554	Sm	Sm	Sm(pec)
1574	S	?	S:
1605	Sd	Sd	Sd
1623	unknown	unknown	dI/BCD
1685	Sd	Sd	Sd
1713	unknown	unknown	dI/BCD
1804	ImIII/BCD	Im/BCD	dI/BCD
1933	Sa	Sm	Sm?
1955	Spec/BCD	S/BCD	dE(bc)
1960	ImIII/BCD?	Im/BCD	dI/BCD
2007	ImIII/BCD:	Im/BCD	dI/BCD
2037	ImIII/BCD	Im/BCD	dI

The reclassification of the VCC galaxies.

Table 3.4: Comparison between certain and possible: $\langle M_r \rangle$.

Type	Certain	σ	Possible	σ
BCDs	-16.29	1.25	-16.39	1.11
dI	-15.67	0.92	-15.45	1.14
Sa	-20.21	0.93	-19.43	1.70
Sb	-19.99	1.14	-19.79	1.10
Sc	-18.91	1.24	-18.74	1.46
Sd	-17.43	1.27	-16.95	0.65
Sm	-16.88	1.18	-15.99	1.52

3.4.4 Difference between certain and possible cluster members

As mention in Section 3.2.1, the membership of the Virgo galaxies is divided into certain and possible members. However, this membership was not taken into account in diagrams of the last sections. The following Tabs. 3.4 to 3.7 show the differences between the parameters of the certain and possible members. Errors are given by an 1σ deviation from the average. Morphological types without any possible member (e.g. Amorphous) are not listed.
To calculate the averages of the parameters, the morphological classes after the reclassification are used, as well as the distance informations from GOLDMine.
The BCDs show no significant deviation between the certain and possible members, except for the (g-i)-colours, which are slightly bluer for the certain members.
The spiral galaxies from Sa to Sm show no major differences between certain and possible members. If there are any differences in the parameters, then they are within the 1σ deviation of the averages.
These minor differences of the certain and possible members in Tabs. 3.4 to 3.7 retroactively justify the treatment as one group without any differentiation in the diagrams.

3.4.5 Comparison with semi analytical models

Semi analytical models (SAMs) are used to simulate the evolution of galaxies, using analytical recipes to dark matter merger trees. The results of our analysis of the late-type galaxies was included in a study of Weinmann et al. (2011) using SAMs from the study of Guo et al. (2011). The SAMs of Guo et al. (2011) based on the models of De Lucia and Blaizot (2007) with some modifications to account for the

Table 3.5: Comparison between certain and possible: $\langle R_{eff} \rangle$ [kpc].

Type	Certain	σ	Possible	σ
BCDs	0.64	0.30	0.73	0.31
dI	1.48	0.72	1.68	1.55
Sa	2.57	1.22	2.15	0.88
Sb	2.80	1.33	2.09	1.18
Sc	2.38	1.40	2.09	1.12
Sd	2.24	1.37	1.53	0.34
Sm	1.41	0.65	0.89	0.43

Table 3.6: Comparison between certain and possible: $\langle(g-i)\rangle$.

Type	Certain	σ	Possible	σ
BCDs	0.47	0.32	0.60	0.16
dI	0.63	0.17	0.66	0.22
Sa	1.06	0.10	1.07	0.19
Sb	0.95	0.28	1.05	0.21
Sc	0.75	0.20	0.78	0.18
Sd	0.58	0.19	0.59	0.15
Sm	0.56	0.14	0.56	0.24

Table 3.7: Comparison between certain and possible: $\langle\langle\mu\rangle\rangle$.

Type	Certain	σ	Possible	σ
BCDs	21.08	1.04	21.35	0.87
dI	23.52	0.89	23.67	0.86
Sa	20.18	0.66	20.62	1.14
Sb	20.59	0.81	20.11	1.01
Sc	21.25	0.77	21.14	0.90
Sd	22.55	0.67	22.49	0.34
Sm	22.19	1.01	22.16	0.77

Table 3.8: Comparison between certain and possible: $\langle b/a \rangle$.

Type	Certain	σ	Possible	σ
BCDs	0.64	0.20	0.61	0.18
dI	0.66	0.17	0.72	0.19
Sa	0.56	0.19	0.54	0.23
Sb	0.56	0.27	0.50	0.15
Sc	0.52	0.25	0.58	0.24
Sd	0.54	0.29	0.61	0.29
Sm	0.54	0.14	0.58	0.16

increased influence of the effects like SNe- and AGN-feedback or environmental effects due to the shallow gravitational potential of the dwarf galaxies. In addition, the SAMs of Guo et al. (2011) use the high resolution Millennium-II simulation (Boylan-Kolchin et al., 2009), which enables the investigation of dwarf galaxies down to a stellar mass of $\sim 10^{7.5} M_{\odot}$. Furthermore, the disc sizes of the SAMs galaxies are calibrated to fit the observation of 140000 galaxies from the SDSS by Shen et al. (2003), what makes a comparison with our sample possible.
In Fig. 3.38 the black dots corresponds to the results of the SAMs and the coloured points to the results of this study and additionally the results of Janz and Lisker (2008); Janz and Lisker (2009). The overlap of our sample with the SAM predictions fit quite well.

3.4.6 Comparison with the literature

A compilation of data from the literature is given by the study of Graham and Worley (2008) (hereafter G08). The medians of the structural parameters of G08 were given for the different morphological types of spirals including irregular galaxies (Irr in G08). In this study the scale length h of the different types of spirals are given and can be transformed (Mo et al., 2010) into R_{eff} via:

$$R_{eff} = 1.67 \cdot h. \tag{3.15}$$

The scale lengths of G08 are given in the B and I band, therefore the effective radii in g and i of our sample are used for comparison. In Tab. 3.9 the results of R_{eff} are summarised. Interestingly, there is a huge difference between our results and the ones of G08, which accounts for more than a factor of two. It has to be pointed out that

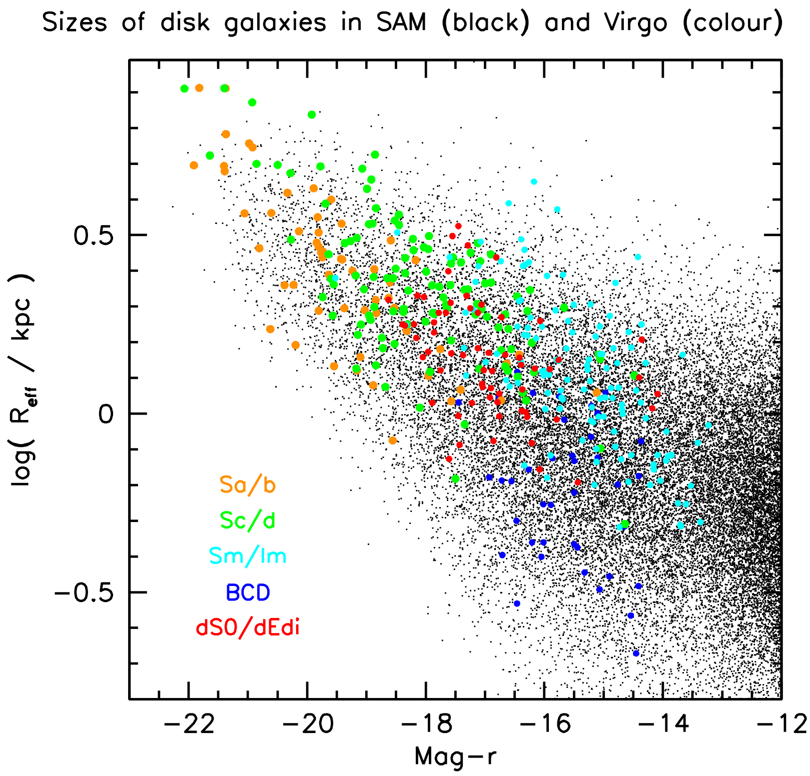

Figure 3.38: Comparison of our results of the late-type galaxies within the Virgo cluster with the SAMs of Guo et al. (2011) (Courtesy: T. Lisker).

Equation 3.15 is valid for pure disc galaxies, therefore, in presence of a dominant bulge like in Sa galaxies, the effective radii are slightly underestimated. However, also in systems with a low bulge-to-disc ratio (e.g. Sc or Sd), the differences between our results and the ones of G08 are impressive. This finding is quite puzzling, since our results fit well to the predictions of the SAMs of Section 3.4.5 and therefore also with the calibration sample from the SDSS of Shen et al. (2003).

Table 3.9: Comparison of R_{eff} between Graham and Worley (2008) and our study.

Type	$R_{eff,B}$ [kpc] (Graham)	$R_{eff,g}$ [kpc] (our study)	$R_{eff,I}$ [kpc] (Graham)	$R_{eff,i}$ [kpc] (our study)
Sa	5.01	2.53	5.73	2.43
Sb	6.15	2.66	6.43	2.49
Sc	5.63	2.26	5.68	2.21
Sd	5.54	1.99	6.11	1.99
Sm	6.21	1.25	7.06	1.32
Irr	3.44	2.22	3.32	2.31

3.5 Summary and outlook

In this chapter we analysed the structural properties of the late-type galaxies within the Virgo cluster. Within the parameter-space the results of the photometry were compared within the different morphological classes and outliers were investigated in more detail and were cross-checked with the GOLDMine data base. If possible, these outliers were reclassified and an updated version of the VCC was created. The results of the reclassification are particular interesting for future investigations, since new found dE(bc)s can be the target for further projects to study their possible connection to other dwarf galaxies, like BCDs.

We also found that there is no clear distinction between dwarf galaxies (dEs, dIs, BCDs) and low-luminosity spiral galaxies. This is particular true for the late spirals of the morphological type Sc to Sm.

After the inspection of the structural parameters of the late-type galaxies within the Virgo cluster, the question arises how these parameters will evolve with time and how the descendants of today's late-type galaxies will look like. To answer these questions, we use the evolutionary synthesis models GALEV (Kotulla et al., 2009). Therefore, the results of this section are the foundation of the next section, which analyses the evolution with time of the late-types and investigates their possible connections to the early-type Virgo population.

Chapter 4 The evolution of late-type galaxies

In the prior sections the structural parameters of the late-type galaxies of the Virgo cluster were derived. In this section the evolution of these galaxies is investigated and finally compared to the early-type galaxy population. For this purpose the evolutionary synthesis models of GALEV are used, which are also able to account for the influence of the dense cluster environment.
The results of this section will shed light on the possible evolutionary connections between late-type and early-type galaxies.

This study will be timely published together with Thorsten Lisker and Ralf Kotulla.

4.1 Introduction: Transformation scenarios for turning late-type into early-types

Several studies on the Virgo cluster revealed a number of substructure (e.g. Binggeli et al., 1985, 1993) and a large variety in morphology, with a dependence of the fraction of blue-to-red galaxies on the distance to the cluster centre, which is expressed by the morphology-density relation (Dressler, 1980). This substructure, as well as the variety in morphology, could also be confirmed by the results of the previous Chapter 3. As expected, our results have shown that late-type galaxies differ from early-type galaxies, but they have similarities too. Especially in the case of the LSB-components of BCDs, there are striking similarities in the structural and photometric properties, making an evolutionary connection between these two morphological types possible. Naturally the question arises, how the other late-types (e.g. spiral galaxies) will evolve with time and how they will look like in several billion years? Thus the question is, whether the descendants of today's late-type galaxies have similar properties as the early-type galaxies, which are observed in the Virgo cluster today?
When studying the evolution of galaxies it is crucial to take into account effects that

influence the behaviour of galaxies. Since the galaxies of our study are located in the Virgo cluster, environmental effects like ram pressure stripping (RPS), starvation and harassment play an important role in the evolution of late-type galaxies.
When moving through the cluster, the inter stellar medium (ISM) of the galaxies interacts with the hot intra cluster medium (ICM). This interaction removes parts or the entire gas of the galaxies, which consequently will influence the star formation (SF) of these galaxies. In case of RPS (Gunn and Gott, 1972) the entire gas reservoir is removed from the galaxies on a very short time scale of a few 100 Myr (Roediger, 2009, and references therein). As a consequence the star formation rate (SFR) will decrease very rapidly on a comparable time scale. As an example, Boselli et al. (2008) *assumed* a time scale for the decrease of the SFR of $\sim$ 150 Myr. Simulations of RPS have been applied to disc galaxies (Abadi et al., 1999) as well as dwarfs (Mayer et al., 2006).
In the starvation scenario only the surrounding gas envelope of a galaxy is removed, but not the gas in the disc. Hence, the SF will not stop until the remaining gas is exhausted (Larson et al., 1980).
The above described processes of RPS and starvation act on the gas reservoirs of the galaxies due to the dense cluster environment. But also the interaction among the galaxies themselves has an influence on the evolution of galaxies. Due to high-speed encounters between galaxies within the cluster, the gas *and* the stellar population are disturbed. In the case of disc galaxies, the stellar disc may become thickened by the interaction with other galaxies. The scenario is called galaxy harassment (Farouki and Shapiro, 1981; Moore et al., 1996; Mastropietro et al., 2005) and was also applied to simulations of low mass dwarfs (e.g. González-García et al., 2005; Smith et al., 2010).
Apart from the external processes, there are also processes within the galaxies itself, which drive the evolution too. First of all, every galaxy will simply evolve due to the evolution of the stellar population, since the lifetime of stars is set by their initial mass and metallicity (Sparke and Gallagher, 2000). If a galaxy forms plenty of very high mass stars[1] within a short time span - a so called starburst - then these stars will end up their lives by supernovae (SNe) explosions at almost the same time. Due to the simultaneous explosions of SNe in a small region within the galaxy, a galactic wind may be formed, which is able to “blow out” gaseous material from the galaxies

[1]Of course, not only massive stars, but also low- and intermediate mass stars are formed (see *initial mass function* in Section 4.2.3).

(Dekel and Silk, 1986; Izotov et al., 1996; Heckman et al., 2001). The loss of gaseous material not only affects the chemical composition of the galaxy, but also decreases the gas reservoir, which is needed to fuel the SF.
In summary, all the above described effects remove gas from galaxies, resulting in a decrease of the SF. Over the past decades it became clear that one of the key parameter in the evolution of galaxies is the star formation and therefore the star formation history (SFH). The SFH characterises the evolution of the SFR, which in turn describes the amount of stellar mass formed within a year. The SFR is expressed in units of $M_\odot/yr$ and strongly depends on the morphological galaxy type. This can be explained by the Kennicutt-Schmidt law, which describes a power law dependence of the gas surface density and the SFR of the galaxy (Schmidt, 1959; Kennicutt, 1998).
To model the evolution of galaxies and therefore the SFH, several programs and codes were developed over the last decades. One of these codes is GALEV (GALaxy EVolution; Kotulla et al., 2009, 2010) and forms the foundation of our here presented study. GALEV models were successfully applied to the entire range of SFHs that characterise the different morphological types of galaxies (e.g. Krüger et al., 1991, 1995; Falkenberg et al., 2009) and are therefore ideally suited to our study.

4.2 Stellar population synthesis models

There are two approaches to model the spectrum of a stellar population and therefore also of a galaxy. The first approach uses a linear combination of stellar spectra to fit the observation and is called *stellar population synthesis*. The interpretation of the results is limited to the actual observation and no predications of the evolution are made.
The second approach — the *evolutionary synthesis models* — tries to fit the observation by the means of integrated spectra, colours or the spectral energy distribution (SED) of the galaxy and were first investigated by Tinsley (1968). Current examples for these evolutionary synthesis models are the codes by Leitherer et al. (1999) (Starburst99), Bruzual and Charlot (2003) (BC03), Fioc and Rocca-Volmerange (1997) (PEGASE), Maraston (2005) and GALEV, which is used in the here presented study. In contrast to the stellar population synthesis, all evolutionary synthesis models have to assume an *initial stellar mass function* (IMF) and SFH, and are able to model the evolution of the galaxy via stellar isochrones. The IMF describes the number of stars that are formed in a specific mass interval. Studies showed that stars are not equally formed per mass bin, but instead less massive stars are formed more often than massive stars. There are

different IMF laws in the literature, which differ in the slopes of the IMF and therefore in the number abundance of star in certain mass bins (see Section 4.2.3).
Thus, with the assumption (or knowledge) of e.g. the IMF and SFH of a stellar population, we are able to investigate its evolution over an arbitrary period and are able to make predications of the future of the stellar population.

4.2.1 Why GALEV?

GALEV (GALaxy EVolution) is an evolutionary synthesis code, which models the evolution of galaxies over time. It was developed by Prof. Dr. U. Fritze and her group at the University of Göttingen (Germany) and is maintained by the GALEV-team. To run GALEV models one can use a web interface at www.galev.org, which provides standard configurations, for instance star formation histories or Galactic extinction. To apply more sophisticated configurations like modified SFHs (see Section 4.2.2) one can also use a local installation of GALEV.
To calculate the time evolution of galaxies of different types, GALEV models the spectral evolution of a stellar population and the ISM at the same time. The foundation of the evolution of a stellar population in GALEV are the BaSeL libraries of model atmospheres (Lejeune et al., 1997, 1998) and the stellar evolutionary tracks or isochrones from the Padova group (Bertelli et al., 1994).
The advantage of GALEV over other evolutionary synthesis models (Starburst99, BC03 and PEGASE) is the inclusion of the chemical evolution of the gas additionally to the stellar population. The yields of the stellar population are depending on the metallicity, which is taken into account by GALEV models and is called the "chemical consistent treatment". The yields of the stellar population are taken from Woosley and Weaver (1995) and van den Hoek and Groenewegen (1997) for the different stellar mass ranges.
Also included are the contributions of the nebular emission lines and the continuum of the young stellar population, which could contribute up to 50-60 % to the total flux (Anders and Fritze-v. Alvensleben, 2003) and is therefore from particular interest for our study.
GALEV does not provide the magnitude in different filters of a galaxy. It just provides the SFHs and the spectra of galaxies of different types at a given time. To obtain the magnitudes as a function of time for a given SFH, the subroutine "COCOS" is used. With the subroutine COCOS, also input parameters like the extinction laws, attenuation and filter systems enter into the analysis.

To obtain the associated magnitudes in each filter of the model, the spectra are folded with the requested filter curve. In the concrete case of this work, the filter curves of SDSS are used, but others, like IR or UV filters, can easily be attached. With the subroutine COCOS one finally obtains the magnitudes for each time step in each filter. To emphasise again, no observational data is used at this point and only theoretically based models are used.
At the moment of writing, galaxies are treated by GALEV as one solid unit without any spatial resolution and internal dynamics.

4.2.2 Input parameters

To model the evolution of late-type galaxies one has to choose a reasonable SFH. There are several SFH laws in the literature, like the exponential declining SFR which can be used for elliptical galaxies, or the below described exponential-delayed. The exponential-delayed SFHs are parametrised by a formula given by Gavazzi et al. (2002), which was first introduced by Sandage (1986) using the study of Gallagher et al. (1984):

$$\mathrm{SFR(t)} = \frac{\mathrm{t}}{\tau^2} \cdot \exp\left(-\frac{\mathrm{t}^2}{2\tau^2}\right). \tag{4.1}$$

All of these exponential-delayed SFHs show an increase[2] of the SFR up to the point τ and then an exponential decrease with time (see Fig. 4.1). Different values of τ correspond to various SFHs of the different spectral galaxy types. For instance, an elliptical galaxy will form almost all its stellar mass within a short period of some Gyrs (e.g. $\tau \lesssim 1$ Gyr), whereas spiral galaxies continuously forming stars until now, but with different strength of SF ($\tau > 1$ Gyr). Therefore, the value τ can be used as indicator for the spectral type of the galaxy. With some limitations, these spectral types can be associated with the morphological type (MacArthur et al., 2004).
Figure 4.1 shows the SFH for different values τ for a galaxy with an initial gas mass of $\mathrm{M} = 1 \cdot 10^{10}\mathrm{M}_\odot$.

4.2.3 Starbursts and truncations

The SFH of a galaxy is not always a smooth curve as given by Equation 4.1, but could show short periods of intense SF (starbursts). GALEV models are able to account for these starbursts, which is particular important for BCDs (Krüger et al., 1991;

[2]Negative values of τ will lead to increasing SFRs.

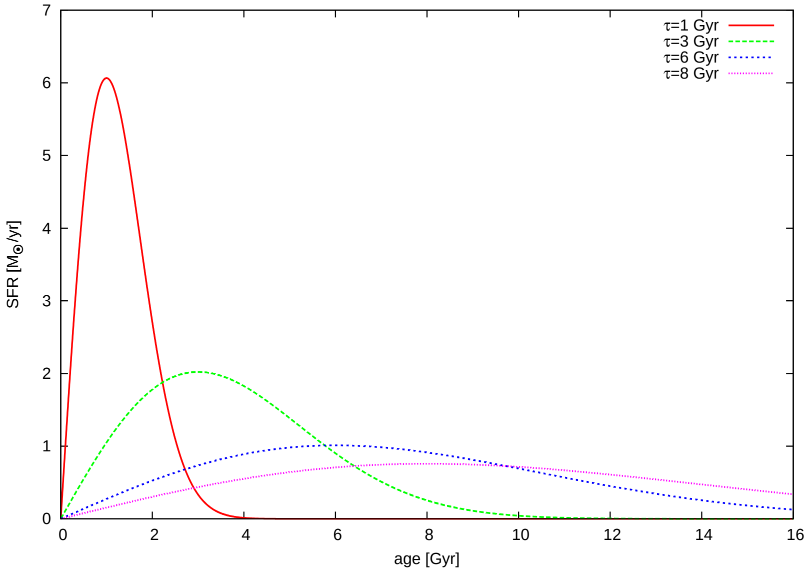

Figure 4.1: SFHs for different sets of τ.

Krüger and Fritze-v. Alvensleben, 1994). The starburst was modelled by a gaussian increase and an exponential decrease of the SFR. The strength of the burst is given by the burst parameter b, which is defined as

$$b = \frac{M_{*,\mathrm{formed}}}{M_{\mathrm{gas}}}, \tag{4.2}$$

where $M_{*,\mathrm{formed}}$ is the total mass of stars formed during the starburst and M_{gas} is the available gas mass at the beginning of the burst. For models with a bursts, the burst parameter was set to b=0.1. That means 10% of the available gas is transformed into stars. As shown by several studies, the starburst phenomenon cannot last for more than 10^7 yrs (Thuan, 1991; Thornley et al., 2000), owing to the fact that the gas reservoir in BCDs is limited. Therefore, the starburst in the models is also limited to this time scale.

Since the galaxies are located in the dense environment of the Virgo cluster, there are several mechanisms - ram pressure stripping (Gunn and Gott, 1972), harassment (Moore et al., 1996) and tidal forces (Mayer et al., 2001) - acting on the cluster galaxies and which depend on the cluster centric radii. As commonality all these mechanisms remove gas from the galaxies and therefore reduce or truncate the SFR. Regarding to the lifetime of a galaxy, the removal of gas in a cluster mostly acts on very short time scales. In the GALEV models the truncation of SFR is simulated by a stop of the SF at a given time (Bicker et al., 2002), which is illustrated as a red line in Fig. 4.2. In our models we assume that the SF stops today at t = 13.7 Gyr. The decline of the SFR due to RPS acts on very short time scales, therefore a decline time scale of 150 Myr (Boselli et al., 2008) was chosen.

At this point, GALEV provides the following initial mass functions (IMFs): Salpeter (1955) and Kroupa (2001). In the nearby future also the IMF of Chabrier (2003) will be implemented, which accounts the different components of a galaxy (disc, bulge, globular clusters). The IMF of Salpeter uses a power law with exponent $\alpha = 2.35$ for the entire mass range, while the Kroupa IMF uses a broken power-law for the different mass regimes with various slopes ($\alpha_1 = 1.3$ for $0.1 < M < 0.5\ M_\odot$ and $\alpha_2 = 2.3$ for $M > 0.5\ M_\odot$). These two IMF-laws mainly differ at the low mass slopes. For our galaxies the IMF of Salpeter (1955) was chosen.

To correct the flux for reddening and extinction of the interstellar dust, there are two extinction laws used by GALEV: Cardelli et al. (1989) and Calzetti et al. (2000). Since late-type galaxies with active star formation are in the scope of this study, the extinction law by Calzetti et al. (2000) was chosen for the models. The dust physics in GALEV is quite simple compared to other studies (e.g. Möllenhoff et al., 2006; Piovan et al., 2006a,b), which use the two dimensional structure of the galaxies. Since GALEV has no spatial resolution and the galaxies are therefore treated as one dimensional units, no assumption of the geometry of the galaxy is necessary, which in turn justifies the simple dust approach of a constant value per galaxy.

The chemical abundance of each galaxy can be fixed to a constant value or the evolution of the ISM and stellar population is modelled too. This second approach is called “the chemically consistent treatment” (Moeller et al., 1997).

After the determination of the appropriate SFH for each galaxy, all galaxies can evolve with and without any disturbance, respectively. As an illustration for the evolution of a galaxy with the different model parameters, Fig. 4.2 shows the SFH for a galaxy with $\tau = 5$ Gyr and an initial gas mass of $M = 1 \cdot 10^{10} M_\odot$ for an undisturbed (green curve), a truncated (red line) and a starbursting (blue line) evolution.

The spectral evolution of a galaxy is shown in Fig. 4.3. The figure displays the spectra of the galaxy at different time steps $t_1 = 1$ Gyr and $t_2 = 13.6$ Gyr. The red spectrum displays the galaxy after 1 Gyr and the green spectrum after 13.6 Gyr. Obviously, the flux of the galaxy decreases with time and the strong emission lines disappear too. This is intelligible, since the flux in the UV and blue regime of the spectrum is dominated by young and massive stars, which have a very short lifetime compared to the intermediate stars (Green and Jones, 2004). Therefore, after the death of the massive stars, the

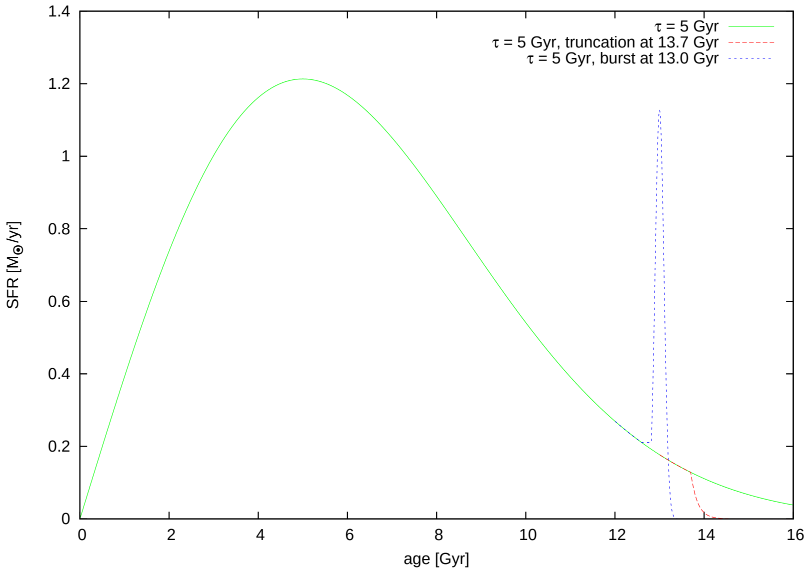

Figure 4.2: SFH for an example galaxy with $\tau = 5$ Gyr, an initial gas mass of $M = 1 \cdot 10^{10} M_{\odot}$ and three SF-modes: undisturbed (green line), truncation (red line) and burst (blue line).

light is dominated by the intermediate and low mass stellar population, which radiates mostly at optical and infrared wavelength.

Up to this point we just work with theoretical models, but the main question is how these models fit to the observations? To answer this question, the models have to be transformed into observables, which was achieved by folding the theoretical spectrum of the galaxy with the desired filter system. In this study the filter curves of the SDSS (but other filter systems are also possible, like the ones of UKIDSS or HST) are used to obtain the corresponding magnitude (here AB magnitudes, Bohlin and Gilliland, 2004) in a certain filter. The filter curves of SDSS and UKIDSS are exemplary over plotted in Fig. 4.3. The height of the filter curves corresponds to the throughput of the SDSS telescope and illustrates the coverage of the used filter system.

4.3 Fitting the observed SEDs with GALEV models

4.3.1 GAZELLE

The most important step is the fitting of the observed data to the models. The finding of the best fitting model enables the investigation of the time evolution of the galaxies. This was done with the program "GAZELLE", which uses a slightly

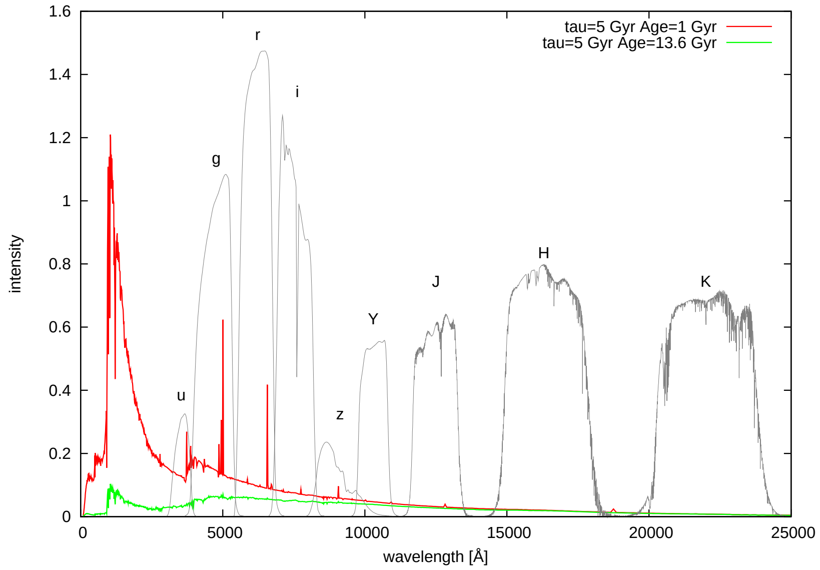

Figure 4.3: Spectra of a model galaxy. Additionally plotted are the filter curves of the SDSS (u, g, r, i and z) and UKIDSS (Y, J, H and K).

modified χ^2 minimisation algorithm (Kotulla et al., 2009). As input parameters a set of theoretical SFHs from GALEV, magnitudes from the observations with corresponding photometric errors (see Equation 3.2), the preferred dust extinction law and a filter system are used. The χ^2 algorithm uses the following formula for the minimisation[3]:

$$\chi^2 = \sum_{\mathrm{i}}^{\mathrm{n}} \left[\frac{\mathrm{F_{i,mod}} - \alpha \cdot \mathrm{F_{i,obs}}}{\sqrt{\sigma^2_{i,mod} + \sigma^2_{i,obs}}} \right]^2 . \tag{4.3}$$

In this equation $\mathrm{F_{i,mod}}$ and $\mathrm{F_{i,obs}}$ correspond to the fluxes in the different filters i to n of the model and the observations with the uncertainties given by $\sigma^2_{\mathrm{i,mod}}$ and $\sigma^2_{\mathrm{i,obs}}$. The uncertainties in the models are due to the limited knowledge of the input physics, like the IMF and incomplete stellar libraries. The drawbacks of evolutionary synthesis models due to incomplete knowledge of the input physics are reviewed in Conroy et al. (2009), Conroy et al. (2010) and Conroy and Gunn (2010). At the moment a model uncertainty of $\sigma^2_{\mathrm{i,mod}} = 0.1$ is assumed, independent of the used filter.
For our analysis one of the most important factors is α, which scales the model luminosity to fit the observation. By scaling the luminosity, it also scales the properties like the mass and SFR of the corresponding galaxy.

[3]The χ^2 algorithm of GAZELLE is slightly modified from the classical definition.

The different distributions of the χ^2 values are displayed in Fig. 4.4 for a galaxy with a variable age (left) and fixed age of 13.7 Gyr (right). In our study, we assume a constant age of 13.7 Gyr to reduce the number of free parameters, what is also supported by observations of galaxies, where in almost all cases contributions of an old stellar population can be found[4]. Due to the constant age, all χ^2 values are on a vertical line on the right hand side of Fig. 4.4. Colour coded are the different GALEV-models of the grid - and therefore also the different values of τ that are correlated to the spectral galaxy type - which can be found in Tab. 4.1. The model with the lowest χ^2 value was chosen as the best fitting model. Looking at Fig. 4.4, one also realises that the best fitting values of χ^2 are below unity and not at unity, as one may expects. This is due to the application of the uncertainties of the model $\sigma^2_{\mathrm{i,mod}}$ and the photometry $\sigma^2_{\mathrm{i,obs}}$ in Equation 4.4. The classical χ^2 would only uses the uncertainties of the photometry $\sigma^2_{\mathrm{i,obs}}$, leading to χ^2 values close to unity. However, GAZELLE additionally uses the uncertainties of the models $\sigma^2_{\mathrm{i,mod}}$, which in turn leads to the χ^2 values below unity.

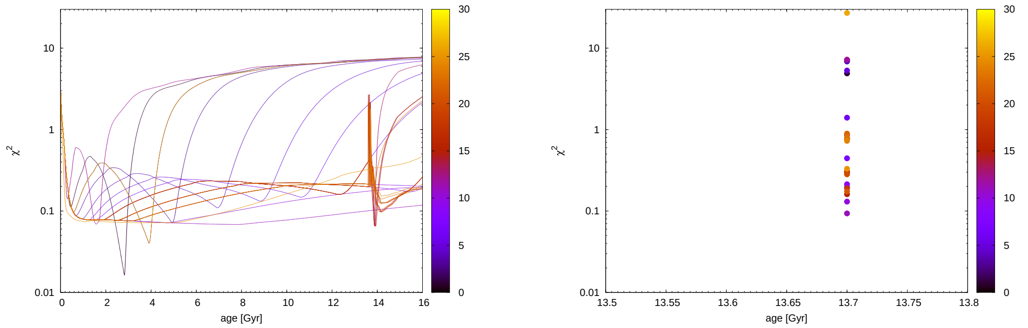

Figure 4.4: χ^2 distribution of a galaxy with variable galaxy age (left) and a constant age of 13.7 Gyr (right). Colour coded are the model-numbers according to Tab. 4.1.

Figure 4.5 shows the spectral energy distribution (SED) for two galaxies. In both cases the galaxies were fitted with and without dust. The observed r-band magnitudes of the galaxies are the results of Chapter 3 and are displayed via black data points in Fig. 4.5. The horizontal bars indicate the FWHM of the corresponding SDSS filters. Blue circles in the SEDs show the best fits to the observations when dust extinction is not taken into account, while the red circles belong to the models with dust extinction. The difference between the SED with dust extinction and without are not large, but not negligible. The models that include the dust extinction fit the observation sightly

[4]Even the age estimates of the most metal-poor BCD I Zw18 changes over the last years, making it older with every new and deeper observation (e.g. Hunt et al., 2003; Aloisi et al., 2007).

better. It is also possible that for the same galaxy, different values of τ are the best fit for the case of extinction and no extinction. It also has to be pointed out that the extinction is not simply set to zero (see Equation 4.4), but instead we re-run the entire fitting algorithm of GAZELLE to find the best fitting model. If one just set the used dust extinction for a model to zero, the differences of the observed and model SEDs became quite large. For instance, in case of an edge-on spiral, the difference is up to 1 magnitude within a filter.

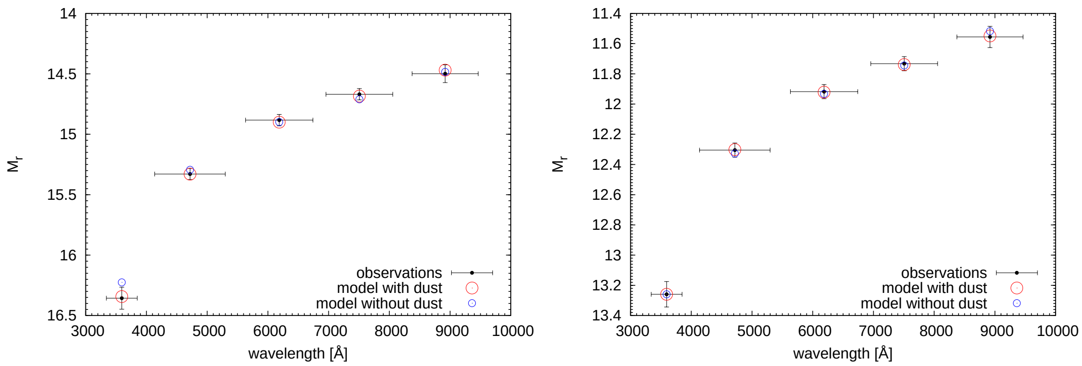

Figure 4.5: SEDs of two galaxies of different types. Horizontal error bars correspond to the width of each SDSS filter, while the vertical ones display the photometric errors of the data. Left: VCC-0024 (BCD); Right: VCC-0025 (Sc).

4.3.2 The grid

To model the observed properties of the galaxies, a model grid was created, using the above mentioned input parameters. τ was chosen in the range of $0.5 \leq \tau \leq 25$ Gyr. The study of Sandage (1986) assumed for the Sm galaxies a SFH that is rising with time (their Fig. 10 b). Thus, in case of the "Sm" model an exponential increasing SFR was assumed with $\tau = -4$ Gyr in Equation 4.1 (see also MacArthur et al., 2004). This τ was chosen to reach the minimal (g-i)-colours of the Sm galaxies of our sample. Sm-models with $\tau < -4$ Gyr do not significantly differ in (g-i)-colours from the $\tau = -4$ Gyr model. Therefore, we only include the Sm-model with $\tau = -4$ Gyr.
For all models the chemically consistent treatment of the ISM of the galaxy was applied. Table 4.1 summarised the used models with the corresponding input parameters. The last model in the table was included as a tracer for errors in the fitting of the models to the observations. If no model matches to the observation, the last model in the list is automatically chosen as the best-fit model. Therefore, we

include a model of a massive and metal rich elliptical galaxy, which should not describe the spectral properties of today's late-type galaxies. Thus, if a galaxy is fitted by the elliptical model it pointed to a failure in the modelling.

To model the analysed galaxies, the grid should cover the entire range of the photometric parameters. Figure 4.6 shows the evolution with time of the (g-i)-colours of the different models for an undisturbed evolution without any interaction. The black vertical line at 13.7 Gyr corresponds to the (g-i)-colour of range $0.1 < (g - i) < 1.2$ mag of the observed late-type galaxies, without including the BCDs with their partially extreme blue colours. Except for the very red (g-i)-colours of $(g - i) > 1.1$ mag, the grid covers the entire colour-space of the late-type galaxies.

Figures 4.7 and 4.8 show the same models, but with an additional burst and truncation, respectively. The burst was not applied to every single model, but only to models with $\tau > 5$ Gyr, which is typical for bursting dwarfs. It is also possible that the BCDs are in different phases of the starburst. For example, one BCDs perhaps just ignites the starburst, while another is at the end of the starburst. Therefore, we applied different starting points for the starburst - from 13.68 Gyr (20 Myr ago) up to 13.60 Gyr (100 Myr ago). The bursts are necessary to reach the extreme blue colours of the BCDs with their strong starburst. In the extreme case of VCC-1313, the (g-i)-colour of the entire galaxy reaches a value of $(g - i) = -0.3$ mag. Interestingly, the influence of the starburst on the (g-i)-colour is minor 1 Gyr after the onset of the burst and is almost invisible after the 2 Gyr.

The truncation was used to simulate the interaction between the galaxy and the ICM of the cluster via RPS, resulting in a gas loss and a decrease of the SF. The truncation starts at 13.7 Gyr with a time scale of $\tau_{\rm trunc} = 150$ Myr (Boselli et al., 2008). Figure 4.8 shows the time evolution of the (g-i)-colours of the models if one applies a truncation. Before the truncation sets in, the difference between the minimal and maximal (g-i)-colour of the models is $\Delta(g - i) \approx 0.85$ mag. However, after 2 Gyr the difference of the models became minimal with $\Delta(g - i) \approx 0.3$ mag. Thus, the application of a truncation to the time evolution of the galaxies will bring all galaxies into a narrow (g-i)-colour region of $0.8 < (g - i) < 1.1$ mag.

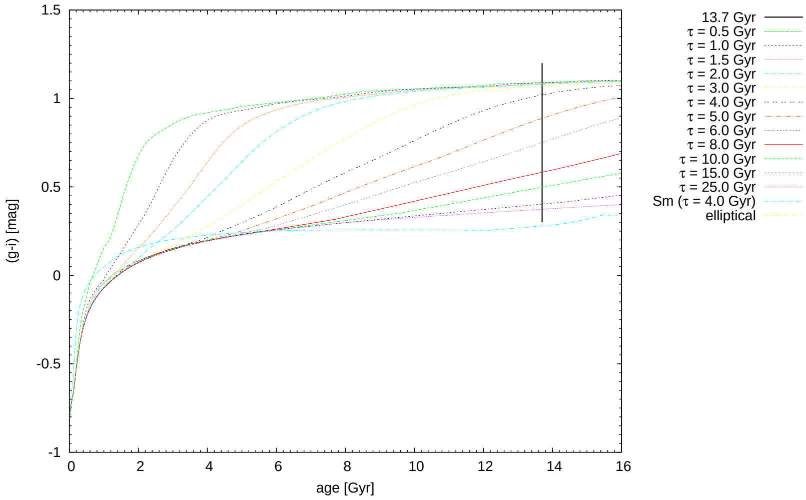

Figure 4.6: (g-i)-colour evolution with time of the different models. The vertical line indicates the position of today (t = 13.7 Gyr).

Table 4.1: Used model grid for GALEV.

Model-id	Model name	τ [Gyr]	Truncation [Gyr]	Burst [Gyr]
model_01	gavazzi_tau50e08_CC	0.5	-	-
model_01	gavazzi_tau10e09_CC	1.0	-	-
model_02	gavazzi_tau15e09_CC	1.5	-	-
model_03	gavazzi_tau20e09_CC	2.0	-	-
model_04	gavazzi_tau30e09_CC	3.0	-	-
model_05	gavazzi_tau40e09_CC	4.0	-	-
model_06	gavazzi_tau50e09_CC	5.0	-	-
model_07	gavazzi_tau60e09_CC	6.0	-	-
model_08	gavazzi_tau80e09_CC	8.0	-	-
model_09	gavazzi_tau10e10_CC	10.0	-	-
model_10	gavazzi_tau15e10_CC	15.0	-	-
model_11	gavazzi_tau25e10_CC	25.0	-	-
model_33	gavazzi_tau50e08_CC_trunc137e09	0.5	13.7	-
model_22	gavazzi_tau10e09_CC_trunc137e09	1.0	13.7	-
model_23	gavazzi_tau15e09_CC_trunc137e09	1.5	13.7	-

continued

Model-id	Model name	τ [Gyr]	Truncation [Gyr]	Burst [Gyr]
model_24	gavazzi_tau20e09_CC_trunc137e09	2.0	13.7	-
model_25	gavazzi_tau30e09_CC_trunc137e09	3.0	13.7	-
model_26	gavazzi_tau40e09_CC_trunc137e09	4.0	13.7	-
model_27	gavazzi_tau50e09_CC_trunc137e09	5.0	13.7	-
model_28	gavazzi_tau60e09_CC_trunc137e09	6.0	13.7	-
model_29	gavazzi_tau80e09_CC_trunc137e09	8.0	13.7	-
model_30	gavazzi_tau10e10_CC_trunc137e09	10.0	13.7	-
model_31	gavazzi_tau15e10_CC_trunc137e09	15.0	13.7	-
model_32	gavazzi_tau25e10_CC_trunc137e09	25.0	13.7	-
model_34	gavazzi_tau60e09_CC_burst20	6.0	-	13.68
model_35	gavazzi_tau60e09_CC_burst50	6.0	-	13.648
model_36	gavazzi_tau60e09_CC_burst100	6.0	-	13.60
model_37	gavazzi_tau80e09_CC_burst20	8.0	-	13.68
model_38	gavazzi_tau80e09_CC_burst50	8.0	-	13.648
model_39	gavazzi_tau80e09_CC_burst100	8.0	-	13.60
model_40	gavazzi_tau10e10_CC_burst20	10.0	-	13.68
model_41	gavazzi_tau10e10_CC_burst50	10.0	-	13.648
model_42	gavazzi_tau10e10_CC_burst100	10.0	-	13.60
model_43	Sm_40e09	-4.0	-	-
model_44	elliptical_fake	-	-	-

The model grid.

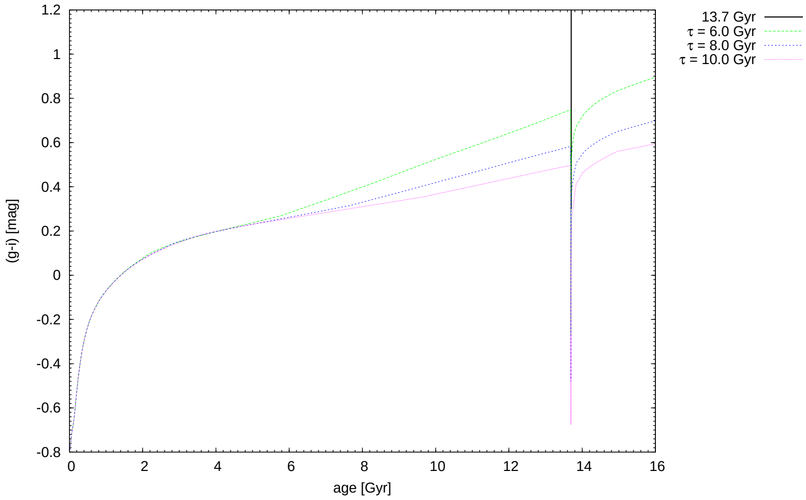

Figure 4.7: Same as Fig. 4.6, but additionally a starburst was assumed in a subset of the models.

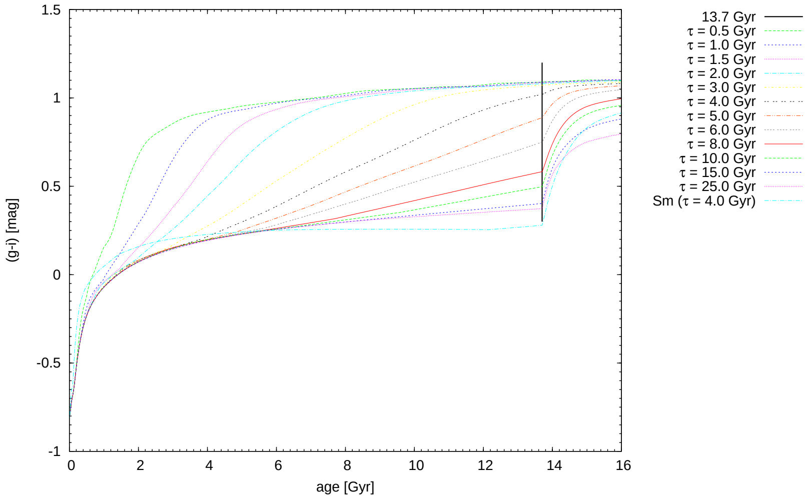

Figure 4.8: Same as Fig. 4.6, but with a truncation at t = 13.7 Gyr.

4.4 Results

4.4.1 The output

After the determination of the best fitting SFH and the convolution with the SDSS observation, GALEV gives plenty of output parameters, which are summarised in Tab. 4.2. The offsets α of Equation 4.4, which are applied to the models to fit the observations, are particular important to model the time evolution of the galaxies. The evolution of the magnitude M of the corresponding galaxy can be calculated by:

$$M(t) = M_{mod}(t) - \alpha + \left[E(B-V)(t) \cdot \left(SFR_{mod}(t)/SFR_{obs} \cdot 10^{(-0.4 \cdot \alpha)}\right) \cdot A_M(t)\right], \quad (4.4)$$

with the parameters of Tab. 4.2.

Since GALEV calculates the evolution of the magnitude for all input filters, we are also able to investigate the evolution of the different colours, like the (g-i)-colours of Chapter 3.

Table 4.2: Output parameters from the GALEV/GAZELLE models.

Parameter	Description
mod_{fit}	Best fitting model
age	Age of the galaxy (held constant to 13.7 Gyr)
α	Applied offset to the model to fit the observations
M_{tot}	Total mass (gas+stars) of the galaxy in units of $M_{\odot}$
$M_{stellar}$	Stellar mass of the galaxy in units of $M_{\odot}$
M_{gas}	Gas mass of the galaxy in units of $M_{\odot}$
$M_{non-vis}$	Non visible mass of the galaxy in units of $M_{\odot}$
Z_{gas}	Gas metallicity
SFR_{obs}	Best fitting SFR to the observation
SFR_{mod}	SFR of the model without offsets
M_{mod}	Magnitude of the model without offsets
A_M	Dust correction
E(B-V)	Applied extinction

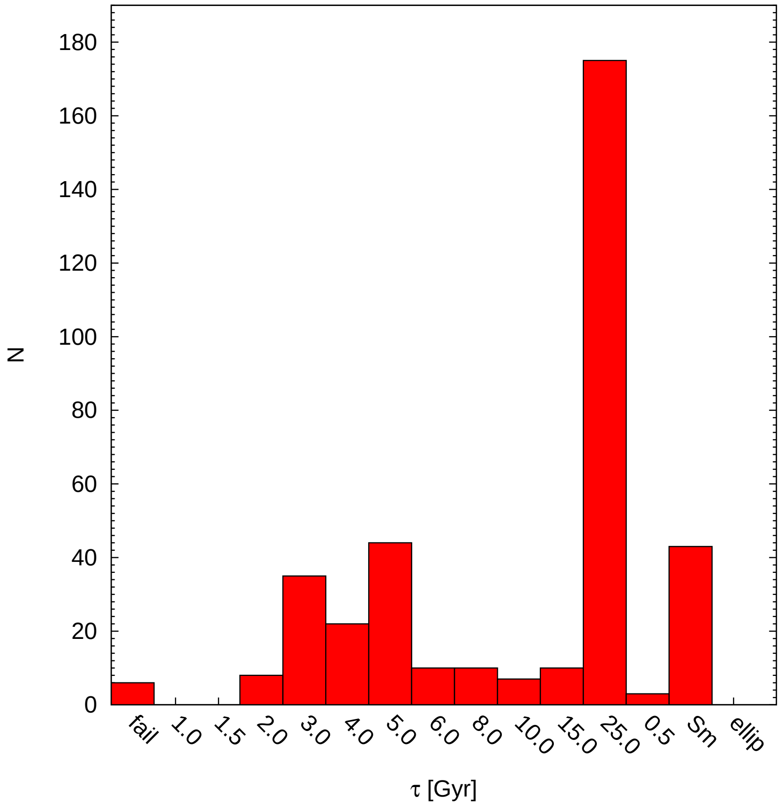

Figure 4.9: Distribution of the different values of τ of the models for the Virgo sample. The first bar ("fail") includes all galaxies, where no appropriate model was found by GAZELLE.

4.4.2 Number distribution of the galaxies among the model grid

Figure 4.9 shows the number distribution of the different values of τ used by the GALEV models. In most of the cases a model with τ = 25 Gyr was chosen (model-11 in Tab. 4.1) . The right hand side of Fig. 4.10 shows the distribution of the different morphological galaxy types within the τ = 25 Gyr model. In most of the cases this model was used to fit galaxies of the type Sc, dI and dE/dI, a class that is treated as a subclass of the dIs in our analysis and that corresponds to the "dE/Im" class of the VCC. Due to the relatively large value of τ (τ = 25 Gyr) it is reasonable that most of the dIs are fitted with this model.

Figure 4.11 shows the (g-i)-colours as a function of τ. As expected, there is a clear trend for $\tau \leq 15$ Gyr of being redder with decreasing τ, which shows the connection between τ and the morphological/spectral type of the galaxies.

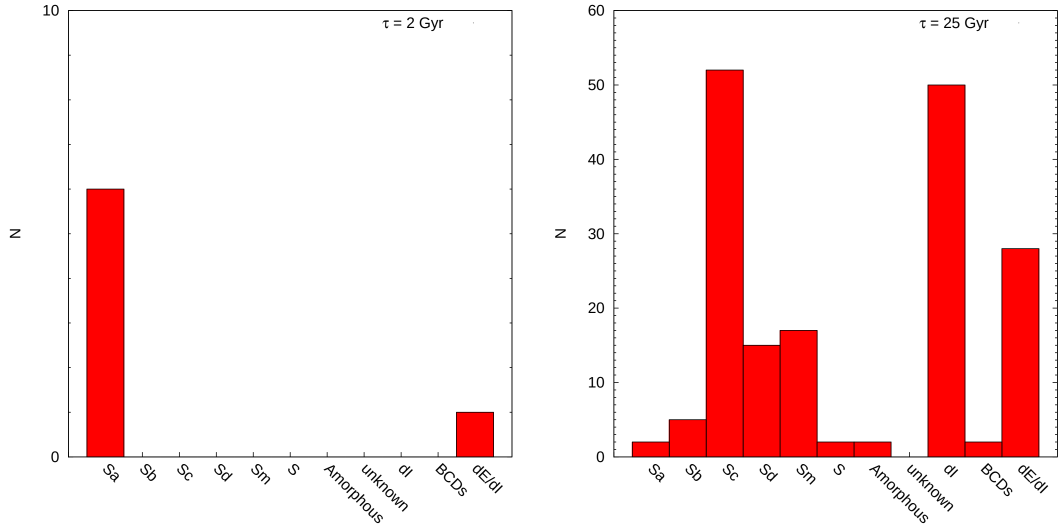

Figure 4.10: Distribution of morphological galaxy types with τ = 2 Gyr (left panel) and τ = 25 Gyr (right panel).

Figures 4.12 and 4.13 show the relative number of each morphological type from the VCC as a function of τ. The majority of the late-type galaxies in the sample avoid the region of $6 \leq \tau \leq 15$ Gyr. In the regime of $16 \leq \tau \leq 24$ Gyr there is no models in our grid, which therefore explains the gap in this region in Figs. 4.12 and 4.13. In case of the Sa galaxies, almost 50 % of them were fitted with $\tau = 3.0$ Gyr, but also about 5 % were fitted with a quite large τ of $\tau = 25$ Gyr. Over 70% of the Sd galaxies were fitted with $\tau = 25$ Gyr and the rest with $\tau \leq 25$ Gyr.

4.4.3 Physical properties of the morphological types

Figure 4.14 shows the average total masses of the different morphological types of the sample. The most massive galaxies in Fig. 4.14 are the early spirals of type Sa to Sc with $M_{tot} \approx 7 \cdot 10^{10} M_\odot$. The late spirals (Sd and Sm), together with the loosely classified type of S galaxies, have significantly lower averaged total masses in the range of $5.5 \cdot 10^9 < M_{tot} < 9.5 \cdot 10^9 M_\odot$.
The unknown and dI galaxies have the lowest averaged total mass of the entire sample with $M_{tot} < 2 \cdot 10^9 M_\odot$.
The BCDs have an averaged total mass of $M_{tot} = 5.5 \cdot 10^9 M_\odot$, similar to the Sm galaxies.
Other output parameters, like the gas metallicity, do not scale with the luminosity.

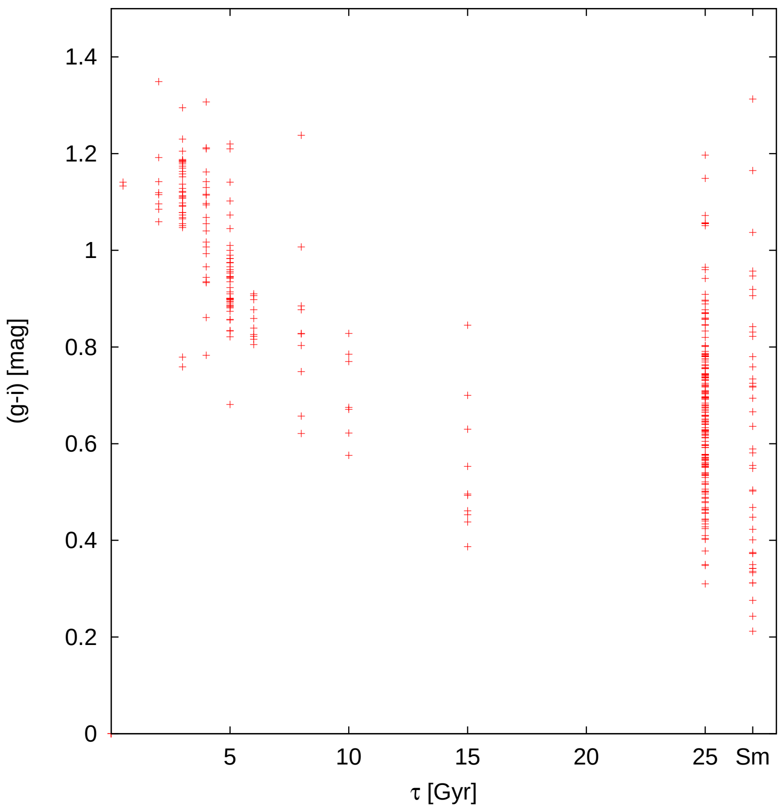

Figure 4.11: (g-i)-colours of the model galaxies vs. the best fitting value of τ.

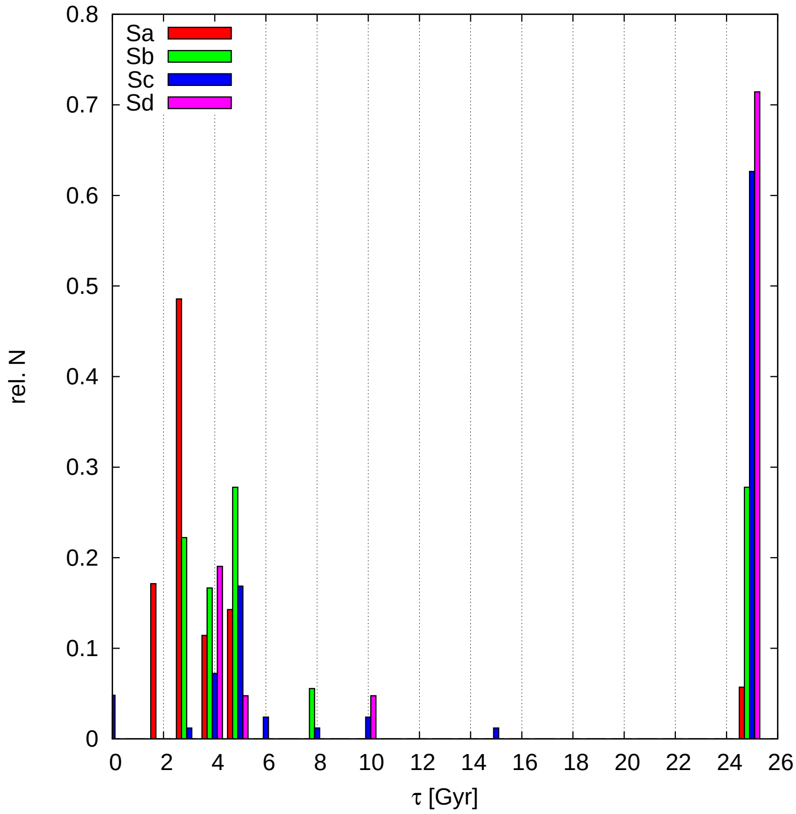

Figure 4.12: Relative number of the different morphological types from Sa to Sm vs. the best fitting value of τ.

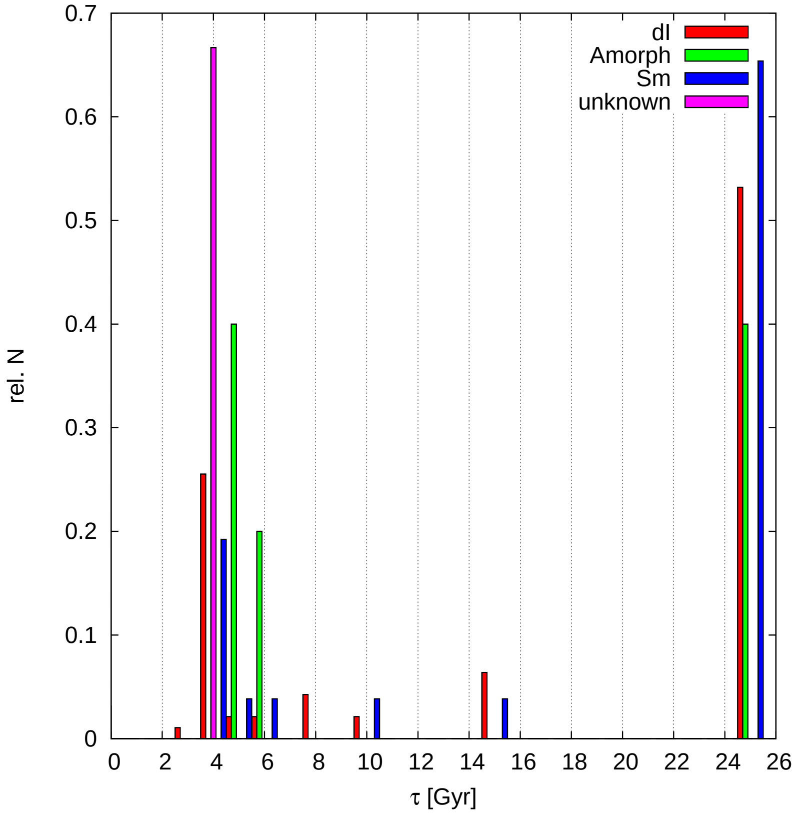

Figure 4.13: Same as Fig. 4.12, but for the Sm, dI, unknown and Amorphous galaxies.

Therefore, all galaxies with the same τ will also have the same metallicity. Figure 4.15 shows the evolution with time of the gas metallicity for a set of different values of τ for an undisturbed and truncated evolution, respectively. In the case of an undisturbed evolution, the metallicity of the models with $\tau \geq 5$ Gyr gradually increases, while for the truncation the models with $\tau > 5$ Gyr and ages of t > 13.7 Gyr show an almost constant metallicity due to the cease of the star formation.

Figure 4.17 shows the mass-metallicity relation of the sample. The median masses are calculated within each metallicity bin, while metallicities with $Z > 0.031$ are summarised into one bin. As one can see, the most massive galaxies also have the highest metallicity and vice versa in case of the low-mass galaxies, as expected from the observations and theory (e.g. Tremonti et al., 2004). Additionally shown in Fig. 4.18 is the stellar mass M_{stellar} (left) and the metallicity Z (right) as a function of τ. For $\tau < 5$ Gyr the stellar mass remains almost constant, while the metallicity increases with τ. For $\tau > 5$ Gyr both parameters decrease, which again reflects the behaviour of the mass-metallicity relation and shows the connection between τ and the spectral galaxy type.

4.4.4 Colour-colour diagram

Figure 4.19 shows the colour-colour diagram of the sample galaxies, combined with the theoretical evolutionary tracks of the model colours. Randomly for some galaxies are also shown the representative error bars of the photometry. The red lines in the diagram correspond to the evolution with time of the colour using the different models without the application of dust reddening. The current data point of the models at 13.7 Gyr is indicated by a big black data point. In the figure, the different values of τ are colour coded. The green data points correspond to galaxies that are fitted with the "Sm-model".

Data points that are not located in the regions of the bulk of the galaxies have relatively large errors. Since the errors of photometry enter into the fitting routine of GALEV/GAZELLE, the results for these galaxies should be handled with care. A check of the galaxies with large error bars reveals mostly galaxies classified as dI with low S/N.

As one can see, observational data points with $(u - r) \gtrsim 1.75$ mag are mostly fitted by models with $\tau \leq 6$ Gyr and vice versa for galaxies with $(u - r) < 1.75$ mag, which are fitted with models with $\tau > 6$ Gyr. This behaviour shows again the connection between τ and the spectral galaxy type.

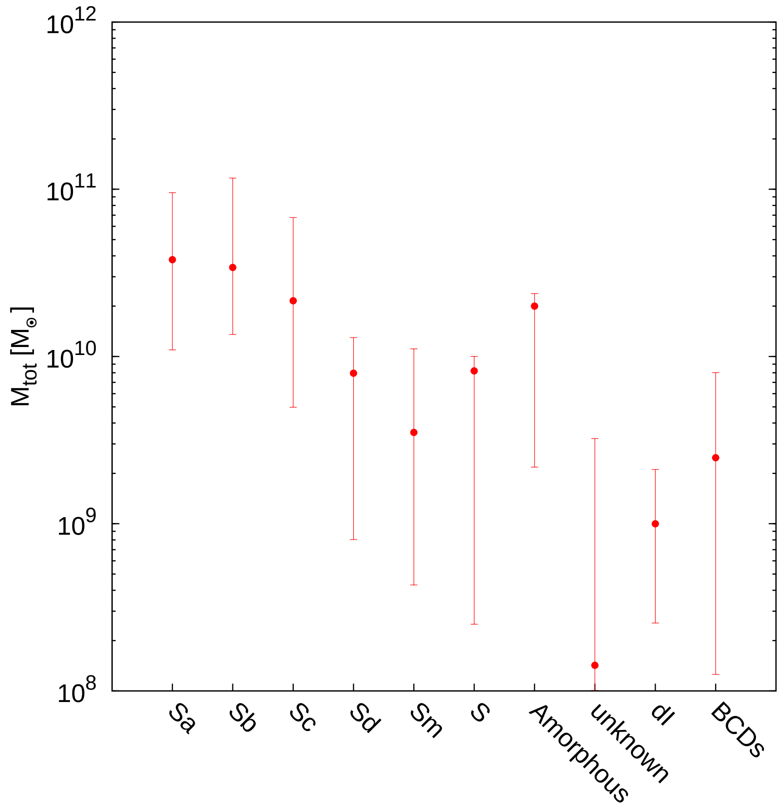

Figure 4.14: Mass distribution of the different morphological types. For all galaxies a constant distance of 16.5 Mpc was applied.

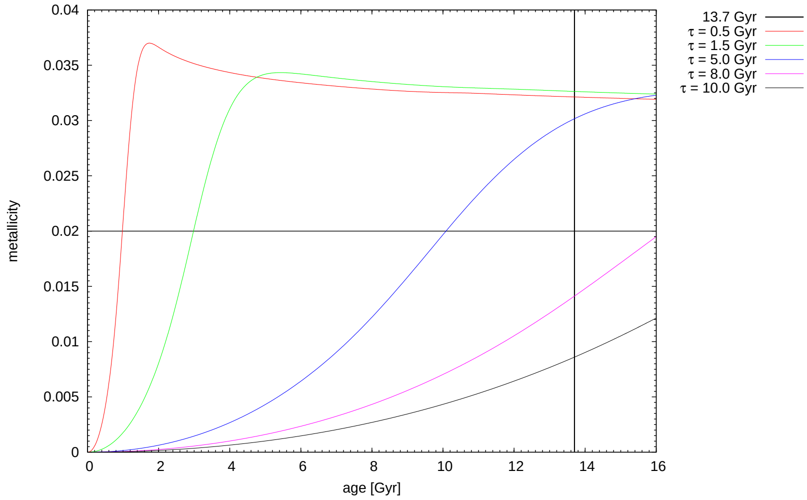

Figure 4.15: Evolution of the gas metallicity of an undisturbed galaxy for different sets of τ. The black horizontal line indicates the solar metallicity and the vertical line shows the position of t=13.7 Gyr.

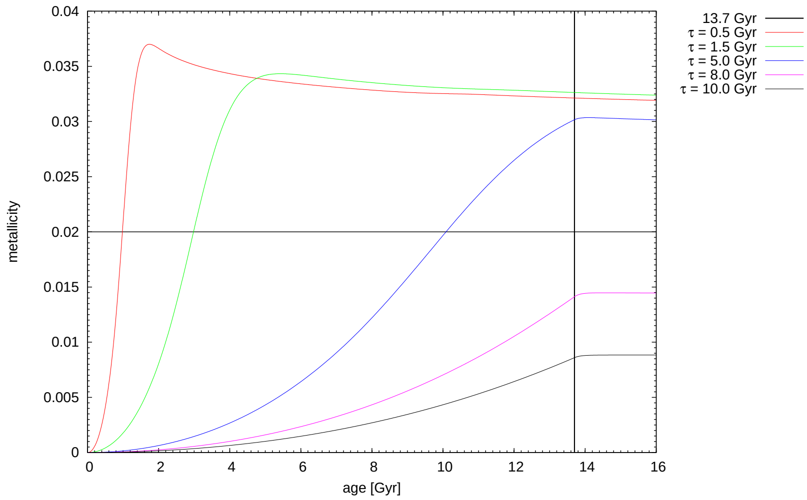

Figure 4.16: Same as Fig. 4.15, but for a truncation.

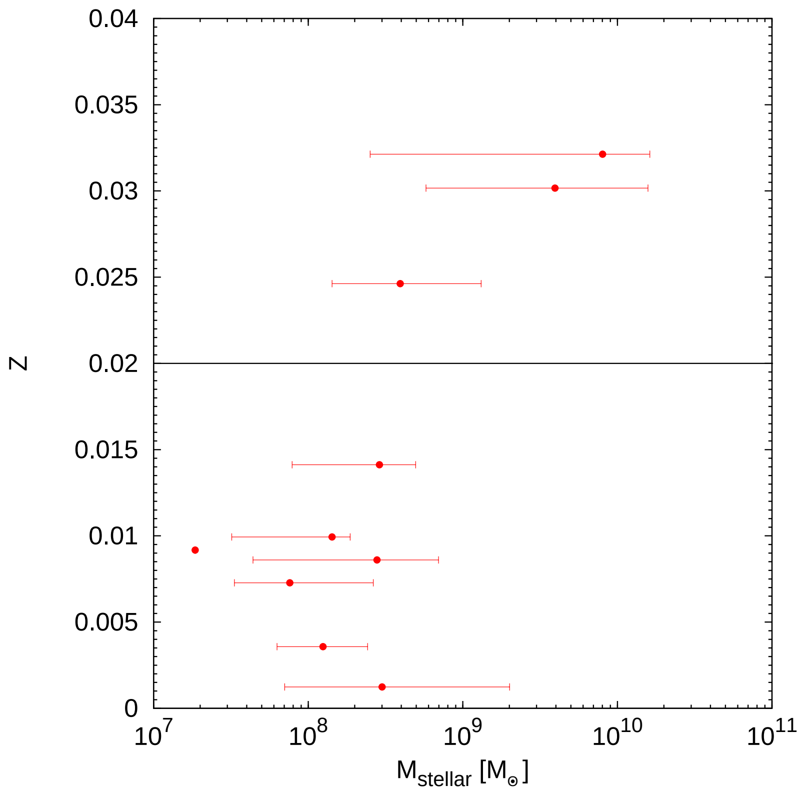

Figure 4.17: Mass-metallicity relation of the GALEV-models. Data points display the median values and the 1σ deviations of the galaxies sample within the corresponding metallicity bin. The horizontal line corresponds to the solar metallicity.

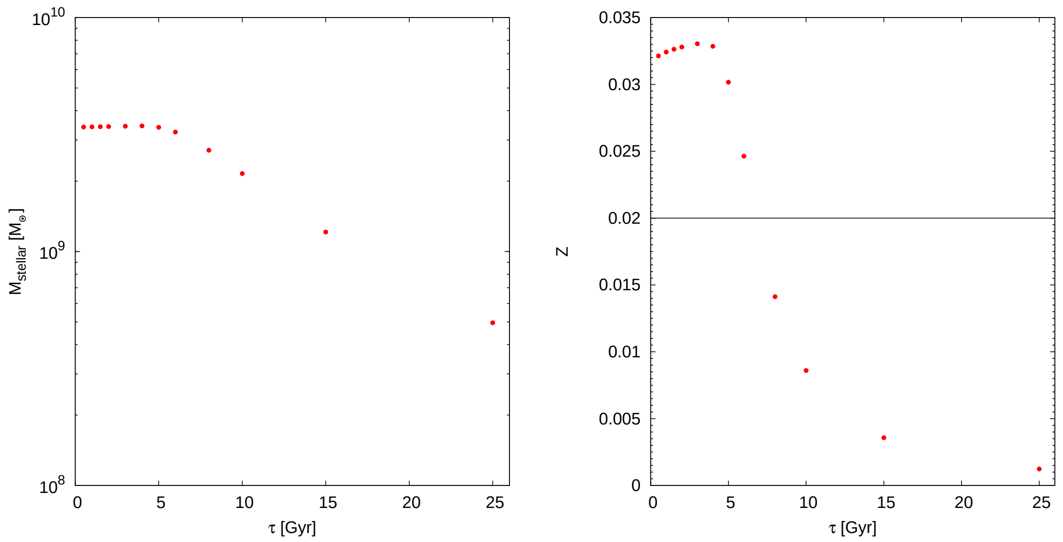

Figure 4.18: τ vs. the stellar mass $M_{stellar}$ and metallicity Z of the GALEV-models. As in Fig. 4.17, the horizontal line corresponds to the solar metallicity.

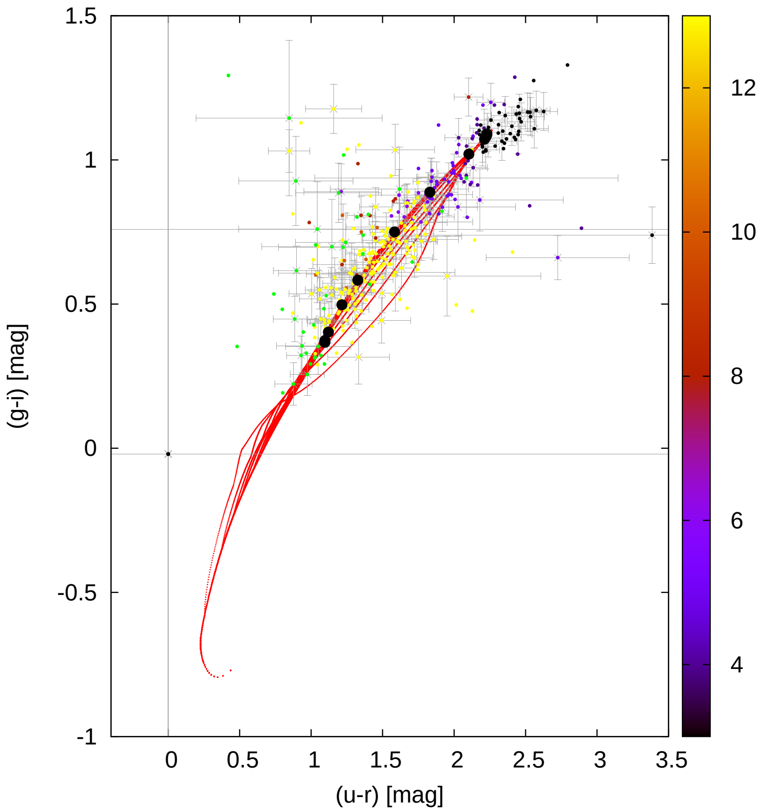

Figure 4.19: (u-r)-(gi) diagram. Shown are the colours of the observed galaxies and the theoretical predictions of the GALEV models. Red lines correspond to the colour evolution of the different models and the big black data points display the colours of the models at 13.7 Gyr (today), without the application of any offsets. Colour coded are the different values of τ, while the "Sm-model" is displayed by green data points.

4.4.5 The time evolution of the CMDs

Figures 4.20 to 4.26 show the CMDs of the sample galaxies at different time steps from 13.7 Gyr to 15.7 Gyr in steps of 0.5 Gyr. Additionally, the sample of ETGs from Janz and Lisker (2009) is shown for comparison (black data points). The upper panels of each morphological type show the undisturbed evolution without any interaction with the cluster, while the lower panels show the evolution with an applied truncation starting at 13.7 Gyr and a truncation time scale of 150 Myr.

In case of the truncation most of the late-type galaxies lie on distinct lines after 2 Gyr – e.g. at $(g-i) = 0.78$ mag and $(g-i) = 0.95$ mag in case of the BCDs. This artificial behaviour can be explained by the time evolution of the (g-i)-colours in Fig. 4.8. For instance, the difference of today's colours for a model with $\tau = 6$ Gyr to a model with $\tau = 8$ Gyr is $(g-i) = 0.2$ mag. However, after 2 Gyr the difference between these two models is almost negligible with $(g-i) = 0.05$ mag. Even though modelled with different values of τ, these galaxies will share the same region in the colour space.

The evolution of the CMDs of the BCDs is shown in Fig. 4.20. The upper panels show the undisturbed evolution of the BCDs. In contrast to the other morphological galaxy types, the BCDs are fitted with models that have additional bursts superposed on the SFH (see again Fig. 4.2). To account for the different phases of the starburst, the onset of the starburst varies from 13.60 Gyr to 13.68 Gyr.

Due to the star formation of today's BCDs, they have bluer (g-i)-colours than the comparison sample of the dEs. Even after 2 Gyr of undisturbed evolution the BCDs have on average bluer (g-i)-colours than the dEs, indicating the ongoing star formation in most of the BCDs. However, for the undisturbed evolution of the BCDs, there are about eight BCDs after 2 Gyr that share the same region in CMD as the dEs.

If the SFR is decreased due to the truncation, which starts today, the resulting CMD after 2 Gyr looks quite different. Two Gyr after the truncation, the colours of the BCDs are in the same region as the dE population. However, the bulk of the evolved BCDs are still slightly bluer than the dEs (see also discussion of Chapter 2).

The dIs in Fig. 4.21 show almost the same behaviour as the BCDs. On average the dIs have bluer (g-i)-colour after 2 Gyr of undisturbed evolution, while in the case of a truncation most of the dIs are located at three distinct lines at (g-i)=0.79 mag, (g-i)=0.87 mag and (g-i)=0.90 mag. These lines are well located within the region of the dEs.

The undisturbed evolving spiral galaxies in Figs. 4.22 to 4.26 show only a weak evolution in the CMDs. This can be explained by the usage of larger values of τ

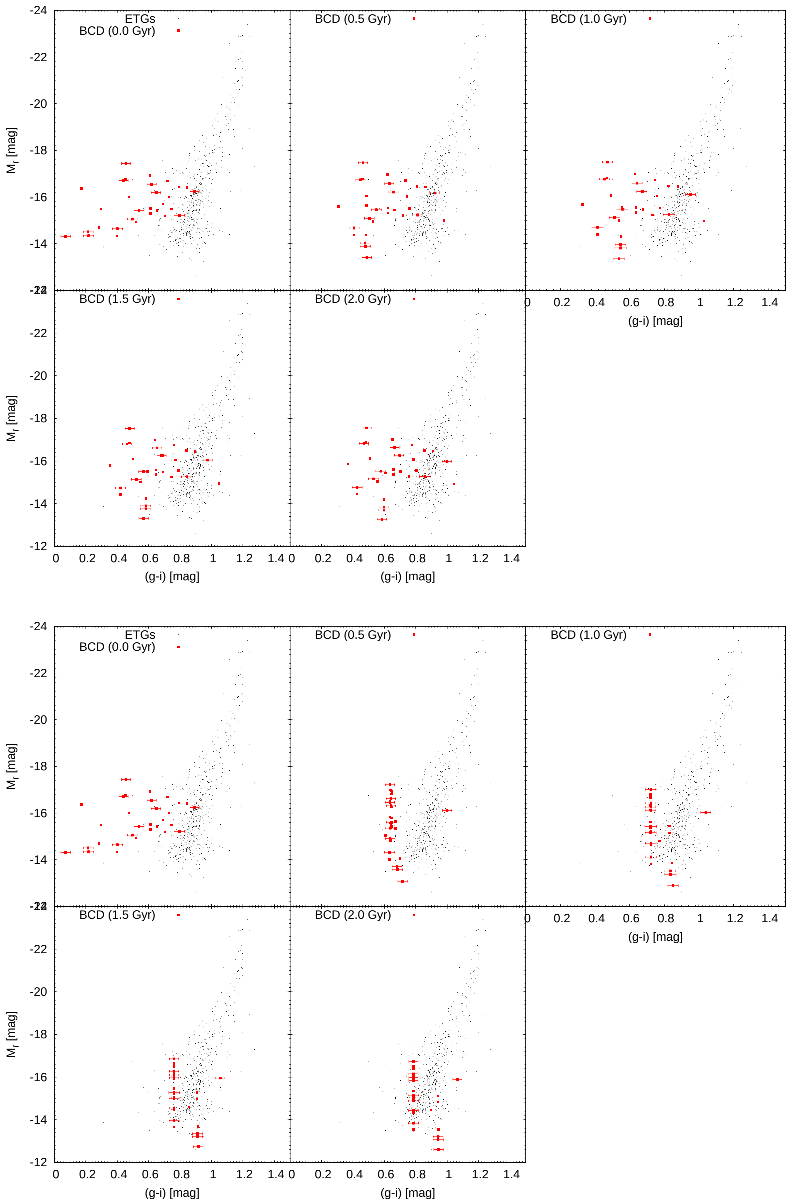

Figure 4.20: Evolution of the BCDs (red data points) at different time steps of the GALEV simulation. Upper panel shows the undisturbed evolution, while the lower panel displays the evolution with a truncation at 13.7 Gyr. The evolution of the galaxies is shown in time steps of 0.5 Gyr, starting from t = 13.7 Gyr (today) up to t = 15.7 Gyr. For comparison the results of Janz and Lisker (2009) for Virgo ETGs are shown in black data points.

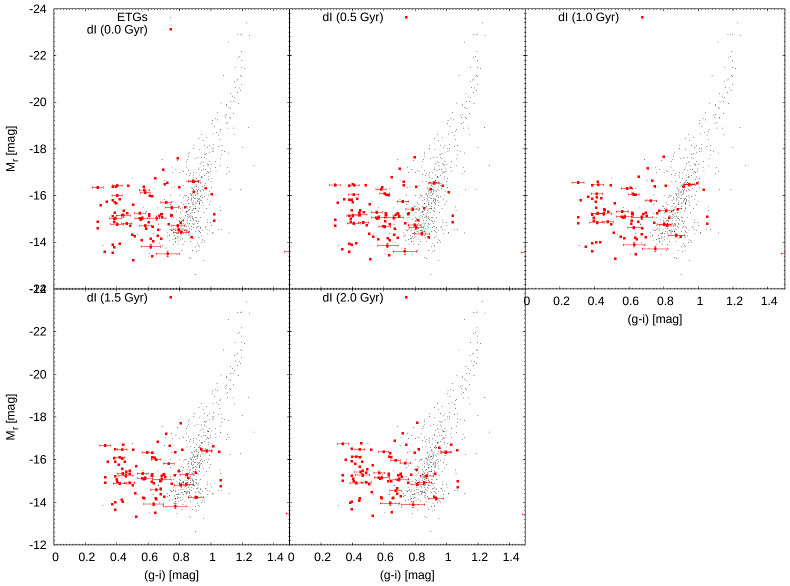

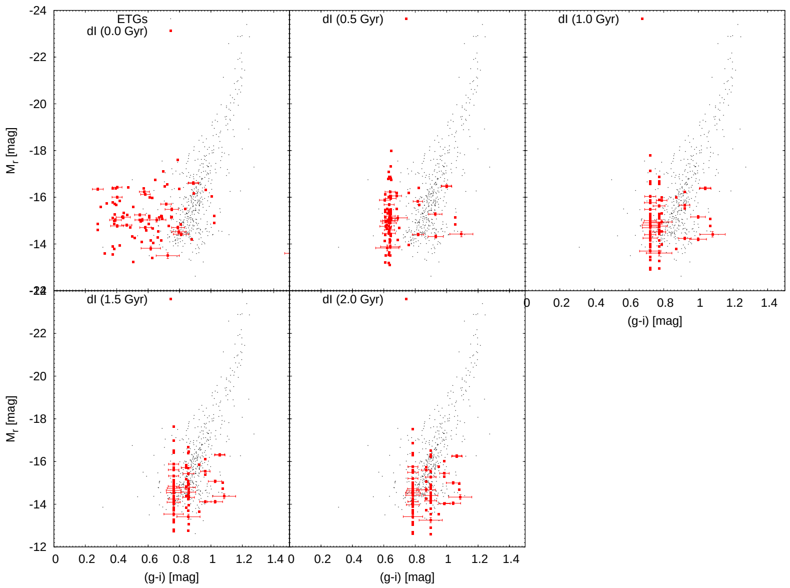

Figure 4.21: Same as Fig. 4.20, but for the dIs.

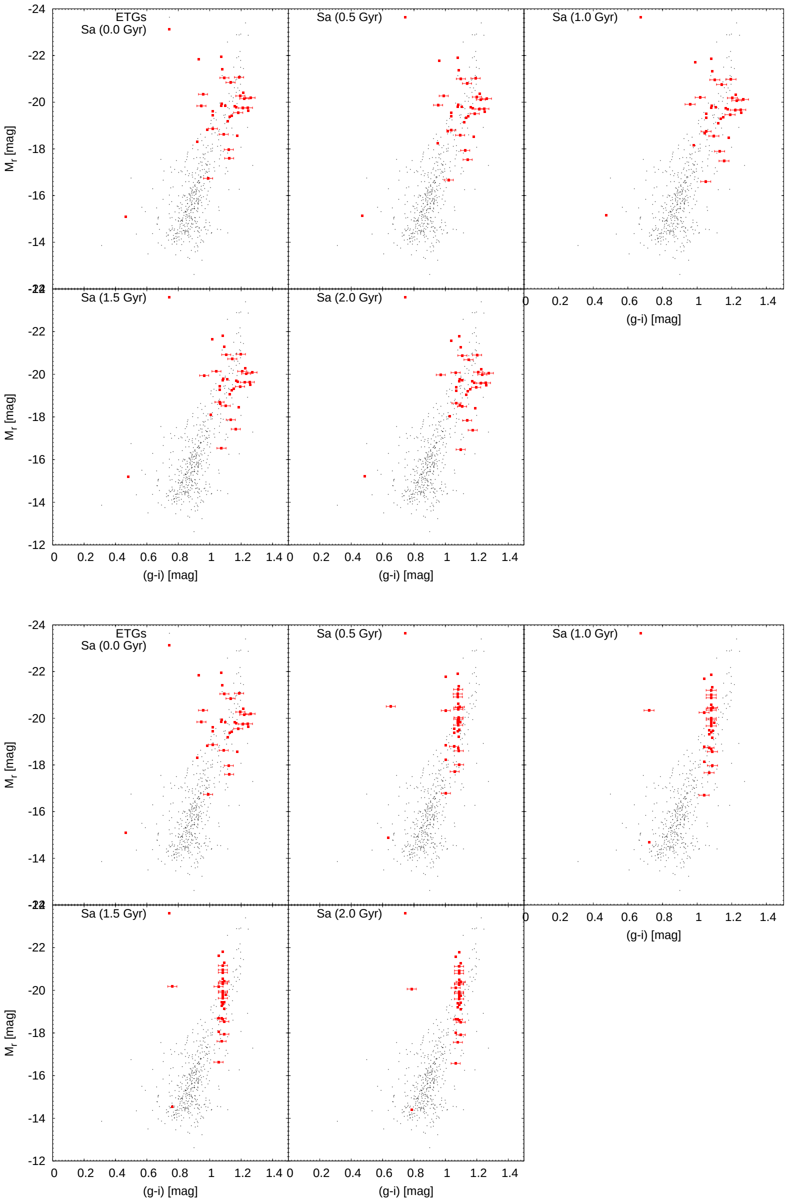

Figure 4.22: Same as Fig. 4.20, but for the Sa galaxies.

by GAZELLE. If the SFR is almost constant over the next 2 Gyr, no large variations in the colours can be expected.
The evolution of the spiral galaxies in the case of the truncation is more obvious. It can also be seen in Figs. 4.22 to 4.26 that the changes in the CMDs from 13.7 Gyr to 14.2 Gyr are very prominent, while the evolution from 14.2 Gyr to 15.7 Gyr is minor. This is reasonable, since the truncation time scale is chosen to be very short with $\tau_{\mathrm{trunc}} = 150$ Myr. When the star formation stops due to the lack of gas, the massive stars will end up their life on a short time scale of several million years, what in turn will redden the integrated colours of the galaxies due to the dominance of the still remaining intermediate and low-mass stars.
In case of the Sa galaxies, one might have the impression that some of the galaxies became bluer after the truncation starts. The reason for this behaviour can be found in Equation 4.4 and in the colours of the used model grid for the truncation. When the truncation starts, the SFR of the model will decrease and therefore also the third term in Equation 4.4 with the extinction will become less important. Thus, the (g-i)-colour of the model grid only reaches a maximum of (g-i)=1.1 mag (see Fig. 4.6) and with that almost all Sa galaxies will gather around this (g-i)-colour in the lower panel of Fig. 4.22.
The brighter truncated Sb galaxies ($M_r < -19$ mag) are on average redder than the faint Sb's and are also located in the same region as the ETGs in Fig. 4.23. The opposite is the case for the truncated Sc galaxies in Fig. 4.24. The most brightest Sc's ($M_r < -20.6$ mag) also have the bluest colours of (g-i)= 0.78 mag. Sc galaxies with $(g-i) > 0.79$ cover the same region in the CMD as the dEs, while for galaxies with (g-i)=0.79, only the faintest ones ($M_r > -16$ mag) share the same region.
The lower panel of Fig. 4.25 shows the evolution of the Sd galaxies in the case of a truncation. The Sd galaxies can be found in the region of $0.79 < (g-i) < 0.95$ mag and $M_r > -18$ mag, with one exception at (g-i)=1.06 mag and $M_r = -18.4$ mag. All Sc galaxies with $(g-i) > 0.9$ mag are located in the same regime as the dEs. At a colour of (g-i)=0.79 mag, only the faintest galaxies ($M_r > -17$ mag) match with the dEs. However, all Sc galaxies are well within the 2σ deviation of the dEs.
The Sm galaxies with a truncation show the same behaviour as the Sc galaxies. In the CMD, they are clearly in the same location as the dEs after a truncated evolution of 2 Gyr (Fig. 4.26).
The loosely classified S galaxies are shown in Fig. 4.27. The evolution of the undisturbed and truncated S galaxies is less, thus one can conclude that the galaxies

have been modelled with a low gas mass fraction.
Figure 4.28 displays the evolution of the Amorphous and unknown galaxies within the CMD. After the truncation, the two unknown galaxies have the same (g-i)-colour ((g-i)=0.86 mag) and also the same magnitudes with values of M_r = 14.3 mag and M_r = 14.6 mag after 2 Gyr. In the class of the Amorphous galaxies, only for two galaxies a significant influence due to the truncation can be observed. Four out of five of the truncated Amorphous galaxies are well located in the same region as the dEs.

Figures 4.29 and 4.32 show the average r-band magnitudes and colours of the different morphological types after an evolution of 2 Gyr. The averages on the left hand side of the figures are for the undisturbed evolving galaxies, without any interaction. The right hand side of the figures show the averages after 2 Gyr with the application of a truncation at t_{trunc} = 13.7 Gyr. Additionally plotted are the averages of today's early-type galaxy population, subdivided into the contribution of the entire population (ETG), dEs, dE(bc) and dEs with a disc structure (dE(di), Lisker et al., 2006b).
Regarding the magnitudes, the morphological types of Sa and Sb are on average brighter than the entire ETG population for both (undisturbed and truncated) evolutionary scenarios. We also found that the Sa galaxies have too red colours compared to the ETGs, which may seem disconcerting. In this case, one has to take care about the calculation of the averages, since the ETGs do not follow a constant $(g - i) - M_r$ relation in the CMD, but show "S"-shape slope (see Janz and Lisker, 2009) in the way that fainter dEs are bluer than the bright ellipticals. Therefore, the results of the Sa galaxies are not in contradiction with other observations.
The Sd and Sm galaxies show a large overlapping region with the ETGs for an undisturbed evolution after 2 Gyr. With an additionally truncation, the r-band magnitude and (g-i)-(u-r)-colours are in an even better agreement with the ETGs. However, the (i-z)-colours, which are most sensitive to the metallicity, show significant differences to the ETGs. The ETGs have lower (i-z)-colours ($(i - z) \approx 0.13$ mag) compared to the undisturbed Sd and Sm galaxies ($(i - z) \approx 0.21$ mag), but these (i-z)-colours are within the 1σ deviation of the ETGs. In case of a truncation the Sd and Sm galaxies still have higher (i-z)-colours ($(i - z) \approx 0.18$ mag) than the ETGs, but the differences are now less prominent. These differences in the (i-z)-colours are also visible for all other late-type galaxies in both evolutionary scenarios in Fig. 4.32.
After 2 Gyr of undisturbed evolution, the dIs are bluer and slightly fainter than the ETGs. The difference in magnitude become even larger, when a truncation is applied. Thus, the dIs are on average fainter than the ETGs, but with an overlap region regarding

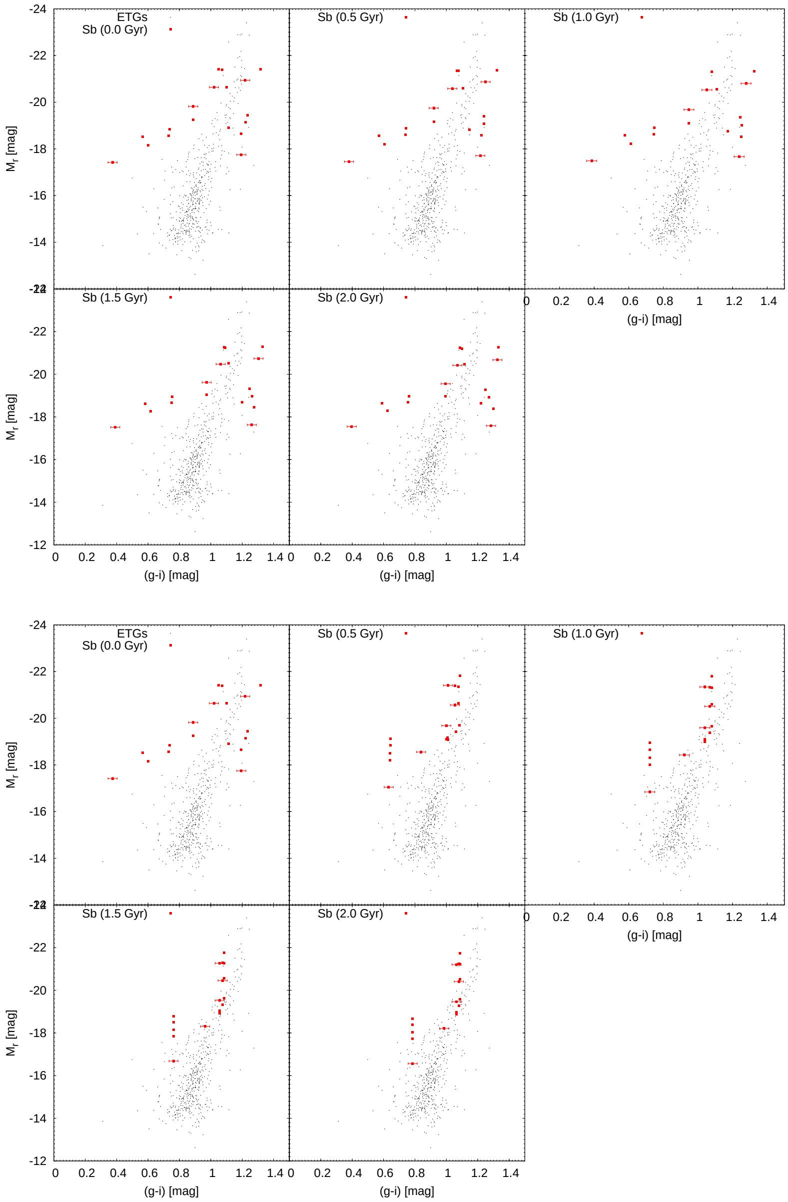

Figure 4.23: Same as Fig. 4.20, but for the Sb galaxies.

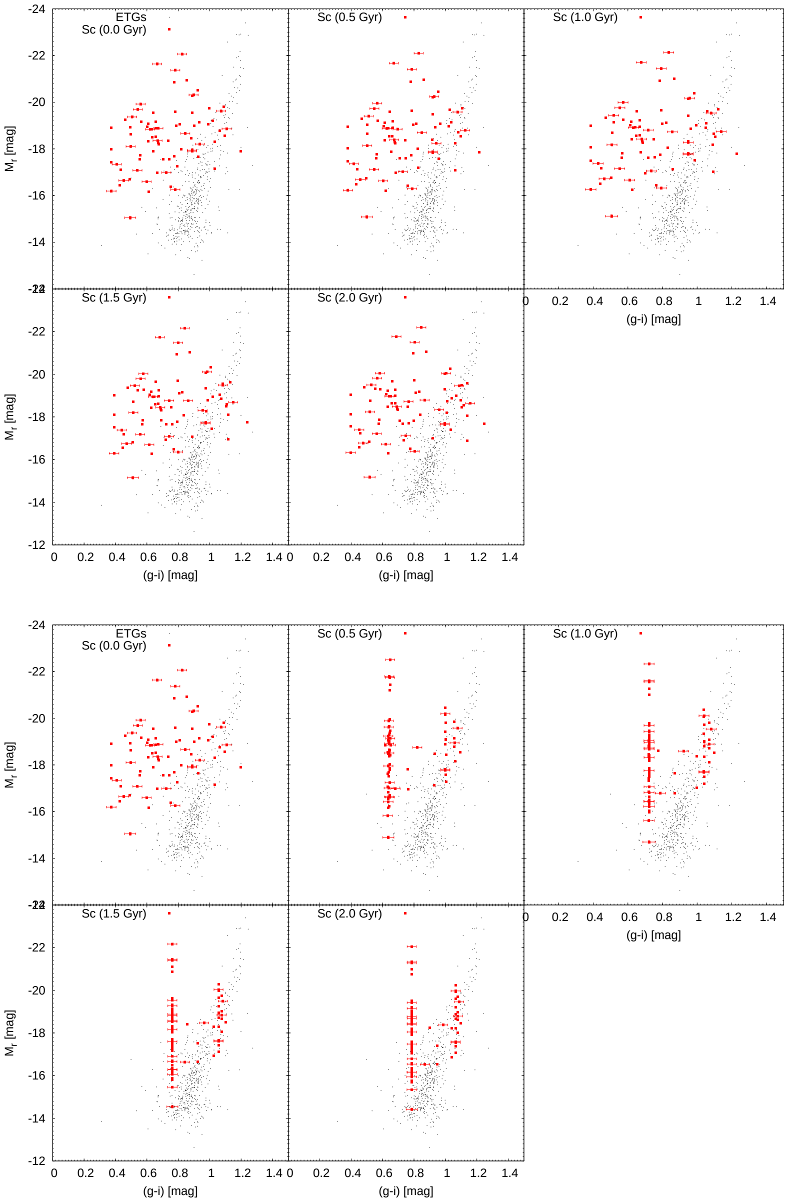

Figure 4.24: Same as Fig. 4.20, but for the Sc galaxies.

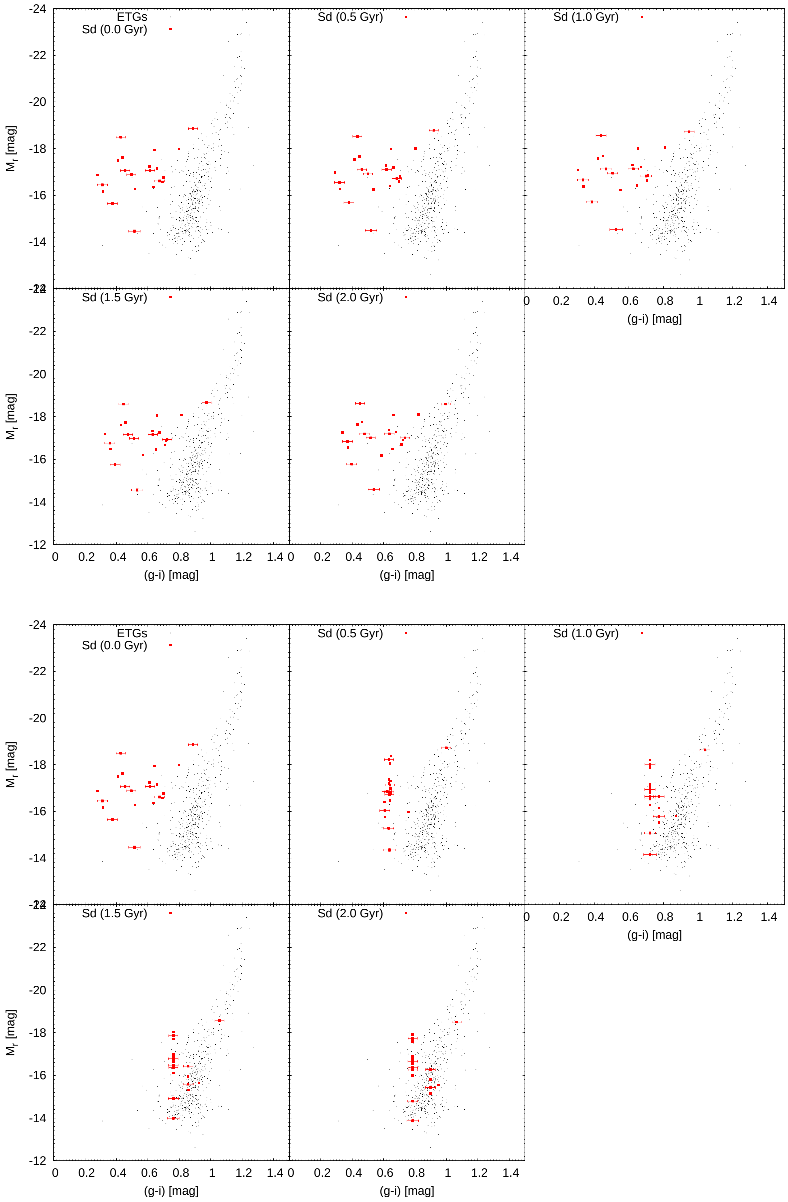

Figure 4.25: Same as Fig. 4.20, but for the Sd galaxies.

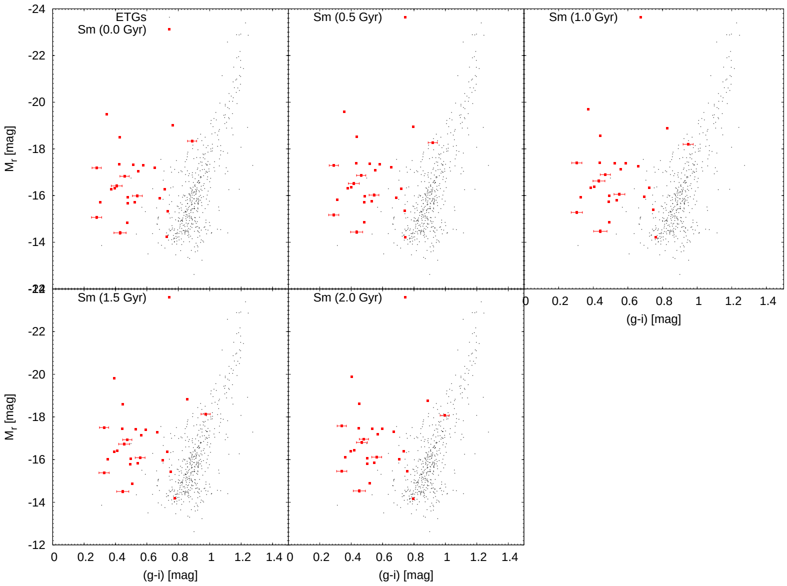

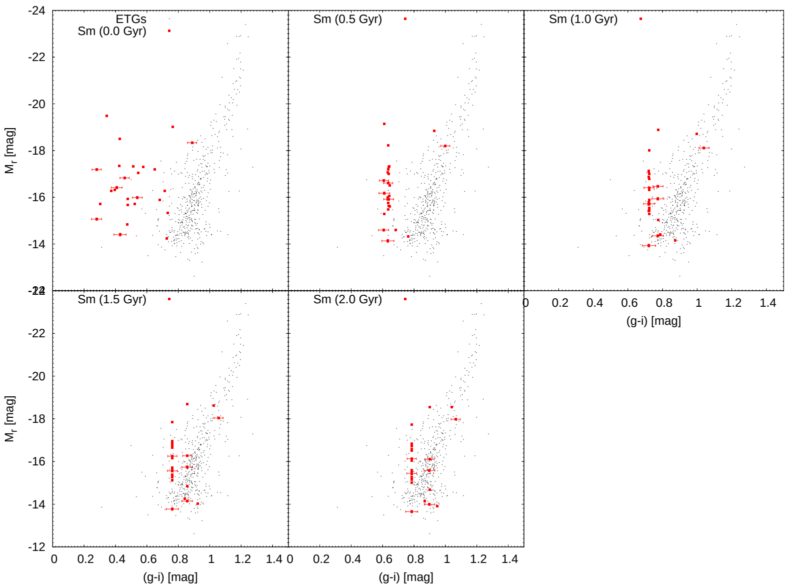

Figure 4.26: Same as Fig. 4.20, but for the Sm galaxies.

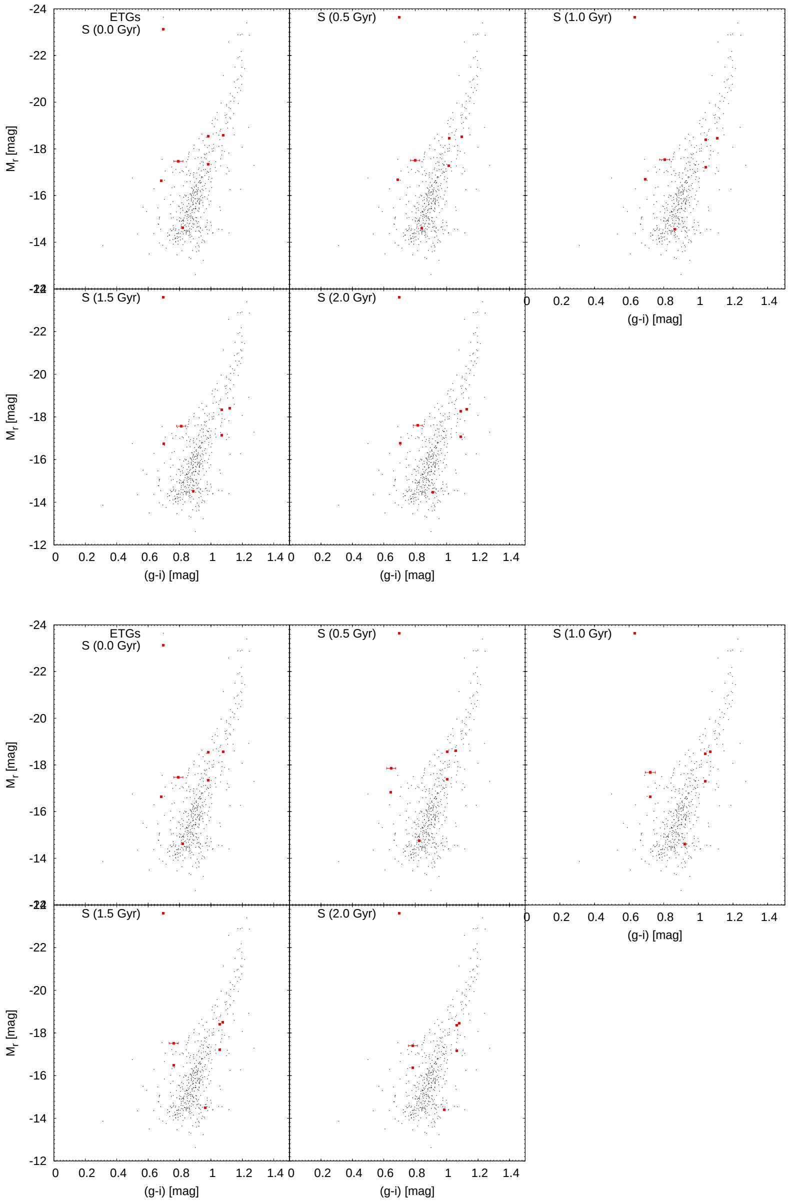

Figure 4.27: Same as Fig. 4.20, but for the S galaxies.

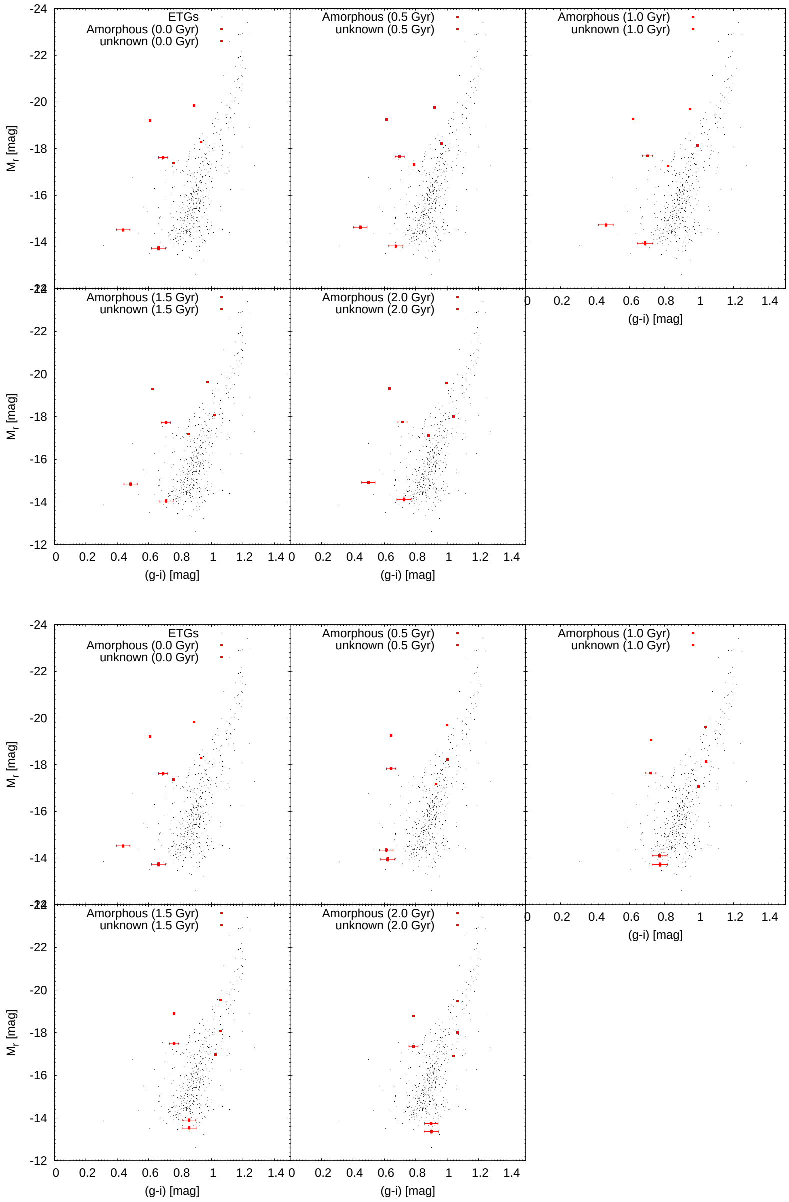

Figure 4.28: Same as Fig. 4.20, but for the unknown and Amorphous galaxies.

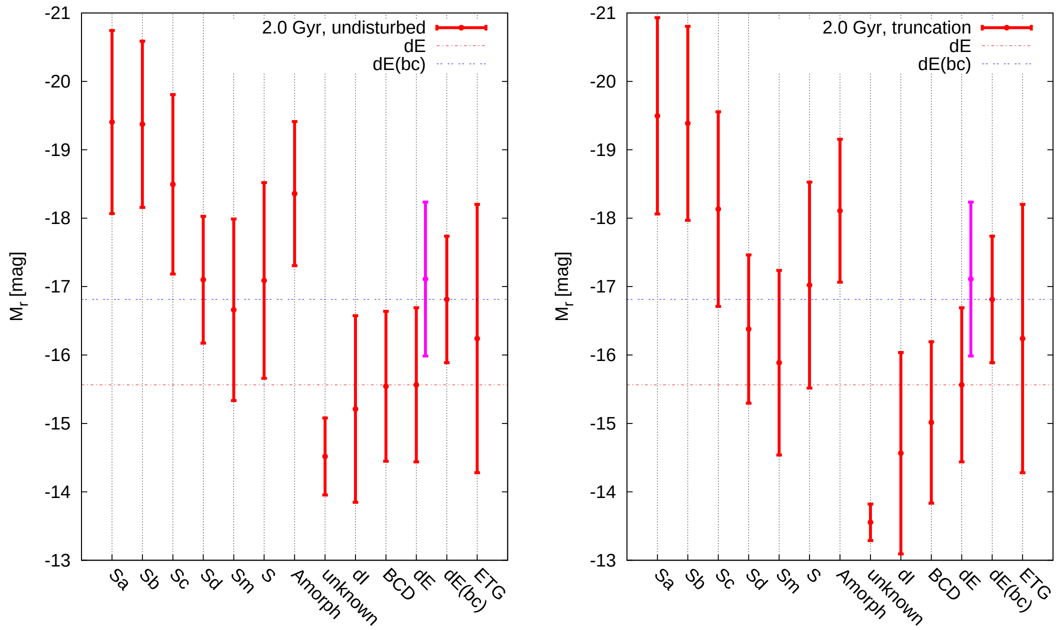

Figure 4.29: Average values of the r-band magnitudes after 2 Gyr with an undisturbed (left) and truncated (right) evolution, respectively. Error bars indicate the 1σ deviation. In case of the ETGs, dEs and dE(bc)s the averages of today's galaxies are used for comparison. The red and blue lines correspond to the averages of the dEs and dE(bc)s. Also shown in a pink bar are the averages of dEs in which discs were identified by Lisker et al. (2006b) (so called dE(di)).

the 1σ deviations.

In the case of the "unknown", "S" and Amorphous galaxies, any given average suffers from the small number of galaxies within the bin. Additionally, these types are only loosely classified and do not belong to the standard scheme of the morphological types. Therefore, these three morphological types will not be included into the discussion about the possible progenitors of early-type dwarf galaxies.

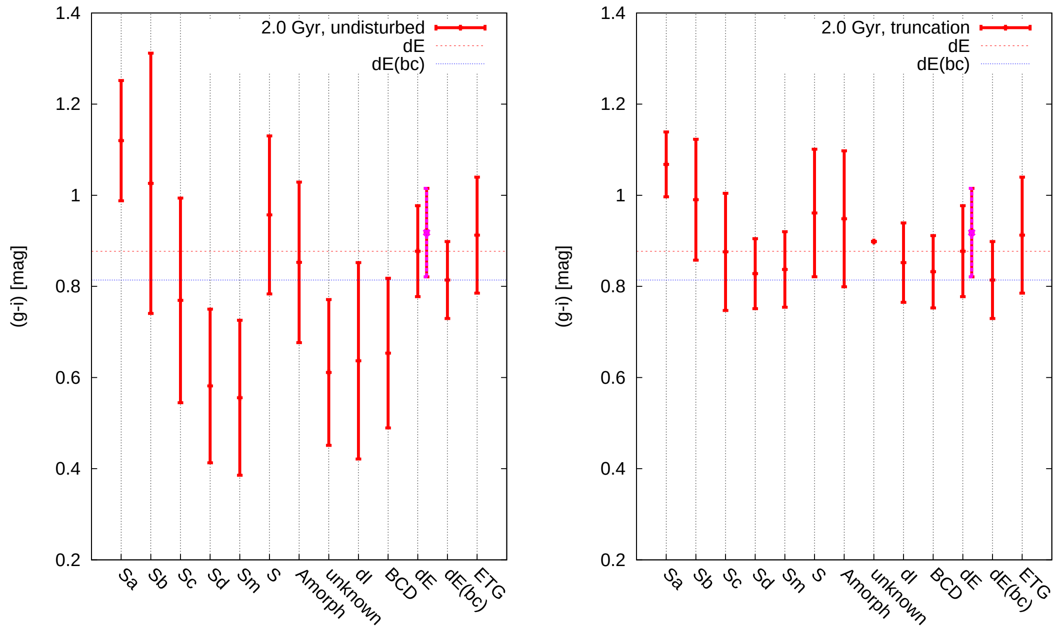

Figure 4.30: Same as Fig. 4.29, but for the (g-i)-colours.

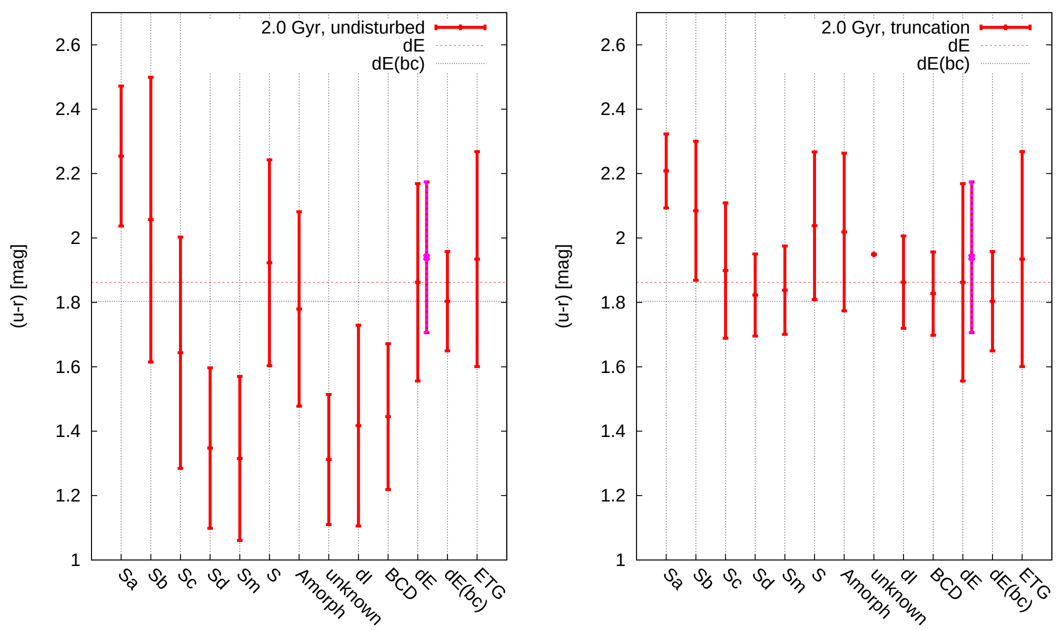

Figure 4.31: Same as Fig. 4.29, but for the (u-r)-colours.

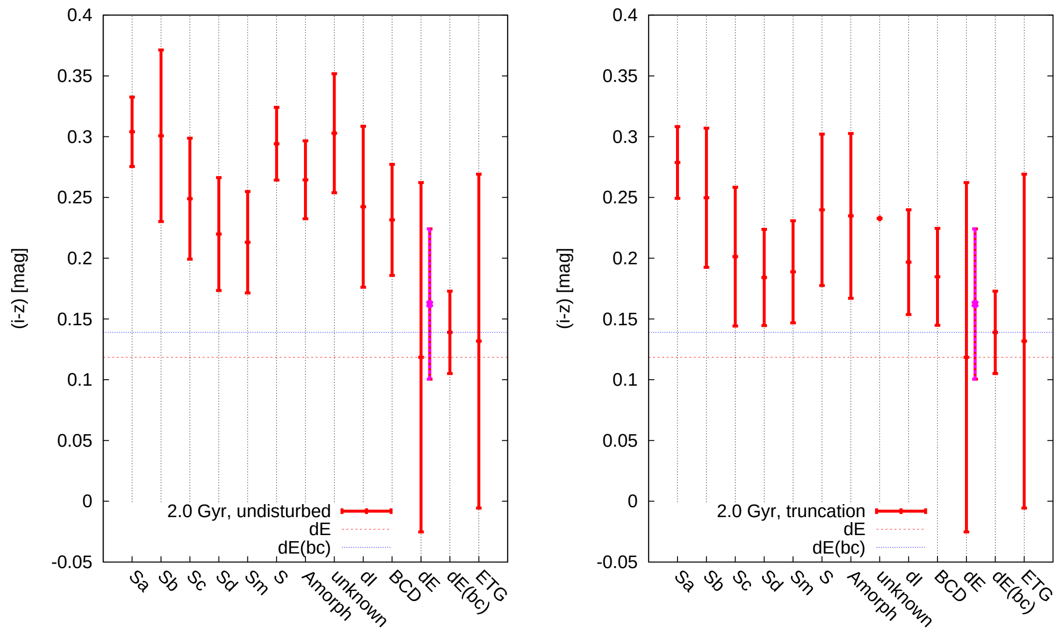

Figure 4.32: Same as Fig. 4.29, but for the (i-z)-colours.

4.4.6 The evolution of the surface brightness profiles

As seen in the last section, the r-band magnitudes and the (g-i)-colours of some late-type galaxies fit very well to the parameters of the dEs, if a truncation is assumed. However, the matching of these two parameters does not imply that late-type and early-type are structurally similar. Therefore, the investigation of the evolution of the effective radius R_{eff} and the mean surface brightness $\langle\mu\rangle_{eff}$ is of particular interest.

Since GALEV has no spacial resolution, it is not possible to simply derive the evolution of R_{eff} and $\langle\mu\rangle_{eff}$. Therefore, we divided every galaxy into four regions with 0.5, 1.0, 1.5 and 2.0 half light semi-major axis $a_{hl,r}$ in r-band (see Fig. 4.33). The shape of the galaxy ($a_{hl,r}$, ellipticity ϵ and position angle p.a.) was determined by using the method described in Chapter 3.2.4.

The different fluxes of the galaxy were measured within the area A_i with the limiting radii R_{i-1} and R_i (i= 1 . . .n). Using the corresponding magnitude of the area A_i and the radius

$$R'_i = \frac{(R_i + R_{i-1})}{2}, \tag{4.5}$$

a surface brightness profile (SBP) was created and for simplicity this SBP was fitted by an exponential law with Sérsic-index of η=1:

$$\mu(R) = \mu_0 + 1.086 \cdot \left(\frac{R}{\alpha}\right)^{1/\eta}, \tag{4.6}$$

with the central surface brightness μ_0 and the scale length α. This exponential fit was used to obtain a first-order approximation of the change of R_{eff} and $\langle\mu\rangle_{eff}$ due to the different evolutionary scenarios.

The surface brightness of the area A_i at the radius R'_i was calculated with the following equation:

$$\mu_i(R'_i) = m_i + 2.5 \cdot \log\left[\pi \cdot (R_i^2 - R_{i-1}^2)\right], \tag{4.7}$$

with the magnitude m_i of the area A_i.

The magnitudes of each area A_i in the five SDSS filters are then used as input parameters for a new GAZELLE run to simulate the evolution of the magnitudes within the different areas A_i, using the model grid of Tab. 4.1. As a result we obtain the evolution of the SBP at the different radii R'_i. The new profile was again fitted by an exponential law with η=1, resulting in new values of the central surface brightness μ_0 and the scale length α of the linear fit at different times, ranging from 13.7 Gyr (today,

t=0 Gyr) to 15.7 Gyr (t=2 Gyr). For all galaxies we simulate the undisturbed evolution and the evolution with a truncation.
Using μ_0 and a Sérsic-index of η=1, we are able to derive $\langle\mu\rangle_{\mathrm{eff,r}}$ at different times, with several equations given in Graham and Driver (2005):

$$\langle\mu\rangle_{\mathrm{eff,r}} = \mu_{\mathrm{e}} - 0.699, \tag{4.8}$$

with effective surface brightness[5] μ_{e} at $\mathrm{R_{eff}}$, defined as:

$$\mu_{\mathrm{e}} = \mu_0 + 8.327. \tag{4.9}$$

To calculate $\mathrm{R_{eff}}$, we used the scale length α of the SBP and the formula

$$\mathrm{R_{eff}} = 1.678 \cdot \alpha, \tag{4.10}$$

what finally leads to the total magnitude $\mathrm{m_{tot}}$ of the entire galaxy:

$$\mathrm{m_{tot}} = \langle\mu\rangle_{\mathrm{eff,r}} - 2.5 \cdot \log\left(2\pi \cdot \mathrm{R_{eff}^2} \cdot \sqrt{b/a}\right). \tag{4.11}$$

The axis ratio b/a was used to account for the elliptical shape of the galaxy and was determined in the course of Chapter 3.
Figures 4.34 and 4.35 show the evolution of the SBPs of two galaxies (VCC-0004 and VCC-0017) within several time steps and evolutionary scenarios. The red data points in the figures display the surface brightness at different radii $\mathrm{R_i'}$ of the galaxies, which was measured from the observations. The blue lines correspond to linear fits to the SBPs for an undisturbed evolution after 2.0 Gyr. In contrast to this, the black lines show the SBPs after 2.0 Gyr with an applied truncation. The influence to the SBP of an undisturbed galaxies is minor, resulting in a minor change in $\mathrm{R_{eff}}$. The increase of the SBP can be explained by the ongoing SF, which in case of the Sm-model will increase over the next 2.0 Gyr.
In case of the truncation the change of the SBP is considerable. The central surface brightness changes from $\mu_{0;\,0004} = 22.0$ mag/arsec^2 ($\mu_{0;\,0017} = 22.1$ mag/arsec^2) for the present SBP to $\mu_{0;\,0004} = 23.0$ mag/arsec^2 ($\mu_{0;\,0017} = 23.1$ mag/arsec^2) for the SBP in 2.0 Gyr with a truncation. Therefore, $\mathrm{R_{eff}}$ changes from $\mathrm{R_{eff;\,0004}} = 0.82$ kpc ($\mathrm{R_{eff;\,0017}} = 1.38$ kpc) to $\mathrm{R_{eff;\,0004}} = 0.87$ kpc ($\mathrm{R_{eff;\,0017}} = 1.54$ kpc). A summary of the results of each galaxy can be found in Tab. 6.6 of the appendix.

[5] Note that the *mean effective surface brightness* $\langle\mu\rangle_{\mathrm{eff,r}}$ and the *effective surface brightness* at $\mathrm{R_{eff}}$ are different quantities.

Table 4.3 shows the median variation of R_{eff} in kpc for an undisturbed evolution and a truncation, respectively. For each morphological type, the median variation of R_{eff} was calculated. Also displayed are the 1σ deviations from the medians. It has to be pointed out that the deviation are large and therefore any interpretation has to be treated with caution.

After 2.0 Gyr of an undisturbed evolution, the BCDs show a slightly decrease of R_{eff} of 3.9 %. If we apply additionally a truncation of the SFR, the BCDs became larger and therefore R_{eff} increases by 12 %.

In case of the dIs, the effective radius remains almost constant for an undisturbed evolution after a period of 2.0 Gyr. Using the truncation scenario, R_{eff} increases by about 19.4 %. However, the 1σ deviation is large with 13.4 %.

In contrast to the star forming dwarf, the spiral galaxies show a different behaviour in the evolution of the effective radius. The undisturbed spirals of type Sa, Sc and Sd show almost no change in R_{eff}, while the Sb galaxies increase by $\sim$ 6%. In case of the undisturbed Sm and "S" spirals, the change in R_{eff} is negative, meaning that R_{eff} decreases by -7.1% and -6.1%, respectively.

If we apply a truncation to the spiral galaxies, the types from Sa to Sb show an opposite behaviour than the BCDs and dIs, in a way that R_{eff} is getting smaller by -3.7% and -7.9%, respectively. In contrast to this, the change of R_{eff} for the Sc, Sd, Sm and S galaxies is positive and in the order of a few percent (<10 %). This behaviour is reasonable for the early spiral galaxies of type Sa and Sb, due to the existence of the prominent red bulge in the centre of the galaxy and the surrounding blue disc. Therefore, GAZELLE modelled the bulge with a small τ, which has almost no gas and an old stellar population, while the disc is modelled with larger values of τ. As a result, the colours of the gas abundant discs are more affected by the truncation than the inner bulge regions, which in turn explains the decrease in R_{eff} of the early spiral galaxies.

The Sm galaxies show a similar evolution of R_{eff} as the star forming dwarfs, especially in case of the BCDs. The radius of the undisturbed Sm galaxies decreases by -7.1%, but increases by 5.2% for the truncated evolution. This result for the evolution of R_{eff} for the Sm galaxies is expected, since they have similar properties as the star forming dwarf galaxies.

The "unknown" galaxies show a slightly change in R_{eff} in case of an undisturbed evolution, but show the largest change of R_{eff} of the entire morphological sequence, with 28.9 %. However, it should be kept in mind that these results are based on only a small number of galaxies, which could strongly influence the statistic.

The effective radius of the Amorphous galaxies is almost constant for an undisturbed evolution and is only noticeable in the fourth post decimal position. In case of a truncation, $R_{\rm eff}$ increases by 13.5%. But as already mentioned for the S and unknown galaxies, these findings only have a low number statistic.
In Tab. 4.4, the median variations of $\langle\mu\rangle_{\rm eff,r}$ are shown in the same manner as for Tab. 4.3. In this table a negative change in $\langle\mu\rangle_{\rm eff,r}$ implies an increase of the surface brightness (SB) and vice versa for positive changes.
The BCDs show a small decrease of the surface brightness for the undisturbed evolution, while in the case of a truncation the SB decreases by about 0.9 mag/arcsec^2. The dIs show an opposite behaviour, with an increase of the SB for the undisturbed evolution by about -0.6% and a decrease by 3.5% in case of a truncation.
The SB for the spirals of type Sa and Sb decreases for an undisturbed evolution, while the SB for Sc, Sd, Sm, S and unknown galaxies increases, and vice versa for the truncation. Overall, the differences between the SB of an undisturbed and truncated evolution are minor – in all of the case below 1 mag/arcsec^2 – for all morphological types.
Figure 4.36 compares the results of the SBP analysis of the different morphological types and in addition the results of today's dEs, dE(bc)s, ETGs and LSB-components (see Chapter 2) are shown. To obtain the change of the effective radius and mean effective surface brightness of today's late-type galaxies due to the undisturbed and truncated evolution, we use the information of Tabs. 4.3 and 4.4, and applied the percentage terms of the changes of the effective radius ($\Delta R_{\rm eff}$) and mean effective surface brightness ($\Delta\,\langle\mu\rangle_{\rm eff,r}$). For instance, the dIs within the Virgo cluster have an average observed effective radius of $R_{\rm eff}$ = 1.6 kpc and change their radius after 2 Gyr due to a truncation by about 19 %, which in turn results in a new effective radius of $R_{\rm eff,2Gyr,trunc}$ = 1.9 kpc.

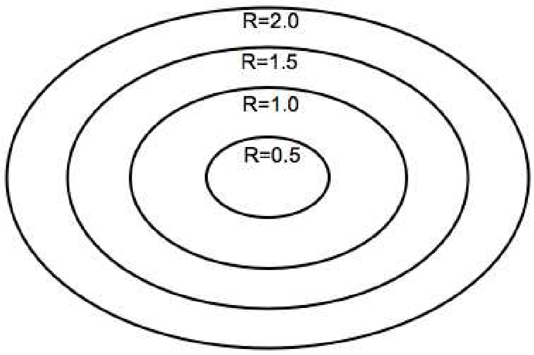

Figure 4.33: Schematic division of the SBP.

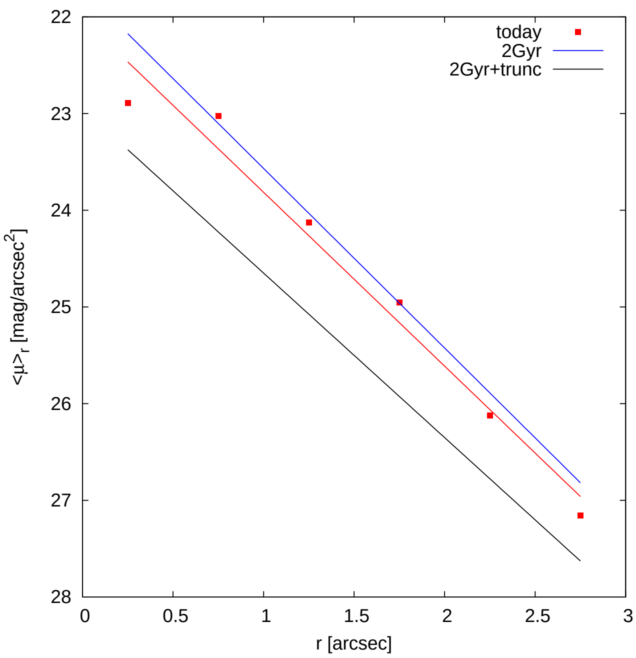

Figure 4.34: Evolution with time of a SBP of galaxy VCC-0004.

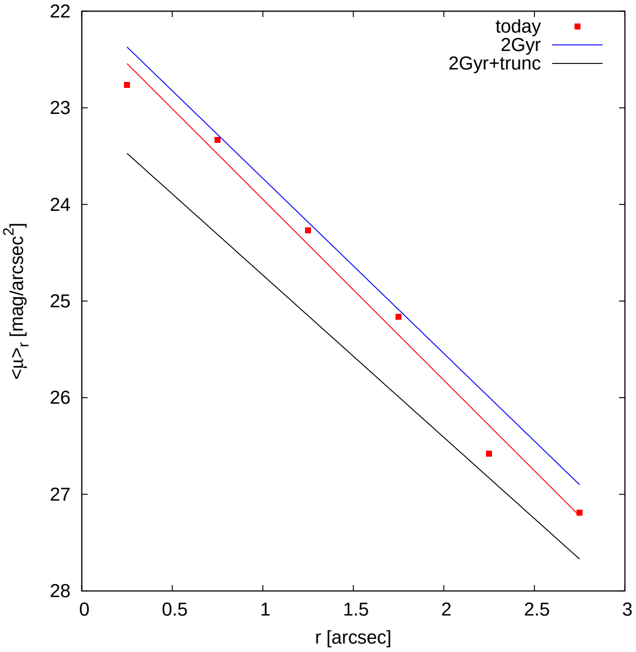

Figure 4.35: Evolution with time of a SBP of galaxy VCC-0017.

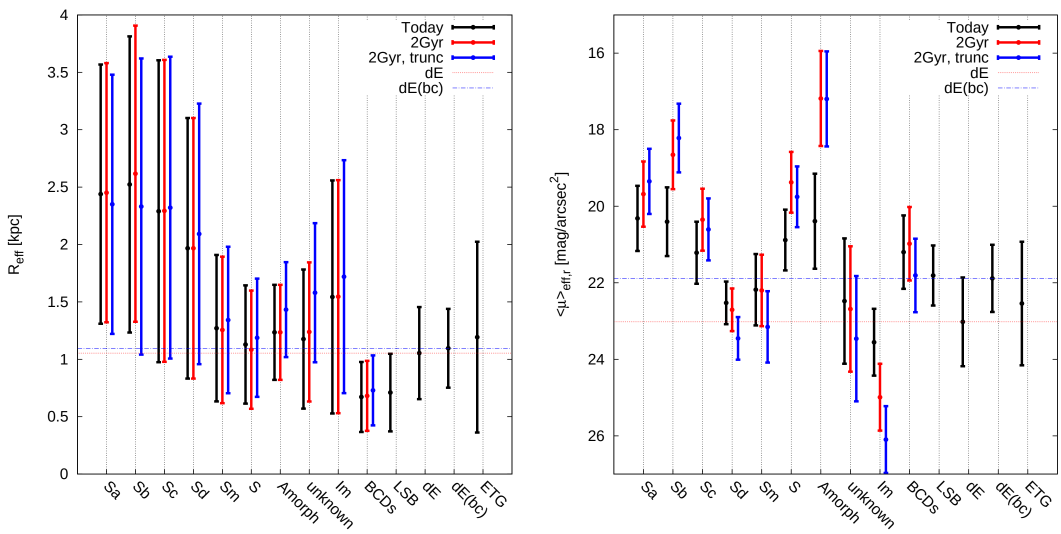

Figure 4.36: Effective radius R_{eff} and mean effective surface brightness $\langle\mu\rangle_{eff,r}$ at different evolutionary stages of the morphological types. Today's values with the 1σ deviations are displayed by a black bar. The red and blue bars correspond to the same morphological types but after an undisturbed evolution after 2 Gyr (red bar) and after 2 Gyr with an additional truncation (black). Furthermore, today's results of the ETGs, dEs, dE(bc)s and LSB-components are displayed, but without any time evolution.

Table 4.3: Change of R_{eff} after 2 Gyr for undisturbed evolution and evolution with truncation.

Type	Number	$\Delta R_{eff,2Gyr}$[kpc]	σ[%]	$\Delta R_{eff,2Gyr,trunc}$[kpc]	σ[%]
BCDs	33	-0.021 (-3.9 %)	5.046	0.064 (12.0 %)	6.061
Im	87	0.005 (0.4 %)	11.095	0.260 (19.4 %)	13.394
Sa	35	0.008 (0.3 %)	19.846	-0.167 (-6.0 %)	17.507
Sb	17	0.125 (5.8 %)	21.617	-0.206 (-9.7 %)	19.842
Sc	79	0.029 (1.3 %)	19.456	0.043 (1.9 %)	16.970
Sd	21	0.000 (0.0 %)	12.180	0.204 (9.6 %)	11.380
Sm	26	-0.116 (-7.1 %)	10.255	0.085 (5.2 %)	10.898
S	5	-0.087 (-6.1 %)	10.872	0.054 (3.8 %)	10.245
unknown	3	0.046 (8.6 %)	3.993	0.153 (28.9 %)	6.924
amorph	5	0.000 (0.0 %)	7.247	0.247 (13.7 %)	7.033

Table 4.4: Change of $\langle\mu\rangle_{eff}$ after 2 Gyr for undisturbed evolution and evolution with truncation.

Type	Number	$\Delta\langle\mu\rangle_{eff,2Gyr}$	σ	$\Delta\langle\mu\rangle_{eff,2Gyr,trunc}$	σ
BCDs	33	0.122 (0.6 %)	1.342	0.915 (4.3 %)	1.316
Im	87	-0.151 (-0.6 %)	0.891	0.830 (3.5 %)	0.950
Sa	35	0.294 (1.4 %)	0.720	-0.033 (-0.2 %)	1.042
Sb	17	0.143 (0.7 %)	0.728	-0.305 (-1.5 %)	1.078
Sc	79	-0.018 (-0.1 %)	0.762	0.230 (1.1 %)	1.021
Sd	21	-0.085 (-0.4 %)	0.504	0.615 (2.7 %)	0.740
Sm	26	-0.290 (-1.3 %)	0.912	0.603 (2.7 %)	0.986
S	5	-0.087 (-0.4 %)	0.831	0.302 (1.4 %)	0.841
unknown	3	-0.119 (-0.5 %)	1.733	0.631 (2.7 %)	2.130
amorph	5	0.175 (0.9 %)	1.245	0.188 (0.9 %)	1.201

4.5 Discussion

4.5.1 Classification by models

In Chapter 3 the galaxies were reclassified based on their morphology and distribution in the parameter-space. In Fig. 4.12, there are four Sa galaxies that are modelled with $\tau = 25$ Gyr. This value of τ is relatively large for Sa galaxies, since they commonly formed their stellar content within the first Gyrs (Sandage, 1986; Gavazzi et al., 2002). Interestingly, when using the number distribution of the morphological types based on the original morphological types of the VCC, then also misclassified[6] galaxies are included, which in turn should be noticeable in the results of the SEDs. Apart from the check of the classification with the results of the photometry, we are now able to check the classification on the basis of the SED fitting routine.

In the course of Chapter 3, three out of four conspicuous Sa galaxies were reclassified as Sc, Sm and dE(bc), respectively. This finding is also supported by the analysis of the SED fitting. For example, the SED of VCC-0015 on the left hand side of Fig. 4.37 – which was initially classified as Sa galaxy by the VCC and GOLDMine – shows large differences from the SEDs of other Sa galaxies. From its morphology and position in the parameter-space, VCC-0015 was reclassified as Sc galaxy and indeed the SED supports this reclassification to a later spectral type.

Only one Sa galaxy (VCC-0979) is still puzzling. The SED on the right panel of Fig. 4.37 shows that the r, i and z filters have similar properties as the other SEDs of Sa galaxies in the same wavelength range. However, the u and g filters do not fit to the SEDs of this spectral sequence of the Sa galaxies. The inspection of the gri-SDSS image in Fig. 4.38 reveals a disc galaxy with apparent blue regions in the core. The blue colours of the regions point to an ongoing or recent star formation, which therefore would explain the enhanced magnitudes in the u and g filter. From this perspective, it also points to a misclassification of VCC-0979, but the exact type is still unknown.

4.5.2 Models vs. observation

Looking at the results of our analysis in the CMDs of Figs. 4.20 to 4.28, one realises – especially in the case of the truncation – that the models are too simple. When modelling the galaxies with a truncation event, the galaxies fall on discrete lines in the

[6] In this context *misclassified* means that the classification by blue sensitive photo-plates differs from the classification by our parameter-space.

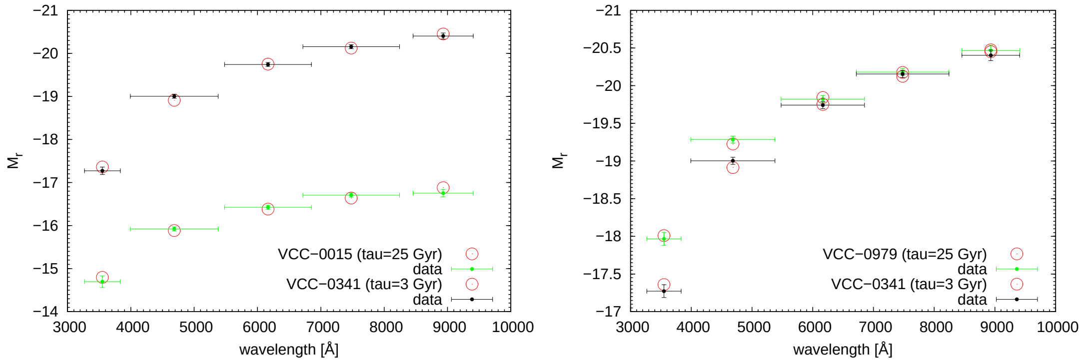

Figure 4.37: Comparison of the SEDs for Sa galaxies, which were modelled with different values of τ. The differences in the SEDs indicate a misclassification in the case of VCC-0015 (left) and VCC-0979 (right).

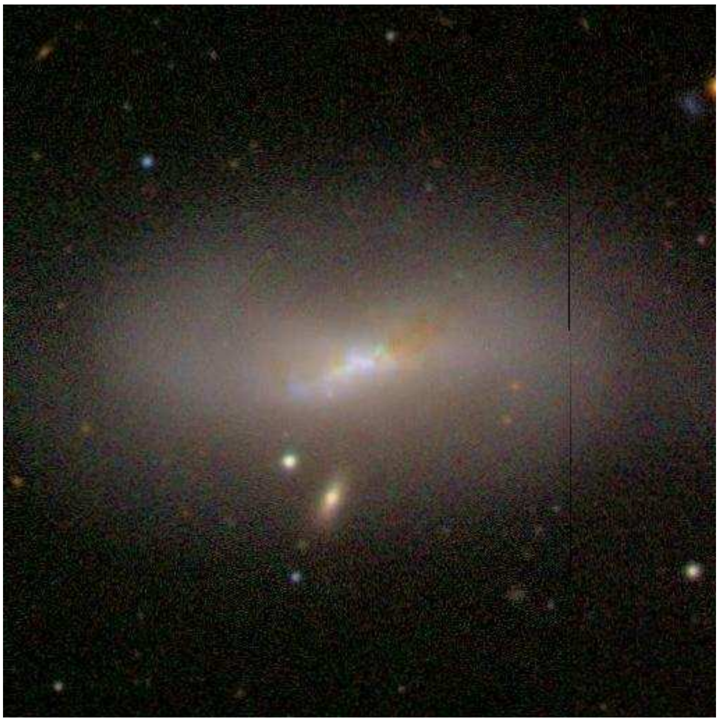

Figure 4.38: gri-SDSS image of VCC-0979, which shows blue region in the centre of the galaxy.

CMDs, which therefore gives an artificial impression.
As e.g. shown by McQuinn et al. (2010a) and McQuinn et al. (2010b), the SFHs of galaxies do not have to be smooth curves like the ones of our study. Also the assumption that the truncation time scale is constant for all different morphological types might be too simple. For instance, the ram pressure stripping event, which is responsible for the truncation, is not only able to significantly decrease the SFR of a galaxy, but it is also able to induce new star formation (Gavazzi et al., 1995; Fujita and Nagashima, 1999). Thus, the decreasing SFR will be a superposition a truncation and star formation, which may increase the truncation time scale to values with $\tau_{\rm trunc} > 150$ Myr. However, a larger $\tau_{\rm trunc}$ will result in bluer (g-i)-colours for the galaxies after 2 Gyr, which in turn also influences the comparison with dEs.
Another simplification of the models concerns the gas content of the galaxies after the truncation. In case of a truncation, GALEV just decreases the SFR but does not "physically" create a gas-poor galaxy. Therefore, the behaviour of the gas metallicity of GALEV and the reality are different. The metallicity of the remaining gas of a real galaxy would increase due to the enrichment by the yields of SNe after the truncation event, which is not the case for the GALEV models.
The evolution of BCDs was modelled by a SFH that has one single strong starburst, superposed on a "normal" SFH given by Equation 4.1. However, it is commonly believed that the SFH of BCDs shows oscillation in the SFR, from episodes with short and strong bursts to long quiescence phases (Thuan, 1991). Our models for the BCDs do not account for the bursty evolution of the SFR, but it was also shown that the influence of a strong burst is less and almost not visible in the (g-i)-colours after several Gyr (see Fig. 4.7). Thus, the induced errors by this simplification of the SFH of BCDs may have a minor effect on the overall evolution of the photometric parameters of the BCDs.
Another issue one has to consider is the mass dependence of mechanisms, which remove the gas from the late-type galaxies. Following Mo et al. (2010), the binding force, which prevents the gas to be removed from a disc galaxy, is proportional to the mean surface density of the ISM and the mean mass density of the disc. If two galaxies move through the cluster with the same velocity[7], the one with the lower density is more influenced by the stripping event. In case of a starvation the galaxy will proceed its SF over a longer time scale due to the still existing gas reservoir in the disc, which

[7]Except for a face-on galaxy, the inclination angle between the galaxy and ICM only plays a minor role (Quilis et al., 2000; Marcolini et al., 2003).

again increased τ_{trunc}. Therefore, also the results of simulations of spiral galaxies in the Virgo cluster (van Gorkom, 2004; Fumagalli and Gavazzi, 2008; Vollmer et al., 2012) should be included in the treatment of the environmental effects, which act on the late-type population. However, an increase of τ will only affect the parameters in the arbitrarily chosen time span of 2 Gyr. If we take much larger time spans of about 4 Gyr or even longer, then the environmental effects will also remove the remaining gas. Thus, we do not have to ask *if* the derived parameter-space is reached by different sets of τ_{trunc}, but *when* the parameter-space is reached.

Also related to the mass of the galaxies is the completeness limit of the VCC and the applied magnitude cut-off ($M_B \leq -13.09$ mag). Especially in the case of the dI one has to account for this when computing average model masses. Due to the magnitude cut-off, low surface brightness dIs are not included in our study, which could influence the derived average model masses.

The evolution of the SBPs of the late-type sample shows that an undisturbed evolving galaxy will only slightly change its effective radius within the next 2.0 Gyr. However, in the case of a truncation, which in turn reduces the SFR, the effects become more prominent for the star forming dwarf galaxies of the type BCD and dI. For these star forming dwarfs the effective radius does indeed change within 2.0 Gyr, but only on the order of a few percent. However, these calculations are only a first-order approximation, since all SBPs are approximated by an exponential law with a Sérsic-index of η=1, which definitely does not describe the real shape of all galaxies in the sample. Thus, a possible improvement in the fitting procedure of the SBPs would be the inclusion of the Sérsic-index as a free parameter in the fitting procedure of the SBPs.

In agreement with our study, Boselli et al. (2008) also stated that the effective radius is almost constant at larger wavelength when the galaxies evolve with time. To increase our understanding of the evolution of the effective radius, but also of the other parameters, detailed simulations are need for the entire morphological sequence of late-type galaxies. Such studies on the effect of the environment on spiral galaxies in the Virgo cluster already exist (e.g. Vollmer, 2009), but further studies, including the low mass galaxies like dIs and BCDs, are desirable in the future.

4.5.3 The possible progenitors of dEs

Using all the derived results of our analysis, we are finally able to investigate the possible progenitors of today's dEs by comparing the structural properties of the

different morphological types. In Chapter 2 it was shown that the parameters of the BCDs — when the contribution of the starburst region is subtracted and only the old stellar population of the LSB-component is taken into account — fit very well to the population of the dEs. Furthermore, we found that the LSB-components of BCDs are on average more compact and fainter than early-type dwarf galaxies with a blue core. In comparison to the LSB-components, the dIs in Virgo are less compact and have a lower surface brightness, which is noticeable by a clear separation between these two morphological types in the $M_r - R_{eff} - \langle\mu\rangle_{eff,r}$ parameter-space. Also in terms of the spatial distribution within the Virgo cluster of the BCDs and dEs, there is a probability that these two types are related to each other.
But what about the other morphological types in the Virgo cluster and how will they look like in the future?
The time evolution of the late-type galaxies by the means of GALEV/GAZELLE models (Figs. 4.20 to 4.28 and Fig. 4.36) showed that the structural parameters (R_{eff}, (g-i) and $\langle\mu\rangle_{eff}$) of the late-types partly fit to the ones of the early-type (dwarf) galaxies for an undisturbed evolution of two Gyr. Since the late-type galaxies are located within the cluster environment, there are several forces acting on theses galaxies, which may transform them. Therefore, a truncation of the SFR was applied, which simulates the removal of gas due to forces like ram pressure stripping. The results of the GAZELLE runs showed that the structural parameters of late-type galaxies become even more similar to the ones of the ETGs, but this finding depends strongly on the morphological type. The early spirals of type Sa and Sb are in many respects not comparable to the dEs, since they are too bright in the r-band magnitude, have too large effective radii and too high surface brightness. As expected, we can conclude that the descendants of Sa and Sb galaxies will not share the same parameter-space as today's dEs.
Looking at the spirals of type Sc and Sd, we found more overlap with dEs in Virgo. The r-band magnitude and (g-i)-colours of the Sc and Sd galaxies are between the ones of the dEs and the dE(bc)s. Compared to the dEs, the Sc and Sd galaxies are rather large in radii and have a relatively high surface brightness. However, the overlap within the 1σ deviations of the Sc and Sd to the ones of the dEs and dE(bc)s showed that they are not completely different according to our parameter-space.
Among the spirals, the Sm galaxies show the best overlap with the dEs in the entire parameter-space, even though the radii are slightly larger.
Using the metallicity sensitive (i-z)-colours, we found that there are differences between the ETGs and the late-type galaxies after two Gyr (with and without truncation),

which may points to different chemical abundances (see Fig. 4.32). However, looking in more detail at the early-types in Fig. 4.32, one realises that the Sd and Sm galaxies are within the 1σ deviations of the (i-z)-colours of the ETGs.

The parameter-space of today's dI galaxies is in agreement with the dEs, but the evolution with time and the influence of the cluster environment change this behaviour. After a truncated evolution of two Gyr, the (g-i)-colours of the dIs are in the same region as the dEs. However, the dIs become fainter than the dEs and also the surface brightness is getting too low, even when accounting for the 1σ deviations of both populations. Therefore, only the faintest dEs with $\langle\mu\rangle_{\mathrm{eff,r}} \approx 26$ mag/arcsec^2 have the possibility to be related to the dIs. These faint dIs might be related to the dSph galaxies, which are treated as dEs in our analysis. However, Grebel et al. (2003) showed that the mean stellar metallicity of dSph galaxies is higher than that of the dIs (see also e.g. Richer and McCall, 1995; Richer et al., 1998, for other metallicity estimates for dSphs and diffuse ellipticals), pointing to differences in the SFH of these two types. The low surface brightness field dIs of the sample of Thuan (1985) also show "mutually exclusive metallicity ranges"[8] compared to the Virgo dEs. The metallicity sensitive (i-z)-colours of Fig. 4.32 show that the Virgo dEs and dIs do not differ extremely and that the (i-z)-colours of the dIs are within the 1σ deviations of the dEs. Therefore, we are not able to give such a strong statement as Thuan (1985) regarding the different metallicities. The study of Bothun et al. (1986) also supports our findings, since their Virgo dIs have to fade by $m_B = 1.5$ mag to have the same photometric properties as the dEs. Consequently, this would lead to very low surface brightnesses, which are not comparable with the Virgo dEs. Hence, our results and the above mentioned studies indicate that there are no evolutionary connections between dIs and dEs (+dSph) in the Virgo cluster, which is in contrast to other early studies (e.g. Lin and Faber, 1983; Kormendy, 1985).

In summary, we found that there are some morphological types among the late-type galaxies that share a similar region in the parameter-space as the dEs after a truncated evolution of two Gyr within the Virgo cluster. The most promising types are the late spirals of the type Sd and Sm, and the LSB-components of the BCDs, when star formation has ceased. Apart from the *photometric* and *structural* properties of the late-type and early-type galaxies of our study, one also has to consider the intrinsic kinematics of the galaxies. Galaxies with an ordered motion of their stars and/or gas will not lose their angular moment on short time scales. Therefore, the progenitors

[8]Citation from Thuan (1985).

must have similar kinematical properties as today's ETGs. In the last years, studies of dEs in the Virgo cluster (e.g. Geha et al., 2003; de Rijcke et al., 2005; Chilingarian, 2009; Toloba et al., 2011) found that parts of the dE population indeed have kinematics that point to rotational flattened or rational supported dEs (see Lisker, 2012, for a recent review). Interestingly, Toloba et al. (2011) found the tendency of two kinematically different populations of dEs in Virgo. The ones at large cluster centric radius are rotational supported and have younger ages, while dEs in the core of Virgo are pressure supported and older. Furthermore, other studies found dEs in the Virgo cluster that are rotational supported and contain HI gas (e.g. Pedraz et al., 2002; Conselice et al., 2003; van Zee et al., 2004) and together with the results of Lisker et al. (2006b), who found dEs with disc features, it points to a possible transformation of gas abundant late-type galaxies into dEs, since the dEs still have the imprints of the late-type galaxies.

Harassment-simulations of model late-type dwarf disc galaxies in Virgo by Smith et al. (2010) showed that the harassed discs are able to form spiral structure, which was also confirmed by Lisker et al. (2007) in Virgo dEs from the SDSS. However, Smith et al. (2010) also pointed out that the initial model galaxies were smooth and featureless and therefore not easily comparable with typical late-type galaxies of our sample. As seen in Chapter 2, there is one BCD (VCC-0213) in the Virgo sample that shows spiral features and furthermore, these spiral arms show a colour gradient from left to right[9], which could be interpreted as a sign of interaction with the dense cluster environment.

Another important and interesting question is whether the late-type galaxies will lose their entire gas reservoir when moving through the Virgo cluster. The GALEV/GAZELLE settings used here do not account for gas loss due to external forces — which can be achieved by the inclusion of gas outflows — therefore we consult other studies. The study by Chung et al. (2007) on ~ 50 VLA HI Virgo spirals showed that seven of them, which are located at intermediate cluster centric radii, have extended HI tails, indicating the influence of the cluster environment (especially RPS). Furthermore, a subsequent study by (Chung et al., 2009) showed that galaxies at a small distance from the core of the Virgo cluster have HI discs that are smaller than the stellar disc. N-body simulations by Vollmer et al. (2001) also showed that galaxies will lose gas when moving through the core region of Virgo, however, the star formation will not completely stop and furthermore, parts of the gas, which is removed by RPS, can be re-accreted by the galaxies and may amount for up to 10%.

Therefore, the above described effects of harassment and RPS are insufficient to create

[9] The spiral arm on the left is bluer than the right one (see lower panel of Fig. 2.16)

the “red and dead” gas-poor dE. Interestingly, a recent study by Hallenbeck et al. (2012) (see also Conselice et al., 2003) found gas-bearing Virgo dEs, which have HI and stellar masses similar to BCDs and dI. Thus, we may also have to change our view of a “red and dead” gas-poor dE and have to focus on the structural properties of these HI dEs. But, from our analysis of Chapter 2 we also saw that dEs with a blue core do not share the same properties in the $M_r - R_{eff}$ parameter-space as the LSB-components of the Virgo BCDs.

If the late-type galaxies of the type BCD, Sd and Sm will completely (which is highly unlikely) evolve into a galaxy type that is comparable to the dE population of Virgo, it also interesting to ask whether the number distribution of these “new dEs” is in the same order as the one of today’s dEs. Only accounting for galaxies in the outer part of Virgo with a distance to M87 of $D_{M87} > 0.6$ Mpc (see Fig. 2.24 of Chapter 2 and Fig. 3.8 of Chapter 3), we found that both populations are almost equally numerous (late-types = 25 and dEs = 27). If we also take into account *parts* of the Sc galaxies and dIs then the late-types outnumber the dEs. However, if the number distribution of the entire Virgo cluster (see Fig. 3.3 of Chapter 3) is used then the late-types (Sc+Sd+Sm+BCDs+dI) are severely outnumbered by the dEs (amount of dEs ~400). Therefore, a formation of the *entire* dE population from in-falling late-type galaxies is not possible. Conselice et al. (2001) found that parts of the dEs in Virgo are not formed in-situ, but originate from in-falling late-types, which therefore supports our findings from a different point of view.

4.6 Outlook

4.6.1 GALEV in the zoom

At the time of writing the galaxies of the sample are treated as 1-zone objects without any change with increasing galaxy radius. However, it was shown that galaxies do change their appearance with radius. Examples are the spiral arms in late-type galaxies, but also dEs with a blue cores.

As a new feature, which is in the testing phase, GALEV/GAZELLE is now able to analyse each galaxy pixel by pixel. The procedure is the same as for the entire galaxy, but now for each single pixel or pixel area (e.g. 4x4 pixels) a best fitting model is determined by using the same model grid as for the entire sample (see Tab. 4.1). From each morphological class a median galaxy was chosen and analysed by the pixel-pixel analysis. This was done by using the results from Chapter 3.4.3 to minimise the scatter due to a misclassification. Table 4.5 summarises the galaxies used for this analysis.

Table 4.5: Subsample of different morphological types.

VCC number	Morphological type
VCC-0030	dI
VCC-0048	Sd
VCC-0641	BCD
VCC-0679	Sm
VCC-0938	Sc
VCC-1188	Amorphous
VCC-1290	Sb

As a result of our analysis we obtain spatially resolved maps of stellar mass and SFR density. Some of the preliminary results are shown in Fig. 4.39 for a small subsample of our galaxies. To create these maps we broke down each of the fits files into resolution elements of 5x5 pixels and fitted the resulting SEDs with GALEV simple stellar populations models, yielding the light-weighted stellar population age, stellar mass and extinction for each element. By comparing the stellar mass maps of the dEs with ones of e.g. dIs, we are able to conclude if both morphological classes have the same stellar mass distribution. In this case it is obvious that the dEs have much higher surface mass densities as the dIs. It is also possible to conclude how the star formation rate of a dI has to change to fit the mass regime of the dEs.

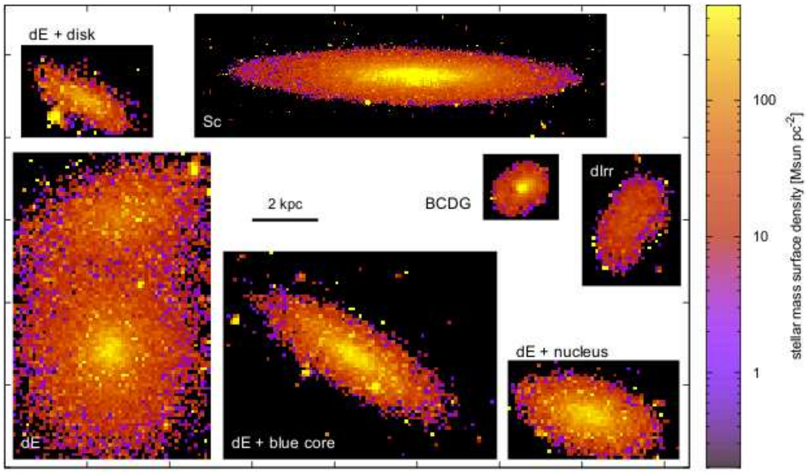

Figure 4.39: Stellar mass surface density maps of a sample of Virgo galaxies.

Another example is shown in Fig. 4.40 for the Sb galaxy VCC-1290. The left panel displays the age map and the right panel the dust reddening map. Obvious features in these maps are the younger ages of the spiral arms and the old stellar population of the bulge. Furthermore, the bulge region is less influenced by dust reddening than the surrounded disc. Figure 4.41 shows the age maps of a BCD and Sm galaxy. Interestingly, these two galaxies have a quite similar age distribution, making further and more detailed investigations worthwhile.
In a next step the results of the pixel-by-pixel analysis will be extended to the entire sample. Furthermore, the impact of the truncation event on the stellar mass and SF density can be investigated in more detail.
To develop further, it might be also possible in the future to refine the truncation and RPS/starvation physics to account for the radius dependence of these processes on disc galaxies.

4.6.2 New observation

For the pixel-by-pixel analysis of the galaxy using GALEV/GAZELLE, the resolution of the detector and the quality of the observational conditions (seeing) at the observatory are one of the crucial limitations. Since the resolution of the SDSS is low (0.396 arsec/pix) and the median seeing is about 1.6 arcsec, new observations of Virgo galaxies were performed by us (H.T. Meyer and R. Kotulla), using the 3.5 m WIYN

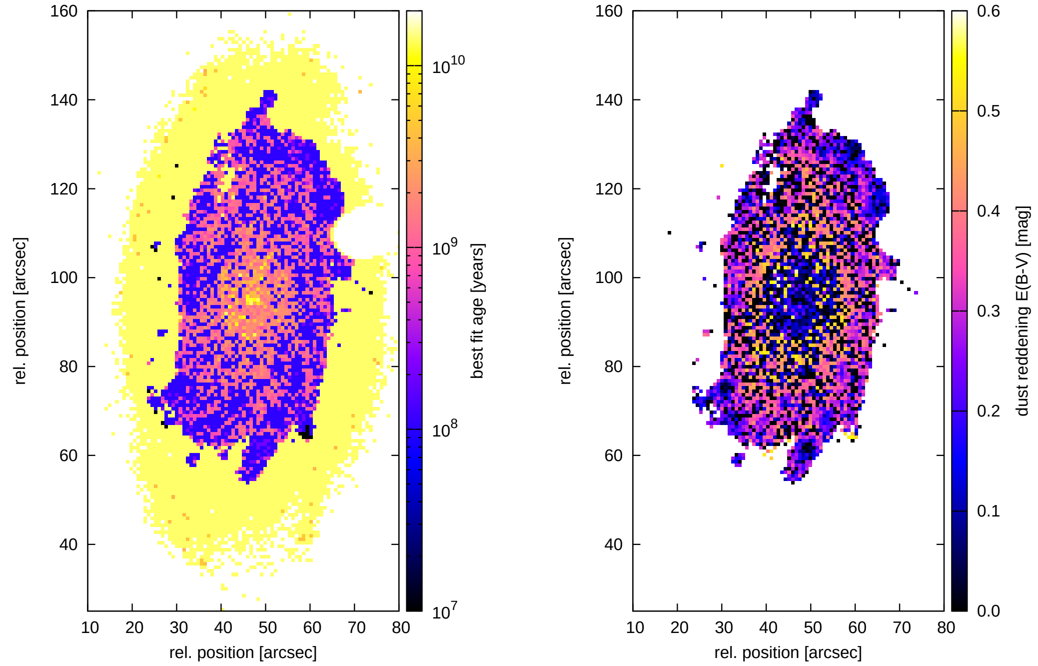

Figure 4.40: Pixel-by-pixel analysis of VCC-1290. Left: age map; Right: dust reddening map.

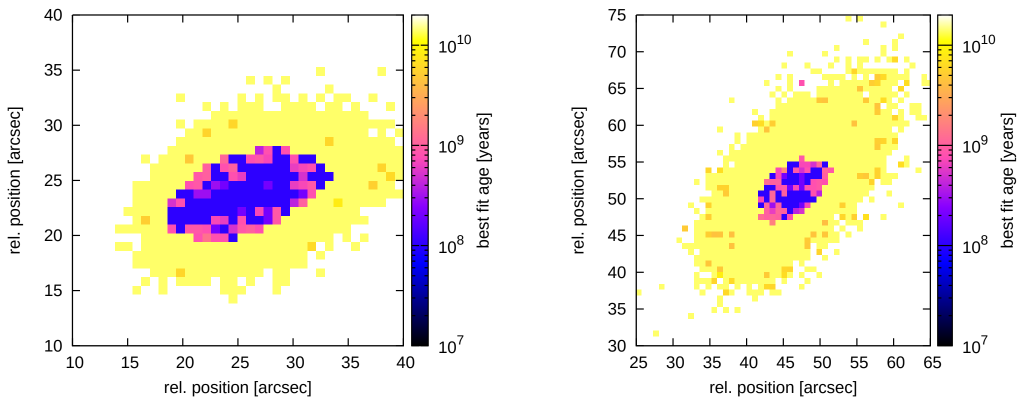

Figure 4.41: Pixel-by-pixel analysis of the BCD VCC-1290 (left) and the Sm galaxy VCC-0679 (right). Shown are the best fitting ages of the galaxies.

telescope[10] at the Kitt Peak National Observatory (KPNO, USA). The targets of the observing run are summarised in Tab 4.6. In the first run the galaxies were observed for 2 nights using the WIYN Mini-Mosaic Imager (MIMO), which has a resolution

[10]Abbreviation for “Wisconsin Indiana Yale NOAO” telescope.

of 0.14 arsec/pixel and a field of view of 9.6x9.6 arcmin. The used filters for the first observing run were the Harris UBR filters (central wavelenghts: 3640 Å; 4304 Å; 6394 Å)[11].

The second run was performed with the WIYN High Resolution Infrared Camera (WHIRC) and was scheduled for one night. WHIRC has a resolution of 0.1 arsec/pixel and a field of view of 3.3x3.3 arcmin. In this run the galaxies have been observed in the infrared, using the J filter (1.250 μm), H filter (1.651 μm), and K_s filter (2.168 μm)[12]. Owing to the fact that the observation was performed in H and with the superb observing conditions, an average seeing of 1.0 arcsec and below would be possible. However, due to variations in the weather conditions, this seeing was unfortunately not achieved for the entire sample of our observation.

The combination of the resolutions of the instruments and the superb observational conditions at Kitt Peak allows a detailed study of a set of Virgo galaxies, which will be published in an upcoming paper together with R. Kotulla. At the time of writing the data of these observing runs are partly reduced and are applied to first tests with the GALEV/GAZELLE-code.

Table 4.6: Subsample of different morphological types that was observed with the WIYN telescope. Shown are the used filters and the exposure times in each filter.

VCC number	Observed filter	Exposure time in UBRJHK [sec]
VCC-0001	U,B,R	1200 / 600 / 600 / - / - / -
VCC-0087	H	- / - / - / - / 2000 / -
VCC-0226	U,B,R,H,K	1200 / 600 / 600 / - / 2000 / 4320
VCC-0241	J,K	- / - / - / 80 / - / 2640
VCC-0849	U,B,R,K	1200 / 600 / 600 / - / - / 2720
VCC-1488	U,B,R,J,K	1200 / 600 / 600 / 2560 / - / 2320
VCC-1507	U,B,R,J,K	1200 / 600 / 600 / 480 / - / 2560
VCC-1566	U,B,R,J,K	1200 / 600 / 600 / 660 / - / 2560
VCC-1789	U,B,R,J,K	1200 / 600 / 600 / 60 / - / 2560
NGC-4565	J,K	- / - / - / 3255 / - / 80

[11] http://www.wiyn.org/Observe/wiynfilters.html.

[12] http://www.noao.edu/kpno/manuals/whirc/filters.html.

Chapter 5 Conclusions and outlook

5.1 The possible progenitors of early-type dwarf galaxies

In Chapter 2 the structural properties of the Blue Compact Dwarf Galaxies (BCDs) in the Virgo cluster were analysed by a special algorithm. This algorithm accounts for possible irregularities and multiple star forming regions of a BCDs and enables us to investigate the underlying old stellar population through the creation of surface brightness brightness profiles (SBPs). The SBPs were decomposed into the contribution of the starburst and old stellar component, which is also called low surface brightness (LSB-) component or host galaxy. With this decomposition algorithm we are in the excellent position to analyse only the parameters of the underlying LSB-component, which contributes mainly to the galaxy mass. It turns out that the parameters of the LSB-components of the BCDs and the ones of compact Dwarf Ellipticals (dEs) are in good agreement. Regarding the used parameter-space ($M_r - (g - i) - R_{eff} - \langle\mu\rangle_{eff}$) of this thesis, we concluded that BCDs are the possible progenitors of compact dEs in the Virgo cluster.

Apart from the BCDs, also all other late-type galaxies of the Virgo cluster were analysed in the course of Chapter 3. The parameters of the different morphological types of the Virgo Cluster Catalog (VCC) were reviewed and if necessary reclassified. As expected, the parameters of the late-type galaxies show significant differences to the dEs. However, the morphological class of the Irregular Galaxies (dI) and the late spirals of type Sd and Sm show some similarity to the dEs according to the parameter-space.

These differences between late- and early-type galaxies are not surprisingly, but the most interesting question is how the late-type galaxies will look like in several billion years? To answer this question, evolutionary synthesis models of GALEV and GAZELLE are used, which model the evolution of galaxies based on a set of input parameters, like a star formation history and our observed magnitudes of Chapter 3.

Since the late-type galaxies are members of the Virgo cluster, it is crucial to take into account the influence of the dense cluster environment, which is able to remove the gas from a galaxy and therefore halting the star formation on very short time-scales (a so called truncation).
In Chapter 4 of this thesis, we found that also the Sd and Sm galaxies, after two Gyr of a truncated evolution, are located in the same parameter-space as the dEs of the Virgo cluster. The dIs, which cover almost the same parameter-space of *today's* dEs, will evolve into very faint galaxies with a very low surface brightness. Therefore, these future dIs will not fall into the locus of today's dEs and may share the structural properties of dSph of the Local Group.
The findings of Chapter 4 point to evolutionary connections between the late spirals (Sd and Sm) and the dEs.
In summary, we found that future BCDs and late spirals (Sd and Sm), when star formation has ceased, will share the same parameter-space like Virgo dEs. Therefore, the results of this thesis supports the idea that these galaxy types will be transformed by the environment of the Virgo cluster, resulting in objects quite similar to today's early-type dwarf galaxies.

5.2 Outlook

As seen in the course of this thesis, there are several galaxies within the VCC, which are not or only partly covered by the SDSS. With the new data releases of the SDSS, it will be possible to increase the coverage of this sample of Virgo galaxies. However, due to the overlap with other galaxies (and stars) in the fore- or background, we will never reached an 100% coverage of the Virgo galaxies within a certain completeness limit.
As always in observational astronomy, it would be a great pleasure to have much more deeper observations of the Virgo galaxies. This will be achieved by the Next Generation Virgo Cluster Survey (NGVS; Ferrarese et al., 2012). The results of the NGVS will be in particular interest with respect to the low-luminosity dwarf irregular galaxies, with their low S/N. Furthermore, the NGVS will also shed more light on the faint underlying LSB-components of BCDs and may reveal new features in their structure.
In respect to the BCDs, it would be also very interesting to investigate in more details the differences of structure of BCDs in clusters and in the field. Also the comparison of

BCDs in different clusters, especially clusters at different stages of virialisation, would be of great interest. Of course, this is true for all kind of late-type galaxies.
To check the results of our GALEV/GAZELLE analysis, it would also be useful to compare our results with other evolutionary synthesis models and codes (Hansson, 2012; Hansson et al., 2012). Also the inclusion of spatially resolved maps, e.g. of the stellar mass density and star formation, and the comparison of the different morphological types is of major interest. A first step to these spatially resolved maps was already taken in Chapter 4 and we are excited to see the results of our entire Virgo sample.

Acknowledgement

Mein besonderer Dank gilt meinem Doktorvater Priv.-Doz. Dr. Thorsten Lisker für die Ermöglichung und Betreuung dieser Arbeit. Ich bedanke mich auch recht herzlich für seine Geduld und dass sein Büro immer für mich offen stand.

Ich danke Prof. Dr. Volker Springel für die Übernahme der Begutachtung dieser Arbeit.

Besonders herzlich bedanken möchte ich mich bei Dr. Ralf Kotulla für die Diskussionen über die Themen dieser Arbeit, die große Unterstützung bei den GALEV-Modellen und für seine Freundschaft. Auch für seine Gastfreundschaft während meiner Aufenthalte in Milwaukee und Hertfordshire möchte ich mich bedanken.

Den Leuten aus der Weberstraße und meiner X-Astro Gruppe möchte ich für die schöne Zeit während meiner Promotion danken.

Priv.-Doz. Dr. Polychronis Papaderos möchte ich für die Diskussionen und nützlichen Anmerkungen danken und dass er mein Interesse an den Zwerggalaxien geweckt hat.

Des Weiteren danke ich Dr. Markus Hartmann für das Korrekturlesen und die letzten Anmerkungen zu dieser Arbeit.

Bei meinen Eltern möchte ich mich für die Ermöglichung meines Studiums herzlich bedanken und dass sie immer Vertrauen in mich hatten.

Zum Schluss bedanke ich mich aus tiefstem Herzen bei meiner Lebensgefährtin Maria Worgt für das Interesse an meiner Arbeit und dass sie immer für mich da war.

Bibliography

Abadi, M. G., Moore, B., and Bower, R. G.: 1999, *MNRAS* **308**, 947

Abell, G. O., Corwin, Jr., H. G., and Olowin, R. P.: 1989, *ApJS* **70**, 1

Adelman-McCarthy, J. K., Agüeros, M. A., Allam, S. S., Anderson, K. S. J., Anderson, S. F., Annis, J., Bahcall, N. A., Bailer-Jones, C. A. L., and et al.: 2007, *ApJS* **172**, 634

Aloisi, A., Clementini, G., Tosi, M., Annibali, F., Contreras, R., Fiorentino, G., Mack, J., Marconi, M., Musella, I., Saha, A., Sirianni, M., and van der Marel, R. P.: 2007, *ApJ* **667**, L151

Amorín, R., Alfonso, J., Aguerri, J. A. L., Muñoz-Tuñón, C., and Cairós, L. M.: 2009, *A&A* **501**, 75

Anders, P. and Fritze-v. Alvensleben, U.: 2003, *A&A* **401**, 1063

Athanassoula, E.: 2005, *MNRAS* **358**, 1477

Bekki, K.: 2008, *MNRAS* **388**, L10

Bertelli, G., Bressan, A., Chiosi, C., Fagotto, F., and Nasi, E.: 1994, *A&AS* **106**, 275

Bertin, E. and Arnouts, S.: 1996, *A&AS* **117**, 393

Bicker, J., Fritze-v. Alvensleben, U., and Fricke, K. J.: 2002, *A&A* **387**, 412

Binggeli, B. and Cameron, L. M.: 1991, *A&A* **252**, 27

Binggeli, B., Popescu, C. C., and Tammann, G. A.: 1993, *A&AS* **98**, 275

Binggeli, B., Sandage, A., and Tammann, G. A.: 1985, *AJ* **90**, 1681

Binggeli, B., Tammann, G. A., and Sandage, A.: 1987, *AJ* **94**, 251

Binggeli, B., Tarenghi, M., and Sandage, A.: 1990, *A&A* **228**, 42

Binney, J. and Tremaine, S.: 2008, *Galactic Dynamics: Second Edition*, Princeton University Press

Blakeslee, J. P., Jordán, A., Mei, S., Côté, P., Ferrarese, L., Infante, L., Peng, E. W., Tonry, J. L., and West, M. J.: 2009, *ApJ* **694**, 556

Blanton, M. R., Dalcanton, J., Eisenstein, D., Loveday, J., Strauss, M. A., SubbaRao, M., Weinberg, D. H., Anderson, Jr., J. E., and et al.: 2001, *AJ* **121**, 2358

Bohlin, R. C. and Gilliland, R. L.: 2004, *AJ* **128**, 3053

Boselli, A., Boissier, S., Cortese, L., and Gavazzi, G.: 2008, *ApJ* **674**, 742

Boselli, A. and Gavazzi, G.: 2006, *PASP* **118**, 517

Bothun, G. D., Mould, J. R., Caldwell, N., and MacGillivray, H. T.: 1986, *AJ* **92**, 1007

Boylan-Kolchin, M., Springel, V., White, S. D. M., Jenkins, A., and Lemson, G.: 2009, *MNRAS* **398**, 1150

Bruzual, G. and Charlot, S.: 2003, *MNRAS* **344**, 1000

Cairós, L. M., Caon, N., Papaderos, P., Noeske, K., Vílchez, J. M., García Lorenzo, B., and Muñoz-Tuñón, C.: 2003, *ApJ* **593**, 312

Cairós, L. M., Caon, N., Vílchez, J. M., González-Pérez, J. N., and Muñoz-Tuñón, C.: 2001a, *ApJS* **136**, 393

Cairós, L. M., Vílchez, J. M., González Pérez, J. N., Iglesias-Páramo, J., and Caon, N.: 2001b, *ApJS* **133**, 321

Calzetti, D., Armus, L., Bohlin, R. C., Kinney, A. L., Koornneef, J., and Storchi-Bergmann, T.: 2000, *ApJ* **533**, 682

Cardelli, J. A., Clayton, G. C., and Mathis, J. S.: 1989, *ApJ* **345**, 245

Carroll, B. W. and Ostlie, D. A.: 2006, *An introduction to modern astrophysics and cosmology*

Chabrier, G.: 2003, *PASP* **115**, 763

Chilingarian, I. V.: 2009, *MNRAS* **394**, 1229

Chung, A., van Gorkom, J. H., Kenney, J. D. P., Crowl, H., and Vollmer, B.: 2009, *AJ* **138**, 1741

Chung, A., van Gorkom, J. H., Kenney, J. D. P., and Vollmer, B.: 2007, *ApJ* **659**, L115

Clemens, M. S., Panuzzo, P., Rampazzo, R., Vega, O., and Bressan, A.: 2011, *MNRAS* **412**, 2063

Conroy, C. and Gunn, J. E.: 2010, *ApJ* **712**, 833

Conroy, C., Gunn, J. E., and White, M.: 2009, *ApJ* **699**, 486

Conroy, C., White, M., and Gunn, J. E.: 2010, *ApJ* **708**, 58

Conselice, C. J., Gallagher, III, J. S., and Wyse, R. F. G.: 2001, *ApJ* **559**, 791

Conselice, C. J., O'Neil, K., Gallagher, J. S., and Wyse, R. F. G.: 2003, *ApJ* **591**, 167

Côté, P., Blakeslee, J. P., Ferrarese, L., Jordán, A., Mei, S., Merritt, D., Milosavljević, M., Peng, E. W., Tonry, J. L., and West, M. J.: 2004, *ApJS* **153**, 223

Cunow, B.: 1999, *Astrophysics and Space Science Supplement* **269**, 621

Davies, J. I. and Phillipps, S.: 1988, *MNRAS* **233**, 553

De Lucia, G. and Blaizot, J.: 2007, *MNRAS* **375**, 2

de Rijcke, S., Michielsen, D., Dejonghe, H., Zeilinger, W. W., and Hau, G. K. T.: 2005, *A&A* **438**, 491

de Vaucouleurs, G.: 1961, *ApJS* **6**, 213

de Vaucouleurs, G.: 1974, in J. R. Shakeshaft (ed.), *The Formation and Dynamics of Galaxies*, Vol. 58 of *IAU Symposium*, p. 335

Dekel, A. and Silk, J.: 1986, *ApJ* **303**, 39

Dellenbusch, K. E., Gallagher, III, J. S., Knezek, P. M., and Noble, A. G.: 2008, *AJ* **135**, 326

Djorgovski, S. and Davis, M.: 1987, *ApJ* **313**, 59

Dressler, A.: 1980, *ApJ* **236**, 351

Dressler, A., Lynden-Bell, D., Burstein, D., Davies, R. L., Faber, S. M., Terlevich, R., and Wegner, G.: 1987, *ApJ* **313**, 42

Drinkwater, M. and Hardy, E.: 1991, *AJ* **101**, 94

Drinkwater, M. J., Currie, M. J., Young, C. K., Hardy, E., and Yearsley, J. M.: 1996, *MNRAS* **279**, 595

Elmegreen, B. G. and Elmegreen, D. M.: 2010, *ApJ* **722**, 1895

Falkenberg, M. A., Kotulla, R., and Fritze, U.: 2009, *MNRAS* **397**, 1940

Farouki, R. and Shapiro, S. L.: 1981, *ApJ* **243**, 32

Ferguson, H. C. and Binggeli, B.: 1994, *A&AR* **6**, 67

Ferrara, A. and Tolstoy, E.: 2000, *MNRAS* **313**, 291

Ferrarese, L., Côté, P., Cuillandre, J.-C., Gwyn, S. D. J., Peng, E. W., MacArthur, L. A., Duc, P.-A., Boselli, A., and et al.: 2012, *ApJS* **200**, 4

Fioc, M. and Rocca-Volmerange, B.: 1997, *A&A* **326**, 950

Fritz, J. and Hevics Collaboration: 2011, in W. Wang, J. Lu, Z. Luo, Z. Yang, H. Hua, and Z. Chen (eds.), *Galaxy Evolution: Infrared to Millimeter Wavelength Perspective*, Vol. 446 of *Astronomical Society of the Pacific Conference Series*, p. 77

Fujita, Y. and Nagashima, M.: 1999, *ApJ* **516**, 619

Fumagalli, M. and Gavazzi, G.: 2008, *A&A* **490**, 571

Gallagher, III, J. S., Hunter, D. A., and Tutukov, A. V.: 1984, *ApJ* **284**, 544

Gardner, J. P., Mather, J. C., Clampin, M., Doyon, R., Greenhouse, M. A., Hammel, H. B., Hutchings, J. B., Jakobsen, P., Lilly, S. J., Long, K. S., Lunine, J. I., McCaughrean, M. J., Mountain, M., Nella, J., Rieke, G. H., Rieke, M. J., Rix, H.-W., Smith, E. P., Sonneborn, G., Stiavelli, M., Stockman, H. S., Windhorst, R. A., and Wright, G. S.: 2006, *Space Sci. Rev.* **123**, 485

Gavazzi, G., Bonfanti, C., Sanvito, G., Boselli, A., and Scodeggio, M.: 2002, *ApJ* **576**, 135

Gavazzi, G., Boselli, A., Donati, A., Franzetti, P., and Scodeggio, M.: 2003, *A&A* **400**, 451

Gavazzi, G., Boselli, A., Mayer, L., Iglesias-Paramo, J., Vílchez, J. M., and Carrasco, L.: 2001, *ApJ* **563**, L23

Gavazzi, G., Boselli, A., Scodeggio, M., Pierini, D., and Belsole, E.: 1999, *MNRAS* **304**, 595

Gavazzi, G., Contursi, A., Carrasco, L., Boselli, A., Kennicutt, R., Scodeggio, M., and Jaffe, W.: 1995, *A&A* **304**, 325

Gavazzi, G., O'Neil, K., Boselli, A., and van Driel, W.: 2006, *A&A* **449**, 929

Geha, M., Guhathakurta, P., and van der Marel, R. P.: 2003, *AJ* **126**, 1794

Gil de Paz, A. and Madore, B. F.: 2005, *ApJS* **156**, 345

González-García, A. C., Aguerri, J. A. L., and Balcells, M.: 2005, *A&A* **444**, 803

Goto, T., Yamauchi, C., Fujita, Y., Okamura, S., Sekiguchi, M., Smail, I., Bernardi, M., and Gomez, P. L.: 2003, *MNRAS* **346**, 601

Graham, A. W. and Driver, S. P.: 2005, *Publications of the Astron. Soc. of Australia* **22**, 118

Graham, A. W. and Worley, C. C.: 2008, *MNRAS* **388**, 1708

Grebel, E. K., Gallagher, III, J. S., and Harbeck, D.: 2003, *AJ* **125**, 1926

Green, S. F. and Jones, M. H.: 2004, *An Introduction to the Sun and Stars*

Gu, Q., Zhao, Y., Shi, L., Peng, Z., and Luo, X.: 2006, *AJ* **131**, 806

Gunn, J. E., Carr, M., Rockosi, C., Sekiguchi, M., Berry, K., Elms, B., de Haas, E., Ivezić, Ž., and et al.: 1998, *AJ* **116**, 3040

Gunn, J. E. and Gott, III, J. R.: 1972, *ApJ* **176**, 1

Gunn, J. E., Siegmund, W. A., Mannery, E. J., Owen, R. E., Hull, C. L., Leger, R. F., Carey, L. N., Knapp, G. R., and et al.: 2006, *AJ* **131**, 2332

Guo, Q., White, S., Boylan-Kolchin, M., De Lucia, G., Kauffmann, G., Lemson, G., Li, C., Springel, V., and Weinmann, S.: 2011, *MNRAS* **413**, 101

Guseva, N. G., Papaderos, P., Izotov, Y. I., Green, R. F., Fricke, K. J., Thuan, T. X., and Noeske, K. G.: 2003, *A&A* **407**, 105

Hallenbeck, G., Papastergis, E., Huang, S., Haynes, M. P., Giovanelli, R., Boselli, A., Boissier, S., Heinis, S., Cortese, L., and Fabello, S.: 2012, *ArXiv e-prints*

Hansson, K. A.: 2012, *Ph.D. thesis*, Heidelberg

Hansson, K. S. A., Lisker, T., and Grebel, E. K.: 2012, *ArXiv e-prints*

Heckman, T. M., Sembach, K. R., Meurer, G. R., Strickland, D. K., Martin, C. L., Calzetti, D., and Leitherer, C.: 2001, *ApJ* **554**, 1021

Hensler, G.: 2012, *Morphological Mutations of Dwarf Galaxies*, p. 75

Hubble, E. P.: 1922, *ApJ* **56**, 162

Hubble, E. P.: 1926, *ApJ* **64**, 321

Hubble, E. P.: 1929, *ApJ* **69**, 103

Hunt, L. K., Thuan, T. X., and Izotov, Y. I.: 2003, *ApJ* **588**, 281

Izotov, Y. I., Chaffee, F. H., Foltz, C. B., Green, R. F., Guseva, N. G., and Thuan, T. X.: 1999a, *ApJ* **527**, 757

Izotov, Y. I., Dyak, A. B., Chaffee, F. H., Foltz, C. B., Kniazev, A. Y., and Lipovetsky, V. A.: 1996, *ApJ* **458**, 524

Izotov, Y. I., Papaderos, P., Thuan, T. X., Fricke, K. J., Foltz, C. B., and Guseva, N. G.: 1999b, *ArXiv Astrophysics e-prints*

Janz, J., Laurikainen, E., Lisker, T., Salo, H., Peletier, R. F., Niemi, S.-M., den Brok, M., Toloba, E., Falcón-Barroso, J., Boselli, A., and Hensler, G.: 2012, *ApJ* **745**, L24

Janz, J. and Lisker, T.: 2008, *ApJ* **689**, L25

Janz, J. and Lisker, T.: 2009, *ApJ* **696**, L102

Jedrzejewski, R. I.: 1987, *MNRAS* **226**, 747

Jerjen, H.: 2012, *Dwarf Elliptical Galaxies: United and Divided*, p. 133

Jerjen, H., Kalnajs, A., and Binggeli, B.: 2000, *A&A* **358**, 845

Jester, S., Schneider, D. P., Richards, G. T., Green, R. F., Schmidt, M., Hall, P. B., Strauss, M. A., Vanden Berk, D. E., Stoughton, C., Gunn, J. E., Brinkmann, J., Kent, S. M., Smith, J. A., Tucker, D. L., and Yanny, B.: 2005, *AJ* **130**, 873

Jones, M. H. and Lambourne, R. J. A.: 2004, *An Introduction to Galaxies and Cosmology*

Kenney, J. D. P., van Gorkom, J. H., and Vollmer, B.: 2004, *AJ* **127**, 3361

Kennicutt, Jr., R. C.: 1998, *ApJ* **498**, 541

Kissler-Patig, M., Küpcü Yoldaş, A., and Liske, J.: 2009, *The Messenger* **138**, 11

Kniazev, A. Y., Pustilnik, S. A., Grebel, E. K., Lee, H., and Pramskij, A. G.: 2004, *ApJS* **153**, 429

Koleva, M., Prugniel, P., de Rijcke, S., and Zeilinger, W. W.: 2011, *MNRAS* **417**, 1643

Koopmann, R. A. and Kenney, J. D. P.: 2004, *ApJ* **613**, 851

Kormendy, J.: 1985, *ApJ* **295**, 73

Kotulla, R., Anders, P., Weilbacher, P., and Fritze, U.: 2010, in G. Bruzual & S. Charlot (ed.), *IAU Symposium*, Vol. 262 of *IAU Symposium*, pp 366–367

Kotulla, R., Fritze, U., Weilbacher, P., and Anders, P.: 2009, *MNRAS* **396**, 462

Kroupa, P.: 2001, *MNRAS* **322**, 231

Krüger, H. and Fritze-v. Alvensleben, U.: 1994, *A&A* **284**, 793

Krüger, H., Fritze-v. Alvensleben, U., and Loose, H.-H.: 1995, *A&A* **303**, 41

Krüger, H., Fritze-von Alvensleben, U., Loose, H.-H., and Fricke, K. J.: 1991, *A&A* **242**, 343

Krywult, J.: 2009, *Astronomische Nachrichten* **330**, 946

Kunth, D. and Östlin, G.: 2000, *A&AR* **10**, 1

Larson, R. B., Tinsley, B. M., and Caldwell, C. N.: 1980, *ApJ* **237**, 692

Leitherer, C., Schaerer, D., Goldader, J. D., Delgado, R. M. G., Robert, C., Kune, D. F., de Mello, D. F., Devost, D., and Heckman, T. M.: 1999, *ApJS* **123**, 3

Lejeune, T., Cuisinier, F., and Buser, R.: 1997, *A&AS* **125**, 229

Lejeune, T., Cuisinier, F., and Buser, R.: 1998, *A&AS* **130**, 65

Lelli, F., Verheijen, M., Fraternali, F., and Sancisi, R.: 2012, *A&A* **537**, A72

Lieder, S., Lisker, T., Hilker, M., Misgeld, I., and Durrell, P.: 2012, *A&A* **538**, A69

Lin, D. N. C. and Faber, S. M.: 1983, *ApJ* **266**, L21

Lisker, T.: 2012, *Astronomische Nachrichten* **333**, 405

Lisker, T., Glatt, K., Westera, P., and Grebel, E. K.: 2006a, *AJ* **132**, 2432

Lisker, T., Grebel, E. K., and Binggeli, B.: 2006b, *AJ* **132**, 497

Lisker, T., Grebel, E. K., and Binggeli, B.: 2008, *AJ* **135**, 380

Lisker, T., Grebel, E. K., Binggeli, B., and Glatt, K.: 2007, *ApJ* **660**, 1186

Loose, H.: 1985, in *IUE Proposal*, pp 2259–+

Loose, H.-H. and Thuan, T. X.: 1985, in D. Kunth, T. X. Thuan, and J. Tran Thanh van (eds.), *Star-Forming Dwarf Galaxies and Related Objects*, pp 73–+

Loose, H.-H. and Thuan, T. X.: 1986, *ApJ* **309**, 59

Lotz, J. M., Primack, J., and Madau, P.: 2004, *AJ* **128**, 163

MacArthur, L. A., Courteau, S., Bell, E., and Holtzman, J. A.: 2004, *ApJS* **152**, 175

Magrini, L., Bianchi, S., Corbelli, E., Cortese, L., Hunt, L., Smith, M., Vlahakis, C., Davies, J., Bendo, G. J., Baes, M., Boselli, A., Clemens, M., Casasola, V., de Looze, I., Fritz, J., Giovanardi, C., Grossi, M., Hughes, T., Madden, S., Pappalardo, C., Pohlen, M., di Serego Alighieri, S., and Verstappen, J.: 2011, *A&A* **535**, A13

Maraston, C.: 2005, *MNRAS* **362**, 799

Marcolini, A., Brighenti, F., and D'Ercole, A.: 2003, *MNRAS* **345**, 1329

Marquart, T., Fathi, K., Östlin, G., Bergvall, N., Cumming, R. J., and Amram, P.: 2007, *A&A* **474**, L9

Mas-Hesse, J. M. and Kunth, D.: 1999, *A&A* **349**, 765

Mastropietro, C., Moore, B., Mayer, L., Debattista, V. P., Piffaretti, R., and Stadel, J.: 2005, *MNRAS* **364**, 607

Mayer, L., Governato, F., Colpi, M., Moore, B., Quinn, T., Wadsley, J., Stadel, J., and Lake, G.: 2001, *ApJ* **547**, L123

Mayer, L., Mastropietro, C., Wadsley, J., Stadel, J., and Moore, B.: 2006, *MNRAS* **369**, 1021

McGaugh, S. S. and de Blok, W. J. G.: 1997, *ApJ* **481**, 689

McLaughlin, D. E.: 1999, *ApJ* **512**, L9

McQuinn, K. B. W., Skillman, E. D., Cannon, J. M., Dalcanton, J., Dolphin, A., Hidalgo-Rodríguez, S., Holtzman, J., Stark, D., Weisz, D., and Williams, B.: 2010a, *ApJ* **721**, 297

McQuinn, K. B. W., Skillman, E. D., Cannon, J. M., Dalcanton, J., Dolphin, A., Hidalgo-Rodríguez, S., Holtzman, J., Stark, D., Weisz, D., and Williams, B.: 2010b, *ApJ* **724**, 49

Mei, S., Blakeslee, J. P., Côté, P., Tonry, J. L., West, M. J., Ferrarese, L., Jordán, A., Peng, E. W., Anthony, A., and Merritt, D.: 2007, *ApJ* **655**, 144

Meyer, H. T. and Lisker, T.: 2011, in M. Koleva, P. Prugniel, & I. Vauglin (ed.), *EAS Publications Series*, Vol. 48 of *EAS Publications Series*, pp 205–206

Misgeld, I. and Hilker, M.: 2011, *MNRAS* **414**, 3699

Mo, H., van den Bosch, F. C., and White, S.: 2010, *Galaxy Formation and Evolution*

Moeller, C. S., Fritze-v. Alvensleben, U., and Fricke, K. J.: 1997, *A&A* **317**, 676

Möllenhoff, C., Popescu, C. C., and Tuffs, R. J.: 2006, *A&A* **456**, 941

Moore, B., Katz, N., Lake, G., Dressler, A., and Oemler, A.: 1996, *Nature* **379**, 613

Noeske, K. G.: 1999, *Master's thesis*, Göttingen

Noeske, K. G., Guseva, N. G., Fricke, K. J., Izotov, Y. I., Papaderos, P., and Thuan, T. X.: 2000, *A&A* **361**, 33

Noeske, K. G., Koo, D. C., Phillips, A. C., Willmer, C. N. A., Melbourne, J., Gil de Paz, A., and Papaderos, P.: 2006, *ApJ* **640**, L143

Noeske, K. G., Papaderos, P., Cairós, L. M., and Fricke, K. J.: 2003, *A&A* **410**, 481

Oemler, Jr., A.: 1974, *ApJ* **194**, 1

Oke, J. B. and Gunn, J. E.: 1983, *ApJ* **266**, 713

Östlin, G., Amram, P., Masegosa, J., Bergvall, N., and Boulesteix, J.: 1999, *A&AS* **137**, 419

Papaderos, P. and Östlin, G.: 2011, *ArXiv e-prints*

Papaderos, P., Fricke, K. J., Thuan, T. X., Izotov, Y. I., and Nicklas, H.: 1999, *A&A* **352**, L57

Papaderos, P., Guseva, N. G., Izotov, Y. I., and Fricke, K. J.: 2008, *A&A* **491**, 113

Papaderos, P., Guseva, N. G., Izotov, Y. I., Noeske, K. G., Thuan, T. X., and Fricke, K. J.: 2006, *A&A* **457**, 45

Papaderos, P., Izotov, Y. I., Fricke, K. J., Thuan, T. X., and Guseva, N. G.: 1998, *A&A* **338**, 43

Papaderos, P., Izotov, Y. I., Thuan, T. X., Noeske, K. G., Fricke, K. J., Guseva, N. G., and Green, R. F.: 2002, *A&A* **393**, 461

Papaderos, P., Loose, H.-H., Fricke, K. J., and Thuan, T. X.: 1996a, *A&A* **314**, 59

Papaderos, P., Loose, H.-H., Thuan, T. X., and Fricke, K. J.: 1996b, *A&AS* **120**, 207

Papaderos, P., Noeske, K. G., Cairós, L. M., Vílchez, J. M., and Fricke, K. J.: 2001, in K. S. de Boer, R.-J. Dettmar, and U. Klein (eds.), *Dwarf galaxies and their environment*, p. 283

Papaderos, P. and Östlin, G.: 2012, *A&A* **537**, A126

Pedraz, S., Gorgas, J., Cardiel, N., Sánchez-Blázquez, P., and Guzmán, R.: 2002, *MNRAS* **332**, L59

Peletier, R. F., Kutdemir, E., van der Wolk, G., Falcón-Barroso, J., Bacon, R., Bureau, M., Cappellari, M., Davies, R. L., de Zeeuw, P. T., Emsellem, E., Krajnović, D., Kuntschner, H., McDermid, R. M., Sarzi, M., Scott, N., Shapiro, K. L., van den Bosch, R. C. E., and van de Ven, G.: 2012, *MNRAS* **419**, 2031

Peng, C. Y., Ho, L. C., Impey, C. D., and Rix, H.-W.: 2010, *AJ* **139**, 2097

Petrosian, V.: 1976, *ApJ* **209**, L1

Phillipps, S., Parker, Q. A., Schwartzenberg, J. M., and Jones, J. B.: 1998, *ApJ* **493**, L59

Pier, J. R., Munn, J. A., Hindsley, R. B., Hennessy, G. S., Kent, S. M., Lupton, R. H., and Ivezić, Ž.: 2003, *AJ* **125**, 1559

Piovan, L., Tantalo, R., and Chiosi, C.: 2006a, *MNRAS* **366**, 923

Piovan, L., Tantalo, R., and Chiosi, C.: 2006b, *MNRAS* **370**, 1454

Postman, M. and Geller, M. J.: 1984, *ApJ* **281**, 95

Quilis, V., Moore, B., and Bower, R.: 2000, *Science* **288**, 1617

Recchi, S. and Hensler, G.: 2006, *A&A* **445**, L39

Richer, M., McCall, M. L., and Stasińska, G.: 1998, *A&A* **340**, 67

Richer, M. G. and McCall, M. L.: 1995, *ApJ* **445**, 642

Rines, K. and Geller, M. J.: 2008, *AJ* **135**, 1837

Roediger, E.: 2009, *Astronomische Nachrichten* **330**, 888

Roediger, J. C., Courteau, S., MacArthur, L. A., and McDonald, M.: 2011, *MNRAS* **416**, 1996

Rubin, V. C. and Ford, Jr., W. K.: 1970, *ApJ* **159**, 379

Sabatini, S., Davies, J., Scaramella, R., Smith, R., Baes, M., Linder, S. M., Roberts, S., and Testa, V.: 2003, *MNRAS* **341**, 981

Salpeter, E. E.: 1955, *ApJ* **121**, 161

Salzer, J. J., MacAlpine, G. M., and Boroson, T. A.: 1989, *ApJS* **70**, 479

Salzer, J. J. and Norten, S. A.: 1999, *The Low Surface Brightness Universe, IAU Col. 171* 170

Sandage, A.: 1961, *The Hubble atlas of galaxies*

Sandage, A.: 1986, *A&A* **161**, 89

Sandage, A. and Binggeli, B.: 1984, *AJ* **89**, 919

Sandage, A., Binggeli, B., and Tammann, G. A.: 1985, *AJ* **90**, 395

Sandage, A. and Brucato, R.: 1979, *AJ* **84**, 472

Schechter, P.: 1976, *ApJ* **203**, 297

Schlegel, D. J., Finkbeiner, D. P., and Davis, M.: 1998, *ApJ* **500**, 525

Schmidt, M.: 1959, *ApJ* **129**, 243

Searle, L. and Sargent, W. L. W.: 1972, *ApJ* **173**, 25

Sérsic, J. L.: 1968, *Atlas de galaxias australes*, Cordoba, Argentina: Observatorio Astronomico

Shen, S., Mo, H. J., White, S. D. M., Blanton, M. R., Kauffmann, G., Voges, W., Brinkmann, J., and Csabai, I.: 2003, *MNRAS* **343**, 978

Silich, S. A. and Tenorio-Tagle, G.: 1998, *MNRAS* **299**, 249

Smith, J. A., Tucker, D. L., Kent, S., Richmond, M. W., Fukugita, M., Ichikawa, T., Ichikawa, S.-i., Jorgensen, A. M., Uomoto, A., Gunn, J. E., Hamabe, M., Watanabe, M., Tolea, A., Henden, A., Annis, J., Pier, J. R., McKay, T. A., Brinkmann, J., Chen, B., Holtzman, J., Shimasaku, K., and York, D. G.: 2002, *AJ* **123**, 2121

Smith, R., Davies, J. I., and Nelson, A. H.: 2010, *MNRAS* **405**, 1723

Sparke, L. S. and Gallagher, III, J. S.: 2000, *Galaxies in the universe : an introduction*, Cambridge University Press

Staveley-Smith, L., Davies, R. D., and Kinman, T. D.: 1992, *MNRAS* **258**, 334

Sung, E.-C., Chun, M.-S., Freeman, K. C., and Chaboyer, B.: 2002, in G. S. Da Costa, E. M. Sadler, & H. Jerjen (ed.), *The Dynamics, Structure & History of Galaxies: A Workshop in Honour of Professor Ken Freeman*, Vol. 273 of *Astronomical Society of the Pacific Conference Series*, p. 341

Sung, E.-C., Han, C., Ryden, B. S., Chun, M.-S., and Kim, H.-I.: 1998, *ApJ* **499**, 140

Tajiri, Y. Y. and Kamaya, H.: 2002, *A&A* **389**, 367

Telles, E., Melnick, J., and Terlevich, R.: 1997, *MNRAS* **288**, 78

Thornley, M. D., Schreiber, N. M. F., Lutz, D., Genzel, R., Spoon, H. W. W., Kunze, D., and Sternberg, A.: 2000, *ApJ* **539**, 641

Thuan, T. X.: 1985, *ApJ* **299**, 881

Thuan, T. X.: 1991, in C. Leitherer, N. Walborn, T. Heckman, and C. Norman (eds.), *Observations and Models of Blue Compact Dwarf Galaxies*, pp 183–+

Thuan, T. X. and Martin, G. E.: 1981, *ApJ* **247**, 823

Tinsley, B. M.: 1968, *ApJ* **151**, 547

Tody, D.: 1993, in R. J. Hanisch, R. J. V. Brissenden, and J. Barnes (eds.), *Astronomical Data Analysis Software and Systems II*, Vol. 52 of *Astronomical Society of the Pacific Conference Series*, p. 173

Toloba, E., Boselli, A., Cenarro, A. J., Peletier, R. F., Gorgas, J., Gil de Paz, A., and Muñoz-Mateos, J. C.: 2011, *A&A* **526**, A114

Tonnesen, S., Bryan, G. L., and van Gorkom, J. H.: 2007, *ApJ* **671**, 1434

Tremonti, C. A., Heckman, T. M., Kauffmann, G., Brinchmann, J., Charlot, S., White, S. D. M., Seibert, M., Peng, E. W., Schlegel, D. J., Uomoto, A., Fukugita, M., and Brinkmann, J.: 2004, *ApJ* **613**, 898

Trentham, N. and Hodgkin, S.: 2002, *MNRAS* **333**, 423

Tully, R. B. and Fisher, J. R.: 1977, *A&A* **54**, 661

Tully, R. B. and Shaya, E. J.: 1984, *ApJ* **281**, 31

Vaduvescu, O., Richer, M. G., and McCall, M. L.: 2006, *AJ* **131**, 1318 van den Hoek, L. B. and Groenewegen, M. A. T.: 1997, *A&AS* **123**, 305

van Gorkom, J. H.: 2004, *Clusters of Galaxies: Probes of Cosmological Structure and Galaxy Evolution* p. 305

van Zee, L., Salzer, J. J., and Skillman, E. D.: 2001, *AJ* **122**, 121

van Zee, L., Skillman, E. D., and Haynes, M. P.: 2004, *AJ* **128**, 121

van Zee, L., Westpfahl, D., Haynes, M. P., and Salzer, J. J.: 1998, *AJ* **115**, 1000

Vigroux, L., Souviron, J., and Vader, J. P.: 1984, *A&A* **139**, L9

Vilchez, J. M.: 1995, *AJ* **110**, 1090

Vollmer, B.: 2009, *A&A* **502**, 427

Vollmer, B., Cayatte, V., Balkowski, C., and Duschl, W. J.: 2001, *ApJ* **561**, 708

Vollmer, B., Wong, . O. I., Braine, J., Chung, A., and Kenney, J. D. P.: 2012, *ArXiv e-prints*

Weinmann, S. M., Lisker, T., Guo, Q., Meyer, H. T., and Janz, J.: 2011, *ArXiv e-prints*

Whitmore, B. C., Gilmore, D. M., and Jones, C.: 1993, *ApJ* **407**, 489

Willman, B., Masjedi, M., Hogg, D. W., Dalcanton, J. J., Martinez-Delgado, D., Blanton, M., West, A. A., Dotter, A., and Chaboyer, B.: 2006, *ArXiv Astrophysics e-prints*

Woosley, S. E. and Weaver, T. A.: 1995, *ApJS* **101**, 181

Xilouris, E. M., Byun, Y. I., Kylafis, N. D., Paleologou, E. V., and Papamastorakis, J.: 1999, *A&A* **344**, 868

Yasuda, N., Fukugita, M., Narayanan, V. K., Lupton, R. H., Strateva, I., Strauss, M. A., Ivezić, Ž., Kim, R. S. J., Hogg, D. W., Weinberg, D. H., Shimasaku, K., Loveday, J., Annis, J., Bahcall, N. A., Blanton, M., Brinkmann, J., Brunner, R. J., Connolly, A. J., Csabai, I., Doi, M., Hamabe, M., Ichikawa, S.-I., Ichikawa, T., Johnston, D. E., Knapp, G. R., Kunszt, P. Z., Lamb, D. Q., McKay, T. A., Munn, J. A., Nichol, R. C., Okamura, S., Schneider, D. P., Szokoly, G. P., Vogeley, M. S., Watanabe, M., and York, D. G.: 2001, *AJ* **122**, 1104

York, D. G., Adelman, J., Anderson, Jr., J. E., Anderson, S. F., Annis, J., Bahcall, N. A., Bakken, J. A., Barkhouser, R., and SDSS Collaboration: 2000, *AJ* **120**, 1579

Zwicky, F.: 1937, *ApJ* **86**, 217

Zwicky, F.: 1965, *ApJ* **142**, 1293

Chapter 6 Appendix

6.1 Abbreviations

In Tab. 6.1 the abbreviations of the here presented study are summarised.

Table 6.1: Used abbreviations of this study.

Abbreviation	Description
BCD	Blue compact dwarf
CI	Concentration index
CMD	Colour-magnitude diagram
dE	Dwarf elliptical
dE(bc)	Dwarf elliptical with blue core
dI	Dwarf irregular
dSph	Dwarf spheroidal galaxies
E	Elliptical galaxy
E-ELT European Extremely Large Telescope	
ETG	Early-type galaxy
ETDG	Early-type dwarf galaxy
EW	Equivalent width
FWHM	Full width at half maximum
GALEV	GALaxy EVolution code
G08	Graham and Worley (2008)
G99	Gavazzi et al. (1999)
ICM	Intra cluster medium
IMF	Initial mass function
ISM	Inter stellar medium
JL09	Janz and Lisker (2009)

continued

Abbreviation	Description
JWST	James Webb Space Telescope
LF	Luminosity function
LG	Local Group
LSB	Low surface brightness
NED	NASA/IPAC Extragalactic Database
modexp	Modified exponential fitting law
NGVS	Next Generation Virgo Cluster Survey
P96b	Papaderos et al. (1996b)
P08	Papaderos et al. (2008)
pst	Point spread function
RPS	Ram pressure stripping
SAM	Semi analytical model
SB	Starburst
SBP	Surface brightness profile
SDSS	Sloan Digital Sky Survey
SED	Spectral energy distribution
SF	Star formation
SFDG	Star forming dwarf galaxy
SFH	Star formation history
SFR	Star formation rate
sSFR	Specific star formation rate
S/N	Signal to noise ratio
SNe	Supernovae
VCC	Virgo Cluster Catalog
Z	Metallicity

Abbreviations

6.2 Structural parameters of the sample

In Chapter 3 the structural properties of the late-type galaxies were derived. Table 6.2 summarised the results of this analysis.

Table 6.2: Derived structural parameters of the late-type galaxies.

VCC [1]	ms [2]	Type [3]	(g – i) [4]	M_r [5]	$R_{eff,r}$[kpc] [6]	$\langle\mu\rangle_{eff,r}$ [7]	b/a [8]
0015	1	Sa?	0.79	14.67	1.26	22.65	0.73
0020	1	?	0.73	17.38	0.45	23.14	0.85
0025	1	Sc(r)I.4	0.59	11.92	1.25	19.89	0.87
0031	1	?	0.56	15.20	0.38	20.61	0.47
0034	2	Sc:	0.56	14.36	1.18	22.21	0.61
0048	2	Sd(s) / SmIII	0.61	14.03	1.84	22.85	0.87
0058	1	SBb(r)I-II	0.73	12.50	2.18	21.68	0.51
0066	2	SBc(s)II	0.65	11.17	3.72	21.52	0.29
0067	2	Sc(s)pec	0.53	13.51	1.59	22.02	0.36
0073	1	Sb:	1.10	12.20	0.76	19.09	0.40
0081	2	d:Sc	0.58	14.43	1.77	23.16	0.87
0087	2	SmIII	0.55	14.29	1.05	21.88	0.50
0089	1	SBc(sr)II.2	0.78	11.45	2.49	20.92	0.79
0092	2	SbII:	1.05	9.71	4.34	20.39	0.28
0094	1	S0/a	1.11	12.49	0.73	19.30	0.72
0097	1	Sc(s)II	1.00	12.05	1.49	20.41	0.44
0099	1	Sa?	0.97	14.36	0.64	20.90	0.35
0104	2	dE3 or ImV	0.67	17.04	1.51	25.43	0.73
0105	2	SBdIV	0.64	13.14	2.94	22.98	0.87
0113	1	?	0.37	16.61	0.82	23.68	0.53
0119	2	Sc	0.47	14.85	1.24	22.82	0.31
0120	2	Scd(on-edge)	0.67	12.58	1.30	20.64	0.26
0122	1	S014	1.05	12.75	1.04	20.33	0.60
0126	2	SBd	0.56	14.01	2.19	23.20	0.67
0131	1	Sc	0.94	13.45	0.88	20.66	0.20
0135	2	Spec / BCD	0.98	13.75	0.67	20.36	0.51
0137	1	?	0.88	16.19	0.54	22.34	0.68
0143	2	Sc(on-edge):	0.74	14.78	0.68	21.44	0.39
0145	2	Sc(s)	0.86	12.02	2.03	21.05	0.17

continued

VCC [1]	ms [2]	Type [3]	(g – i) [4]	M_r [5]	$R_{eff,r}$[kpc] [6]	$\langle\mu\rangle_{eff,r}$ [7]	b/a [8]
0152	2	Scd(on-edge)	1.09	12.35	1.14	20.13	0.49
0157	2	Sc(s)II-III	0.89	10.82	2.33	20.15	0.57
0162	2	Sd(on-edge)	0.50	14.19	1.06	21.81	0.14
0166	1	S029	1.10	11.89	0.74	18.74	0.39
0167	2	Sb(s)	1.29	9.69	2.47	19.15	0.25
0187	2	Scd(on-edge)	0.96	12.87	1.42	21.13	0.21
0199	1	Sa	1.23	11.46	1.59	19.96	0.42
0213	2	dS? / BCD?	0.80	13.59	0.61	20.01	0.86
0221	1	SBcIII.4	0.65	12.56	1.45	20.86	0.85
0222	1	Sa	1.19	11.32	1.50	19.69	0.28
0226	2	Sc(r)II.8	1.01	11.35	1.67	19.95	0.62
0234	1	Sa	1.14	11.68	1.90	20.56	0.49
0237	1	?	0.38	16.56	0.65	23.13	0.73
0241	2	Sd(on-edge)	0.21	14.19	1.29	22.23	0.30
0267	2	SBbc(s)I-II	0.62	12.92	2.47	22.38	0.84
0289	2	Sc(on-edge)	0.55	13.99	0.74	20.84	0.31
0307	2	Sc(s)I.3	0.74	9.45	4.51	20.22	0.72
0312	1	S016	1.16	12.35	0.58	18.65	0.47
0318	2	SBcd(s)III	0.46	13.74	1.67	22.35	0.56
0323	1	Sa	1.12	13.52	0.61	19.93	0.31
0341	1	SBa(s)	1.15	11.35	1.75	20.05	0.40
0342	1	S017	1.11	13.36	0.40	18.85	0.44
0343	1	SBd(s)II	0.69	14.73	1.06	22.34	0.85
0358	1	SBa(s)	1.09	12.53	0.80	19.55	0.91
0366	1	S016	1.14	13.19	1.11	20.90	0.58
0371	1	S026	1.17	12.42	0.70	19.13	0.41
0373	1	S012	1.12	12.26	1.12	20.01	0.74
0375	1	S016	1.09	11.85	0.94	19.22	0.39
0382	1	SBc(s)II	0.67	11.52	1.50	19.89	0.63
0386	1	SBa	1.08	13.13	1.12	20.87	0.76
0393	1	Sc(s)II	0.72	12.71	1.72	21.39	0.80
0404	1	Scd(on-edge)	1.04	13.96	0.87	21.14	0.18

continued

VCC [1]	ms [2]	Type [3]	(g – i) [4]	M_r [5]	$R_{eff,r}$[kpc] [6]	$\langle\mu\rangle_{eff,r}$ [7]	b/a [8]
0408	1	S036	1.19	10.94	1.33	19.05	0.46
0414	2	dE2 or ImV	0.86	16.68	0.70	23.41	0.62
0415	1	Sd:	0.77	14.53	1.14	22.31	0.56
0429	1	?	0.65	15.99	0.73	22.81	0.53
0446	2	Im / BCD:	0.75	15.15	0.87	22.34	0.58
0449	1	Sbc(on-edge)	1.24	13.34	0.93	20.66	0.37
0450	1	S0pec	0.97	14.76	0.78	21.70	0.47
0453	2	Sm	0.71	15.73	0.49	21.69	0.34
0460	2	Sapec	1.06	10.11	3.78	20.49	0.44
0465	2	SBc(s)II-III	0.54	11.82	1.86	20.66	0.37
0472	2	ImIV-V or dE4	1.04	16.42	0.91	23.71	0.52
0483	2	Sc(s)III	0.00	0.00	0.00	-inf	0.00
0491	2	Scd(s)III	0.40	12.16	1.81	20.94	0.97
0497	2	Sc(on-edge)	0.00	0.00	0.00	-inf	0.00
0509	1	Sd or SmIV	0.58	14.80	1.27	22.82	0.43
0512	2	SBmIV	0.63	15.13	1.52	23.53	0.39
0514	2	Sc(s)pec:	0.77	14.12	1.77	22.86	0.90
0522	2	Sa	0.99	12.22	1.79	20.98	0.49
0524	2	Sbc(on-edge)	1.21	11.67	1.58	20.16	0.21
0534	1	SBapec	1.10	12.49	1.62	21.03	0.48
0559	2	Sab	1.01	11.49	2.04	20.53	0.26
0566	1	SBmIII:	0.24	15.97	0.59	22.31	0.54
0567	1	ScdIII	0.76	13.51	1.30	21.57	0.32
0570	2	Sab	1.12	11.29	2.18	20.47	0.55
0574	2	dE3 or ImV	0.92	16.48	1.22	24.41	0.78
0576	2	Sbc(on-edge)	1.21	12.46	1.11	20.17	0.27
0593	1	S	0.69	14.43	0.74	21.28	0.30
0596	2	Sc(s)I	0.87	9.02	7.62	20.92	0.87
0620	2	SmIII	0.52	15.36	0.63	21.84	0.37
0630	2	Sd(on-edge)	0.89	12.23	2.00	21.23	0.14
0654	2	RSB025	1.13	10.91	2.28	20.19	0.70
0656	1	Sb	1.21	11.99	1.13	19.74	0.61

continued

VCC [1]	ms [2]	Type [3]	(g – i) [4]	M_r [5]	$R_{eff,r}$[kpc] [6]	$\langle\mu\rangle_{eff,r}$ [7]	b/a [8]
0657	1	S017	1.19	12.10	0.27	16.76	0.46
0664	2	ScIII-IV	0.38	13.10	2.01	22.10	0.64
0667	1	Sc(s)	0.89	13.20	1.60	21.71	0.48
0672	1	S018	0.97	13.11	0.70	19.82	0.31
0679	1	?	0.74	15.17	0.86	22.33	0.44
0688	2	Sc(s)II-III	0.87	13.16	1.05	20.76	0.64
0692	2	Sc(s)II.3	0.66	12.21	2.05	21.27	0.72
0697	1	Sc(s)II.2	0.88	13.08	1.75	21.79	0.93
0699	2	Sc(s)III-IV or SmI	0.57	12.99	1.00	20.48	0.92
0713	2	Sc(on-edge)	1.13	12.25	1.77	20.98	0.22
0739	1	SdIII-IV	0.50	13.44	1.95	22.38	0.93
0740	2	SBmIII	0.55	15.40	0.80	22.41	0.53
0768	1	SBc	0.63	14.47	0.69	21.15	0.27
0792	2	Sab(s)	1.07	11.20	3.10	21.15	0.52
0801	2	Amorphu	0.69	11.86	0.82	18.92	0.56
0809	2	Sc(on-edge)	0.82	13.80	0.98	21.26	0.19
0827	2	Sc(on-edge)	0.91	12.64	1.48	20.98	0.19
0836	2	Sab	0.94	10.76	2.27	20.03	0.30
0849	2	Sbc(s)II	0.60	12.56	1.70	21.21	0.74
0851	2	Sc(on-edge)	0.90	13.13	1.33	21.25	0.21
0857	2	SBb(sr)I-II	1.10	10.48	3.48	20.69	0.91
0859	1	Sc(on-edge)	1.21	13.23	1.41	21.47	0.55
0865	2	Sc(s)II	0.72	12.17	2.50	21.65	0.30
0869	2	ImV or dE0	0.86	14.71	2.36	24.07	0.80
0873	2	Sc(on-edge)	1.14	11.31	2.49	20.79	0.26
0874	1	Sc(s) / S0	0.95	11.94	1.40	20.17	0.71
0905	2	SBc(s)II	0.68	12.74	2.61	22.32	0.91
0912	2	SBbc(rs)	0.91	11.85	2.06	20.92	0.67
0938	2	SBc(s)II.2	0.83	12.22	1.90	21.10	0.90
0939	2	Sc(s)II	0.66	12.19	3.32	22.29	0.95
0945	2	SBmIII	0.31	14.86	1.29	22.91	0.48
0950	2	SmIV	0.47	14.73	2.28	24.01	0.77

continued

VCC [1]	ms [2]	Type [3]	(g – i) [4]	M_r [5]	$R_{eff,r}$[kpc] [6]	$\langle\mu\rangle_{eff,r}$ [7]	b/a [8]
0957	1	Sc(s)III	0.65	12.00	1.21	19.91	0.46
0958	2	Sa	1.17	10.86	1.29	18.91	0.31
0975	2	Scd(s)II	0.00	0.00	0.00	-inf	0.00
0979	2	Sapec	0.90	11.27	2.58	20.82	0.53
0980	2	Scd(s)III	0.44	13.69	1.71	22.34	0.41
0984	2	SBa	1.08	11.72	1.14	19.50	0.33
0989	1	Sc or Im	0.56	16.04	0.79	23.01	0.97
0995	2	Sc(on-edge)	0.49	14.64	0.67	21.27	0.28
1011	2	SdmIII	0.72	14.32	1.25	22.29	0.51
1020	2	dE4,N: or ImIV	0.99	16.28	0.66	22.88	0.55
1047	2	SBa(sr)	1.11	11.54	1.28	19.57	0.88
1060	1	SmIII-IV	0.34	15.34	1.00	22.82	0.50
1086	2	S(on-edge)	1.11	12.54	1.16	20.35	0.23
1091	2	Sbc(s)I.8	0.47	13.68	0.77	20.62	0.44
1110	2	Sabpec	1.11	9.70	3.82	20.10	0.64
1118	2	Sc(s)III	0.89	12.41	0.92	19.72	0.60
1126	2	Sc / Sa	1.02	11.91	1.61	20.44	0.44
1145	1	RSb(rs)II	1.07	10.47	1.46	18.78	0.71
1156	1	SBcd(s)II	0.46	13.97	2.07	23.04	0.47
1158	2	Sa	1.19	10.89	1.28	18.92	0.67
1165	2	dE3 or ImV	0.82	17.40	0.91	24.70	0.55
1179	2	ImIII / BCD	0.65	14.75	0.97	22.18	0.34
1186	2	dE0 or ImV	0.72	17.16	0.82	24.23	0.81
1188	2	Amorphu	0.90	12.80	0.83	19.89	0.44
1189	2	Sc(s)II	0.68	13.21	1.51	21.59	0.62
1190	2	Sa	1.18	10.95	1.98	19.92	0.37
1193	2	Sc:	0.72	13.52	0.88	20.73	0.30
1205	1	ScIIIpec	0.67	12.25	1.13	20.01	0.68
1208	1	SmIII	0.56	15.13	0.61	21.55	0.84
1217	2	SBmIV	0.62	14.02	2.62	23.60	0.74
1227	2	dE0 or ImV	1.52	16.52	1.45	24.81	0.88
1237	1	?	0.61	15.22	0.66	21.80	0.76

continued

VCC [1]	ms [2]	Type [3]	(g – i) [4]	M_r [5]	$R_{eff,r}$[kpc] [6]	$\langle\mu\rangle_{eff,r}$ [7]	b/a [8]
1266	1	SdmIII-IV	0.35	14.91	1.19	22.79	0.83
1290	1	Sb(r)II	0.78	12.25	1.58	20.74	0.58
1294	1	S0:	0.94	14.69	0.91	21.98	0.64
1326	2	SBa(s)	0.96	12.26	1.38	20.44	0.52
1330	2	Sa	1.13	11.28	3.09	21.23	0.92
1331	2	dE3 or ImV	0.78	16.57	1.50	24.94	0.84
1336	2	dE1 or ImV	1.06	16.84	1.23	24.78	0.91
1356	2	SmIII / BCD	0.48	14.75	0.54	20.89	0.56
1358	1	Sa:	0.80	14.46	1.14	22.23	0.68
1375	1	SBcIII-IV	0.58	11.40	3.54	21.64	0.83
1379	2	SBc(s)II	0.68	11.93	2.16	21.09	0.48
1393	1	SBc(s)II-III	0.68	12.72	1.60	21.23	0.66
1408	2	dE1 or ImV	0.95	16.99	1.02	24.52	0.74
1410	2	SmIII	0.60	13.77	0.94	21.13	0.54
1412	2	Sa	1.18	10.71	1.59	19.21	0.48
1413	2	dE2 or ImIV-V	0.96	17.20	0.85	24.33	0.63
1419	2	S(dust)pec	0.97	12.54	1.66	21.13	0.73
1427	2	Im / BCD:	0.68	14.64	0.93	21.98	0.58
1442	1	Sd(on-edge)	0.63	13.85	1.27	21.86	0.20
1448	2	ImIV or dE1pec	0.86	13.13	3.27	23.19	0.77
1450	2	Sc(s)II.2	0.57	12.44	1.98	21.42	0.68
1507	2	SmIV:	0.76	14.81	1.21	22.71	0.53
1508	2	SBc(rs)II.2	0.52	11.72	2.57	21.27	0.73
1516	2	Sc / Sb:	0.78	12.10	2.08	21.19	0.24
1524	2	SBd(s)III	0.57	12.64	3.39	22.78	0.88
1529	1	SdmIII-IV	0.74	13.93	1.72	22.60	0.82
1532	1	SBcpec	0.76	12.80	1.87	21.65	0.71
1540	1	Sb(s)II	1.22	10.17	3.07	20.10	0.30
1552	2	Sapec	1.05	11.25	2.48	20.71	0.67
1554	2	SmIII	0.45	11.57	1.65	20.14	0.47
1555	2	SBc(s)I.3	0.87	9.69	6.67	21.31	0.67
1557	1	Scd(on-edge)	0.79	13.39	1.05	20.99	0.25

continued

VCC [1]	ms [2]	Type [3]	(g – i) [4]	M_r [5]	$R_{eff,r}$[kpc] [6]	$\langle\mu\rangle_{eff,r}$ [7]	b/a [8]
1562	1	Sc(s)I	0.87	10.16	4.52	20.93	0.37
1566	2	SdIV	0.69	14.48	1.35	22.63	0.61
1569	2	Scd:	0.62	14.88	1.23	22.82	0.60
1574	1	?	0.89	16.45	0.44	22.16	0.80
1575	2	SBmpec	0.90	12.76	1.51	21.15	0.73
1581	2	SmIV	0.70	13.93	2.08	23.01	0.78
1582	2	ImV or dE2	0.64	16.14	1.34	24.26	0.92
1588	2	Scd(s)III-IV	0.90	11.54	2.09	20.63	0.82
1605	2	Sd:	0.60	16.61	0.61	23.05	0.23
1615	2	SBb(rs)I-II	1.12	9.72	5.31	20.84	0.76
1623	1	?	0.63	15.99	0.58	22.31	0.60
1624	1	Sc(on-edge)	1.07	12.78	1.08	20.45	0.37
1644	2	SmIV	0.56	16.80	0.53	22.90	0.29
1656	2	dE3 or ImIV-V	0.90	15.88	1.24	23.84	0.66
1675	2	pec	0.83	13.72	1.50	22.10	0.62
1678	2	SBdIV	0.44	13.55	2.48	23.02	0.82
1685	1	SBd(on-edge)	0.46	15.42	0.97	22.84	0.24
1686	2	SmIII	0.57	12.61	2.34	21.95	0.52
1690	2	Sab(s)I-II	0.90	9.27	5.26	20.37	0.41
1696	2	Sc(s)II-III	0.96	10.81	4.36	21.50	0.85
1699	2	SBmIII	0.43	13.73	1.13	21.49	0.54
1713	1	?	0.56	15.43	0.75	22.30	0.61
1725	2	SmIII / BCD	0.54	13.76	1.56	22.22	0.66
1726	2	SdmIV	0.28	14.63	1.83	23.44	0.74
1727	2	Sab(s)II	1.11	9.18	4.36	19.87	0.77
1730	2	Sc / Sa	1.08	11.49	2.02	20.51	0.71
1756	2	dE5 or Im	0.76	17.41	0.60	23.80	0.49
1757	2	Sa(s)pec	0.88	12.77	1.40	20.99	0.67
1758	2	Sc(on-edge)	0.74	14.09	0.85	21.24	0.14
1760	1	Sa	1.18	11.36	2.23	20.59	0.61
1776	2	dE2 or ImIV	1.15	16.78	1.89	25.66	0.89
1778	2	Amorphu?	0.65	13.45	1.10	21.15	0.50

continued

VCC [1]	ms [2]	Type [3]	(g – i) [4]	M_r [5]	$R_{eff,r}$[kpc] [6]	$\langle\mu\rangle_{eff,r}$ [7]	b/a [8]
1791	2	SBmIII / BCD	0.34	13.89	1.43	22.15	0.53
1804	2	ImIII / BCD	0.82	15.05	0.92	22.37	0.49
1811	2	Sc(s)II.8	0.60	12.13	1.53	20.55	0.66
1813	2	SBa	1.14	10.03	3.22	20.07	0.78
1821	1	?	0.79	16.88	0.48	22.75	0.56
1825	2	dE2 or ImIV	0.82	15.29	1.08	22.96	0.87
1834	1	S016,N	1.07	12.20	1.29	20.25	0.75
1837	1	?	0.81	15.97	0.99	23.44	0.49
1855	1	S0:	0.86	14.72	0.84	21.83	0.69
1859	2	Sapec	0.94	11.66	1.91	20.56	0.49
1860	1	?	1.05	16.22	0.84	23.33	0.68
1868	2	Scd(on-edge)	1.14	12.57	1.57	21.04	0.20
1873	1	?	0.39	16.27	0.59	22.61	0.43
1883	2	RSB01/2	1.05	11.14	1.40	19.36	0.76
1884	2	dE1 or ImV	0.70	15.83	2.80	25.55	0.92
1898	1	?	0.90	14.99	1.05	22.59	0.72
1900	2	ImV or dE3	0.74	15.48	1.69	24.12	0.78
1902	2	S0 / Sa	0.93	12.34	1.82	21.13	0.88
1905	2	dE2 or ImIV	1.17	16.74	2.39	26.13	0.92
1906	1	S0:	0.94	15.00	0.51	21.02	0.79
1920	1	S0?	0.95	14.68	0.70	21.39	0.86
1923	1	Sbc(s)II-III	0.84	12.06	1.70	20.71	0.76
1929	2	Scd(s)	0.73	12.88	1.82	21.68	0.40
1932	2	Sc(on-edge)	0.89	12.13	1.42	20.39	0.17
1933	1	Sab?	0.53	15.98	1.11	23.70	0.94
1943	2	SBb(r)II	0.91	11.29	1.73	19.97	0.79
1944	1	BCD?	1.16	16.19	0.34	21.37	0.96
1955	2	Spec / BCD	0.85	12.74	2.33	22.07	0.88
1960	1	ImIII / BCD?	0.74	17.39	0.37	22.73	0.58
1987	2	SBc(rs)II	0.80	10.23	3.94	20.70	0.61
1994	2	dE2 or ImV	0.76	16.44	0.99	23.92	0.90
1999	2	Sa	1.06	11.93	1.14	19.72	0.75

continued

VCC [1]	ms [2]	Type [3]	(g − i) [4]	M_r [5]	$R_{eff,r}$[kpc] [6]	$\langle\mu\rangle_{eff,r}$ [7]	b/a [8]
2006	2	Amorphu	0.76	13.06	1.62	21.60	0.30
2007	2	ImIII / BCD:	0.69	15.20	0.68	21.85	0.79
2023	2	SBc(s)II	0.57	13.32	1.49	21.68	0.43
2058	2	Sc(s)II.3	0.92	10.59	4.41	21.31	0.78
2066	2	Amorphu	0.83	11.25	1.70	19.90	0.50
2070	2	Sa	1.16	10.28	2.48	19.75	0.73
2089	1	BCD?	1.35	15.04	0.35	20.28	0.79

Derived structural parameters of the late-type galaxies.

6.3 Results of GAZELLE

Table 6.4 summarised the results for the galaxies from the GALEV/GAZELLE runs of our study, which were analysed in the course of Chapter 4. The complete late-type morphological sequence was included in the GALEV/GAZELLE runs and is summarised in Tab. 6.3. Missing internal identification numbers (Type-ID; e.g. BCDs = 1 *and* 2) in Tab. 6.3 have been used to mark the possible membership to the Virgo cluster in the course of the analysis. Since the differences between certain and possible members are not significant, we did not differentiate the membership within the GALEV/GAZELLE runs.

Table 6.3: The different morphological types according to the VCC and their internal identification number.

Type-ID	Description
1	BCD
3	dI
5	Sb
7	Sc
9	Sd
11	Sm
15	Amorphous
17	Sa
19	S0
23	S
24	unknown
25	dE/dI

Table 6.4: Results from GALEV/GAZELLE runs (Part I). Upper and lower values correspond to the minimum and maximum values of the GAZELLE output.

VCC	Type-ID	$mag_{r,obs}$ [mag]	$mag_{r,mod}$ [mag]	M_{tot} [Gyr]	$M_{stellar}$ [$M_\odot$]	M_{gas} [$M_\odot$]	M_{nonvis} [$M_\odot$]
[1]	[2]	[3]	[4]	[5]	[6]	[7]	[8]
0001	1	14.82 ± 0.05	14.85 ± 0.10	$8.73e+08^{8.73e+08}_{7.83e+09}$	$5.79e+08^{4.17e+08}_{5.83e+08}$	$2.94e+08^{2.94e+08}_{7.41e+09}$	$8.33e+08^{8.33e+08}_{9.57e+09}$
0004	3	16.29 ± 0.06	16.32 ± 0.10	$8.83e+08^{1.66e+08}_{8.83e+08}$	$4.71e+07^{4.64e+07}_{5.24e+07}$	$8.36e+08^{1.19e+08}_{8.36e+08}$	$6.62e+07^{6.62e+07}_{4.74e+08}$
0010	1	15.07 ± 0.05	15.09 ± 0.10	$4.79e+09^{6.11e+08}_{4.79e+09}$	$2.55e+08^{2.55e+08}_{3.69e+08}$	$4.53e+09^{2.42e+08}_{4.53e+09}$	$3.59e+08^{3.59e+08}_{2.13e+09}$
0015	7	14.67 ± 0.05	14.71 ± 0.10	$7.09e+09^{8.75e+08}_{7.09e+09}$	$3.78e+08^{3.78e+08}_{5.28e+08}$	$6.71e+09^{3.47e+08}_{6.71e+09}$	$5.32e+08^{5.32e+08}_{6.30e+09}$
0017	3	15.30 ± 0.05	15.25 ± 0.10	$9.99e+08^{4.59e+08}_{2.52e+09}$	$1.46e+08^{1.29e+08}_{1.46e+08}$	$8.53e+08^{3.31e+08}_{2.38e+09}$	$2.05e+08^{2.05e+08}_{1.16e+09}$
0020	24	17.38 ± 0.08	17.36 ± 0.10	$1.01e+08^{8.76e+07}_{2.22e+08}$	$2.82e+07^{2.82e+07}_{3.86e+07}$	$7.24e+07^{4.90e+07}_{1.89e+08}$	$3.87e+07^{3.87e+07}_{4.18e+08}$
0022	1	15.65 ± 0.05	15.67 ± 0.10	$2.47e+09^{3.90e+08}_{2.47e+09}$	$1.32e+08^{1.32e+08}_{1.72e+08}$	$2.34e+09^{2.18e+08}_{2.34e+09}$	$1.85e+08^{1.85e+08}_{2.53e+09}$
0024	1	14.88 ± 0.05	14.90 ± 0.10	$4.95e+09^{7.83e+08}_{4.95e+09}$	$2.64e+08^{2.64e+08}_{3.45e+08}$	$4.68e+09^{4.38e+08}_{4.68e+09}$	$3.71e+08^{3.71e+08}_{2.09e+09}$
0025	7	11.92 ± 0.05	11.92 ± 0.10	$6.67e+10^{6.67e+10}_{6.67e+10}$	$3.56e+09^{3.56e+09}_{3.56e+09}$	$6.31e+10^{6.31e+10}_{6.31e+10}$	$5.00e+09^{5.00e+09}_{1.50e+10}$
0026	3	17.34 ± 0.08	17.30 ± 0.10	$6.62e+07^{6.62e+07}_{3.53e+08}$	$1.85e+07^{1.85e+07}_{2.80e+07}$	$4.76e+07^{4.76e+07}_{3.34e+08}$	$2.54e+07^{2.54e+07}_{2.30e+08}$
0030	3	16.03 ± 0.06	16.06 ± 0.10	$2.09e+08^{2.09e+08}_{1.13e+09}$	$5.86e+07^{5.86e+07}_{8.73e+07}$	$1.51e+08^{1.51e+08}_{1.07e+09}$	$8.04e+07^{8.04e+07}_{7.24e+08}$
0031	24	15.20 ± 0.05	15.22 ± 0.10	$3.23e+09^{5.19e+08}_{3.23e+09}$	$1.72e+08^{1.72e+08}_{2.29e+08}$	$3.06e+09^{2.90e+08}_{3.06e+09}$	$2.42e+08^{2.42e+08}_{2.77e+09}$
0034	7	14.36 ± 0.05	14.39 ± 0.10	$6.08e+09^{1.28e+09}_{6.08e+09}$	$3.24e+08^{3.24e+08}_{3.98e+08}$	$5.75e+09^{8.86e+08}_{5.76e+09}$	$4.56e+08^{4.56e+08}_{3.48e+09}$
0041	3	16.34 ± 0.09	16.23 ± 0.10	$1.35e+09^{2.12e+08}_{1.35e+09}$	$7.21e+07^{6.90e+07}_{1.62e+08}$	$1.28e+09^{8.21e+07}_{1.28e+09}$	$1.01e+08^{1.01e+08}_{2.06e+09}$
0048	9	14.03 ± 0.05	14.03 ± 0.10	$7.95e+09^{1.78e+09}_{7.95e+09}$	$4.24e+08^{4.24e+08}_{5.52e+08}$	$7.53e+09^{1.23e+09}_{7.53e+09}$	$5.96e+08^{5.96e+08}_{4.64e+09}$

continued

VCC [1]	Type-ID [2]	$mag_{r,obs}$ [mag] [3]	$mag_{r,mod}$ [mag] [4]	M_{tot} [Gyr] [5]	$M_{stellar}$ [$M_\odot$] [6]	M_{gas} [$M_\odot$] [7]	M_{nonvis} [$M_\odot$] [8]
0052	3	17.04 ± 0.09	17.04 ± 0.10	$6.75e+08^{1.06e+08}_{6.76e+08}$	$3.60e+07^{3.60e+07}_{4.69e+07}$	$6.39e+08^{5.95e+07}_{6.40e+08}$	$5.07e+07^{5.07e+07}_{5.20e+08}$
0058	5	12.50 ± 0.05	12.53 ± 0.10	$5.12e+10^{6.49e+09}_{5.12e+10}$	$2.73e+09^{2.73e+09}_{3.92e+09}$	$4.84e+10^{2.58e+09}_{4.85e+10}$	$3.84e+09^{3.84e+09}_{3.10e+10}$
0066	7	11.17 ± 0.05	11.17 ± 0.10	$1.33e+11^{2.16e+10}_{1.33e+11}$	$7.08e+09^{7.08e+09}_{9.52e+09}$	$1.26e+11^{1.21e+10}_{1.26e+11}$	$9.96e+09^{9.96e+09}_{8.12e+10}$
0067	7	13.51 ± 0.05	13.53 ± 0.10	$1.49e+10^{3.12e+09}_{1.49e+10}$	$7.95e+08^{7.95e+08}_{9.66e+08}$	$1.41e+10^{2.15e+09}_{1.41e+10}$	$1.12e+09^{1.12e+09}_{7.13e+09}$
0073	5	12.20 ± 0.05	12.19 ± 0.10	$1.48e+10^{1.43e+10}_{1.33e+11}$	$9.84e+09^{7.07e+09}_{9.89e+09}$	$4.99e+09^{4.47e+09}_{1.25e+11}$	$1.42e+10^{1.42e+10}_{1.19e+11}$
0074	1	15.88 ± 0.05	15.90 ± 0.10	$2.19e+09^{3.45e+08}_{2.19e+09}$	$1.17e+08^{1.17e+08}_{1.52e+08}$	$2.07e+09^{1.93e+08}_{2.07e+09}$	$1.64e+08^{1.64e+08}_{9.24e+08}$
0081	7	14.43 ± 0.05	14.44 ± 0.10	$5.41e+09^{1.22e+09}_{5.41e+09}$	$2.89e+08^{2.89e+08}_{3.78e+08}$	$5.12e+09^{8.41e+08}_{5.12e+09}$	$4.06e+08^{4.06e+08}_{3.16e+09}$
0083	3	15.11 ± 0.05	15.12 ± 0.10	$3.91e+09^{6.19e+08}_{3.91e+09}$	$2.09e+08^{2.09e+08}_{2.73e+08}$	$3.70e+09^{3.46e+08}_{3.70e+09}$	$2.93e+08^{2.93e+08}_{2.37e+09}$
0085	3	16.80 ± 0.10	16.83 ± 0.10	$1.42e+08^{1.19e+08}_{6.75e+08}$	$4.39e+07^{3.60e+07}_{5.27e+07}$	$9.78e+07^{6.68e+07}_{6.39e+08}$	$6.21e+07^{6.21e+07}_{5.48e+08}$
0087	11	14.29 ± 0.05	14.26 ± 0.10	$6.44e+09^{1.44e+09}_{6.44e+09}$	$3.44e+08^{3.44e+08}_{4.45e+08}$	$6.10e+09^{9.91e+08}_{6.10e+09}$	$4.83e+08^{4.83e+08}_{3.12e+09}$
0089	7	11.45 ± 0.05	11.50 ± 0.10	$1.43e+11^{1.77e+10}_{1.43e+11}$	$7.64e+09^{7.64e+09}_{1.07e+10}$	$1.36e+11^{7.01e+09}_{1.36e+11}$	$1.07e+10^{1.07e+10}_{1.14e+11}$
0092	5	9.71 ± 0.05	9.68 ± 0.10	$1.30e+11^{1.30e+11}_{1.61e+11}$	$8.90e+10^{8.90e+10}_{1.10e+11}$	$4.06e+10^{4.06e+10}_{5.07e+10}$	$1.29e+11^{1.29e+11}_{1.10e+12}$
0093	25	16.35 ± 0.05	16.39 ± 0.10	$8.83e+08^{1.64e+08}_{8.83e+08}$	$4.71e+07^{4.59e+07}_{7.82e+07}$	$8.36e+08^{9.93e+07}_{8.36e+08}$	$6.62e+07^{6.62e+07}_{7.60e+08}$
0094	19	12.49 ± 0.05	12.47 ± 0.10	$1.23e+10^{1.23e+10}_{1.45e+10}$	$8.47e+09^{8.47e+09}_{9.87e+09}$	$3.87e+09^{3.87e+09}_{4.60e+09}$	$1.23e+10^{1.23e+10}_{1.49e+11}$
0097	7	12.05 ± 0.05	12.04 ± 0.10	$1.37e+10^{1.37e+10}_{1.23e+11}$	$9.08e+09^{6.54e+09}_{9.78e+09}$	$4.60e+09^{4.46e+09}_{1.16e+11}$	$1.31e+10^{1.31e+10}_{9.89e+10}$
0099	17	14.36 ± 0.05	14.35 ± 0.10	$1.63e+09^{1.63e+09}_{1.46e+10}$	$1.08e+09^{7.78e+08}_{1.17e+09}$	$5.49e+08^{5.31e+08}_{1.38e+10}$	$1.56e+09^{1.56e+09}_{1.18e+10}$
0104	25	17.04 ± 0.14	17.07 ± 0.10	$4.19e+08^{6.67e+07}_{4.19e+08}$	$2.24e+07^{1.87e+07}_{9.79e+07}$	$3.97e+08^{3.89e+07}_{3.97e+08}$	$3.14e+07^{3.14e+07}_{9.72e+08}$
0105	9	13.14 ± 0.05	13.14 ± 0.10	$2.48e+10^{9.75e+09}_{2.48e+10}$	$1.32e+09^{1.32e+09}_{1.42e+09}$	$2.34e+10^{8.32e+09}_{2.34e+10}$	$1.86e+09^{1.86e+09}_{9.58e+09}$
0113	24	16.61 ± 0.07	16.57 ± 0.10	$1.42e+08^{1.42e+08}_{3.09e+08}$	$3.98e+07^{3.98e+07}_{5.50e+07}$	$1.03e+08^{1.02e+08}_{2.64e+08}$	$5.47e+07^{5.47e+07}_{4.47e+08}$
0114	3	16.14 ± 0.07	15.93 ± 0.10	$2.31e+09^{2.85e+08}_{2.31e+09}$	$1.23e+08^{1.17e+08}_{2.15e+08}$	$2.18e+09^{1.09e+08}_{2.18e+09}$	$1.73e+08^{1.73e+08}_{2.89e+09}$

continued

VCC	Type-ID	$mag_{r,obs}$ [mag]	$mag_{r,mod}$ [mag]	M_{tot} [Gyr]	$M_{stellar}$ [$M_\odot$]	M_{gas} [$M_\odot$]	M_{nonvis} [$M_\odot$]
[1]	[2]	[3]	[4]	[5]	[6]	[7]	[8]
0117	3	15.97 ± 0.05	15.98 ± 0.10	$1.15e+09^{1.92e+08}_{1.15e+09}$	$6.11e+07^{5.37e+07}_{6.11e+07}$	$1.08e+09^{1.38e+08}_{1.08e+09}$	$8.59e+07^{8.59e+07}_{4.05e+08}$
0119	7	14.85 ± 0.05	14.90 ± 0.10	$3.11e+09^{5.38e+08}_{3.11e+09}$	$1.66e+08^{1.51e+08}_{1.92e+08}$	$2.94e+09^{3.88e+08}_{2.94e+09}$	$2.33e+08^{2.33e+08}_{1.45e+09}$
0120	7	12.58 ± 0.05	12.59 ± 0.10	$4.09e+10^{4.09e+10}_{4.09e+10}$	$2.18e+09^{2.18e+09}_{2.18e+09}$	$3.87e+10^{3.87e+10}_{3.88e+10}$	$3.07e+09^{3.07e+09}_{9.21e+09}$
0122	19	12.75 ± 0.05	12.74 ± 0.10	$8.64e+09^{7.84e+09}_{9.93e+09}$	$5.93e+09^{5.38e+09}_{6.78e+09}$	$2.71e+09^{2.46e+09}_{3.15e+09}$	$8.64e+09^{8.64e+09}_{1.00e+11}$
0126	9	14.01 ± 0.05	14.03 ± 0.10	$1.05e+10^{1.65e+09}_{1.05e+10}$	$5.59e+08^{5.59e+08}_{7.29e+08}$	$9.92e+09^{9.25e+08}_{9.92e+09}$	$7.85e+08^{7.85e+08}_{7.08e+09}$
0128	25	14.78 ± 0.06	14.78 ± 0.10	$8.54e+09^{1.05e+09}_{8.55e+09}$	$4.56e+08^{4.56e+08}_{6.36e+08}$	$8.09e+09^{4.18e+08}_{8.09e+09}$	$6.41e+08^{6.41e+08}_{4.58e+09}$
0130	1	16.44 ± 0.05	16.45 ± 0.10	$7.80e+08^{1.36e+08}_{7.80e+08}$	$4.16e+07^{4.00e+07}_{4.97e+07}$	$7.38e+08^{8.80e+07}_{7.39e+08}$	$5.85e+07^{5.85e+07}_{6.32e+08}$
0131	7	13.45 ± 0.05	13.44 ± 0.10	$3.40e+09^{3.40e+09}_{3.40e+09}$	$2.26e+09^{2.26e+09}_{2.26e+09}$	$1.15e+09^{1.15e+09}_{1.15e+09}$	$3.25e+09^{3.25e+09}_{9.74e+09}$
0132	3	16.01 ± 0.08	15.94 ± 0.10	$1.33e+09^{2.47e+08}_{1.33e+09}$	$7.11e+07^{6.91e+07}_{9.59e+07}$	$1.26e+09^{1.78e+08}_{1.26e+09}$	$9.99e+07^{9.99e+07}_{9.80e+08}$
0135	23	13.75 ± 0.05	13.75 ± 0.10	$2.81e+09^{2.81e+09}_{2.52e+10}$	$1.87e+09^{1.34e+09}_{2.03e+09}$	$9.47e+08^{9.28e+08}_{2.38e+10}$	$2.69e+09^{2.69e+09}_{2.04e+10}$
0137	25	16.19 ± 0.05	16.22 ± 0.10	$2.36e+08^{2.36e+08}_{1.92e+09}$	$1.43e+08^{1.02e+08}_{1.43e+08}$	$9.37e+07^{9.37e+07}_{1.81e+09}$	$2.04e+08^{2.04e+08}_{1.63e+09}$
0143	7	14.78 ± 0.05	14.84 ± 0.10	$6.63e+09^{8.19e+08}_{6.63e+09}$	$3.54e+08^{3.54e+08}_{4.94e+08}$	$6.28e+09^{3.25e+08}_{6.28e+09}$	$4.97e+08^{4.97e+08}_{5.89e+09}$
0144	1	14.63 ± 0.05	14.73 ± 0.10	$4.02e+08^{3.41e+08}_{5.27e+08}$	$1.43e+08^{1.43e+08}_{1.86e+08}$	$2.59e+08^{1.73e+08}_{3.43e+08}$	$1.97e+08^{1.97e+08}_{2.05e+09}$
0145	7	12.02 ± 0.05	12.04 ± 0.10	$9.13e+10^{1.13e+10}_{9.13e+10}$	$4.87e+09^{4.87e+09}_{6.81e+09}$	$8.64e+10^{4.47e+09}_{8.64e+10}$	$6.84e+09^{6.84e+09}_{5.80e+10}$
0152	7	12.35 ± 0.05	12.32 ± 0.10	$1.17e+10^{1.17e+10}_{1.28e+10}$	$8.02e+09^{8.02e+09}_{8.78e+09}$	$3.66e+09^{3.66e+09}_{4.09e+09}$	$1.16e+10^{1.16e+10}_{8.36e+10}$
0155	25	14.47 ± 0.05	14.49 ± 0.10	$9.65e+09^{1.19e+09}_{9.65e+09}$	$5.15e+08^{5.15e+08}_{8.16e+08}$	$9.14e+09^{4.14e+08}_{9.14e+09}$	$7.23e+08^{7.23e+08}_{1.00e+10}$
0157	7	10.82 ± 0.05	10.81 ± 0.10	$3.57e+10^{3.57e+10}_{3.13e+11}$	$2.37e+10^{1.67e+10}_{2.37e+10}$	$1.20e+10^{1.20e+10}_{2.96e+11}$	$3.41e+10^{3.41e+10}_{1.83e+11}$
0159	3	15.38 ± 0.05	15.37 ± 0.10	$3.94e+08^{3.94e+08}_{8.81e+08}$	$1.10e+08^{1.10e+08}_{1.29e+08}$	$2.84e+08^{2.83e+08}_{7.52e+08}$	$1.51e+08^{1.51e+08}_{8.16e+08}$
0162	9	14.19 ± 0.05	14.21 ± 0.10	$7.21e+09^{2.84e+09}_{7.21e+09}$	$3.85e+08^{3.85e+08}_{4.16e+08}$	$6.82e+09^{2.43e+09}_{6.83e+09}$	$5.41e+08^{5.41e+08}_{2.79e+09}$
0166	19	11.89 ± 0.05	11.89 ± 0.10	$2.24e+10^{2.24e+10}_{2.73e+10}$	$1.54e+10^{1.54e+10}_{1.86e+10}$	$7.03e+09^{7.03e+09}_{8.72e+09}$	$2.24e+10^{2.24e+10}_{3.25e+11}$

continued

VCC [1]	Type-ID [2]	$mag_{r,obs}$ [mag] [3]	$mag_{r,mod}$ [mag] [4]	M_{tot} [Gyr] [5]	$M_{stellar}$ [$M_\odot$] [6]	M_{gas} [$M_\odot$] [7]	M_{nonvis} [$M_\odot$] [8]
0167	5	9.69 ± 0.05	9.67 ± 0.10	$2.25e+11^{2.25e+11}_{2.64e+11}$	$1.55e+11^{1.54e+11}_{1.80e+11}$	$7.05e+10^{7.05e+10}_{8.39e+10}$	$2.25e+11^{2.25e+11}_{2.72e+12}$
0168	3	16.40 ± 0.06	16.39 ± 0.10	$1.61e+09^{1.99e+08}_{1.61e+09}$	$8.60e+07^{8.60e+07}_{1.20e+08}$	$1.53e+09^{7.89e+07}_{1.53e+09}$	$1.21e+08^{1.21e+08}_{1.26e+09}$
0169	3	16.29 ± 0.11	16.22 ± 0.10	$1.49e+08^{1.49e+08}_{9.39e+08}$	$4.17e+07^{4.17e+07}_{5.86e+07}$	$1.07e+08^{1.07e+08}_{8.89e+08}$	$5.73e+07^{5.73e+07}_{4.78e+08}$
0172	1	14.32 ± 0.05	14.34 ± 0.10	$5.95e+09^{1.03e+09}_{5.95e+09}$	$3.17e+08^{3.01e+08}_{4.14e+08}$	$5.63e+09^{6.64e+08}_{5.63e+09}$	$4.46e+08^{4.46e+08}_{6.35e+09}$
0181	25	17.48 ± 0.06	17.52 ± 0.10	$3.97e+08^{6.28e+07}_{3.97e+08}$	$2.12e+07^{2.12e+07}_{2.77e+07}$	$3.76e+08^{3.51e+07}_{3.76e+08}$	$2.97e+07^{2.97e+07}_{2.68e+08}$
0187	7	12.87 ± 0.05	12.88 ± 0.10	$5.23e+10^{6.46e+09}_{5.23e+10}$	$2.79e+09^{2.79e+09}_{3.90e+09}$	$4.95e+10^{2.56e+09}_{4.95e+10}$	$3.92e+09^{3.92e+09}_{2.29e+10}$
0190	25	16.44 ± 0.09	16.44 ± 0.10	$5.43e+08^{1.79e+08}_{1.35e+09}$	$7.94e+07^{7.05e+07}_{1.36e+08}$	$4.64e+08^{6.90e+07}_{1.28e+09}$	$1.12e+08^{1.12e+08}_{1.75e+09}$
0199	17	11.46 ± 0.05	11.45 ± 0.10	$3.85e+10^{3.85e+10}_{4.51e+10}$	$2.64e+10^{2.64e+10}_{3.08e+10}$	$1.21e+10^{1.21e+10}_{1.43e+10}$	$3.85e+10^{3.85e+10}_{4.64e+11}$
0207	1	16.55 ± 0.05	16.58 ± 0.10	$9.06e+07^{8.08e+07}_{1.04e+08}$	$3.20e+07^{2.86e+07}_{3.48e+07}$	$5.86e+07^{5.21e+07}_{6.90e+07}$	$4.45e+07^{4.45e+07}_{2.63e+08}$
0213	23	13.59 ± 0.05	13.62 ± 0.10	$2.07e+10^{2.56e+09}_{2.07e+10}$	$1.11e+09^{1.11e+09}_{1.54e+09}$	$1.96e+10^{1.02e+09}_{1.96e+10}$	$1.55e+09^{1.55e+09}_{1.45e+10}$
0217	3	15.40 ± 0.07	15.35 ± 0.10	$3.66e+08^{3.66e+08}_{2.08e+09}$	$1.03e+08^{1.03e+08}_{1.68e+08}$	$2.64e+08^{2.64e+08}_{1.97e+09}$	$1.41e+08^{1.41e+08}_{1.34e+09}$
0221	7	12.56 ± 0.05	12.58 ± 0.10	$4.28e+10^{1.68e+10}_{4.28e+10}$	$2.28e+09^{2.28e+09}_{2.46e+09}$	$4.05e+10^{1.44e+10}_{4.05e+10}$	$3.21e+09^{3.21e+09}_{1.65e+10}$
0222	17	11.32 ± 0.05	11.33 ± 0.10	$4.27e+10^{4.27e+10}_{5.20e+10}$	$2.93e+10^{2.93e+10}_{3.54e+10}$	$1.34e+10^{1.34e+10}_{1.66e+10}$	$4.27e+10^{4.27e+10}_{5.67e+11}$
0223	1	15.77 ± 0.05	15.80 ± 0.10	$2.04e+09^{3.23e+08}_{2.04e+09}$	$1.09e+08^{1.09e+08}_{1.42e+08}$	$1.93e+09^{1.81e+08}_{1.93e+09}$	$1.53e+08^{1.53e+08}_{1.03e+09}$
0226	7	11.35 ± 0.05	11.34 ± 0.10	$2.64e+10^{2.64e+10}_{2.37e+11}$	$1.75e+10^{1.26e+10}_{1.75e+10}$	$8.89e+09^{8.89e+09}_{2.24e+11}$	$2.52e+10^{2.52e+10}_{1.11e+11}$
0234	17	11.68 ± 0.05	11.66 ± 0.10	$2.87e+10^{2.62e+10}_{3.07e+10}$	$1.96e+10^{1.80e+10}_{2.09e+10}$	$9.06e+09^{8.20e+09}_{9.76e+09}$	$2.87e+10^{2.87e+10}_{3.18e+11}$
0237	29	16.56 ± 0.07	16.55 ± 0.10	$1.24e+08^{1.24e+08}_{2.94e+08}$	$3.46e+07^{3.46e+07}_{4.29e+07}$	$8.92e+07^{8.90e+07}_{2.51e+08}$	$4.75e+07^{4.75e+07}_{2.63e+08}$
0241	9	14.19 ± 0.05	14.22 ± 0.10	$9.43e+08^{9.42e+08}_{5.96e+09}$	$2.64e+08^{2.64e+08}_{3.18e+08}$	$6.79e+08^{6.78e+08}_{5.64e+09}$	$3.62e+08^{3.62e+08}_{1.53e+09}$
0247	3	17.15 ± 0.12	16.89 ± 0.10	$4.84e+08^{1.43e+08}_{1.84e+09}$	$7.07e+07^{6.00e+07}_{1.26e+09}$	$4.13e+08^{4.82e+07}_{1.16e+09}$	$9.95e+07^{9.95e+07}_{7.34e+09}$
0252	25	17.95 ± 0.07	17.96 ± 0.10	$4.94e+07^{4.94e+07}_{4.24e+08}$	$3.28e+07^{2.15e+07}_{4.14e+07}$	$1.66e+07^{1.66e+07}_{4.01e+08}$	$4.72e+07^{4.72e+07}_{7.05e+08}$

continued

VCC	Type-ID	$mag_{r,obs}$ [mag]	$mag_{r,mod}$ [mag]	M_{tot} [Gyr]	$M_{stellar}$ [$M_\odot$]	M_{gas} [$M_\odot$]	M_{nonvis} [$M_\odot$]
[1]	[2]	[3]	[4]	[5]	[6]	[7]	[8]
0260	3	16.11 ± 0.06	16.12 ± 0.10	$1.38e+09^{2.28e+08}_{1.38e+09}$	$7.34e+07^{7.34e+07}_{1.01e+08}$	$1.30e+09^{1.28e+08}_{1.30e+09}$	$1.03e+08^{1.03e+08}_{9.63e+08}$
0267	5	12.92 ± 0.05	12.94 ± 0.10	$2.79e+10^{4.42e+09}_{2.80e+10}$	$1.49e+09^{1.49e+09}_{1.95e+09}$	$2.65e+10^{2.47e+09}_{2.65e+10}$	$2.10e+09^{2.10e+09}_{1.18e+10}$
0274	1	16.72 ± 0.06	16.75 ± 0.10	$5.88e+08^{7.28e+07}_{5.88e+08}$	$3.14e+07^{3.05e+07}_{5.43e+07}$	$5.56e+08^{2.43e+07}_{5.57e+08}$	$4.41e+07^{4.41e+07}_{1.09e+09}$
0275	25	13.92 ± 0.05	13.95 ± 0.10	$1.24e+10^{1.96e+09}_{1.24e+10}$	$6.62e+08^{6.62e+08}_{8.65e+08}$	$1.17e+10^{1.10e+09}_{1.17e+10}$	$9.31e+08^{9.31e+08}_{9.54e+09}$
0282	25	16.93 ± 0.07	16.94 ± 0.10	$7.26e+08^{1.14e+08}_{7.27e+08}$	$3.88e+07^{3.87e+07}_{5.05e+07}$	$6.87e+08^{6.40e+07}_{6.88e+08}$	$5.45e+07^{5.45e+07}_{4.99e+08}$
0286	3	15.94 ± 0.05	15.96 ± 0.10	$1.74e+09^{2.76e+08}_{1.75e+09}$	$9.31e+07^{9.31e+07}_{1.22e+08}$	$1.65e+09^{1.54e+08}_{1.65e+09}$	$1.31e+08^{1.31e+08}_{7.38e+08}$
0289	7	13.99 ± 0.05	14.01 ± 0.10	$9.38e+09^{3.70e+09}_{9.39e+09}$	$5.01e+08^{5.01e+08}_{5.40e+08}$	$8.88e+09^{3.16e+09}_{8.88e+09}$	$7.04e+08^{7.04e+08}_{3.63e+09}$
0293	25	15.26 ± 0.06	15.24 ± 0.10	$7.49e+08^{5.91e+08}_{4.79e+09}$	$3.30e+08^{2.37e+08}_{3.57e+08}$	$4.19e+08^{2.34e+08}_{4.53e+09}$	$4.68e+08^{4.68e+08}_{5.43e+09}$
0304	25	15.98 ± 0.06	16.03 ± 0.10	$1.70e+09^{2.68e+08}_{1.70e+09}$	$9.09e+07^{9.09e+07}_{1.18e+08}$	$1.61e+09^{1.50e+08}_{1.61e+09}$	$1.28e+08^{1.28e+08}_{1.15e+09}$
0307	7	9.45 ± 0.05	9.45 ± 0.10	$7.72e+11^{1.22e+11}_{7.72e+11}$	$4.12e+10^{4.12e+10}_{5.39e+10}$	$7.31e+11^{6.84e+10}_{7.31e+11}$	$5.79e+10^{5.79e+10}_{4.68e+11}$
0309	3	15.76 ± 0.06	15.75 ± 0.10	$1.60e+09^{3.69e+08}_{1.60e+09}$	$8.53e+07^{8.53e+07}_{1.14e+08}$	$1.51e+09^{2.55e+08}_{1.51e+09}$	$1.20e+08^{1.20e+08}_{9.47e+08}$
0312	19	12.35 ± 0.05	12.35 ± 0.10	$1.58e+10^{1.58e+10}_{1.93e+10}$	$1.09e+10^{1.08e+10}_{1.31e+10}$	$4.95e+09^{4.95e+09}_{6.15e+09}$	$1.58e+10^{1.58e+10}_{2.10e+11}$
0318	7	13.74 ± 0.05	13.75 ± 0.10	$3.88e+09^{3.88e+09}_{9.85e+09}$	$5.67e+08^{5.25e+08}_{5.67e+08}$	$3.31e+09^{3.31e+09}_{9.32e+09}$	$7.99e+08^{7.99e+08}_{3.87e+09}$
0320	3	16.03 ± 0.07	15.96 ± 0.10	$4.22e+08^{3.68e+08}_{2.34e+09}$	$1.18e+08^{1.18e+08}_{1.62e+08}$	$3.04e+08^{2.06e+08}_{2.21e+09}$	$1.62e+08^{1.62e+08}_{2.11e+09}$
0322	3	14.36 ± 0.05	14.35 ± 0.10	$8.21e+09^{1.30e+09}_{8.21e+09}$	$4.38e+08^{4.38e+08}_{5.72e+08}$	$7.78e+09^{7.26e+08}_{7.78e+09}$	$6.16e+08^{6.16e+08}_{4.80e+09}$
0323	17	13.52 ± 0.05	13.49 ± 0.10	$4.41e+09^{4.41e+09}_{5.54e+09}$	$3.03e+09^{3.03e+09}_{3.78e+09}$	$1.38e+09^{1.38e+09}_{1.76e+09}$	$4.39e+09^{4.39e+09}_{5.99e+10}$
0324	1	13.64 ± 0.05	13.65 ± 0.10	$1.13e+10^{4.44e+09}_{1.13e+10}$	$6.01e+08^{6.01e+08}_{6.49e+08}$	$1.07e+10^{3.79e+09}_{1.07e+10}$	$8.45e+08^{8.45e+08}_{3.45e+09}$
0328	3	15.81 ± 0.05	15.85 ± 0.10	$1.52e+09^{3.35e+08}_{1.52e+09}$	$8.10e+07^{8.10e+07}_{1.04e+08}$	$1.44e+09^{2.31e+08}_{1.44e+09}$	$1.14e+08^{1.14e+08}_{8.83e+08}$
0329	3	17.56 ± 0.08	17.54 ± 0.10	$2.72e+08^{4.89e+07}_{2.72e+08}$	$1.45e+07^{1.37e+07}_{1.70e+07}$	$2.58e+08^{3.52e+07}_{2.58e+08}$	$2.04e+07^{2.04e+07}_{1.47e+08}$
0334	1	15.08 ± 0.05	15.08 ± 0.10	$3.13e+09^{3.13e+09}_{3.13e+09}$	$1.67e+08^{1.67e+08}_{1.67e+08}$	$2.96e+09^{2.96e+09}_{2.96e+09}$	$2.34e+08^{2.34e+08}_{7.03e+08}$

continued

VCC [1]	Type-ID [2]	$mag_{r,obs}$ [mag] [3]	$mag_{r,mod}$ [mag] [4]	M_{tot} [Gyr] [5]	$M_{stellar}$ [$M_\odot$] [6]	M_{gas} [$M_\odot$] [7]	M_{nonvis} [$M_\odot$] [8]
0340	1	14.16 ± 0.05	14.16 ± 0.10	$9.16e+09^{9.16e+09}_{9.16e+09}$	$4.89e+08^{4.89e+08}_{4.89e+08}$	$8.67e+09^{8.67e+09}_{8.67e+09}$	$6.87e+08^{6.87e+08}_{2.06e+09}$
0341	17	11.35 ± 0.05	11.34 ± 0.10	$4.01e+10^{4.01e+10}_{4.89e+10}$	$2.75e+10^{2.75e+10}_{3.33e+10}$	$1.26e+10^{1.26e+10}_{1.56e+10}$	$4.01e+10^{4.01e+10}_{5.81e+11}$
0342	19	13.36 ± 0.05	13.35 ± 0.10	$5.74e+09^{5.73e+09}_{6.99e+09}$	$3.94e+09^{3.94e+09}_{4.76e+09}$	$1.80e+09^{1.80e+09}_{2.23e+09}$	$5.74e+09^{5.74e+09}_{7.62e+10}$
0343	9	14.73 ± 0.05	14.74 ± 0.10	$5.66e+09^{8.94e+08}_{5.66e+09}$	$3.02e+08^{3.02e+08}_{3.94e+08}$	$5.35e+09^{5.00e+08}_{5.36e+09}$	$4.24e+08^{4.24e+08}_{3.31e+09}$
0350	3	16.03 ± 0.07	16.06 ± 0.10	$1.47e+09^{2.40e+08}_{1.48e+09}$	$7.87e+07^{7.87e+07}_{1.06e+08}$	$1.40e+09^{1.34e+08}_{1.40e+09}$	$1.11e+08^{1.11e+08}_{9.01e+08}$
0354	25	14.89 ± 0.06	14.89 ± 0.10	$8.72e+08^{8.72e+08}_{7.75e+09}$	$5.78e+08^{4.13e+08}_{8.96e+08}$	$2.93e+08^{2.93e+08}_{7.34e+09}$	$8.32e+08^{8.32e+08}_{1.65e+10}$
0358	17	12.53 ± 0.05	12.52 ± 0.10	$1.27e+10^{1.18e+10}_{1.54e+10}$	$8.69e+09^{8.10e+09}_{1.05e+10}$	$3.97e+09^{3.70e+09}_{4.92e+09}$	$1.27e+10^{1.27e+10}_{1.95e+11}$
0364	3	16.56 ± 0.07	16.56 ± 0.10	$2.63e+08^{1.83e+08}_{1.49e+09}$	$7.36e+07^{7.36e+07}_{1.10e+08}$	$1.89e+08^{7.25e+07}_{1.41e+09}$	$1.01e+08^{1.01e+08}_{1.64e+09}$
0366	19	13.19 ± 0.05	13.22 ± 0.10	$4.04e+09^{4.04e+09}_{3.63e+10}$	$2.68e+09^{1.82e+09}_{3.27e+09}$	$1.36e+09^{1.36e+09}_{3.44e+10}$	$3.86e+09^{3.86e+09}_{5.90e+10}$
0367	3	14.91 ± 0.07	14.93 ± 0.10	$1.40e+09^{9.07e+08}_{7.95e+09}$	$3.91e+08^{3.91e+08}_{8.37e+08}$	$1.01e+09^{3.05e+08}_{7.53e+09}$	$5.37e+08^{5.37e+08}_{1.38e+10}$
0371	19	12.42 ± 0.05	12.43 ± 0.10	$1.55e+10^{1.55e+10}_{1.89e+10}$	$1.07e+10^{1.07e+10}_{1.29e+10}$	$4.87e+09^{4.87e+09}_{6.04e+09}$	$1.55e+10^{1.55e+10}_{2.25e+11}$
0373	19	12.26 ± 0.05	12.27 ± 0.10	$1.62e+10^{1.38e+10}_{1.80e+10}$	$1.11e+10^{9.43e+09}_{1.23e+10}$	$5.12e+09^{4.32e+09}_{5.74e+09}$	$1.62e+10^{1.62e+10}_{2.57e+11}$
0375	19	11.85 ± 0.05	11.84 ± 0.10	$2.24e+10^{2.24e+10}_{2.73e+10}$	$1.54e+10^{1.53e+10}_{1.86e+10}$	$7.01e+09^{7.00e+09}_{8.69e+09}$	$2.24e+10^{2.24e+10}_{2.97e+11}$
0379	3	0.00 ± -99999.00	198.00 ± 99.00	$0.00e+00^{0.00e+00}_{0.00e+00}$	$0.00e+00^{0.00e+00}_{0.00e+00}$	$0.00e+00^{0.00e+00}_{0.00e+00}$	$6.95e-310^{6.95e-310}_{6.95e-310}$
0381	3	16.19 ± 0.09	16.07 ± 0.10	$1.42e+09^{2.40e+08}_{1.42e+09}$	$7.60e+07^{7.32e+07}_{1.50e+08}$	$1.35e+09^{9.86e+07}_{1.35e+09}$	$1.07e+08^{1.07e+08}_{1.53e+09}$
0382	7	11.52 ± 0.05	11.54 ± 0.10	$1.08e+11^{1.08e+11}_{1.08e+11}$	$5.78e+09^{5.77e+09}_{5.78e+09}$	$1.02e+11^{1.02e+11}_{1.02e+11}$	$8.12e+09^{8.12e+09}_{2.44e+10}$
0386	17	13.13 ± 0.05	13.12 ± 0.10	$7.21e+09^{6.58e+09}_{8.02e+09}$	$4.93e+09^{4.52e+09}_{5.46e+09}$	$2.28e+09^{2.06e+09}_{2.56e+09}$	$7.21e+09^{7.21e+09}_{8.80e+10}$
0393	7	12.71 ± 0.05	12.75 ± 0.10	$4.21e+10^{5.31e+09}_{4.21e+10}$	$2.25e+09^{2.25e+09}_{3.20e+09}$	$3.99e+10^{2.11e+09}_{3.99e+10}$	$3.16e+09^{3.16e+09}_{3.38e+10}$
0404	7	13.96 ± 0.05	13.94 ± 0.10	$2.58e+09^{2.51e+09}_{2.31e+10}$	$1.71e+09^{1.23e+09}_{1.73e+09}$	$8.68e+08^{7.88e+08}_{2.18e+10}$	$2.46e+09^{2.46e+09}_{1.58e+10}$
0408	19	10.94 ± 0.05	10.93 ± 0.10	$6.30e+10^{6.30e+10}_{7.68e+10}$	$4.33e+10^{4.32e+10}_{5.23e+10}$	$1.97e+10^{1.97e+10}_{2.45e+10}$	$6.30e+10^{6.30e+10}_{9.13e+11}$

continued

VCC [1]	Type-ID [2]	$mag_{r,obs}$ [mag] [3]	$mag_{r,mod}$ [mag] [4]	M_{tot} [Gyr] [5]	$M_{stellar}$ [$M_\odot$] [6]	M_{gas} [$M_\odot$] [7]	M_{nonvis} [$M_\odot$] [8]
0409	25	17.57 ± 0.09	17.61 ± 0.10	$3.78e+08^{5.95e+07}_{3.78e+08}$	$2.02e+07^{2.02e+07}_{2.62e+07}$	$3.58e+08^{3.33e+07}_{3.58e+08}$	$2.84e+07^{2.84e+07}_{2.60e+08}$
0410	1	16.68 ± 0.05	16.75 ± 0.10	$7.97e+07^{5.70e+07}_{5.83e+08}$	$2.82e+07^{2.53e+07}_{3.57e+07}$	$5.15e+07^{2.89e+07}_{5.52e+08}$	$3.91e+07^{3.91e+07}_{6.11e+08}$
0413	3	16.94 ± 0.06	16.94 ± 0.10	$8.10e+08^{1.11e+08}_{8.10e+08}$	$4.32e+07^{4.32e+07}_{6.73e+07}$	$7.66e+08^{4.42e+07}_{7.66e+08}$	$6.07e+07^{6.07e+07}_{7.42e+08}$
0414	25	16.68 ± 0.07	16.69 ± 0.10	$1.58e+08^{1.58e+08}_{1.41e+09}$	$1.05e+08^{7.52e+07}_{1.05e+08}$	$5.33e+07^{5.33e+07}_{1.33e+09}$	$1.51e+08^{1.51e+08}_{1.33e+09}$
0415	9	14.53 ± 0.05	14.53 ± 0.10	$7.55e+09^{1.19e+09}_{7.55e+09}$	$4.03e+08^{4.03e+08}_{5.26e+08}$	$7.14e+09^{6.67e+08}_{7.15e+09}$	$5.66e+08^{5.66e+08}_{5.10e+09}$
0423	3	15.31 ± 0.12	15.04 ± 0.10	$1.52e+09^{9.89e+08}_{8.55e+09}$	$4.26e+08^{4.26e+08}_{9.28e+08}$	$1.10e+09^{3.16e+08}_{8.10e+09}$	$5.85e+08^{5.85e+08}_{1.74e+10}$
0425	3	17.42 ± 0.11	17.49 ± 0.10	$2.49e+08^{2.35e+08}_{2.27e+09}$	$1.71e+08^{1.21e+08}_{2.06e+08}$	$7.80e+07^{7.38e+07}_{2.15e+09}$	$2.49e+08^{2.49e+08}_{5.13e+09}$
0428	1	16.68 ± 0.05	16.79 ± 0.10	$5.51e+07^{4.27e+07}_{6.88e+07}$	$1.85e+07^{1.85e+07}_{3.28e+07}$	$3.66e+07^{1.37e+07}_{4.58e+07}$	$2.57e+07^{2.57e+07}_{2.64e+08}$
0429	29	15.99 ± 0.05	16.02 ± 0.10	$3.58e+08^{2.28e+08}_{7.83e+08}$	$1.00e+08^{1.00e+08}_{1.52e+08}$	$2.58e+08^{7.61e+07}_{6.68e+08}$	$1.37e+08^{1.37e+08}_{2.62e+09}$
0446	29	15.15 ± 0.05	15.17 ± 0.10	$6.52e+08^{6.52e+08}_{4.13e+09}$	$2.87e+08^{2.20e+08}_{2.87e+08}$	$3.65e+08^{3.65e+08}_{3.91e+09}$	$4.08e+08^{4.08e+08}_{2.93e+09}$
0448	3	16.36 ± 0.05	16.39 ± 0.10	$9.54e+08^{2.04e+08}_{9.54e+08}$	$5.09e+07^{5.09e+07}_{6.33e+07}$	$9.04e+08^{1.41e+08}_{9.04e+08}$	$7.15e+07^{7.15e+07}_{5.50e+08}$
0449	5	13.34 ± 0.05	13.34 ± 0.10	$8.45e+09^{6.64e+09}_{1.12e+10}$	$3.73e+09^{3.46e+09}_{4.01e+09}$	$4.73e+09^{2.63e+09}_{7.71e+09}$	$5.29e+09^{5.29e+09}_{3.14e+10}$
0450	19	14.76 ± 0.05	14.76 ± 0.10	$1.10e+09^{1.10e+09}_{9.81e+09}$	$7.30e+08^{5.24e+08}_{7.30e+08}$	$3.70e+08^{3.70e+08}_{9.29e+09}$	$1.05e+09^{1.05e+09}_{3.89e+09}$
0453	11	15.73 ± 0.05	15.77 ± 0.10	$2.59e+09^{3.28e+08}_{2.59e+09}$	$1.38e+08^{1.38e+08}_{1.98e+08}$	$2.45e+09^{1.30e+08}_{2.45e+09}$	$1.94e+08^{1.94e+08}_{2.08e+09}$
0459	1	14.37 ± 0.05	14.38 ± 0.10	$5.60e+09^{5.60e+09}_{5.60e+09}$	$2.99e+08^{2.99e+08}_{2.99e+08}$	$5.30e+09^{5.30e+09}_{5.30e+09}$	$4.20e+08^{4.20e+08}_{1.26e+09}$
0460	17	10.11 ± 0.05	10.05 ± 0.10	$1.07e+11^{1.00e+11}_{1.30e+11}$	$7.35e+10^{6.86e+10}_{8.89e+10}$	$3.35e+10^{3.13e+10}_{4.16e+10}$	$1.07e+11^{1.07e+11}_{1.62e+12}$
0465	7	11.82 ± 0.05	11.83 ± 0.10	$6.09e+10^{2.40e+10}_{6.09e+10}$	$3.25e+09^{3.25e+09}_{3.51e+09}$	$5.76e+10^{2.05e+10}_{5.76e+10}$	$4.56e+09^{4.56e+09}_{2.36e+10}$
0472	25	16.42 ± 0.06	16.37 ± 0.10	$2.59e+08^{2.25e+08}_{2.01e+09}$	$1.78e+08^{1.07e+08}_{2.57e+08}$	$8.11e+07^{7.55e+07}_{1.91e+09}$	$2.57e+08^{2.57e+08}_{5.87e+09}$
0476	3	17.23 ± 0.09	17.27 ± 0.10	$5.29e+08^{8.22e+07}_{5.30e+08}$	$2.82e+07^{2.75e+07}_{6.27e+07}$	$5.01e+08^{3.18e+07}_{5.01e+08}$	$3.97e+07^{3.97e+07}_{7.17e+08}$
0477	3	16.51 ± 0.08	16.51 ± 0.10	$1.94e+08^{1.66e+08}_{1.05e+09}$	$5.43e+07^{5.43e+07}_{7.32e+07}$	$1.40e+08^{9.29e+07}_{9.96e+08}$	$7.45e+07^{7.45e+07}_{8.77e+08}$

continued

VCC	Type-ID	$mag_{r,obs}$ [mag]	$mag_{r,mod}$ [mag]	M_{tot} [Gyr]	$M_{stellar}$ [$M_\odot$]	M_{gas} [$M_\odot$]	M_{nonvis} [$M_\odot$]
[1]	[2]	[3]	[4]	[5]	[6]	[7]	[8]
0479	3	15.84 ± 0.05	15.89 ± 0.10	$1.87e+09^{2.95e+08}_{1.87e+09}$	$9.97e+07^{9.97e+07}_{1.30e+08}$	$1.77e+09^{1.65e+08}_{1.77e+09}$	$1.40e+08^{1.40e+08}_{1.44e+09}$
0483	7	0.00 ± -99999.00	198.00 ± 99.00	$0.00e+00^{0.00e+00}_{0.00e+00}$	$0.00e+00^{0.00e+00}_{0.00e+00}$	$0.00e+00^{0.00e+00}_{0.00e+00}$	$6.95e-310^{6.95e-310}_{6.95e-310}$
0488	3	16.72 ± 0.06	16.81 ± 0.10	$8.75e+08^{1.25e+08}_{8.75e+08}$	$4.67e+07^{4.67e+07}_{7.53e+07}$	$8.28e+08^{4.95e+07}_{8.28e+08}$	$6.56e+07^{6.56e+07}_{8.87e+08}$
0491	7	12.16 ± 0.05	12.18 ± 0.10	$3.81e+10^{6.47e+09}_{3.81e+10}$	$2.03e+09^{1.81e+09}_{2.04e+09}$	$3.61e+10^{4.66e+09}_{3.61e+10}$	$2.86e+09^{2.86e+09}_{1.36e+10}$
0494	25	15.08 ± 0.06	15.02 ± 0.10	$5.68e+09^{7.02e+08}_{5.68e+09}$	$3.03e+08^{2.90e+08}_{7.46e+08}$	$5.38e+09^{2.54e+08}_{5.38e+09}$	$4.26e+08^{4.26e+08}_{1.18e+10}$
0497	7	0.00 ± -99999.00	198.00 ± 99.00	$0.00e+00^{0.00e+00}_{0.00e+00}$	$0.00e+00^{0.00e+00}_{0.00e+00}$	$0.00e+00^{0.00e+00}_{0.00e+00}$	$6.95e-310^{6.95e-310}_{6.95e-310}$
0509	9	14.80 ± 0.05	14.83 ± 0.10	$8.99e+08^{8.99e+08}_{4.28e+09}$	$2.78e+08^{2.29e+08}_{2.78e+08}$	$6.20e+08^{6.20e+08}_{4.06e+09}$	$3.94e+08^{3.94e+08}_{2.20e+09}$
0512	11	15.13 ± 0.05	15.10 ± 0.10	$3.42e+09^{5.76e+08}_{3.42e+09}$	$1.82e+08^{1.82e+08}_{2.54e+08}$	$3.23e+09^{3.22e+08}_{3.24e+09}$	$2.56e+08^{2.56e+08}_{2.31e+09}$
0513	1	14.62 ± 0.05	14.67 ± 0.10	$8.56e+09^{1.04e+09}_{8.56e+09}$	$4.57e+08^{4.57e+08}_{6.91e+08}$	$8.10e+09^{3.50e+08}_{8.11e+09}$	$6.42e+08^{6.42e+08}_{1.11e+10}$
0514	7	14.12 ± 0.05	14.11 ± 0.10	$2.25e+09^{1.70e+09}_{4.23e+09}$	$6.97e+08^{5.41e+08}_{7.49e+08}$	$1.55e+09^{9.51e+08}_{3.62e+09}$	$9.85e+08^{9.85e+08}_{7.44e+09}$
0520	3	17.86 ± 0.11	17.86 ± 0.10	$2.55e+08^{4.71e+07}_{2.55e+08}$	$1.36e+07^{1.32e+07}_{1.66e+07}$	$2.41e+08^{3.39e+07}_{2.41e+08}$	$1.91e+07^{1.91e+07}_{1.64e+08}$
0522	17	12.22 ± 0.05	12.23 ± 0.10	$1.18e+10^{1.18e+10}_{1.59e+10}$	$8.10e+09^{7.89e+09}_{1.09e+10}$	$3.70e+09^{3.70e+09}_{5.04e+09}$	$1.17e+10^{1.17e+10}_{1.80e+11}$
0524	5	11.67 ± 0.05	11.65 ± 0.10	$3.13e+10^{3.13e+10}_{3.67e+10}$	$2.15e+10^{2.15e+10}_{2.50e+10}$	$9.81e+09^{9.81e+09}_{1.17e+10}$	$3.13e+10^{3.13e+10}_{3.78e+11}$
0530	3	14.76 ± 0.06	14.72 ± 0.10	$1.09e+09^{8.32e+08}_{5.21e+09}$	$3.38e+08^{2.78e+08}_{3.67e+08}$	$7.52e+08^{4.66e+08}_{4.93e+09}$	$4.77e+08^{4.77e+08}_{3.68e+09}$
0534	17	12.49 ± 0.05	12.47 ± 0.10	$1.24e+10^{1.13e+10}_{1.33e+10}$	$8.51e+09^{7.79e+09}_{9.08e+09}$	$3.93e+09^{3.56e+09}_{4.23e+09}$	$1.24e+10^{1.24e+10}_{1.38e+11}$
0546	25	15.00 ± 0.05	15.02 ± 0.10	$5.29e+09^{6.53e+08}_{5.29e+09}$	$2.82e+08^{2.82e+08}_{3.94e+08}$	$5.01e+09^{2.59e+08}_{5.01e+09}$	$3.97e+08^{3.97e+08}_{4.22e+09}$
0559	17	11.49 ± 0.05	11.47 ± 0.10	$2.36e+10^{2.36e+10}_{2.12e+11}$	$1.62e+10^{1.13e+10}_{1.90e+10}$	$7.40e+09^{7.40e+09}_{2.01e+11}$	$2.35e+10^{2.35e+10}_{2.48e+11}$
0562	1	15.56 ± 0.05	15.60 ± 0.10	$2.72e+08^{2.09e+08}_{2.72e+08}$	$7.60e+07^{7.60e+07}_{1.05e+08}$	$1.96e+08^{1.06e+08}_{1.96e+08}$	$1.04e+08^{1.04e+08}_{1.36e+09}$
0566	11	15.97 ± 0.05	16.03 ± 0.10	$1.79e+08^{1.79e+08}_{1.13e+09}$	$5.00e+07^{5.00e+07}_{6.01e+07}$	$1.29e+08^{1.29e+08}_{1.07e+09}$	$6.86e+07^{6.86e+07}_{3.75e+08}$
0567	7	13.51 ± 0.05	13.52 ± 0.10	$2.08e+10^{2.59e+09}_{2.08e+10}$	$1.11e+09^{1.11e+09}_{1.57e+09}$	$1.97e+10^{1.03e+09}_{1.97e+10}$	$1.56e+09^{1.56e+09}_{9.15e+09}$

continued

VCC	Type-ID	$mag_{r,obs}$ [mag]	$mag_{r,mod}$ [mag]	M_{tot} [Gyr]	$M_{stellar}$ [$M_\odot$]	M_{gas} [$M_\odot$]	M_{nonvis} [$M_\odot$]
[1]	[2]	[3]	[4]	[5]	[6]	[7]	[8]
0570	17	11.29 ± 0.05	11.26 ± 0.10	$3.93e+10^{3.93e+10}_{4.79e+10}$	$2.70e+10^{2.70e+10}_{3.26e+10}$	$1.23e+10^{1.23e+10}_{1.53e+10}$	$3.93e+10^{3.93e+10}_{5.22e+11}$
0574	25	16.48 ± 0.09	16.49 ± 0.10	$3.25e+08^{2.83e+08}_{7.18e+08}$	$9.10e+07^{9.10e+07}_{1.25e+08}$	$2.34e+08^{1.58e+08}_{6.13e+08}$	$1.25e+08^{1.25e+08}_{1.21e+09}$
0576	5	12.46 ± 0.05	12.44 ± 0.10	$1.36e+10^{1.36e+10}_{1.21e+11}$	$9.00e+09^{6.46e+09}_{9.03e+09}$	$4.56e+09^{4.56e+09}_{1.15e+11}$	$1.29e+10^{1.29e+10}_{8.28e+10}$
0583	3	14.77 ± 0.05	14.74 ± 0.10	$7.47e+09^{9.23e+08}_{7.47e+09}$	$3.98e+08^{3.98e+08}_{5.57e+08}$	$7.07e+09^{3.66e+08}_{7.07e+09}$	$5.60e+08^{5.60e+08}_{7.34e+09}$
0584	3	15.56 ± 0.07	15.61 ± 0.10	$3.77e+08^{3.77e+08}_{3.03e+09}$	$2.28e+08^{1.53e+08}_{2.86e+08}$	$1.50e+08^{1.45e+08}_{2.87e+09}$	$3.26e+08^{3.26e+08}_{3.90e+09}$
0585	3	16.73 ± 0.12	16.76 ± 0.10	$6.95e+08^{1.47e+08}_{6.96e+08}$	$3.71e+07^{3.71e+07}_{4.54e+07}$	$6.58e+08^{1.01e+08}_{6.59e+08}$	$5.22e+07^{5.22e+07}_{4.00e+08}$
0593	23	14.43 ± 0.05	14.45 ± 0.10	$7.98e+09^{1.26e+09}_{7.98e+09}$	$4.26e+08^{4.26e+08}_{5.56e+08}$	$7.55e+09^{7.05e+08}_{7.55e+09}$	$5.98e+08^{5.98e+08}_{3.87e+09}$
0596	7	9.02 ± 0.05	9.03 ± 0.10	$1.50e+12^{1.85e+11}_{1.50e+12}$	$8.01e+10^{8.01e+10}_{1.12e+11}$	$1.42e+12^{7.36e+10}_{1.42e+12}$	$1.13e+11^{1.13e+11}_{6.58e+11}$
0618	3	16.24 ± 0.06	16.24 ± 0.10	$9.21e+08^{3.84e+08}_{9.21e+08}$	$4.91e+07^{4.91e+07}_{5.61e+07}$	$8.72e+08^{3.28e+08}_{8.72e+08}$	$6.90e+07^{6.90e+07}_{3.65e+08}$
0620	11	15.36 ± 0.05	15.37 ± 0.10	$2.61e+09^{1.03e+09}_{2.61e+09}$	$1.39e+08^{1.39e+08}_{1.51e+08}$	$2.47e+09^{8.80e+08}_{2.47e+09}$	$1.96e+08^{1.96e+08}_{1.01e+09}$
0630	9	12.23 ± 0.05	12.23 ± 0.10	$9.62e+09^{9.62e+09}_{9.63e+09}$	$6.39e+09^{6.39e+09}_{6.39e+09}$	$3.24e+09^{3.24e+09}_{3.24e+09}$	$9.18e+09^{9.18e+09}_{2.76e+10}$
0633	25	16.47 ± 0.09	16.42 ± 0.10	$2.03e+08^{2.02e+08}_{1.64e+09}$	$1.35e+08^{8.40e+07}_{2.20e+08}$	$6.83e+07^{6.83e+07}_{1.55e+09}$	$1.94e+08^{1.94e+08}_{3.70e+09}$
0641	1	15.59 ± 0.05	15.66 ± 0.10	$2.04e+09^{2.33e+08}_{2.04e+09}$	$1.09e+08^{1.03e+08}_{1.56e+08}$	$1.93e+09^{7.79e+07}_{1.93e+09}$	$1.53e+08^{1.53e+08}_{3.04e+09}$
0651	25	16.38 ± 0.09	16.24 ± 0.10	$1.59e+09^{2.12e+08}_{1.59e+09}$	$8.48e+07^{8.11e+07}_{2.65e+08}$	$1.50e+09^{8.20e+07}_{1.51e+09}$	$1.19e+08^{1.19e+08}_{3.96e+09}$
0654	19	10.91 ± 0.05	10.89 ± 0.10	$6.59e+10^{6.13e+10}_{8.03e+10}$	$4.52e+10^{4.21e+10}_{5.47e+10}$	$2.06e+10^{1.92e+10}_{2.56e+10}$	$6.59e+10^{6.59e+10}_{1.08e+12}$
0655	1	12.37 ± 0.05	12.39 ± 0.10	$7.09e+10^{8.51e+09}_{7.09e+10}$	$3.78e+09^{3.78e+09}_{5.65e+09}$	$6.71e+10^{2.86e+09}_{6.71e+10}$	$5.32e+09^{5.32e+09}_{5.88e+10}$
0656	5	11.99 ± 0.05	11.96 ± 0.10	$2.15e+10^{2.15e+10}_{2.70e+10}$	$1.48e+10^{1.48e+10}_{1.84e+10}$	$6.74e+09^{6.74e+09}_{8.59e+09}$	$2.14e+10^{2.14e+10}_{2.92e+11}$
0657	19	12.10 ± 0.05	12.11 ± 0.10	$2.32e+10^{2.16e+10}_{2.83e+10}$	$1.60e+10^{1.49e+10}_{1.93e+10}$	$7.29e+09^{6.78e+09}_{9.04e+09}$	$2.32e+10^{2.32e+10}_{3.59e+11}$
0664	7	13.10 ± 0.05	13.10 ± 0.10	$1.63e+10^{2.93e+09}_{1.63e+10}$	$8.72e+08^{8.22e+08}_{8.72e+08}$	$1.55e+10^{2.11e+09}_{1.55e+10}$	$1.22e+09^{1.22e+09}_{4.80e+09}$
0666	3	16.03 ± 0.07	16.01 ± 0.10	$1.92e+09^{3.02e+08}_{1.92e+09}$	$1.02e+08^{1.02e+08}_{1.33e+08}$	$1.82e+09^{1.69e+08}_{1.82e+09}$	$1.44e+08^{1.44e+08}_{1.47e+09}$

continued

VCC [1]	Type-ID [2]	$mag_{r,obs}$ [mag] [3]	$mag_{r,mod}$ [mag] [4]	M_{tot} [Gyr] [5]	$M_{stellar}$ [$M_\odot$] [6]	M_{gas} [$M_\odot$] [7]	M_{nonvis} [$M_\odot$] [8]
0667	7	13.20 ± 0.05	13.19 ± 0.10	$4.01e+09^{4.01e+09}_{3.58e+10}$	$2.66e+09^{1.91e+09}_{2.66e+09}$	$1.35e+09^{1.35e+09}_{3.39e+10}$	$3.82e+09^{3.82e+09}_{1.42e+10}$
0672	19	13.11 ± 0.05	13.12 ± 0.10	$5.19e+09^{5.00e+09}_{4.48e+10}$	$3.56e+09^{2.39e+09}_{4.60e+09}$	$1.63e+09^{1.63e+09}_{4.24e+10}$	$5.16e+09^{5.16e+09}_{7.41e+10}$
0679	11	15.17 ± 0.05	15.21 ± 0.10	$3.96e+09^{5.43e+08}_{3.96e+09}$	$2.11e+08^{2.11e+08}_{3.28e+08}$	$3.75e+09^{2.16e+08}_{3.75e+09}$	$2.97e+08^{2.97e+08}_{3.25e+09}$
0688	7	13.16 ± 0.05	13.14 ± 0.10	$4.16e+09^{4.16e+09}_{3.64e+10}$	$2.76e+09^{1.94e+09}_{2.76e+09}$	$1.40e+09^{1.40e+09}_{3.44e+10}$	$3.97e+09^{3.97e+09}_{2.51e+10}$
0692	7	12.21 ± 0.05	12.24 ± 0.10	$5.56e+10^{8.80e+09}_{5.56e+10}$	$2.97e+09^{2.97e+09}_{3.88e+09}$	$5.27e+10^{4.92e+09}_{5.27e+10}$	$4.17e+09^{4.17e+09}_{3.76e+10}$
0697	7	13.08 ± 0.05	13.11 ± 0.10	$3.46e+10^{4.27e+09}_{3.46e+10}$	$1.85e+09^{1.85e+09}_{2.58e+09}$	$3.27e+10^{1.70e+09}_{3.28e+10}$	$2.59e+09^{2.59e+09}_{2.76e+10}$
0699	7	12.99 ± 0.05	12.99 ± 0.10	$2.23e+10^{4.68e+09}_{2.23e+10}$	$1.19e+09^{1.19e+09}_{1.45e+09}$	$2.11e+10^{3.23e+09}_{2.11e+10}$	$1.67e+09^{1.67e+09}_{9.11e+09}$
0703	3	17.00 ± 0.07	16.94 ± 0.10	$2.94e+08^{1.34e+08}_{7.43e+08}$	$4.30e+07^{3.75e+07}_{4.79e+07}$	$2.51e+08^{9.64e+07}_{7.03e+08}$	$6.05e+07^{6.05e+07}_{5.31e+08}$
0705	25	16.09 ± 0.07	16.08 ± 0.10	$1.05e+09^{3.01e+08}_{2.67e+09}$	$1.54e+08^{1.33e+08}_{2.84e+08}$	$8.98e+08^{1.01e+08}_{2.53e+09}$	$2.16e+08^{2.16e+08}_{5.10e+09}$
0713	7	12.25 ± 0.05	12.23 ± 0.10	$1.37e+10^{1.37e+10}_{1.78e+10}$	$9.39e+09^{9.39e+09}_{1.21e+10}$	$4.29e+09^{4.29e+09}_{5.69e+09}$	$1.36e+10^{1.36e+10}_{1.72e+11}$
0739	9	13.44 ± 0.05	13.47 ± 0.10	$1.30e+10^{2.98e+09}_{1.30e+10}$	$6.92e+08^{6.92e+08}_{9.23e+08}$	$1.23e+10^{2.06e+09}_{1.23e+10}$	$9.73e+08^{9.73e+08}_{6.33e+09}$
0740	11	15.40 ± 0.05	15.42 ± 0.10	$2.30e+09^{4.97e+08}_{2.30e+09}$	$1.23e+08^{1.23e+08}_{1.54e+08}$	$2.18e+09^{3.43e+08}_{2.18e+09}$	$1.72e+08^{1.72e+08}_{1.33e+09}$
0768	7	14.47 ± 0.05	14.50 ± 0.10	$6.62e+09^{1.05e+09}_{6.62e+09}$	$3.53e+08^{3.53e+08}_{4.62e+08}$	$6.27e+09^{5.86e+08}_{6.27e+09}$	$4.96e+08^{4.96e+08}_{2.80e+09}$
0780	25	16.65 ± 0.10	16.55 ± 0.10	$2.63e+08^{1.98e+08}_{1.26e+09}$	$8.13e+07^{6.40e+07}_{8.72e+07}$	$1.81e+08^{1.11e+08}_{1.19e+09}$	$1.15e+08^{1.15e+08}_{1.16e+09}$
0792	17	11.20 ± 0.05	11.17 ± 0.10	$3.70e+10^{3.70e+10}_{4.39e+10}$	$2.54e+10^{2.54e+10}_{3.00e+10}$	$1.16e+10^{1.16e+10}_{1.40e+10}$	$3.70e+10^{3.70e+10}_{4.49e+11}$
0793	3	0.00 ± -99999.00	198.00 ± 99.00	$0.00e+00^{0.00e+00}_{0.00e+00}$	$0.00e+00^{0.00e+00}_{0.00e+00}$	$0.00e+00^{0.00e+00}_{0.00e+00}$	$6.95e-310^{6.95e-310}_{6.95e-310}$
0801	15	11.86 ± 0.05	11.89 ± 0.10	$7.44e+10^{1.18e+10}_{7.44e+10}$	$3.97e+09^{3.97e+09}_{5.19e+09}$	$7.04e+10^{6.59e+09}_{7.04e+10}$	$5.58e+09^{5.58e+09}_{4.51e+10}$
0802	1	16.12 ± 0.05	16.16 ± 0.10	$1.25e+09^{1.72e+08}_{1.25e+09}$	$6.67e+07^{6.34e+07}_{9.63e+07}$	$1.18e+09^{8.73e+07}_{1.18e+09}$	$9.38e+07^{9.38e+07}_{1.83e+09}$
0809	7	13.80 ± 0.05	13.84 ± 0.10	$2.08e+09^{2.08e+09}_{1.68e+10}$	$1.25e+09^{8.98e+08}_{1.25e+09}$	$8.24e+08^{8.24e+08}_{1.59e+10}$	$1.79e+09^{1.79e+09}_{1.26e+10}$
0825	3	15.36 ± 0.05	15.38 ± 0.10	$3.57e+09^{4.67e+08}_{3.57e+09}$	$1.91e+08^{1.91e+08}_{2.82e+08}$	$3.38e+09^{1.85e+08}_{3.38e+09}$	$2.68e+08^{2.68e+08}_{2.89e+09}$

continued

VCC [1]	Type-ID [2]	$mag_{r,obs}$ [mag] [3]	$mag_{r,mod}$ [mag] [4]	M_{tot} [Gyr] [5]	$M_{stellar}$ [$M_\odot$] [6]	M_{gas} [$M_\odot$] [7]	M_{nonvis} [$M_\odot$] [8]
0826	3	14.69 ± 0.06	14.67 ± 0.10	$1.86e+09^{8.57e+08}_{1.86e+09}$	$2.72e+08^{2.40e+08}_{3.11e+08}$	$1.59e+09^{6.17e+08}_{1.59e+09}$	$3.83e+08^{3.83e+08}_{2.25e+09}$
0827	7	12.64 ± 0.05	12.64 ± 0.10	$7.32e+09^{7.32e+09}_{7.32e+09}$	$4.42e+09^{4.42e+09}_{4.42e+09}$	$2.90e+09^{2.90e+09}_{2.90e+09}$	$6.32e+09^{6.32e+09}_{1.89e+10}$
0836	17	10.76 ± 0.05	10.75 ± 0.10	$4.26e+10^{4.26e+10}_{3.81e+11}$	$2.82e+10^{2.03e+10}_{2.84e+10}$	$1.43e+10^{1.43e+10}_{3.61e+11}$	$4.06e+10^{4.06e+10}_{2.91e+11}$
0841	1	14.63 ± 0.05	14.65 ± 0.10	$8.01e+09^{9.89e+08}_{8.01e+09}$	$4.27e+08^{4.27e+08}_{5.97e+08}$	$7.58e+09^{3.92e+08}_{7.58e+09}$	$6.00e+08^{6.00e+08}_{7.84e+09}$
0849	5	12.56 ± 0.05	12.57 ± 0.10	$3.68e+10^{5.95e+09}_{3.69e+10}$	$1.97e+09^{1.97e+09}_{2.62e+09}$	$3.49e+10^{3.33e+09}_{3.49e+10}$	$2.76e+09^{2.76e+09}_{1.80e+10}$
0851	7	13.13 ± 0.05	13.13 ± 0.10	$4.20e+09^{4.20e+09}_{3.62e+10}$	$2.78e+09^{1.93e+09}_{2.79e+09}$	$1.41e+09^{1.41e+09}_{3.42e+10}$	$4.01e+09^{4.01e+09}_{2.52e+10}$
0857	5	10.48 ± 0.05	10.45 ± 0.10	$6.06e+10^{6.06e+10}_{5.52e+11}$	$4.16e+10^{2.94e+10}_{4.88e+10}$	$1.90e+10^{1.90e+10}_{5.22e+11}$	$6.03e+10^{6.03e+10}_{8.39e+11}$
0859	7	13.23 ± 0.05	13.18 ± 0.10	$6.69e+09^{6.68e+09}_{8.73e+09}$	$4.59e+09^{4.59e+09}_{5.95e+09}$	$2.10e+09^{2.09e+09}_{2.78e+09}$	$6.65e+09^{6.65e+09}_{1.06e+11}$
0865	7	12.17 ± 0.05	12.16 ± 0.10	$9.07e+09^{8.92e+09}_{1.98e+10}$	$2.54e+09^{2.54e+09}_{3.93e+09}$	$6.53e+09^{4.99e+09}_{1.69e+10}$	$3.49e+09^{3.49e+09}_{3.34e+10}$
0869	25	14.71 ± 0.06	14.68 ± 0.10	$1.01e+09^{1.01e+09}_{8.79e+09}$	$6.73e+08^{4.69e+08}_{6.74e+08}$	$3.41e+08^{3.41e+08}_{8.32e+09}$	$9.68e+08^{9.68e+08}_{9.25e+09}$
0873	7	11.31 ± 0.05	11.29 ± 0.10	$3.17e+10^{3.17e+10}_{4.15e+10}$	$2.18e+10^{2.18e+10}_{2.83e+10}$	$9.95e+09^{9.94e+09}_{1.32e+10}$	$3.16e+10^{3.16e+10}_{4.45e+11}$
0874	7	11.94 ± 0.05	11.95 ± 0.10	$1.36e+10^{1.36e+10}_{1.22e+11}$	$8.99e+09^{6.48e+09}_{9.06e+09}$	$4.56e+09^{4.56e+09}_{1.15e+11}$	$1.29e+10^{1.29e+10}_{7.00e+10}$
0888	3	14.95 ± 0.05	14.97 ± 0.10	$6.60e+08^{6.60e+08}_{4.09e+09}$	$2.91e+08^{2.18e+08}_{2.91e+08}$	$3.69e+08^{3.69e+08}_{3.87e+09}$	$4.13e+08^{4.13e+08}_{2.60e+09}$
0890	1	16.02 ± 0.05	16.03 ± 0.10	$1.35e+09^{2.82e+08}_{1.35e+09}$	$7.18e+07^{7.18e+07}_{8.75e+07}$	$1.27e+09^{1.95e+08}_{1.27e+09}$	$1.01e+08^{1.01e+08}_{5.50e+08}$
0905	7	12.74 ± 0.05	12.75 ± 0.10	$3.36e+10^{5.31e+09}_{3.36e+10}$	$1.79e+09^{1.79e+09}_{2.34e+09}$	$3.18e+10^{2.97e+09}_{3.18e+10}$	$2.52e+09^{2.52e+09}_{1.96e+10}$
0912	5	11.85 ± 0.05	11.85 ± 0.10	$1.37e+10^{1.37e+10}_{1.21e+11}$	$9.10e+09^{6.43e+09}_{9.10e+09}$	$4.61e+09^{4.61e+09}_{1.14e+11}$	$1.31e+10^{1.31e+10}_{8.31e+10}$
0938	7	12.22 ± 0.05	12.21 ± 0.10	$9.82e+09^{9.82e+09}_{2.44e+10}$	$4.33e+09^{3.13e+09}_{4.33e+09}$	$5.49e+09^{5.49e+09}_{2.08e+10}$	$6.14e+09^{6.14e+09}_{4.84e+10}$
0939	7	12.19 ± 0.05	12.22 ± 0.10	$5.97e+10^{9.44e+09}_{5.97e+10}$	$3.19e+09^{3.19e+09}_{4.16e+09}$	$5.66e+10^{5.28e+09}_{5.66e+10}$	$4.48e+09^{4.48e+09}_{4.04e+10}$
0945	11	14.86 ± 0.05	14.82 ± 0.10	$3.34e+09^{5.75e+08}_{3.34e+09}$	$1.78e+08^{1.61e+08}_{1.78e+08}$	$3.16e+09^{4.14e+08}_{3.16e+09}$	$2.50e+08^{2.50e+08}_{1.19e+09}$
0950	11	14.73 ± 0.05	14.68 ± 0.10	$7.70e+08^{7.69e+08}_{1.68e+09}$	$2.15e+08^{2.15e+08}_{3.12e+08}$	$5.55e+08^{5.54e+08}_{1.44e+09}$	$2.96e+08^{2.96e+08}_{2.46e+09}$

continued

VCC	Type-ID	$mag_{r,obs}$ [mag]	$mag_{r,mod}$ [mag]	M_{tot} [Gyr]	$M_{stellar}$ [$M_\odot$]	M_{gas} [$M_\odot$]	M_{nonvis} [$M_\odot$]
[1]	[2]	[3]	[4]	[5]	[6]	[7]	[8]
0952	3	16.40 ± 0.06	16.48 ± 0.10	$1.17e+08^{1.17e+08}_{7.39e+08}$	$3.28e+07^{3.28e+07}_{4.61e+07}$	$8.46e+07^{8.44e+07}_{7.00e+08}$	$4.51e+07^{4.51e+07}_{3.11e+08}$
0957	7	12.00 ± 0.05	12.00 ± 0.10	$6.69e+10^{1.06e+10}_{6.69e+10}$	$3.57e+09^{3.57e+09}_{4.67e+09}$	$6.33e+10^{5.92e+09}_{6.34e+10}$	$5.02e+09^{5.02e+09}_{3.44e+10}$
0958	17	10.86 ± 0.05	10.82 ± 0.10	$6.26e+10^{6.25e+10}_{7.63e+10}$	$4.30e+10^{4.29e+10}_{5.19e+10}$	$1.96e+10^{1.96e+10}_{2.43e+10}$	$6.26e+10^{6.26e+10}_{8.31e+11}$
0963	3	16.41 ± 0.06	16.42 ± 0.10	$2.24e+08^{1.95e+08}_{4.91e+08}$	$6.28e+07^{6.28e+07}_{8.59e+07}$	$1.62e+08^{1.09e+08}_{4.19e+08}$	$8.62e+07^{8.62e+07}_{8.09e+08}$
0975	7	0.00 ± -99999.00	198.00 ± 99.00	$0.00e+00^{0.00e+00}_{0.00e+00}$	$0.00e+00^{0.00e+00}_{0.00e+00}$	$0.00e+00^{0.00e+00}_{0.00e+00}$	$6.95e-310^{6.95e-310}_{6.95e-310}$
0979	17	11.27 ± 0.05	11.25 ± 0.10	$2.40e+11^{2.67e+10}_{2.40e+11}$	$1.28e+10^{1.28e+10}_{1.79e+10}$	$2.27e+11^{9.00e+09}_{2.27e+11}$	$1.80e+10^{1.80e+10}_{2.18e+11}$
0980	7	13.69 ± 0.05	13.66 ± 0.10	$9.68e+09^{1.72e+09}_{9.68e+09}$	$5.16e+08^{4.81e+08}_{5.17e+08}$	$9.17e+09^{1.24e+09}_{9.17e+09}$	$7.26e+08^{7.26e+08}_{3.50e+09}$
0984	17	11.72 ± 0.05	11.71 ± 0.10	$2.45e+10^{2.45e+10}_{2.99e+10}$	$1.68e+10^{1.68e+10}_{2.04e+10}$	$7.68e+09^{7.68e+09}_{9.53e+09}$	$2.45e+10^{2.45e+10}_{3.26e+11}$
0989	7	16.04 ± 0.06	16.04 ± 0.10	$1.33e+09^{2.82e+08}_{1.33e+09}$	$7.11e+07^{7.11e+07}_{8.73e+07}$	$1.26e+09^{1.94e+08}_{1.26e+09}$	$9.99e+07^{9.99e+07}_{6.55e+08}$
0994	25	17.39 ± 0.05	17.39 ± 0.10	$1.58e+08^{1.57e+08}_{2.08e+08}$	$1.08e+08^{1.08e+08}_{1.42e+08}$	$4.94e+07^{4.94e+07}_{6.65e+07}$	$1.57e+08^{1.57e+08}_{2.02e+09}$
0995	7	14.64 ± 0.05	14.65 ± 0.10	$4.30e+09^{1.70e+09}_{4.30e+09}$	$2.30e+08^{2.29e+08}_{2.48e+08}$	$4.07e+09^{1.45e+09}_{4.07e+09}$	$3.23e+08^{3.23e+08}_{1.67e+09}$
1001	3	16.39 ± 0.06	16.39 ± 0.10	$1.79e+08^{1.79e+08}_{4.46e+08}$	$7.88e+07^{5.70e+07}_{7.88e+07}$	$1.00e+08^{1.00e+08}_{3.81e+08}$	$1.12e+08^{1.12e+08}_{7.90e+08}$
1011	9	14.32 ± 0.05	14.32 ± 0.10	$9.26e+09^{1.46e+09}_{9.26e+09}$	$4.94e+08^{4.94e+08}_{6.44e+08}$	$8.76e+09^{8.18e+08}_{8.77e+09}$	$6.94e+08^{6.94e+08}_{3.91e+09}$
1013	3	16.00 ± 0.06	15.96 ± 0.10	$1.75e+09^{2.78e+08}_{1.76e+09}$	$9.36e+07^{8.96e+07}_{1.22e+08}$	$1.66e+09^{1.55e+08}_{1.66e+09}$	$1.32e+08^{1.32e+08}_{1.48e+09}$
1017	3	14.49 ± 0.05	14.49 ± 0.10	$1.20e+09^{1.12e+09}_{9.10e+09}$	$7.96e+08^{4.61e+08}_{1.29e+09}$	$4.04e+08^{4.04e+08}_{8.61e+09}$	$1.15e+09^{1.15e+09}_{2.11e+10}$
1020	25	16.28 ± 0.06	16.27 ± 0.10	$2.40e+08^{2.40e+08}_{2.12e+09}$	$1.59e+08^{1.13e+08}_{1.59e+08}$	$8.08e+07^{8.08e+07}_{2.00e+09}$	$2.29e+08^{2.29e+08}_{2.06e+09}$
1021	3	14.64 ± 0.05	14.62 ± 0.10	$1.13e+09^{1.13e+09}_{7.12e+09}$	$4.96e+08^{3.80e+08}_{4.96e+08}$	$6.29e+08^{6.29e+08}_{6.74e+09}$	$7.04e+08^{7.04e+08}_{5.64e+09}$
1047	17	11.54 ± 0.05	11.54 ± 0.10	$3.15e+10^{3.15e+10}_{3.85e+10}$	$2.17e+10^{2.16e+10}_{2.62e+10}$	$9.88e+09^{9.88e+09}_{1.23e+10}$	$3.15e+10^{3.15e+10}_{4.57e+11}$
1060	11	15.34 ± 0.05	15.38 ± 0.10	$3.37e+08^{3.37e+08}_{2.04e+09}$	$9.43e+07^{9.43e+07}_{1.09e+08}$	$2.42e+08^{2.42e+08}_{1.93e+09}$	$1.29e+08^{1.29e+08}_{6.94e+08}$
1086	23	12.54 ± 0.05	12.52 ± 0.10	$1.00e+10^{1.00e+10}_{1.24e+10}$	$6.88e+09^{6.88e+09}_{8.44e+09}$	$3.14e+09^{3.14e+09}_{3.91e+09}$	$9.97e+09^{9.97e+09}_{1.25e+11}$

continued

VCC [1]	Type-ID [2]	$mag_{r,obs}$ [mag] [3]	$mag_{r,mod}$ [mag] [4]	M_{tot} [Gyr] [5]	$M_{stellar}$ [$M_\odot$] [6]	M_{gas} [$M_\odot$] [7]	M_{nonvis} [$M_\odot$] [8]
1091	5	13.68 ± 0.05	13.67 ± 0.10	$9.60e+09^{4.05e+09}_{9.60e+09}$	$5.12e+08^{5.12e+08}_{5.92e+08}$	$9.09e+09^{3.46e+09}_{9.09e+09}$	$7.20e+08^{7.20e+08}_{3.83e+09}$
1098	3	16.67 ± 0.11	16.55 ± 0.10	$1.11e+09^{1.59e+08}_{1.11e+09}$	$5.93e+07^{5.81e+07}_{9.61e+07}$	$1.05e+09^{6.31e+07}_{1.05e+09}$	$8.34e+07^{8.34e+07}_{1.30e+09}$
1102	3	16.93 ± 0.06	17.00 ± 0.10	$6.19e+08^{1.02e+08}_{6.20e+08}$	$3.31e+07^{3.30e+07}_{4.47e+07}$	$5.86e+08^{5.68e+07}_{5.87e+08}$	$4.65e+07^{4.65e+07}_{4.81e+08}$
1106	3	16.64 ± 0.07	16.67 ± 0.10	$1.57e+08^{1.57e+08}_{1.27e+09}$	$9.46e+07^{6.79e+07}_{9.46e+07}$	$6.21e+07^{6.21e+07}_{1.21e+09}$	$1.35e+08^{1.35e+08}_{1.08e+09}$
1110	17	9.70 ± 0.05	9.69 ± 0.10	$1.59e+11^{1.44e+11}_{1.78e+11}$	$1.09e+11^{9.87e+10}_{1.22e+11}$	$5.02e+10^{4.50e+10}_{5.69e+10}$	$1.59e+11^{1.59e+11}_{1.78e+12}$
1114	3	13.98 ± 0.05	13.99 ± 0.10	$1.25e+10^{1.25e+10}_{1.25e+10}$	$6.69e+08^{6.69e+08}_{6.69e+08}$	$1.19e+10^{1.19e+10}_{1.19e+10}$	$9.40e+08^{9.40e+08}_{2.82e+09}$
1118	7	12.41 ± 0.05	12.43 ± 0.10	$6.77e+10^{8.22e+09}_{6.77e+10}$	$3.61e+09^{3.61e+09}_{5.45e+09}$	$6.41e+10^{2.77e+09}_{6.41e+10}$	$5.08e+09^{5.08e+09}_{5.64e+10}$
1121	3	16.22 ± 0.08	16.18 ± 0.10	$3.10e+08^{2.90e+08}_{2.61e+09}$	$2.13e+08^{1.39e+08}_{3.07e+08}$	$9.70e+07^{9.70e+07}_{2.47e+09}$	$3.08e+08^{3.08e+08}_{7.12e+09}$
1126	7	11.91 ± 0.05	11.88 ± 0.10	$1.62e+10^{1.62e+10}_{1.89e+10}$	$1.11e+10^{1.11e+10}_{1.30e+10}$	$5.07e+09^{5.07e+09}_{5.94e+09}$	$1.61e+10^{1.61e+10}_{9.91e+10}$
1128	3	16.07 ± 0.09	16.06 ± 0.10	$7.07e+08^{3.25e+08}_{1.76e+09}$	$1.03e+08^{9.11e+07}_{1.15e+08}$	$6.04e+08^{2.34e+08}_{1.67e+09}$	$1.45e+08^{1.45e+08}_{1.28e+09}$
1141	1	15.59 ± 0.05	15.59 ± 0.10	$3.11e+09^{3.86e+08}_{3.11e+09}$	$1.66e+08^{1.66e+08}_{2.33e+08}$	$2.94e+09^{1.53e+08}_{2.94e+09}$	$2.33e+08^{2.33e+08}_{3.85e+09}$
1145	5	10.47 ± 0.05	10.45 ± 0.10	$7.46e+10^{7.45e+10}_{8.74e+10}$	$5.12e+10^{5.12e+10}_{5.96e+10}$	$2.34e+10^{2.34e+10}_{2.78e+10}$	$7.45e+10^{7.45e+10}_{8.99e+11}$
1156	7	13.97 ± 0.05	13.99 ± 0.10	$7.92e+09^{3.14e+09}_{7.92e+09}$	$4.23e+08^{4.23e+08}_{4.59e+08}$	$7.50e+09^{2.68e+09}_{7.50e+09}$	$5.94e+08^{5.94e+08}_{3.07e+09}$
1158	17	10.89 ± 0.05	10.90 ± 0.10	$7.10e+10^{6.03e+10}_{7.90e+10}$	$4.86e+10^{4.14e+10}_{5.38e+10}$	$2.24e+10^{1.89e+10}_{2.52e+10}$	$7.10e+10^{7.10e+10}_{1.01e+12}$
1165	25	17.40 ± 0.11	17.31 ± 0.10	$1.19e+08^{1.03e+08}_{6.53e+08}$	$3.35e+07^{3.35e+07}_{4.53e+07}$	$8.60e+07^{5.75e+07}_{6.18e+08}$	$4.59e+07^{4.59e+07}_{5.91e+08}$
1166	3	16.32 ± 0.08	16.32 ± 0.10	$1.56e+09^{1.99e+08}_{1.56e+09}$	$8.32e+07^{7.94e+07}_{1.91e+08}$	$1.48e+09^{7.66e+07}_{1.48e+09}$	$1.17e+08^{1.17e+08}_{2.47e+09}$
1168	3	16.51 ± 0.05	16.28 ± 0.10	$1.01e+09^{1.91e+08}_{1.01e+09}$	$5.41e+07^{5.35e+07}_{2.31e+08}$	$9.59e+08^{7.86e+07}_{9.59e+08}$	$7.60e+07^{7.60e+07}_{3.02e+09}$
1169	3	17.48 ± 0.08	17.50 ± 0.10	$4.95e+07^{4.94e+07}_{2.87e+08}$	$1.38e+07^{1.38e+07}_{1.53e+07}$	$3.56e+07^{3.56e+07}_{2.72e+08}$	$1.90e+07^{1.90e+07}_{1.00e+08}$
1179	29	14.75 ± 0.05	14.75 ± 0.10	$5.62e+09^{2.22e+09}_{5.62e+09}$	$3.00e+08^{3.00e+08}_{3.24e+08}$	$5.32e+09^{1.89e+09}_{5.32e+09}$	$4.21e+08^{4.21e+08}_{2.18e+09}$
1186	25	17.16 ± 0.12	17.11 ± 0.10	$1.34e+08^{1.15e+08}_{2.93e+08}$	$3.77e+07^{3.76e+07}_{5.08e+07}$	$9.68e+07^{6.44e+07}_{2.51e+08}$	$5.17e+07^{5.17e+07}_{5.54e+08}$

continued

VCC [1]	Type-ID [2]	$mag_{r,obs}$ [mag] [3]	$mag_{r,mod}$ [mag] [4]	M_{tot} [Gyr] [5]	$M_{stellar}$ [$M_\odot$] [6]	M_{gas} [$M_\odot$] [7]	M_{nonvis} [$M_\odot$] [8]
1188	15	12.80 ± 0.05	12.81 ± 0.10	$6.12e+09^{6.12e+09}_{5.48e+10}$	$4.06e+09^{2.92e+09}_{4.08e+09}$	$2.06e+09^{2.06e+09}_{5.19e+10}$	$5.84e+09^{5.84e+09}_{5.71e+10}$
1189	7	13.21 ± 0.05	13.20 ± 0.10	$4.98e+09^{3.76e+09}_{9.36e+09}$	$1.54e+09^{1.37e+09}_{1.66e+09}$	$3.43e+09^{2.10e+09}_{8.00e+09}$	$2.18e+09^{2.18e+09}_{1.51e+10}$
1190	17	10.95 ± 0.05	10.94 ± 0.10	$5.88e+10^{5.88e+10}_{7.17e+10}$	$4.04e+10^{4.04e+10}_{4.89e+10}$	$1.84e+10^{1.84e+10}_{2.29e+10}$	$5.88e+10^{5.88e+10}_{7.82e+11}$
1193	7	13.52 ± 0.05	13.53 ± 0.10	$1.93e+10^{1.93e+10}_{1.93e+10}$	$1.03e+09^{1.03e+09}_{1.03e+09}$	$1.83e+10^{1.83e+10}_{1.83e+10}$	$1.45e+09^{1.45e+09}_{4.35e+09}$
1200	3	14.70 ± 0.05	14.72 ± 0.10	$3.67e+09^{1.55e+09}_{3.67e+09}$	$1.96e+08^{1.96e+08}_{2.27e+08}$	$3.48e+09^{1.33e+09}_{3.48e+09}$	$2.75e+08^{2.75e+08}_{1.15e+09}$
1205	7	12.25 ± 0.05	12.25 ± 0.10	$5.44e+10^{8.61e+09}_{5.44e+10}$	$2.90e+09^{2.90e+09}_{3.79e+09}$	$5.15e+10^{4.81e+09}_{5.15e+10}$	$4.08e+09^{4.08e+09}_{1.76e+10}$
1208	11	15.13 ± 0.05	15.16 ± 0.10	$2.92e+09^{6.29e+08}_{2.92e+09}$	$1.56e+08^{1.56e+08}_{1.95e+08}$	$2.76e+09^{4.34e+08}_{2.77e+09}$	$2.19e+08^{2.19e+08}_{1.41e+09}$
1217	11	14.02 ± 0.05	14.04 ± 0.10	$9.21e+09^{1.93e+09}_{9.21e+09}$	$4.91e+08^{4.91e+08}_{5.98e+08}$	$8.72e+09^{1.33e+09}_{8.72e+09}$	$6.91e+08^{6.91e+08}_{5.26e+09}$
1227	25	16.52 ± 0.11	16.66 ± 0.10	$5.24e+08^{3.92e+08}_{5.24e+08}$	$3.57e+08^{2.53e+08}_{3.57e+08}$	$1.67e+08^{1.24e+08}_{1.67e+08}$	$5.24e+08^{5.24e+08}_{8.23e+09}$
1237	29	15.22 ± 0.05	15.24 ± 0.10	$3.71e+09^{4.96e+08}_{3.71e+09}$	$1.98e+08^{1.87e+08}_{2.58e+08}$	$3.51e+09^{2.52e+08}_{3.51e+09}$	$2.78e+08^{2.78e+08}_{4.66e+09}$
1257	3	15.96 ± 0.05	15.94 ± 0.10	$2.53e+08^{2.53e+08}_{1.39e+09}$	$7.07e+07^{7.07e+07}_{8.04e+07}$	$1.82e+08^{1.82e+08}_{1.31e+09}$	$9.71e+07^{9.71e+07}_{6.22e+08}$
1266	9	14.91 ± 0.05	14.92 ± 0.10	$5.23e+08^{5.23e+08}_{5.23e+08}$	$1.46e+08^{1.46e+08}_{1.46e+08}$	$3.76e+08^{3.76e+08}_{3.77e+08}$	$2.01e+08^{2.01e+08}_{6.03e+08}$
1273	3	14.45 ± 0.05	14.46 ± 0.10	$1.23e+09^{1.23e+09}_{1.02e+10}$	$8.18e+08^{5.43e+08}_{8.18e+08}$	$4.15e+08^{4.15e+08}_{9.64e+09}$	$1.18e+09^{1.18e+09}_{9.88e+09}$
1287	3	25.67 ± 5.10	25.79 ± 0.10	$2.23e+04^{2.23e+04}_{1.36e+05}$	$6.23e+03^{6.23e+03}_{1.79e+04}$	$1.61e+04^{1.18e+04}_{1.28e+05}$	$8.56e+03^{8.56e+03}_{1.88e+05}$
1290	5	12.25 ± 0.05	12.25 ± 0.10	$6.65e+10^{8.38e+09}_{6.65e+10}$	$3.55e+09^{3.55e+09}_{5.06e+09}$	$6.29e+10^{3.32e+09}_{6.30e+10}$	$4.99e+09^{4.99e+09}_{3.60e+10}$
1294	19	14.69 ± 0.05	14.70 ± 0.10	$9.93e+08^{9.93e+08}_{8.70e+09}$	$6.59e+08^{4.64e+08}_{6.59e+08}$	$3.34e+08^{3.34e+08}_{8.24e+09}$	$9.48e+08^{9.48e+08}_{9.12e+09}$
1313	1	16.64 ± 0.05	16.77 ± 0.10	$5.58e+07^{4.24e+07}_{9.34e+07}$	$1.87e+07^{1.87e+07}_{3.24e+07}$	$3.71e+07^{1.36e+07}_{6.73e+07}$	$2.61e+07^{2.61e+07}_{5.35e+08}$
1326	17	12.26 ± 0.05	12.27 ± 0.10	$1.09e+10^{1.09e+10}_{9.80e+10}$	$7.26e+09^{5.23e+09}_{7.91e+09}$	$3.68e+09^{3.61e+09}_{9.27e+10}$	$1.04e+10^{1.04e+10}_{1.34e+11}$
1330	17	11.28 ± 0.05	11.25 ± 0.10	$4.29e+10^{3.51e+10}_{4.29e+10}$	$2.92e+10^{2.41e+10}_{2.92e+10}$	$1.37e+10^{1.10e+10}_{1.37e+10}$	$4.29e+10^{4.29e+10}_{4.82e+11}$
1331	25	16.57 ± 0.11	16.50 ± 0.10	$2.65e+08^{2.31e+08}_{1.48e+09}$	$7.42e+07^{7.42e+07}_{1.02e+08}$	$1.91e+08^{1.29e+08}_{1.40e+09}$	$1.02e+08^{1.02e+08}_{1.33e+09}$

continued

VCC	Type-ID	$mag_{r,obs}$ [mag]	$mag_{r,mod}$ [mag]	M_{tot} [Gyr]	$M_{stellar}$ [$M_\odot$]	M_{gas} [$M_\odot$]	M_{nonvis} [$M_\odot$]
[1]	[2]	[3]	[4]	[5]	[6]	[7]	[8]
1336	25	16.84 ± 0.10	16.88 ± 0.10	$6.45e+08^{1.13e+08}_{6.46e+08}$	$3.44e+07^{3.22e+07}_{1.45e+08}$	$6.11e+08^{4.51e+07}_{6.11e+08}$	$4.84e+07^{4.84e+07}_{1.98e+09}$
1356	11	14.75 ± 0.05	14.77 ± 0.10	$3.61e+09^{1.47e+09}_{3.61e+09}$	$1.93e+08^{1.93e+08}_{2.15e+08}$	$3.42e+09^{1.26e+09}_{3.42e+09}$	$2.71e+08^{2.71e+08}_{1.12e+09}$
1358	30	14.46 ± 0.05	14.54 ± 0.10	$8.51e+09^{1.05e+09}_{8.51e+09}$	$4.54e+08^{4.54e+08}_{6.34e+08}$	$8.05e+09^{4.17e+08}_{8.06e+09}$	$6.38e+08^{6.38e+08}_{8.33e+09}$
1361	25	16.77 ± 0.11	16.76 ± 0.10	$1.77e+09^{1.93e+08}_{1.77e+09}$	$9.43e+07^{9.43e+07}_{1.75e+08}$	$1.67e+09^{6.06e+07}_{1.67e+09}$	$1.33e+08^{1.33e+08}_{3.89e+09}$
1374	1	14.10 ± 0.05	14.10 ± 0.10	$6.48e+09^{6.48e+09}_{6.48e+09}$	$3.46e+08^{3.46e+08}_{3.46e+08}$	$6.13e+09^{6.13e+09}_{6.13e+09}$	$4.86e+08^{4.86e+08}_{1.46e+09}$
1375	7	11.40 ± 0.05	11.40 ± 0.10	$1.04e+11^{1.04e+11}_{1.04e+11}$	$5.55e+09^{5.54e+09}_{5.55e+09}$	$9.84e+10^{9.84e+10}_{9.84e+10}$	$7.79e+09^{7.79e+09}_{2.34e+10}$
1377	3	14.70 ± 0.06	14.71 ± 0.10	$7.34e+08^{7.33e+08}_{4.03e+09}$	$2.05e+08^{2.05e+08}_{2.36e+08}$	$5.28e+08^{5.27e+08}_{3.82e+09}$	$2.82e+08^{2.82e+08}_{2.11e+09}$
1379	7	11.93 ± 0.05	11.94 ± 0.10	$7.72e+10^{1.22e+10}_{7.73e+10}$	$4.12e+09^{4.12e+09}_{5.39e+09}$	$7.31e+10^{6.84e+09}_{7.32e+10}$	$5.79e+09^{5.79e+09}_{3.75e+10}$
1393	7	12.72 ± 0.05	12.74 ± 0.10	$3.76e+10^{5.95e+09}_{3.76e+10}$	$2.01e+09^{2.01e+09}_{2.62e+09}$	$3.56e+10^{3.33e+09}_{3.56e+10}$	$2.82e+09^{2.82e+09}_{1.83e+10}$
1397	3	17.72 ± 0.09	17.68 ± 0.10	$3.71e+08^{5.65e+07}_{3.71e+08}$	$1.98e+07^{1.94e+07}_{3.41e+07}$	$3.51e+08^{2.24e+07}_{3.51e+08}$	$2.78e+07^{2.78e+07}_{4.39e+08}$
1403	3	16.25 ± 0.07	16.25 ± 0.10	$3.56e+08^{3.14e+08}_{7.92e+08}$	$9.96e+07^{9.96e+07}_{1.38e+08}$	$2.57e+08^{1.75e+08}_{6.76e+08}$	$1.37e+08^{1.37e+08}_{1.49e+09}$
1408	25	16.99 ± 0.11	16.95 ± 0.10	$2.12e+08^{1.35e+08}_{1.18e+09}$	$5.95e+07^{5.95e+07}_{1.28e+08}$	$1.53e+08^{4.53e+07}_{1.12e+09}$	$8.16e+07^{8.16e+07}_{2.07e+09}$
1410	11	13.77 ± 0.05	13.78 ± 0.10	$1.23e+10^{1.95e+09}_{1.23e+10}$	$6.54e+08^{6.54e+08}_{8.59e+08}$	$1.16e+10^{1.09e+09}_{1.16e+10}$	$9.19e+08^{9.19e+08}_{7.18e+09}$
1411	1	14.90 ± 0.05	14.90 ± 0.10	$4.99e+09^{7.87e+08}_{4.99e+09}$	$2.66e+08^{2.66e+08}_{3.47e+08}$	$4.72e+09^{4.40e+08}_{4.72e+09}$	$3.74e+08^{3.74e+08}_{4.67e+09}$
1412	17	10.71 ± 0.05	10.69 ± 0.10	$7.29e+10^{7.29e+10}_{8.55e+10}$	$5.01e+10^{5.01e+10}_{5.83e+10}$	$2.29e+10^{2.28e+10}_{2.72e+10}$	$7.29e+10^{7.29e+10}_{8.80e+11}$
1413	25	17.20 ± 0.10	17.16 ± 0.10	$2.30e+08^{1.44e+08}_{1.29e+09}$	$6.44e+07^{6.44e+07}_{9.92e+07}$	$1.66e+08^{4.53e+07}_{1.22e+09}$	$8.84e+07^{8.84e+07}_{1.85e+09}$
1419	23	12.54 ± 0.05	12.56 ± 0.10	$8.44e+09^{8.44e+09}_{7.55e+10}$	$5.60e+09^{4.03e+09}_{6.09e+09}$	$2.84e+09^{2.78e+09}_{7.15e+10}$	$8.05e+09^{8.05e+09}_{9.62e+10}$
1426	3	14.81 ± 0.05	14.78 ± 0.10	$1.83e+09^{1.19e+09}_{1.05e+10}$	$5.11e+08^{5.11e+08}_{7.88e+08}$	$1.32e+09^{4.00e+08}_{9.90e+09}$	$7.02e+08^{7.02e+08}_{1.26e+10}$
1427	29	14.64 ± 0.05	14.69 ± 0.10	$6.61e+09^{8.84e+08}_{6.61e+09}$	$3.53e+08^{3.53e+08}_{5.33e+08}$	$6.26e+09^{3.50e+08}_{6.26e+09}$	$4.95e+08^{4.95e+08}_{5.99e+09}$
1435	3	13.49 ± 0.05	13.49 ± 0.10	$2.32e+10^{2.87e+09}_{2.32e+10}$	$1.24e+09^{1.24e+09}_{1.73e+09}$	$2.20e+10^{1.14e+09}_{2.20e+10}$	$1.74e+09^{1.74e+09}_{2.27e+10}$

continued

VCC [1]	Type-ID [2]	$mag_{r,obs}$ [mag] [3]	$mag_{r,mod}$ [mag] [4]	M_{tot} [Gyr] [5]	$M_{stellar}$ [$M_\odot$] [6]	M_{gas} [$M_\odot$] [7]	M_{nonvis} [$M_\odot$] [8]
1437	1	14.38 ± 0.05	14.40 ± 0.10	$8.91e+09^{1.15e+09}_{8.91e+09}$	$4.75e+08^{4.75e+08}_{6.97e+08}$	$8.43e+09^{4.58e+08}_{8.43e+09}$	$6.68e+08^{6.68e+08}_{1.03e+10}$
1442	9	13.85 ± 0.05	13.85 ± 0.10	$1.22e+10^{1.93e+09}_{1.22e+10}$	$6.52e+08^{6.52e+08}_{8.52e+08}$	$1.16e+10^{1.08e+09}_{1.16e+10}$	$9.16e+08^{9.16e+08}_{5.94e+09}$
1448	25	13.13 ± 0.05	13.14 ± 0.10	$2.58e+10^{4.09e+09}_{2.58e+10}$	$1.38e+09^{1.38e+09}_{1.80e+09}$	$2.44e+10^{2.29e+09}_{2.44e+10}$	$1.94e+09^{1.94e+09}_{1.98e+10}$
1450	7	12.44 ± 0.05	12.47 ± 0.10	$3.60e+10^{7.54e+09}_{3.60e+10}$	$1.92e+09^{1.92e+09}_{2.34e+09}$	$3.41e+10^{5.21e+09}_{3.41e+10}$	$2.70e+09^{2.70e+09}_{1.47e+10}$
1455	3	15.89 ± 0.05	15.89 ± 0.10	$2.13e+09^{3.36e+08}_{2.13e+09}$	$1.14e+08^{1.14e+08}_{1.48e+08}$	$2.02e+09^{1.88e+08}_{2.02e+09}$	$1.60e+08^{1.60e+08}_{1.44e+09}$
1459	1	15.88 ± 0.05	15.87 ± 0.10	$2.61e+09^{3.22e+08}_{2.61e+09}$	$1.39e+08^{1.33e+08}_{1.94e+08}$	$2.47e+09^{1.28e+08}_{2.47e+09}$	$1.96e+08^{1.96e+08}_{4.09e+09}$
1465	3	15.05 ± 0.06	14.74 ± 0.10	$5.82e+08^{5.81e+08}_{3.67e+09}$	$1.63e+08^{1.63e+08}_{9.73e+08}$	$4.19e+08^{3.31e+08}_{3.48e+09}$	$2.23e+08^{2.23e+08}_{1.23e+10}$
1468	3	15.46 ± 0.05	15.50 ± 0.10	$2.98e+08^{2.98e+08}_{1.83e+09}$	$8.36e+07^{8.36e+07}_{9.76e+07}$	$2.15e+08^{2.15e+08}_{1.73e+09}$	$1.15e+08^{1.15e+08}_{6.19e+08}$
1507	11	14.81 ± 0.05	14.83 ± 0.10	$5.93e+09^{7.76e+08}_{5.93e+09}$	$3.16e+08^{3.16e+08}_{4.69e+08}$	$5.61e+09^{3.08e+08}_{5.61e+09}$	$4.45e+08^{4.45e+08}_{3.85e+09}$
1508	7	11.72 ± 0.05	11.72 ± 0.10	$7.26e+10^{7.26e+10}_{7.26e+10}$	$3.87e+09^{3.87e+09}_{3.87e+09}$	$6.88e+10^{6.87e+10}_{6.88e+10}$	$5.44e+09^{5.44e+09}_{1.63e+10}$
1515	3	17.18 ± 0.09	17.20 ± 0.10	$3.73e+08^{5.95e+07}_{3.73e+08}$	$1.99e+07^{1.67e+07}_{1.01e+08}$	$3.53e+08^{3.42e+07}_{3.53e+08}$	$2.79e+07^{2.79e+07}_{1.13e+09}$
1516	7	12.10 ± 0.05	12.09 ± 0.10	$8.42e+10^{1.04e+10}_{8.42e+10}$	$4.49e+09^{4.49e+09}_{6.27e+09}$	$7.97e+10^{4.12e+09}_{7.97e+10}$	$6.31e+09^{6.31e+09}_{5.88e+10}$
1524	9	12.64 ± 0.05	12.60 ± 0.10	$2.83e+10^{5.13e+09}_{2.83e+10}$	$1.51e+09^{1.44e+09}_{1.63e+09}$	$2.68e+10^{3.69e+09}_{2.68e+10}$	$2.12e+09^{2.12e+09}_{1.49e+10}$
1529	9	13.93 ± 0.05	13.94 ± 0.10	$1.22e+10^{1.94e+09}_{1.23e+10}$	$6.54e+08^{6.53e+08}_{8.54e+08}$	$1.16e+10^{1.08e+09}_{1.16e+10}$	$9.19e+08^{9.19e+08}_{8.29e+09}$
1532	7	12.80 ± 0.05	12.83 ± 0.10	$3.47e+10^{5.50e+09}_{3.48e+10}$	$1.85e+09^{1.85e+09}_{2.42e+09}$	$3.29e+10^{3.08e+09}_{3.29e+10}$	$2.61e+09^{2.61e+09}_{2.39e+10}$
1540	5	10.17 ± 0.05	10.15 ± 0.10	$1.17e+11^{1.13e+11}_{1.04e+12}$	$7.74e+10^{5.55e+10}_{8.27e+10}$	$3.93e+10^{3.53e+10}_{9.85e+11}$	$1.11e+11^{1.11e+11}_{1.06e+12}$
1552	17	11.25 ± 0.05	11.24 ± 0.10	$3.43e+10^{3.42e+10}_{4.25e+10}$	$2.35e+10^{2.35e+10}_{2.90e+10}$	$1.07e+10^{1.07e+10}_{1.36e+10}$	$3.43e+10^{3.43e+10}_{4.62e+11}$
1554	11	11.57 ± 0.05	11.60 ± 0.10	$1.18e+10^{1.18e+10}_{6.70e+10}$	$3.30e+09^{3.30e+09}_{3.58e+09}$	$8.49e+09^{8.49e+09}_{6.35e+10}$	$4.53e+09^{4.53e+09}_{2.36e+10}$
1555	7	9.69 ± 0.05	9.72 ± 0.10	$7.39e+11^{9.13e+10}_{7.39e+11}$	$3.94e+10^{3.94e+10}_{5.51e+10}$	$6.99e+11^{3.62e+10}_{7.00e+11}$	$5.54e+10^{5.54e+10}_{5.89e+11}$
1557	7	13.39 ± 0.05	13.41 ± 0.10	$2.45e+10^{3.03e+09}_{2.45e+10}$	$1.31e+09^{1.31e+09}_{1.83e+09}$	$2.32e+10^{1.20e+09}_{2.32e+10}$	$1.84e+09^{1.84e+09}_{1.27e+10}$

continued

VCC	Type-ID	$mag_{r,obs}$ [mag]	$mag_{r,mod}$ [mag]	M_{tot} [Gyr]	$M_{stellar}$ [$M_\odot$]	M_{gas} [$M_\odot$]	M_{nonvis} [$M_\odot$]
[1]	[2]	[3]	[4]	[5]	[6]	[7]	[8]
1562	7	10.16 ± 0.05	10.16 ± 0.10	$5.58e+11^{6.90e+10}_{5.58e+11}$	$2.98e+10^{2.98e+10}_{4.16e+10}$	$5.28e+11^{2.73e+10}_{5.28e+11}$	$4.18e+10^{4.18e+10}_{1.85e+11}$
1566	9	14.48 ± 0.05	14.48 ± 0.10	$1.46e+09^{1.29e+09}_{3.21e+09}$	$4.09e+08^{4.09e+08}_{5.68e+08}$	$1.05e+09^{7.21e+08}_{2.74e+09}$	$5.62e+08^{5.62e+08}_{5.45e+09}$
1569	7	14.88 ± 0.05	14.92 ± 0.10	$4.60e+09^{7.25e+08}_{4.60e+09}$	$2.45e+08^{2.45e+08}_{3.19e+08}$	$4.35e+09^{4.05e+08}_{4.35e+09}$	$3.45e+08^{3.45e+08}_{3.53e+09}$
1572	1	15.35 ± 0.05	15.39 ± 0.10	$5.27e+08^{3.99e+08}_{6.90e+08}$	$1.87e+08^{1.87e+08}_{2.76e+08}$	$3.40e+08^{1.33e+08}_{4.76e+08}$	$2.59e+08^{2.59e+08}_{6.15e+09}$
1574	23	16.45 ± 0.05	16.46 ± 0.10	$2.51e+08^{1.96e+08}_{1.59e+09}$	$1.11e+08^{8.49e+07}_{1.19e+08}$	$1.40e+08^{7.79e+07}_{1.51e+09}$	$1.57e+08^{1.57e+08}_{1.34e+09}$
1575	11	12.76 ± 0.05	12.76 ± 0.10	$5.95e+09^{5.95e+09}_{5.95e+09}$	$3.95e+09^{3.95e+09}_{3.95e+09}$	$2.00e+09^{2.00e+09}_{2.00e+09}$	$5.68e+09^{5.68e+09}_{1.70e+10}$
1581	11	13.93 ± 0.05	13.91 ± 0.10	$1.24e+10^{1.97e+09}_{1.24e+10}$	$6.63e+08^{6.63e+08}_{8.66e+08}$	$1.18e+10^{1.10e+09}_{1.18e+10}$	$9.32e+08^{9.32e+08}_{7.27e+09}$
1582	25	16.14 ± 0.07	16.14 ± 0.10	$1.68e+09^{2.66e+08}_{1.68e+09}$	$8.97e+07^{8.97e+07}_{1.17e+08}$	$1.59e+09^{1.49e+08}_{1.59e+09}$	$1.26e+08^{1.26e+08}_{1.30e+09}$
1585	3	14.66 ± 0.05	14.66 ± 0.10	$1.66e+09^{1.66e+09}_{4.14e+09}$	$2.42e+08^{2.21e+08}_{2.42e+08}$	$1.42e+09^{1.42e+09}_{3.92e+09}$	$3.41e+08^{3.41e+08}_{1.64e+09}$
1588	7	11.54 ± 0.05	11.54 ± 0.10	$1.83e+10^{1.83e+10}_{1.57e+11}$	$1.21e+10^{8.37e+09}_{1.21e+10}$	$6.14e+09^{6.14e+09}_{1.49e+11}$	$1.74e+10^{1.74e+10}_{1.22e+11}$
1596	3	17.14 ± 0.07	17.16 ± 0.10	$4.18e+08^{7.72e+07}_{4.18e+08}$	$2.23e+07^{2.16e+07}_{3.12e+07}$	$3.96e+08^{5.56e+07}_{3.96e+08}$	$3.14e+07^{3.14e+07}_{2.81e+08}$
1605	9	16.61 ± 0.06	16.63 ± 0.10	$8.03e+08^{1.42e+08}_{8.04e+08}$	$4.29e+07^{4.29e+07}_{6.26e+07}$	$7.61e+08^{7.95e+07}_{7.61e+08}$	$6.03e+07^{6.03e+07}_{5.50e+08}$
1615	5	9.72 ± 0.05	9.69 ± 0.10	$1.43e+11^{1.43e+11}_{1.77e+11}$	$9.79e+10^{9.79e+10}_{1.21e+11}$	$4.47e+10^{4.47e+10}_{5.64e+10}$	$1.43e+11^{1.43e+11}_{2.09e+12}$
1623	29	15.99 ± 0.05	16.05 ± 0.10	$1.67e+09^{1.92e+08}_{1.67e+09}$	$8.92e+07^{8.46e+07}_{1.51e+08}$	$1.58e+09^{6.43e+07}_{1.58e+09}$	$1.25e+08^{1.25e+08}_{3.36e+09}$
1624	7	12.78 ± 0.05	12.78 ± 0.10	$7.46e+09^{7.29e+09}_{6.68e+10}$	$4.95e+09^{3.56e+09}_{5.01e+09}$	$2.51e+09^{2.28e+09}_{6.32e+10}$	$7.12e+09^{7.12e+09}_{4.09e+10}$
1644	11	16.80 ± 0.06	16.69 ± 0.10	$6.57e+08^{1.22e+08}_{6.57e+08}$	$3.50e+07^{3.41e+07}_{4.80e+07}$	$6.22e+08^{8.78e+07}_{6.22e+08}$	$4.92e+07^{4.92e+07}_{4.17e+08}$
1645	25	17.57 ± 0.14	17.61 ± 0.10	$6.95e+07^{6.04e+07}_{4.45e+08}$	$3.06e+07^{2.27e+07}_{3.65e+07}$	$3.89e+07^{2.40e+07}_{4.21e+08}$	$4.35e+07^{4.35e+07}_{5.18e+08}$
1654	3	15.48 ± 0.05	15.49 ± 0.10	$2.25e+09^{4.74e+08}_{2.25e+09}$	$1.20e+08^{1.20e+08}_{1.47e+08}$	$2.13e+09^{3.27e+08}_{2.13e+09}$	$1.69e+08^{1.69e+08}_{1.29e+09}$
1656	25	15.88 ± 0.06	15.92 ± 0.10	$2.92e+08^{2.92e+08}_{2.37e+09}$	$1.76e+08^{1.27e+08}_{2.16e+08}$	$1.16e+08^{1.09e+08}_{2.25e+09}$	$2.52e+08^{2.52e+08}_{2.71e+09}$
1675	15	13.72 ± 0.05	13.72 ± 0.10	$2.18e+09^{2.18e+09}_{1.76e+10}$	$1.32e+09^{9.41e+08}_{1.32e+09}$	$8.64e+08^{8.64e+08}_{1.67e+10}$	$1.88e+09^{1.88e+09}_{1.34e+10}$

continued

VCC [1]	Type-ID [2]	$mag_{r,obs}$ [mag] [3]	$mag_{r,mod}$ [mag] [4]	M_{tot} [Gyr] [5]	$M_{stellar}$ [$M_\odot$] [6]	M_{gas} [$M_\odot$] [7]	M_{nonvis} [$M_\odot$] [8]
1678	9	13.55 ± 0.05	13.59 ± 0.10	$1.10e+10^{4.39e+09}_{1.10e+10}$	$5.89e+08^{5.89e+08}_{6.42e+08}$	$1.04e+10^{3.75e+09}_{1.04e+10}$	$8.27e+08^{8.27e+08}_{4.29e+09}$
1685	9	15.42 ± 0.05	15.44 ± 0.10	$1.88e+09^{3.39e+08}_{1.88e+09}$	$1.00e+08^{9.49e+07}_{1.16e+08}$	$1.78e+09^{2.44e+08}_{1.78e+09}$	$1.41e+08^{1.41e+08}_{8.81e+08}$
1686	11	12.61 ± 0.05	12.60 ± 0.10	$2.83e+10^{6.61e+09}_{2.83e+10}$	$1.51e+09^{1.51e+09}_{2.05e+09}$	$2.68e+10^{4.56e+09}_{2.68e+10}$	$2.12e+09^{2.12e+09}_{1.68e+10}$
1690	17	9.27 ± 0.05	9.25 ± 0.10	$1.62e+11^{1.62e+11}_{1.45e+12}$	$1.07e+11^{7.73e+10}_{1.08e+11}$	$5.44e+10^{5.44e+10}_{1.37e+12}$	$1.54e+11^{1.54e+11}_{1.64e+12}$
1696	7	10.81 ± 0.05	10.78 ± 0.10	$3.73e+10^{3.73e+10}_{3.35e+11}$	$2.48e+10^{1.79e+10}_{2.50e+10}$	$1.26e+10^{1.26e+10}_{3.17e+11}$	$3.56e+10^{3.56e+10}_{3.16e+11}$
1699	11	13.73 ± 0.05	13.74 ± 0.10	$9.84e+09^{3.88e+09}_{9.84e+09}$	$5.25e+08^{5.25e+08}_{5.67e+08}$	$9.31e+09^{3.31e+09}_{9.31e+09}$	$7.37e+08^{7.37e+08}_{3.81e+09}$
1713	29	15.43 ± 0.05	15.40 ± 0.10	$2.39e+09^{4.14e+08}_{2.39e+09}$	$1.28e+08^{1.28e+08}_{1.56e+08}$	$2.27e+09^{2.68e+08}_{2.27e+09}$	$1.79e+08^{1.79e+08}_{2.20e+09}$
1725	11	13.76 ± 0.05	13.77 ± 0.10	$1.11e+10^{1.11e+10}_{1.11e+10}$	$5.93e+08^{5.93e+08}_{5.93e+08}$	$1.05e+10^{1.05e+10}_{1.05e+10}$	$8.33e+08^{8.33e+08}_{2.50e+09}$
1726	9	14.63 ± 0.05	14.64 ± 0.10	$6.73e+08^{6.72e+08}_{6.73e+08}$	$1.88e+08^{1.88e+08}_{1.88e+08}$	$4.85e+08^{4.84e+08}_{4.85e+08}$	$2.58e+08^{2.58e+08}_{7.75e+08}$
1727	17	9.18 ± 0.05	9.15 ± 0.10	$2.35e+11^{2.18e+11}_{2.70e+11}$	$1.62e+11^{1.50e+11}_{1.85e+11}$	$7.37e+10^{6.84e+10}_{8.57e+10}$	$2.35e+11^{2.35e+11}_{2.74e+12}$
1728	3	15.91 ± 0.05	15.96 ± 0.10	$1.95e+09^{2.74e+08}_{1.95e+09}$	$1.04e+08^{1.04e+08}_{1.65e+08}$	$1.84e+09^{1.09e+08}_{1.85e+09}$	$1.46e+08^{1.46e+08}_{1.79e+09}$
1730	7	11.49 ± 0.05	11.47 ± 0.10	$2.78e+10^{2.78e+10}_{3.45e+10}$	$1.91e+10^{1.91e+10}_{2.35e+10}$	$8.72e+09^{8.72e+09}_{1.10e+10}$	$2.78e+10^{2.78e+10}_{3.42e+11}$
1744	1	16.33 ± 0.05	16.40 ± 0.10	$1.26e+08^{9.79e+07}_{8.01e+08}$	$4.43e+07^{3.58e+07}_{6.76e+07}$	$8.14e+07^{3.29e+07}_{7.58e+08}$	$6.17e+07^{6.17e+07}_{1.21e+09}$
1756	25	17.41 ± 0.11	17.33 ± 0.10	$1.19e+08^{1.03e+08}_{2.61e+08}$	$3.33e+07^{3.33e+07}_{4.53e+07}$	$8.57e+07^{5.75e+07}_{2.23e+08}$	$4.58e+07^{4.58e+07}_{4.93e+08}$
1757	17	12.77 ± 0.05	12.79 ± 0.10	$6.10e+09^{6.10e+09}_{5.46e+10}$	$4.05e+09^{2.91e+09}_{4.85e+09}$	$2.05e+09^{2.05e+09}_{5.17e+10}$	$5.82e+09^{5.82e+09}_{7.59e+10}$
1758	7	14.09 ± 0.05	14.11 ± 0.10	$1.18e+10^{1.51e+09}_{1.18e+10}$	$6.28e+08^{6.28e+08}_{9.14e+08}$	$1.11e+10^{6.01e+08}_{1.11e+10}$	$8.82e+08^{8.82e+08}_{5.26e+09}$
1760	17	11.36 ± 0.05	11.31 ± 0.10	$3.80e+10^{3.79e+10}_{4.63e+10}$	$2.61e+10^{2.61e+10}_{3.15e+10}$	$1.19e+10^{1.19e+10}_{1.48e+10}$	$3.80e+10^{3.80e+10}_{5.06e+11}$
1776	25	16.78 ± 0.17	16.66 ± 0.10	$1.68e+09^{1.91e+08}_{1.68e+09}$	$8.98e+07^{8.46e+07}_{1.83e+08}$	$1.59e+09^{6.44e+07}_{1.59e+09}$	$1.26e+08^{1.26e+08}_{3.40e+09}$
1778	15	13.45 ± 0.05	13.47 ± 0.10	$2.00e+10^{2.71e+09}_{2.00e+10}$	$1.07e+09^{1.07e+09}_{1.63e+09}$	$1.90e+10^{1.07e+09}_{1.90e+10}$	$1.50e+09^{1.50e+09}_{1.64e+10}$
1784	3	15.87 ± 0.07	15.89 ± 0.10	$4.04e+08^{3.83e+08}_{3.45e+09}$	$2.77e+08^{1.84e+08}_{4.00e+08}$	$1.27e+08^{1.27e+08}_{3.26e+09}$	$4.02e+08^{4.02e+08}_{8.93e+09}$

continued

VCC [1]	Type- ID [2]	$mag_{r,obs}$ [mag] [3]	$mag_{r,mod}$ [mag] [4]	M_{tot} [Gyr] [5]	$M_{stellar}$ [$M_\odot$] [6]	M_{gas} [$M_\odot$] [7]	M_{nonvis} [$M_\odot$] [8]
1789	3	14.51 ± 0.05	14.53 ± 0.10	$7.88e+09^{1.02e+09}_{7.89e+09}$	$4.21e+08^{4.21e+08}_{6.15e+08}$	$7.46e+09^{4.04e+08}_{7.46e+09}$	$5.91e+08^{5.91e+08}_{5.59e+09}$
1791	11	13.89 ± 0.05	13.90 ± 0.10	$1.26e+09^{1.26e+09}_{1.26e+09}$	$3.53e+08^{3.53e+08}_{3.53e+08}$	$9.07e+08^{9.07e+08}_{9.09e+08}$	$4.85e+08^{4.85e+08}_{1.45e+09}$
1804	29	15.05 ± 0.05	15.07 ± 0.10	$5.72e+09^{7.06e+08}_{5.72e+09}$	$3.05e+08^{3.05e+08}_{4.26e+08}$	$5.41e+09^{2.80e+08}_{5.41e+09}$	$4.29e+08^{4.29e+08}_{3.43e+09}$
1811	7	12.13 ± 0.05	12.15 ± 0.10	$5.77e+10^{9.12e+09}_{5.77e+10}$	$3.08e+09^{3.08e+09}_{4.02e+09}$	$5.46e+10^{5.10e+09}_{5.46e+10}$	$4.32e+09^{4.32e+09}_{2.80e+10}$
1813	17	10.03 ± 0.05	10.02 ± 0.10	$1.29e+11^{1.29e+11}_{1.51e+11}$	$8.85e+10^{8.84e+10}_{1.03e+11}$	$4.04e+10^{4.04e+10}_{4.80e+10}$	$1.29e+11^{1.29e+11}_{1.55e+12}$
1816	3	15.49 ± 0.06	15.42 ± 0.10	$1.99e+09^{3.73e+08}_{1.99e+09}$	$1.06e+08^{1.05e+08}_{1.92e+08}$	$1.89e+09^{2.44e+08}_{1.89e+09}$	$1.50e+08^{1.50e+08}_{1.78e+09}$
1821	11	16.88 ± 0.06	16.85 ± 0.10	$1.99e+08^{1.50e+08}_{9.58e+08}$	$6.17e+07^{5.11e+07}_{6.63e+07}$	$1.37e+08^{8.41e+07}_{9.07e+08}$	$8.72e+07^{8.72e+07}_{7.49e+08}$
1822	3	15.86 ± 0.05	15.84 ± 0.10	$1.76e+09^{2.92e+08}_{1.76e+09}$	$9.36e+07^{9.36e+07}_{1.29e+08}$	$1.66e+09^{1.63e+08}_{1.66e+09}$	$1.32e+08^{1.32e+08}_{1.18e+09}$
1825	25	15.29 ± 0.06	15.31 ± 0.10	$5.65e+08^{5.64e+08}_{4.91e+09}$	$3.75e+08^{2.62e+08}_{4.72e+08}$	$1.90e+08^{1.90e+08}_{4.65e+09}$	$5.39e+08^{5.39e+08}_{7.43e+09}$
1834	19	12.20 ± 0.05	12.17 ± 0.10	$1.24e+10^{1.24e+10}_{1.67e+10}$	$8.51e+09^{8.51e+09}_{1.14e+10}$	$3.88e+09^{3.88e+09}_{5.29e+09}$	$1.23e+10^{1.23e+10}_{1.89e+11}$
1837	25	15.97 ± 0.06	16.01 ± 0.10	$2.79e+08^{2.79e+08}_{2.27e+09}$	$1.68e+08^{1.21e+08}_{1.68e+08}$	$1.11e+08^{1.11e+08}_{2.15e+09}$	$2.41e+08^{2.41e+08}_{1.92e+09}$
1855	19	14.72 ± 0.05	14.73 ± 0.10	$9.27e+08^{9.27e+08}_{7.50e+09}$	$5.59e+08^{4.00e+08}_{5.59e+08}$	$3.67e+08^{3.67e+08}_{7.10e+09}$	$8.00e+08^{8.00e+08}_{4.26e+09}$
1859	17	11.66 ± 0.05	11.64 ± 0.10	$2.02e+10^{1.94e+10}_{1.74e+11}$	$1.39e+10^{9.28e+09}_{1.79e+10}$	$6.33e+09^{6.33e+09}_{1.65e+11}$	$2.01e+10^{2.01e+10}_{3.23e+11}$
1860	25	16.22 ± 0.06	16.34 ± 0.10	$1.11e+09^{1.87e+08}_{1.11e+09}$	$5.92e+07^{5.92e+07}_{2.42e+08}$	$1.05e+09^{7.49e+07}_{1.05e+09}$	$8.32e+07^{8.32e+07}_{3.34e+09}$
1868	7	12.57 ± 0.05	12.52 ± 0.10	$1.32e+10^{1.01e+10}_{1.32e+10}$	$9.00e+09^{6.96e+09}_{9.00e+09}$	$4.21e+09^{3.18e+09}_{4.21e+09}$	$1.32e+10^{1.32e+10}_{1.48e+11}$
1873	11	16.27 ± 0.06	16.26 ± 0.10	$4.30e+08^{1.97e+08}_{1.09e+09}$	$6.28e+07^{5.52e+07}_{6.29e+07}$	$3.67e+08^{1.42e+08}_{1.03e+09}$	$8.85e+07^{8.85e+07}_{5.80e+08}$
1883	19	11.14 ± 0.05	11.12 ± 0.10	$3.85e+10^{3.85e+10}_{4.78e+10}$	$2.64e+10^{2.64e+10}_{3.26e+10}$	$1.21e+10^{1.21e+10}_{1.52e+10}$	$3.85e+10^{3.85e+10}_{4.73e+11}$
1884	25	15.83 ± 0.10	15.64 ± 0.10	$1.58e+09^{2.52e+08}_{1.58e+09}$	$8.40e+07^{7.06e+07}_{4.62e+08}$	$1.49e+09^{1.43e+08}_{1.49e+09}$	$1.18e+08^{1.18e+08}_{6.01e+09}$
1885	3	15.59 ± 0.06	15.59 ± 0.10	$5.77e+08^{5.77e+08}_{1.45e+09}$	$2.54e+08^{1.84e+08}_{2.54e+08}$	$3.23e+08^{3.23e+08}_{1.24e+09}$	$3.61e+08^{3.61e+08}_{2.86e+09}$
1898	25	14.99 ± 0.05	14.99 ± 0.10	$8.10e+08^{8.10e+08}_{7.24e+09}$	$5.38e+08^{3.86e+08}_{5.39e+08}$	$2.73e+08^{2.73e+08}_{6.85e+09}$	$7.73e+08^{7.73e+08}_{5.53e+09}$

continued

VCC	Type-ID	mag$_{\mathrm{r,obs}}$ [mag]	mag$_{\mathrm{r,mod}}$ [mag]	M$_{\mathrm{tot}}$ [Gyr]	M$_{\mathrm{stellar}}$ [M$_\odot$]	M$_{\mathrm{gas}}$ [M$_\odot$]	M$_{\mathrm{nonvis}}$ [M$_\odot$]
[1]	[2]	[3]	[4]	[5]	[6]	[7]	[8]
1900	25	15.48 ± 0.06	15.54 ± 0.10	$3.53e+09^{4.35e+08}_{3.53e+09}$	$1.88e+08^{1.76e+08}_{3.09e+08}$	$3.34e+09^{1.56e+08}_{3.34e+09}$	$2.65e+08^{2.65e+08}_{4.58e+09}$
1902	19	12.34 ± 0.05	12.35 ± 0.10	$1.05e+10^{1.04e+10}_{1.53e+10}$	$7.23e+09^{6.93e+09}_{1.04e+10}$	$3.30e+09^{3.30e+09}_{4.88e+09}$	$1.05e+10^{1.05e+10}_{2.05e+11}$
1905	25	16.74 ± 0.17	16.76 ± 0.10	$3.59e+08^{2.26e+08}_{1.98e+09}$	$1.00e+08^{1.00e+08}_{2.02e+08}$	$2.58e+08^{7.08e+07}_{1.87e+09}$	$1.38e+08^{1.38e+08}_{3.87e+09}$
1906	19	15.00 ± 0.05	15.00 ± 0.10	$9.14e+08^{8.71e+08}_{7.77e+09}$	$6.28e+08^{4.14e+08}_{9.05e+08}$	$2.86e+08^{2.86e+08}_{7.36e+09}$	$9.09e+08^{9.09e+08}_{1.80e+10}$
1918	3	16.09 ± 0.05	16.11 ± 0.10	$1.03e+09^{1.03e+09}_{1.03e+09}$	$5.51e+07^{5.51e+07}_{5.51e+07}$	$9.78e+08^{9.78e+08}_{9.78e+08}$	$7.75e+07^{7.75e+07}_{2.32e+08}$
1920	19	14.68 ± 0.05	14.71 ± 0.10	$9.84e+08^{9.84e+08}_{8.63e+09}$	$6.53e+08^{4.60e+08}_{6.53e+08}$	$3.31e+08^{3.31e+08}_{8.17e+09}$	$9.39e+08^{9.39e+08}_{5.95e+09}$
1923	11	12.06 ± 0.05	12.07 ± 0.10	$9.99e+09^{9.99e+09}_{8.08e+10}$	$6.03e+09^{4.31e+09}_{6.03e+09}$	$3.96e+09^{3.96e+09}_{7.65e+10}$	$8.62e+09^{8.62e+09}_{5.40e+10}$
1929	7	12.88 ± 0.05	12.89 ± 0.10	$3.31e+10^{5.24e+09}_{3.31e+10}$	$1.77e+09^{1.77e+09}_{2.31e+09}$	$3.13e+10^{2.93e+09}_{3.13e+10}$	$2.48e+09^{2.48e+09}_{1.67e+10}$
1931	3	15.08 ± 0.05	15.09 ± 0.10	$2.74e+09^{4.97e+08}_{2.74e+09}$	$1.46e+08^{1.39e+08}_{1.62e+08}$	$2.60e+09^{3.58e+08}_{2.60e+09}$	$2.06e+08^{2.06e+08}_{1.26e+09}$
1932	7	12.13 ± 0.05	12.10 ± 0.10	$1.11e+10^{1.11e+10}_{1.00e+11}$	$7.40e+09^{5.33e+09}_{7.46e+09}$	$3.75e+09^{3.75e+09}_{9.47e+10}$	$1.06e+10^{1.06e+10}_{7.63e+10}$
1933	17	15.98 ± 0.07	16.00 ± 0.10	$1.32e+09^{2.43e+08}_{1.32e+09}$	$7.05e+07^{6.81e+07}_{9.12e+07}$	$1.25e+09^{1.75e+08}_{1.25e+09}$	$9.90e+07^{9.90e+07}_{8.65e+08}$
1943	5	11.29 ± 0.05	11.27 ± 0.10	$2.33e+10^{2.33e+10}_{2.07e+11}$	$1.55e+10^{1.10e+10}_{1.55e+10}$	$7.85e+09^{7.85e+09}_{1.96e+11}$	$2.23e+10^{2.23e+10}_{1.20e+11}$
1944	31	16.19 ± 0.05	16.16 ± 0.10	$3.67e+08^{3.66e+08}_{4.81e+08}$	$2.52e+08^{2.48e+08}_{3.28e+08}$	$1.15e+08^{1.15e+08}_{1.54e+08}$	$3.64e+08^{3.64e+08}_{5.49e+09}$
1952	3	15.82 ± 0.05	15.82 ± 0.10	$2.58e+08^{2.58e+08}_{2.58e+08}$	$7.22e+07^{7.22e+07}_{7.22e+07}$	$1.86e+08^{1.86e+08}_{1.86e+08}$	$9.91e+07^{9.91e+07}_{2.97e+08}$
1955	30	12.74 ± 0.05	12.79 ± 0.10	$4.56e+10^{5.63e+09}_{4.56e+10}$	$2.43e+09^{2.43e+09}_{3.88e+09}$	$4.32e+10^{1.97e+09}_{4.32e+10}$	$3.42e+09^{3.42e+09}_{4.75e+10}$
1960	29	17.39 ± 0.06	17.37 ± 0.10	$4.52e+08^{7.20e+07}_{4.52e+08}$	$2.41e+07^{2.41e+07}_{3.17e+07}$	$4.28e+08^{4.03e+07}_{4.28e+08}$	$3.39e+07^{3.39e+07}_{3.48e+08}$
1965	3	15.88 ± 0.06	15.90 ± 0.10	$2.11e+09^{3.32e+08}_{2.11e+09}$	$1.13e+08^{1.13e+08}_{1.46e+08}$	$2.00e+09^{1.86e+08}_{2.00e+09}$	$1.58e+08^{1.58e+08}_{1.45e+09}$
1970	3	0.00 ± -99999.00	198.00 ± 99.00	$0.00e+00^{0.00e+00}_{0.00e+00}$	$0.00e+00^{0.00e+00}_{0.00e+00}$	$0.00e+00^{0.00e+00}_{0.00e+00}$	$6.95e-310^{6.95e-310}_{6.95e-310}$
1987	7	10.23 ± 0.05	10.24 ± 0.10	$4.49e+11^{5.55e+10}_{4.49e+11}$	$2.40e+10^{2.40e+10}_{3.35e+10}$	$4.25e+11^{2.20e+10}_{4.26e+11}$	$3.37e+10^{3.37e+10}_{1.97e+11}$
1992	3	15.28 ± 0.05	15.30 ± 0.10	$2.15e+09^{3.65e+08}_{2.15e+09}$	$1.14e+08^{1.02e+08}_{1.73e+08}$	$2.03e+09^{2.63e+08}_{2.03e+09}$	$1.61e+08^{1.61e+08}_{1.38e+09}$

continued

VCC	Type-ID	$mag_{r,obs}$ [mag]	$mag_{r,mod}$ [mag]	M_{tot} [Gyr]	$M_{stellar}$ [$M_\odot$]	M_{gas} [$M_\odot$]	M_{nonvis} [$M_\odot$]
[1]	[2]	[3]	[4]	[5]	[6]	[7]	[8]
1994	25	16.44 ± 0.07	16.37 ± 0.10	$4.19e+08^{3.90e+08}_{3.55e+09}$	$2.88e+08^{1.89e+08}_{3.47e+08}$	$1.31e+08^{1.22e+08}_{3.36e+09}$	$4.19e+08^{4.19e+08}_{8.46e+09}$
1999	17	11.93 ± 0.05	11.91 ± 0.10	$2.17e+10^{1.98e+10}_{2.41e+10}$	$1.48e+10^{1.36e+10}_{1.64e+10}$	$6.85e+09^{6.19e+09}_{7.69e+09}$	$2.17e+10^{2.17e+10}_{2.89e+11}$
2006	9	13.06 ± 0.05	13.11 ± 0.10	$3.34e+10^{4.12e+09}_{3.34e+10}$	$1.78e+09^{1.78e+09}_{2.49e+09}$	$3.16e+10^{1.64e+09}_{3.16e+10}$	$2.50e+09^{2.50e+09}_{2.97e+10}$
2007	29	15.20 ± 0.05	15.22 ± 0.10	$3.80e+09^{6.01e+08}_{3.81e+09}$	$2.03e+08^{2.03e+08}_{2.65e+08}$	$3.60e+09^{3.36e+08}_{3.60e+09}$	$2.85e+08^{2.85e+08}_{2.92e+09}$
2015	1	15.60 ± 0.05	15.58 ± 0.10	$2.49e+09^{3.93e+08}_{2.49e+09}$	$1.33e+08^{1.33e+08}_{1.73e+08}$	$2.36e+09^{2.20e+08}_{2.36e+09}$	$1.87e+08^{1.87e+08}_{8.06e+08}$
2023	7	13.32 ± 0.05	13.35 ± 0.10	$1.76e+10^{2.89e+09}_{1.76e+10}$	$9.41e+08^{9.40e+08}_{1.27e+09}$	$1.67e+10^{1.61e+09}_{1.67e+10}$	$1.32e+09^{1.32e+09}_{1.04e+10}$
2033	1	14.54 ± 0.05	14.54 ± 0.10	$6.57e+09^{1.04e+09}_{6.58e+09}$	$3.51e+08^{3.51e+08}_{4.58e+08}$	$6.22e+09^{5.82e+08}_{6.23e+09}$	$4.93e+08^{4.93e+08}_{6.17e+09}$
2034	3	15.10 ± 0.05	15.09 ± 0.10	$3.90e+09^{6.17e+08}_{3.90e+09}$	$2.08e+08^{2.08e+08}_{2.72e+08}$	$3.69e+09^{3.45e+08}_{3.69e+09}$	$2.92e+08^{2.92e+08}_{2.68e+09}$
2037	3	14.83 ± 0.05	14.86 ± 0.10	$4.57e+09^{7.29e+08}_{4.57e+09}$	$2.44e+08^{2.36e+08}_{4.54e+08}$	$4.33e+09^{2.99e+08}_{4.33e+09}$	$3.43e+08^{3.43e+08}_{5.49e+09}$
2058	7	10.59 ± 0.05	10.57 ± 0.10	$4.73e+10^{4.73e+10}_{4.25e+11}$	$3.14e+10^{2.26e+10}_{3.17e+10}$	$1.59e+10^{1.59e+10}_{4.02e+11}$	$4.52e+10^{4.52e+10}_{2.44e+11}$
2066	15	11.25 ± 0.05	11.25 ± 0.10	$2.38e+10^{2.38e+10}_{2.09e+11}$	$1.58e+10^{1.11e+10}_{1.58e+10}$	$8.00e+09^{8.00e+09}_{1.98e+11}$	$2.27e+10^{2.27e+10}_{1.78e+11}$
2070	17	10.28 ± 0.05	10.25 ± 0.10	$9.54e+10^{9.54e+10}_{1.16e+11}$	$6.55e+10^{6.55e+10}_{7.92e+10}$	$2.99e+10^{2.99e+10}_{3.71e+10}$	$9.54e+10^{9.54e+10}_{1.16e+12}$
2089	31	15.04 ± 0.05	15.08 ± 0.10	$1.88e+09^{1.71e+09}_{2.09e+09}$	$1.29e+09^{1.18e+09}_{1.42e+09}$	$5.94e+08^{5.37e+08}_{6.67e+08}$	$1.88e+09^{1.88e+09}_{2.30e+10}$
2090	25	15.00 ± 0.05	14.99 ± 0.10	$5.38e+09^{6.71e+08}_{5.39e+09}$	$2.87e+08^{2.87e+08}_{4.05e+08}$	$5.10e+09^{2.66e+08}_{5.10e+09}$	$4.04e+08^{4.04e+08}_{4.41e+09}$
2094	3	17.68 ± 0.12	17.59 ± 0.10	$9.06e+07^{7.88e+07}_{5.04e+08}$	$2.53e+07^{2.53e+07}_{3.47e+07}$	$6.53e+07^{4.41e+07}_{4.78e+08}$	$3.48e+07^{3.48e+07}_{4.14e+08}$

Results from GALEV/GAZELLE runs (Part I).

Table 6.5: Results from GALEV/GAZELLE runs (Part II). Upper and lower values correspond to the minimum and maximum values of the GAZELLE output.

VCC	Type-ID	Z_{gas}	SFR [$M_{\odot}$/yr]	τ [Gyr]	E(B-V) [mag]
[1]	[2]	[3]	[4]	[5]	[6]
0001	1	$0.030^{0.001}_{0.030}$	$0.022^{0.022}_{0.159}$	5^{5}_{25}	$0.0025^{0.0025}_{0.2804}$
0004	3	$0.001^{0.001}_{0.007}$	$0.018^{0.017}_{0.033}$	25^{4}_{25}	$0.0153^{0.0000}_{0.0648}$
0010	1	$0.001^{0.001}_{0.025}$	$0.097^{0.032}_{0.097}$	25^{6}_{25}	$0.1877^{0.0000}_{0.1877}$
0015	7	$0.001^{0.001}_{0.025}$	$0.144^{0.046}_{0.144}$	25^{6}_{25}	$0.2002^{0.0012}_{0.2002}$
0017	3	$0.004^{0.001}_{0.007}$	$0.048^{0.048}_{0.091}$	15^{4}_{25}	$0.0093^{0.0093}_{0.0737}$
0020	24	$0.007^{0.004}_{0.014}$	$0.020^{0.007}_{0.020}$	4^{4}_{15}	$0.2008^{0.0506}_{0.2009}$
0022	1	$0.001^{0.001}_{0.014}$	$0.050^{0.031}_{0.050}$	25^{8}_{25}	$0.1473^{0.0386}_{0.2276}$
0024	1	$0.001^{0.001}_{0.014}$	$0.100^{0.063}_{0.100}$	25^{8}_{25}	$0.1434^{0.0356}_{0.1434}$
0025	7	$0.001^{0.001}_{0.001}$	$1.352^{1.352}_{1.353}$	25^{25}_{25}	$0.0998^{0.0998}_{0.0998}$
0026	3	$0.007^{0.001}_{0.009}$	$0.013^{0.007}_{0.013}$	4^{4}_{25}	$0.0552^{0.0000}_{0.0552}$
0030	3	$0.007^{0.001}_{0.009}$	$0.042^{0.022}_{0.042}$	4^{4}_{25}	$0.0587^{0.0000}_{0.0588}$
0031	24	$0.001^{0.001}_{0.014}$	$0.065^{0.042}_{0.065}$	25^{8}_{25}	$0.1027^{0.0000}_{0.1363}$
0034	7	$0.001^{0.001}_{0.009}$	$0.123^{0.099}_{0.123}$	25^{10}_{25}	$0.0621^{0.0000}_{0.0621}$
0041	3	$0.001^{0.001}_{0.030}$	$0.027^{0.006}_{0.049}$	25^{4}_{25}	$0.1219^{0.0000}_{0.1619}$
0048	9	$0.001^{0.001}_{0.009}$	$0.161^{0.137}_{0.161}$	25^{10}_{25}	$0.0431^{0.0000}_{0.0431}$

continued

VCC	Type-ID	Z_{gas}	SFR $[M_\odot/yr]$	τ [Gyr]	E(B-V) [mag]
[1]	[2]	[3]	[4]	[5]	[6]
0052	3	$0.001^{0.001}_{0.014}$	$0.014^{0.009}_{0.014}$	25^{8}_{25}	$0.1370^{0.0254}_{0.1370}$
0058	5	$0.001^{0.001}_{0.025}$	$1.038^{0.339}_{1.038}$	25^{6}_{25}	$0.1895^{0.0000}_{0.1895}$
0066	7	$0.001^{0.001}_{0.014}$	$2.692^{1.734}_{2.693}$	25^{8}_{25}	$0.0984^{0.0000}_{0.0984}$
0067	7	$0.001^{0.001}_{0.009}$	$0.302^{0.240}_{0.302}$	25^{10}_{25}	$0.0948^{0.0301}_{0.0948}$
0073	5	$0.030^{0.001}_{0.033}$	$0.372^{0.069}_{2.688}$	5^{4}_{25}	$0.1210^{0.0388}_{0.3980}$
0074	1	$0.001^{0.001}_{0.014}$	$0.044^{0.028}_{0.044}$	25^{8}_{25}	$0.1746^{0.0661}_{0.1747}$
0081	7	$0.001^{0.001}_{0.009}$	$0.110^{0.094}_{0.110}$	25^{10}_{25}	$0.0417^{0.0000}_{0.0417}$
0083	3	$0.001^{0.001}_{0.014}$	$0.079^{0.050}_{0.079}$	25^{8}_{25}	$0.1327^{0.0245}_{0.1328}$
0085	3	$0.009^{0.001}_{0.014}$	$0.011^{0.010}_{0.014}$	10^{8}_{25}	$0.0098^{0.0000}_{0.0764}$
0087	11	$0.001^{0.001}_{0.009}$	$0.131^{0.111}_{0.131}$	25^{10}_{25}	$0.0444^{0.0000}_{0.0445}$
0089	7	$0.001^{0.001}_{0.025}$	$2.904^{0.924}_{2.904}$	25^{6}_{25}	$0.2145^{0.0158}_{0.2145}$
0092	5	$0.033^{0.030}_{0.033}$	$0.626^{0.000}_{3.382}$	4^{2}_{5}	$0.0158^{0.0000}_{0.0983}$
0093	25	$0.001^{0.001}_{0.014}$	$0.018^{0.014}_{0.033}$	25^{4}_{25}	$0.0362^{0.0000}_{0.0822}$
0094	19	$0.033^{0.032}_{0.033}$	$0.001^{0.000}_{0.001}$	3^{0}_{3}	$0.0340^{0.0276}_{0.0340}$
0097	7	$0.030^{0.001}_{0.033}$	$0.343^{0.069}_{2.485}$	5^{4}_{25}	$0.0541^{0.0000}_{0.3319}$
0099	17	$0.030^{0.001}_{0.033}$	$0.041^{0.008}_{0.296}$	5^{4}_{25}	$0.0544^{0.0000}_{0.3313}$
0104	25	$0.001^{0.001}_{0.033}$	$0.009^{0.001}_{0.013}$	25^{4}_{25}	$0.0000^{0.0000}_{0.0000}$
0105	9	$0.001^{0.001}_{0.004}$	$0.502^{0.472}_{0.502}$	25^{15}_{25}	$0.1414^{0.1193}_{0.1414}$
0113	24	$0.007^{0.004}_{0.009}$	$0.028^{0.014}_{0.028}$	4^{4}_{15}	$0.0826^{0.0000}_{0.0826}$
0114	3	$0.001^{0.001}_{0.030}$	$0.047^{0.008}_{0.083}$	25^{4}_{25}	$0.1993^{0.0000}_{0.2399}$

continued

VCC	Type-ID	Z_{gas}	SFR [$M_\odot$/yr]	τ [Gyr]	E(B-V) [mag]
[1]	[2]	[3]	[4]	[5]	[6]
0117	3	$0.001^{0.001}_{0.007}$	$0.023^{0.023}_{0.038}$	25^{4}_{25}	$0.0000^{0.0000}_{0.0161}$
0119	7	$0.001^{0.001}_{0.007}$	$0.063^{0.063}_{0.107}$	25^{4}_{25}	$0.0000^{0.0000}_{0.0281}$
0120	7	$0.001^{0.001}_{0.001}$	$0.830^{0.830}_{0.830}$	25^{25}_{25}	$0.1382^{0.1382}_{0.1382}$
0122	19	$0.033^{0.033}_{0.033}$	$0.001^{0.000}_{0.038}$	3^{0}_{4}	$0.0000^{0.0000}_{0.0216}$
0126	9	$0.001^{0.001}_{0.014}$	$0.212^{0.133}_{0.212}$	25^{8}_{25}	$0.1267^{0.0179}_{0.1267}$
0128	25	$0.001^{0.001}_{0.025}$	$0.173^{0.055}_{0.173}$	25^{6}_{25}	$0.2771^{0.0780}_{0.2771}$
0130	1	$0.001^{0.001}_{0.010}$	$0.016^{0.011}_{0.028}$	25^{4}_{25}	$0.0145^{0.0000}_{0.1023}$
0131	7	$0.030^{0.030}_{0.030}$	$0.085^{0.085}_{0.085}$	5^{5}_{5}	$0.0210^{0.0210}_{0.0211}$
0132	3	$0.001^{0.001}_{0.009}$	$0.027^{0.024}_{0.049}$	25^{4}_{25}	$0.0357^{0.0000}_{0.0803}$
0135	23	$0.030^{0.001}_{0.033}$	$0.070^{0.014}_{0.511}$	5^{4}_{25}	$0.0505^{0.0000}_{0.3280}$
0137	25	$0.025^{0.001}_{0.025}$	$0.012^{0.012}_{0.039}$	6^{6}_{25}	$0.0309^{0.0309}_{0.2300}$
0143	7	$0.001^{0.001}_{0.025}$	$0.134^{0.043}_{0.134}$	25^{6}_{25}	$0.2152^{0.0163}_{0.2152}$
0144	1	$0.010^{0.009}_{0.016}$	$0.032^{0.028}_{0.074}$	10^{8}_{10}	$0.0064^{0.0000}_{0.0700}$
0145	7	$0.001^{0.001}_{0.025}$	$1.851^{0.589}_{1.851}$	25^{6}_{25}	$0.2299^{0.0313}_{0.2299}$
0152	7	$0.033^{0.030}_{0.033}$	$0.057^{0.001}_{0.305}$	4^{3}_{5}	$0.0244^{0.0000}_{0.1068}$
0155	25	$0.001^{0.001}_{0.030}$	$0.196^{0.031}_{0.196}$	25^{5}_{25}	$0.2314^{0.0000}_{0.2314}$
0157	7	$0.030^{0.001}_{0.030}$	$0.896^{0.895}_{6.347}$	5^{5}_{25}	$0.0000^{0.0000}_{0.2700}$
0159	3	$0.007^{0.004}_{0.007}$	$0.078^{0.043}_{0.078}$	4^{4}_{15}	$0.0559^{0.0000}_{0.0559}$
0162	9	$0.001^{0.001}_{0.004}$	$0.146^{0.138}_{0.146}$	25^{15}_{25}	$0.0639^{0.0421}_{0.0639}$
0166	19	$0.033^{0.032}_{0.033}$	$0.002^{0.000}_{0.002}$	3^{0}_{3}	$0.0532^{0.0465}_{0.0532}$

continued

VCC [1]	Type-ID [2]	Z_{gas} [3]	SFR $[M_\odot/yr]$ [4]	τ [Gyr] [5]	E(B-V) [mag] [6]
0167	5	$0.033^{0.032}_{0.033}$	$0.020^{0.000}_{0.020}$	3^{0}_{3}	$0.1329^{0.1265}_{0.1329}$
0168	3	$0.001^{0.001}_{0.025}$	$0.033^{0.010}_{0.033}$	25^{6}_{25}	$0.2199^{0.0205}_{0.2199}$
0169	3	$0.007^{0.001}_{0.007}$	$0.030^{0.019}_{0.030}$	4^{4}_{25}	$0.0000^{0.0000}_{0.0000}$
0172	1	$0.001^{0.001}_{0.010}$	$0.121^{0.082}_{0.214}$	25^{4}_{25}	$0.0421^{0.0000}_{0.1281}$
0181	25	$0.001^{0.001}_{0.014}$	$0.008^{0.005}_{0.008}$	25^{8}_{25}	$0.1088^{0.0000}_{0.1088}$
0187	7	$0.001^{0.001}_{0.025}$	$1.060^{0.338}_{1.060}$	25^{6}_{25}	$0.2974^{0.0992}_{0.2974}$
0190	25	$0.004^{0.001}_{0.030}$	$0.026^{0.005}_{0.050}$	15^{4}_{25}	$0.1597^{0.0000}_{0.2250}$
0199	17	$0.033^{0.032}_{0.033}$	$0.003^{0.000}_{0.003}$	3^{0}_{3}	$0.0934^{0.0871}_{0.0935}$
0207	1	$0.010^{0.009}_{0.010}$	$0.007^{0.006}_{0.008}$	10^{10}_{10}	$0.0000^{0.0000}_{0.0782}$
0213	23	$0.001^{0.001}_{0.025}$	$0.420^{0.134}_{0.420}$	25^{6}_{25}	$0.2214^{0.0227}_{0.2214}$
0217	3	$0.007^{0.001}_{0.009}$	$0.073^{0.042}_{0.073}$	4^{4}_{25}	$0.0304^{0.0000}_{0.0304}$
0221	7	$0.001^{0.001}_{0.004}$	$0.867^{0.814}_{0.867}$	25^{15}_{25}	$0.1492^{0.1271}_{0.1492}$
0222	17	$0.033^{0.032}_{0.033}$	$0.004^{0.000}_{0.004}$	3^{0}_{3}	$0.0926^{0.0863}_{0.0926}$
0223	1	$0.001^{0.001}_{0.014}$	$0.041^{0.026}_{0.041}$	25^{8}_{25}	$0.1260^{0.0179}_{0.1261}$
0226	7	$0.030^{0.001}_{0.030}$	$0.661^{0.661}_{4.797}$	5^{5}_{25}	$0.0584^{0.0584}_{0.3362}$
0234	17	$0.033^{0.032}_{0.033}$	$0.000^{0.000}_{0.002}$	2^{0}_{3}	$0.0330^{0.0297}_{0.0361}$
0237	29	$0.007^{0.004}_{0.007}$	$0.025^{0.014}_{0.025}$	4^{4}_{15}	$0.0367^{0.0000}_{0.0367}$
0241	9	$0.007^{0.001}_{0.007}$	$0.187^{0.121}_{0.187}$	4^{4}_{25}	$0.0000^{0.0000}_{0.0000}$
0247	3	$0.004^{0.001}_{0.033}$	$0.023^{0.000}_{0.043}$	15^{2}_{25}	$0.2507^{0.0000}_{0.7669}$
0252	25	$0.030^{0.001}_{0.033}$	$0.001^{0.000}_{0.015}$	5^{4}_{25}	$0.0000^{0.0000}_{0.3004}$

continued

VCC	Type-ID	Z_{gas}	SFR [$M_\odot$/yr]	τ [Gyr]	E(B-V) [mag]
[1]	[2]	[3]	[4]	[5]	[6]
0260	3	$0.001^{0.001}_{0.014}$	$0.028^{0.018}_{0.028}$	25^{8}_{25}	$0.0950^{0.0000}_{0.0950}$
0267	5	$0.001^{0.001}_{0.014}$	$0.567^{0.355}_{0.567}$	25^{8}_{25}	$0.1198^{0.0119}_{0.1199}$
0274	1	$0.001^{0.001}_{0.030}$	$0.012^{0.004}_{0.022}$	25^{4}_{25}	$0.0138^{0.0000}_{0.1014}$
0275	25	$0.001^{0.001}_{0.014}$	$0.252^{0.158}_{0.252}$	25^{8}_{25}	$0.1569^{0.0491}_{0.1569}$
0282	25	$0.001^{0.001}_{0.014}$	$0.015^{0.009}_{0.015}$	25^{8}_{25}	$0.1304^{0.0194}_{0.1305}$
0286	3	$0.001^{0.001}_{0.014}$	$0.035^{0.022}_{0.035}$	25^{8}_{25}	$0.1230^{0.0149}_{0.1231}$
0289	7	$0.001^{0.001}_{0.004}$	$0.190^{0.179}_{0.190}$	25^{15}_{25}	$0.0877^{0.0658}_{0.0878}$
0293	25	$0.014^{0.001}_{0.025}$	$0.060^{0.031}_{0.168}$	8^{4}_{25}	$0.1153^{0.0283}_{0.2621}$
0304	25	$0.001^{0.001}_{0.014}$	$0.035^{0.021}_{0.035}$	25^{8}_{25}	$0.1364^{0.0255}_{0.1364}$
0307	7	$0.001^{0.001}_{0.014}$	$15.659^{9.809}_{15.662}$	25^{8}_{25}	$0.1539^{0.0465}_{0.1540}$
0309	3	$0.001^{0.001}_{0.009}$	$0.032^{0.028}_{0.032}$	25^{10}_{25}	$0.0370^{0.0000}_{0.0370}$
0312	19	$0.033^{0.032}_{0.033}$	$0.001^{0.000}_{0.001}$	3^{0}_{3}	$0.0754^{0.0691}_{0.0754}$
0318	7	$0.004^{0.001}_{0.004}$	$0.188^{0.188}_{0.200}$	15^{15}_{25}	$0.0027^{0.0027}_{0.0245}$
0320	3	$0.007^{0.001}_{0.014}$	$0.084^{0.030}_{0.084}$	4^{4}_{25}	$0.2452^{0.0950}_{0.2452}$
0322	3	$0.001^{0.001}_{0.014}$	$0.167^{0.104}_{0.167}$	25^{8}_{25}	$0.1432^{0.0349}_{0.1432}$
0323	17	$0.033^{0.032}_{0.033}$	$0.021^{0.000}_{0.021}$	4^{0}_{4}	$0.0558^{0.0173}_{0.0559}$
0324	1	$0.001^{0.001}_{0.004}$	$0.228^{0.215}_{0.228}$	25^{15}_{25}	$0.0436^{0.0217}_{0.0436}$
0328	3	$0.001^{0.001}_{0.009}$	$0.031^{0.026}_{0.031}$	25^{10}_{25}	$0.0488^{0.0000}_{0.0489}$
0329	3	$0.001^{0.001}_{0.007}$	$0.006^{0.006}_{0.010}$	25^{4}_{25}	$0.0000^{0.0000}_{0.0359}$
0334	1	$0.001^{0.001}_{0.001}$	$0.063^{0.063}_{0.063}$	25^{25}_{25}	$0.0542^{0.0542}_{0.0542}$

continued

VCC [1]	Type-ID [2]	Z_{gas} [3]	SFR $[M_\odot/yr]$ [4]	τ [Gyr] [5]	E(B-V) [mag] [6]
0340	1	$0.001^{0.001}_{0.001}$	$0.186^{0.186}_{0.186}$	25^{25}_{25}	$0.1233^{0.1232}_{0.1233}$
0341	17	$0.033^{0.032}_{0.033}$	$0.004^{0.000}_{0.004}$	3^{0}_{3}	$0.0754^{0.0690}_{0.0754}$
0342	19	$0.033^{0.032}_{0.033}$	$0.001^{0.000}_{0.001}$	3^{0}_{3}	$0.0478^{0.0414}_{0.0478}$
0343	9	$0.001^{0.001}_{0.014}$	$0.115^{0.072}_{0.115}$	25^{8}_{25}	$0.1379^{0.0296}_{0.1380}$
0350	3	$0.001^{0.001}_{0.014}$	$0.030^{0.019}_{0.030}$	25^{8}_{25}	$0.1001^{0.0000}_{0.1002}$
0354	25	$0.030^{0.001}_{0.033}$	$0.022^{0.000}_{0.157}$	5^{2}_{25}	$0.0148^{0.0000}_{0.2888}$
0358	17	$0.033^{0.032}_{0.033}$	$0.001^{0.000}_{0.057}$	3^{0}_{4}	$0.0550^{0.0486}_{0.0866}$
0364	3	$0.007^{0.001}_{0.025}$	$0.052^{0.010}_{0.052}$	4^{4}_{25}	$0.2704^{0.0378}_{0.2704}$
0366	19	$0.030^{0.001}_{0.033}$	$0.101^{0.023}_{1.293}$	5^{4}_{25}	$0.0114^{0.0000}_{0.3312}$
0367	3	$0.007^{0.001}_{0.033}$	$0.277^{0.000}_{0.277}$	4^{3}_{25}	$0.3199^{0.0000}_{0.3199}$
0371	19	$0.033^{0.032}_{0.033}$	$0.001^{0.000}_{0.001}$	3^{0}_{3}	$0.0916^{0.0852}_{0.0916}$
0373	19	$0.033^{0.030}_{0.033}$	$0.000^{0.000}_{0.356}$	2^{0}_{5}	$0.0300^{0.0266}_{0.1443}$
0375	19	$0.033^{0.032}_{0.033}$	$0.002^{0.000}_{0.002}$	3^{0}_{3}	$0.0385^{0.0319}_{0.0385}$
0379	3	$1.000^{1.000}_{1.000}$	$0.000^{0.000}_{0.000}$	0^{0}_{0}	$0.0000^{0.0000}_{0.0000}$
0381	3	$0.001^{0.001}_{0.025}$	$0.029^{0.013}_{0.052}$	25^{4}_{25}	$0.0908^{0.0000}_{0.1325}$
0382	7	$0.001^{0.001}_{0.001}$	$2.195^{2.195}_{2.196}$	25^{25}_{25}	$0.1403^{0.1403}_{0.1403}$
0386	17	$0.033^{0.032}_{0.033}$	$0.000^{0.000}_{0.001}$	2^{0}_{3}	$0.0221^{0.0188}_{0.0252}$
0393	7	$0.001^{0.001}_{0.025}$	$0.854^{0.277}_{0.854}$	25^{6}_{25}	$0.1920^{0.0000}_{0.1920}$
0404	7	$0.030^{0.001}_{0.033}$	$0.065^{0.012}_{0.468}$	5^{4}_{25}	$0.0772^{0.0000}_{0.3545}$
0408	19	$0.033^{0.032}_{0.033}$	$0.006^{0.000}_{0.006}$	3^{0}_{3}	$0.0992^{0.0925}_{0.0992}$

continued

VCC	Type-ID	Z_{gas}	SFR [$M_\odot$/yr]	τ [Gyr]	E(B-V) [mag]
[1]	[2]	[3]	[4]	[5]	[6]
0409	25	$0.001^{0.001}_{0.014}$	$0.008^{0.005}_{0.008}$	25^{8}_{25}	$0.1203^{0.0086}_{0.1204}$
0410	1	$0.010^{0.001}_{0.017}$	$0.006^{0.005}_{0.018}$	10^{4}_{25}	$0.0000^{0.0000}_{0.1181}$
0413	3	$0.001^{0.001}_{0.025}$	$0.016^{0.006}_{0.016}$	25^{6}_{25}	$0.1640^{0.0000}_{0.1640}$
0414	25	$0.030^{0.001}_{0.030}$	$0.004^{0.004}_{0.029}$	5^{5}_{25}	$0.0000^{0.0000}_{0.2735}$
0415	9	$0.001^{0.001}_{0.014}$	$0.153^{0.096}_{0.153}$	25^{8}_{25}	$0.1681^{0.0600}_{0.1681}$
0423	3	$0.007^{0.001}_{0.033}$	$0.302^{0.000}_{0.302}$	$4^{0.5}_{25}$	$0.3796^{0.0000}_{0.3797}$
0425	3	$0.033^{0.001}_{0.033}$	$0.000^{0.000}_{0.046}$	3^{0}_{25}	$0.2543^{0.2477}_{0.6539}$
0428	1	$0.009^{0.009}_{0.031}$	$0.009^{0.004}_{0.024}$	10^{6}_{10}	$0.0000^{0.0000}_{0.0000}$
0429	29	$0.007^{0.004}_{0.030}$	$0.071^{0.012}_{0.071}$	4^{4}_{15}	$0.2101^{0.0602}_{0.2101}$
0446	29	$0.014^{0.001}_{0.014}$	$0.052^{0.052}_{0.084}$	8^{8}_{25}	$0.0540^{0.0540}_{0.1626}$
0448	3	$0.001^{0.001}_{0.009}$	$0.019^{0.016}_{0.019}$	25^{10}_{25}	$0.0587^{0.0000}_{0.0587}$
0449	5	$0.014^{0.009}_{0.025}$	$0.678^{0.347}_{0.861}$	8^{6}_{10}	$0.3230^{0.2338}_{0.3659}$
0450	19	$0.030^{0.001}_{0.030}$	$0.028^{0.028}_{0.199}$	5^{5}_{25}	$0.0482^{0.0482}_{0.3243}$
0453	11	$0.001^{0.001}_{0.025}$	$0.053^{0.017}_{0.053}$	25^{6}_{25}	$0.1900^{0.0000}_{0.1900}$
0459	1	$0.001^{0.001}_{0.001}$	$0.114^{0.114}_{0.114}$	25^{25}_{25}	$0.0352^{0.0352}_{0.0353}$
0460	17	$0.033^{0.032}_{0.033}$	$0.010^{0.000}_{0.484}$	3^{0}_{4}	$0.0116^{0.0053}_{0.0439}$
0465	7	$0.001^{0.001}_{0.004}$	$1.234^{1.161}_{1.234}$	25^{15}_{25}	$0.0462^{0.0244}_{0.0462}$
0472	25	$0.033^{0.001}_{0.033}$	$0.001^{0.000}_{0.041}$	4^{0}_{25}	$0.0000^{0.0000}_{0.2936}$
0476	3	$0.001^{0.001}_{0.030}$	$0.011^{0.002}_{0.020}$	25^{4}_{25}	$0.1284^{0.0000}_{0.1732}$
0477	3	$0.007^{0.001}_{0.014}$	$0.038^{0.013}_{0.039}$	4^{4}_{25}	$0.1607^{0.0056}_{0.1607}$

continued

VCC	Type-ID	Z_{gas}	SFR $[M_{\odot}/yr]$	τ [Gyr]	E(B-V) [mag]
[1]	[2]	[3]	[4]	[5]	[6]
0479	3	$0.001^{0.001}_{0.014}$	$0.038^{0.024}_{0.038}$	25^{8}_{25}	$0.1234^{0.0140}_{0.1234}$
0483	7	$1.000^{1.000}_{1.000}$	$0.000^{0.000}_{0.000}$	0^{0}_{0}	$0.0000^{0.0000}_{0.0000}$
0488	3	$0.001^{0.001}_{0.025}$	$0.018^{0.007}_{0.018}$	25^{6}_{25}	$0.1519^{0.0000}_{0.1519}$
0491	7	$0.001^{0.001}_{0.007}$	$0.774^{0.774}_{1.284}$	25^{4}_{25}	$0.0000^{0.0000}_{0.0222}$
0494	25	$0.001^{0.001}_{0.033}$	$0.115^{0.000}_{0.206}$	25^{3}_{25}	$0.2189^{0.0000}_{0.2591}$
0497	7	$1.000^{1.000}_{1.000}$	$0.000^{0.000}_{0.000}$	0^{0}_{0}	$0.0000^{0.0000}_{0.0000}$
0509	9	$0.009^{0.001}_{0.009}$	$0.069^{0.069}_{0.087}$	10^{10}_{25}	$0.0105^{0.0105}_{0.0749}$
0512	11	$0.001^{0.001}_{0.014}$	$0.069^{0.046}_{0.069}$	25^{8}_{25}	$0.0875^{0.0000}_{0.0875}$
0513	1	$0.001^{0.001}_{0.030}$	$0.174^{0.026}_{0.174}$	25^{5}_{25}	$0.2480^{0.0000}_{0.2801}$
0514	7	$0.009^{0.004}_{0.014}$	$0.173^{0.136}_{0.384}$	10^{4}_{15}	$0.0890^{0.0459}_{0.1948}$
0520	3	$0.001^{0.001}_{0.009}$	$0.005^{0.004}_{0.009}$	25^{4}_{25}	$0.0703^{0.0032}_{0.1141}$
0522	17	$0.033^{0.030}_{0.033}$	$0.057^{0.000}_{0.298}$	4^{0}_{5}	$0.0000^{0.0000}_{0.0714}$
0524	5	$0.033^{0.032}_{0.033}$	$0.003^{0.000}_{0.003}$	3^{0}_{3}	$0.0881^{0.0816}_{0.0882}$
0530	3	$0.009^{0.001}_{0.014}$	$0.084^{0.067}_{0.106}$	10^{8}_{25}	$0.0397^{0.0000}_{0.1057}$
0534	17	$0.033^{0.032}_{0.033}$	$0.000^{0.000}_{0.001}$	2^{0}_{3}	$0.0045^{0.0011}_{0.0076}$
0546	25	$0.001^{0.001}_{0.025}$	$0.107^{0.034}_{0.107}$	25^{6}_{25}	$0.1987^{0.0000}_{0.1988}$
0559	17	$0.033^{0.001}_{0.033}$	$0.114^{0.002}_{4.309}$	4^{3}_{25}	$0.0000^{0.0000}_{0.3477}$
0562	1	$0.007^{0.007}_{0.017}$	$0.054^{0.017}_{0.054}$	4^{4}_{10}	$0.0091^{0.0000}_{0.1299}$
0566	11	$0.007^{0.001}_{0.007}$	$0.035^{0.023}_{0.035}$	4^{4}_{25}	$0.0000^{0.0000}_{0.0000}$
0567	7	$0.001^{0.001}_{0.025}$	$0.421^{0.136}_{0.421}$	25^{6}_{25}	$0.1950^{0.0000}_{0.1950}$

continued

VCC	Type-ID	Z_{gas}	SFR $[M_\odot/yr]$	τ [Gyr]	E(B-V) [mag]
[1]	[2]	[3]	[4]	[5]	[6]
0570	17	$0.033^{0.032}_{0.033}$	$0.004^{0.000}_{0.004}$	3^{0}_{3}	$0.0463^{0.0399}_{0.0463}$
0574	25	$0.007^{0.004}_{0.014}$	$0.065^{0.023}_{0.065}$	4^{4}_{15}	$0.3145^{0.1654}_{0.3145}$
0576	5	$0.030^{0.001}_{0.030}$	$0.340^{0.340}_{2.454}$	5^{5}_{25}	$0.1628^{0.1628}_{0.4393}$
0583	3	$0.001^{0.001}_{0.025}$	$0.151^{0.048}_{0.151}$	25^{6}_{25}	$0.2247^{0.0261}_{0.2247}$
0584	3	$0.025^{0.001}_{0.030}$	$0.020^{0.011}_{0.108}$	6^{4}_{25}	$0.0000^{0.0000}_{0.2331}$
0585	3	$0.001^{0.001}_{0.009}$	$0.014^{0.011}_{0.014}$	25^{10}_{25}	$0.0668^{0.0013}_{0.0668}$
0593	23	$0.001^{0.001}_{0.014}$	$0.162^{0.101}_{0.162}$	25^{8}_{25}	$0.1630^{0.0549}_{0.1630}$
0596	7	$0.001^{0.001}_{0.025}$	$30.433^{9.689}_{30.437}$	25^{6}_{25}	$0.2376^{0.0392}_{0.2377}$
0618	3	$0.001^{0.001}_{0.004}$	$0.019^{0.019}_{0.019}$	25^{15}_{25}	$0.0059^{0.0000}_{0.0059}$
0620	11	$0.001^{0.001}_{0.004}$	$0.053^{0.050}_{0.053}$	25^{15}_{25}	$0.0795^{0.0574}_{0.0795}$
0630	9	$0.030^{0.030}_{0.030}$	$0.241^{0.241}_{0.241}$	5^{5}_{5}	$0.0000^{0.0000}_{0.0000}$
0633	25	$0.030^{0.001}_{0.033}$	$0.005^{0.000}_{0.060}$	5^{2}_{25}	$0.0000^{0.0000}_{0.2812}$
0641	1	$0.001^{0.001}_{0.030}$	$0.041^{0.013}_{0.073}$	25^{4}_{25}	$0.0873^{0.0000}_{0.1282}$
0651	25	$0.001^{0.001}_{0.033}$	$0.032^{0.000}_{0.058}$	25^{2}_{25}	$0.1744^{0.0000}_{0.2135}$
0654	19	$0.033^{0.032}_{0.033}$	$0.006^{0.000}_{0.297}$	3^{0}_{4}	$0.1012^{0.0948}_{0.1324}$
0655	1	$0.001^{0.001}_{0.030}$	$1.438^{0.213}_{1.438}$	25^{5}_{25}	$0.2526^{0.0000}_{0.2527}$
0656	5	$0.033^{0.032}_{0.033}$	$0.104^{0.000}_{0.104}$	4^{0}_{4}	$0.1082^{0.0700}_{0.1084}$
0657	19	$0.033^{0.032}_{0.033}$	$0.002^{0.000}_{0.105}$	3^{0}_{4}	$0.1255^{0.1191}_{0.1566}$
0664	7	$0.001^{0.001}_{0.007}$	$0.331^{0.331}_{0.583}$	25^{4}_{25}	$0.0000^{0.0000}_{0.0405}$
0666	3	$0.001^{0.001}_{0.014}$	$0.039^{0.024}_{0.039}$	25^{8}_{25}	$0.1674^{0.0563}_{0.1674}$

continued

VCC	Type-ID	Z_{gas}	SFR [$M_{\odot}$/yr]	τ [Gyr]	E(B-V) [mag]
[1]	[2]	[3]	[4]	[5]	[6]
0667	7	$0.030^{0.001}_{0.030}$	$0.101^{0.100}_{0.726}$	5^{5}_{25}	$0.0000^{0.0000}_{0.2766}$
0672	19	$0.033^{0.001}_{0.033}$	$0.025^{0.000}_{0.908}$	4^{2}_{25}	$0.0000^{0.0000}_{0.3326}$
0679	11	$0.001^{0.001}_{0.025}$	$0.080^{0.028}_{0.080}$	25^{6}_{25}	$0.1628^{0.0000}_{0.1628}$
0688	7	$0.030^{0.001}_{0.030}$	$0.104^{0.104}_{0.737}$	5^{5}_{25}	$0.0000^{0.0000}_{0.2693}$
0692	7	$0.001^{0.001}_{0.014}$	$1.128^{0.706}_{1.128}$	25^{8}_{25}	$0.1351^{0.0272}_{0.1352}$
0697	7	$0.001^{0.001}_{0.025}$	$0.702^{0.223}_{0.702}$	25^{6}_{25}	$0.2346^{0.0360}_{0.2346}$
0699	7	$0.001^{0.001}_{0.009}$	$0.452^{0.360}_{0.452}$	25^{10}_{25}	$0.0648^{0.0006}_{0.0648}$
0703	3	$0.004^{0.001}_{0.009}$	$0.014^{0.012}_{0.027}$	15^{4}_{25}	$0.1129^{0.0666}_{0.1735}$
0705	25	$0.004^{0.001}_{0.033}$	$0.051^{0.000}_{0.094}$	15^{3}_{25}	$0.2621^{0.0000}_{0.3204}$
0713	7	$0.033^{0.032}_{0.033}$	$0.066^{0.000}_{0.066}$	$4^{0.5}_{4}$	$0.0470^{0.0083}_{0.0471}$
0739	9	$0.001^{0.001}_{0.009}$	$0.263^{0.230}_{0.263}$	25^{10}_{25}	$0.0348^{0.0000}_{0.0349}$
0740	11	$0.001^{0.001}_{0.009}$	$0.047^{0.038}_{0.047}$	25^{10}_{25}	$0.0548^{0.0000}_{0.0548}$
0768	7	$0.001^{0.001}_{0.014}$	$0.134^{0.084}_{0.134}$	25^{8}_{25}	$0.1185^{0.0108}_{0.1185}$
0780	25	$0.009^{0.001}_{0.014}$	$0.020^{0.016}_{0.045}$	10^{4}_{25}	$0.1198^{0.0760}_{0.2276}$
0792	17	$0.033^{0.032}_{0.033}$	$0.003^{0.000}_{0.003}$	3^{0}_{3}	$0.0017^{0.0000}_{0.0017}$
0793	3	$1.000^{1.000}_{1.000}$	$0.000^{0.000}_{0.000}$	0^{0}_{0}	$0.0000^{0.0000}_{0.0000}$
0801	15	$0.001^{0.001}_{0.014}$	$1.509^{0.945}_{1.509}$	25^{8}_{25}	$0.1239^{0.0165}_{0.1240}$
0802	1	$0.001^{0.001}_{0.017}$	$0.025^{0.014}_{0.045}$	25^{4}_{25}	$0.0769^{0.0000}_{0.1592}$
0809	7	$0.025^{0.001}_{0.025}$	$0.109^{0.109}_{0.341}$	6^{6}_{25}	$0.0233^{0.0233}_{0.2220}$
0825	3	$0.001^{0.001}_{0.025}$	$0.072^{0.024}_{0.072}$	25^{6}_{25}	$0.1799^{0.0000}_{0.1800}$

continued

VCC	Type-ID	Z_{gas}	SFR [$M_\odot$/yr]	τ [Gyr]	E(B-V) [mag]
[1]	[2]	[3]	[4]	[5]	[6]
0826	3	$0.004^{0.004}_{0.009}$	$0.090^{0.077}_{0.170}$	15^{4}_{15}	$0.0381^{0.0000}_{0.1021}$
0827	7	$0.025^{0.025}_{0.025}$	$0.383^{0.382}_{0.383}$	6^{6}_{6}	$0.0709^{0.0708}_{0.0709}$
0836	17	$0.030^{0.001}_{0.030}$	$1.066^{1.066}_{7.734}$	5^{5}_{25}	$0.0371^{0.0371}_{0.3149}$
0841	1	$0.001^{0.001}_{0.025}$	$0.162^{0.052}_{0.162}$	25^{6}_{25}	$0.2210^{0.0222}_{0.2210}$
0849	5	$0.001^{0.001}_{0.014}$	$0.747^{0.478}_{0.747}$	25^{8}_{25}	$0.1011^{0.0000}_{0.1011}$
0851	7	$0.030^{0.001}_{0.030}$	$0.105^{0.105}_{0.733}$	5^{5}_{25}	$0.0000^{0.0000}_{0.2641}$
0857	5	$0.033^{0.001}_{0.033}$	$0.294^{0.006}_{11.186}$	4^{3}_{25}	$0.0000^{0.0000}_{0.3517}$
0859	7	$0.033^{0.030}_{0.033}$	$0.032^{0.000}_{0.174}$	4^{0}_{5}	$0.0956^{0.0572}_{0.1766}$
0865	7	$0.007^{0.004}_{0.014}$	$1.801^{0.716}_{1.801}$	4^{4}_{15}	$0.1120^{0.0000}_{0.1120}$
0869	25	$0.030^{0.001}_{0.030}$	$0.025^{0.025}_{0.178}$	5^{5}_{25}	$0.0000^{0.0000}_{0.2649}$
0873	7	$0.033^{0.032}_{0.033}$	$0.153^{0.000}_{0.154}$	4^{0}_{4}	$0.0373^{0.0000}_{0.0374}$
0874	7	$0.030^{0.001}_{0.030}$	$0.339^{0.339}_{2.465}$	5^{5}_{25}	$0.0246^{0.0246}_{0.3027}$
0888	3	$0.014^{0.001}_{0.014}$	$0.053^{0.053}_{0.083}$	8^{8}_{25}	$0.0000^{0.0000}_{0.1015}$
0890	1	$0.001^{0.001}_{0.009}$	$0.027^{0.022}_{0.027}$	25^{10}_{25}	$0.0644^{0.0000}_{0.0644}$
0905	7	$0.001^{0.001}_{0.014}$	$0.681^{0.426}_{0.681}$	25^{8}_{25}	$0.1244^{0.0168}_{0.1244}$
0912	5	$0.030^{0.001}_{0.030}$	$0.344^{0.344}_{2.446}$	5^{5}_{25}	$0.0000^{0.0000}_{0.2712}$
0938	7	$0.014^{0.004}_{0.014}$	$0.788^{0.788}_{2.217}$	8^{4}_{15}	$0.0476^{0.0476}_{0.1969}$
0939	7	$0.001^{0.001}_{0.014}$	$1.212^{0.758}_{1.212}$	25^{8}_{25}	$0.1498^{0.0418}_{0.1498}$
0945	11	$0.001^{0.001}_{0.007}$	$0.068^{0.068}_{0.114}$	25^{4}_{25}	$0.0000^{0.0000}_{0.0266}$
0950	11	$0.007^{0.004}_{0.009}$	$0.153^{0.078}_{0.153}$	4^{4}_{15}	$0.0670^{0.0000}_{0.0670}$

continued

VCC	Type-ID	Z_{gas}	SFR [$M_\odot$/yr]	τ [Gyr]	E(B-V) [mag]
[1]	[2]	[3]	[4]	[5]	[6]
0952	3	$0.007^{0.001}_{0.007}$	$0.023^{0.015}_{0.023}$	4^{4}_{25}	$0.0000^{0.0000}_{0.0000}$
0957	7	$0.001^{0.001}_{0.014}$	$1.357^{0.850}_{1.357}$	25^{8}_{25}	$0.1242^{0.0166}_{0.1243}$
0958	17	$0.033^{0.032}_{0.033}$	$0.006^{0.000}_{0.006}$	3^{0}_{3}	$0.0665^{0.0601}_{0.0665}$
0963	3	$0.007^{0.004}_{0.014}$	$0.045^{0.016}_{0.045}$	4^{4}_{15}	$0.1825^{0.0316}_{0.1825}$
0975	7	$1.000^{1.000}_{1.000}$	$0.000^{0.000}_{0.000}$	0^{0}_{0}	$0.0000^{0.0000}_{0.0000}$
0979	17	$0.001^{0.001}_{0.030}$	$4.863^{0.670}_{4.863}$	25^{5}_{25}	$0.3029^{0.0249}_{0.3029}$
0980	7	$0.001^{0.001}_{0.007}$	$0.196^{0.196}_{0.341}$	25^{4}_{25}	$0.0000^{0.0000}_{0.0362}$
0984	17	$0.033^{0.032}_{0.033}$	$0.002^{0.000}_{0.002}$	3^{0}_{3}	$0.0301^{0.0237}_{0.0302}$
0989	7	$0.001^{0.001}_{0.009}$	$0.027^{0.022}_{0.027}$	25^{10}_{25}	$0.0635^{0.0000}_{0.0635}$
0994	25	$0.033^{0.032}_{0.033}$	$0.001^{0.000}_{0.001}$	4^{0}_{4}	$0.1360^{0.1027}_{0.1361}$
0995	7	$0.001^{0.001}_{0.004}$	$0.087^{0.082}_{0.087}$	25^{15}_{25}	$0.0285^{0.0069}_{0.0285}$
1001	3	$0.014^{0.004}_{0.014}$	$0.014^{0.014}_{0.040}$	8^{4}_{15}	$0.0000^{0.0000}_{0.1483}$
1011	9	$0.001^{0.001}_{0.014}$	$0.188^{0.117}_{0.188}$	25^{8}_{25}	$0.1719^{0.0634}_{0.1719}$
1013	3	$0.001^{0.001}_{0.014}$	$0.036^{0.022}_{0.064}$	25^{4}_{25}	$0.1239^{0.0149}_{0.1661}$
1017	3	$0.030^{0.001}_{0.033}$	$0.030^{0.000}_{0.327}$	5^{2}_{25}	$0.0000^{0.0000}_{0.2598}$
1020	25	$0.030^{0.001}_{0.030}$	$0.006^{0.006}_{0.043}$	5^{5}_{25}	$0.0078^{0.0078}_{0.2789}$
1021	3	$0.014^{0.001}_{0.014}$	$0.090^{0.090}_{0.144}$	8^{8}_{25}	$0.0641^{0.0641}_{0.1724}$
1047	17	$0.033^{0.032}_{0.033}$	$0.003^{0.000}_{0.003}$	3^{0}_{3}	$0.0590^{0.0527}_{0.0590}$
1060	11	$0.007^{0.001}_{0.007}$	$0.067^{0.041}_{0.067}$	4^{4}_{25}	$0.0122^{0.0000}_{0.0122}$
1086	23	$0.033^{0.033}_{0.033}$	$0.048^{0.000}_{0.049}$	4^{0}_{4}	$0.0313^{0.0000}_{0.0314}$

continued

VCC	Type-ID	Z_{gas}	SFR [$M_\odot$/yr]	τ [Gyr]	E(B-V) [mag]
[1]	[2]	[3]	[4]	[5]	[6]
1091	5	$0.001^{0.001}_{0.004}$	$0.195^{0.195}_{0.196}$	25^{15}_{25}	$0.0000^{0.0000}_{0.0000}$
1098	3	$0.001^{0.001}_{0.025}$	$0.023^{0.008}_{0.041}$	25^{4}_{25}	$0.1527^{0.0000}_{0.1991}$
1102	3	$0.001^{0.001}_{0.014}$	$0.013^{0.008}_{0.013}$	25^{8}_{25}	$0.0980^{0.0000}_{0.0981}$
1106	3	$0.025^{0.001}_{0.025}$	$0.008^{0.008}_{0.026}$	6^{6}_{25}	$0.0314^{0.0314}_{0.2313}$
1110	17	$0.033^{0.032}_{0.033}$	$0.000^{0.000}_{0.013}$	2^{0}_{3}	$0.0000^{0.0000}_{0.0000}$
1114	3	$0.001^{0.001}_{0.001}$	$0.254^{0.254}_{0.254}$	25^{25}_{25}	$0.1705^{0.1705}_{0.1706}$
1118	7	$0.001^{0.001}_{0.030}$	$1.373^{0.206}_{1.374}$	25^{5}_{25}	$0.2485^{0.0000}_{0.2486}$
1121	3	$0.033^{0.001}_{0.033}$	$0.001^{0.000}_{0.053}$	4^{0}_{25}	$0.0000^{0.0000}_{0.3204}$
1126	7	$0.033^{0.030}_{0.033}$	$0.078^{0.002}_{0.420}$	4^{3}_{5}	$0.0000^{0.0000}_{0.0805}$
1128	3	$0.004^{0.001}_{0.009}$	$0.034^{0.029}_{0.065}$	15^{4}_{25}	$0.1327^{0.0861}_{0.1958}$
1141	1	$0.001^{0.001}_{0.025}$	$0.063^{0.020}_{0.063}$	25^{6}_{25}	$0.1968^{0.0000}_{0.2764}$
1145	5	$0.033^{0.032}_{0.033}$	$0.007^{0.000}_{0.007}$	3^{0}_{3}	$0.0154^{0.0089}_{0.0154}$
1156	7	$0.001^{0.001}_{0.004}$	$0.161^{0.152}_{0.161}$	25^{15}_{25}	$0.0318^{0.0110}_{0.0319}$
1158	17	$0.033^{0.032}_{0.033}$	$0.000^{0.000}_{0.291}$	2^{0}_{4}	$0.0967^{0.0932}_{0.1309}$
1165	25	$0.007^{0.001}_{0.014}$	$0.024^{0.008}_{0.024}$	4^{4}_{25}	$0.2395^{0.0864}_{0.2395}$
1166	3	$0.001^{0.001}_{0.033}$	$0.032^{0.001}_{0.056}$	25^{4}_{25}	$0.1892^{0.0000}_{0.2277}$
1168	3	$0.001^{0.001}_{0.033}$	$0.021^{0.000}_{0.038}$	25^{3}_{25}	$0.0477^{0.0000}_{0.0989}$
1169	3	$0.007^{0.001}_{0.007}$	$0.010^{0.006}_{0.010}$	4^{4}_{25}	$0.0233^{0.0000}_{0.0233}$
1179	29	$0.001^{0.001}_{0.004}$	$0.114^{0.107}_{0.114}$	25^{15}_{25}	$0.1412^{0.1193}_{0.1412}$
1186	25	$0.007^{0.004}_{0.014}$	$0.027^{0.009}_{0.027}$	4^{4}_{15}	$0.2186^{0.0639}_{0.2186}$

continued

VCC	Type-ID	Z_{gas}	SFR [$M_\odot$/yr]	τ [Gyr]	E(B-V) [mag]
[1]	[2]	[3]	[4]	[5]	[6]
1188	15	$0.030^{0.001}_{0.030}$	$0.153^{0.153}_{1.112}$	5^{5}_{25}	$0.0236^{0.0236}_{0.3014}$
1189	7	$0.009^{0.004}_{0.014}$	$0.383^{0.302}_{0.453}$	10^{8}_{15}	$0.0745^{0.0313}_{0.1170}$
1190	17	$0.033^{0.032}_{0.033}$	$0.005^{0.000}_{0.005}$	3^{0}_{3}	$0.0801^{0.0737}_{0.0801}$
1193	7	$0.001^{0.001}_{0.001}$	$0.392^{0.392}_{0.392}$	25^{25}_{25}	$0.1748^{0.1748}_{0.1749}$
1200	3	$0.001^{0.001}_{0.004}$	$0.074^{0.074}_{0.075}$	25^{15}_{25}	$0.0000^{0.0000}_{0.0000}$
1205	7	$0.001^{0.001}_{0.014}$	$1.103^{0.691}_{1.103}$	25^{8}_{25}	$0.1302^{0.0227}_{0.1303}$
1208	11	$0.001^{0.001}_{0.009}$	$0.059^{0.048}_{0.059}$	25^{10}_{25}	$0.0559^{0.0000}_{0.0559}$
1217	11	$0.001^{0.001}_{0.009}$	$0.187^{0.149}_{0.187}$	25^{10}_{25}	$0.0910^{0.0261}_{0.0910}$
1227	25	$0.032^{0.025}_{0.033}$	$0.000^{0.000}_{0.022}$	0.5^{0}_{6}	$0.1815^{0.1815}_{0.3403}$
1237	29	$0.001^{0.001}_{0.017}$	$0.075^{0.041}_{0.133}$	25^{4}_{25}	$0.1516^{0.0432}_{0.2326}$
1257	3	$0.007^{0.001}_{0.007}$	$0.050^{0.027}_{0.050}$	4^{4}_{25}	$0.0811^{0.0171}_{0.0811}$
1266	9	$0.007^{0.007}_{0.007}$	$0.104^{0.104}_{0.104}$	4^{4}_{4}	$0.0174^{0.0174}_{0.0175}$
1273	3	$0.030^{0.001}_{0.030}$	$0.031^{0.031}_{0.207}$	5^{5}_{25}	$0.0000^{0.0000}_{0.2493}$
1287	3	$0.007^{0.001}_{0.025}$	$0.000^{0.000}_{0.000}$	4^{4}_{25}	$0.0000^{0.0000}_{0.0000}$
1290	5	$0.001^{0.001}_{0.025}$	$1.348^{0.438}_{1.349}$	25^{6}_{25}	$0.1919^{0.0000}_{0.1919}$
1294	19	$0.030^{0.001}_{0.030}$	$0.025^{0.025}_{0.176}$	5^{5}_{25}	$0.0000^{0.0000}_{0.2696}$
1313	1	$0.009^{0.007}_{0.031}$	$0.009^{0.004}_{0.024}$	10^{4}_{10}	$0.0000^{0.0000}_{0.0000}$
1326	17	$0.030^{0.001}_{0.033}$	$0.274^{0.056}_{1.987}$	5^{4}_{25}	$0.0506^{0.0000}_{0.3280}$
1330	17	$0.032^{0.032}_{0.033}$	$0.000^{0.000}_{0.003}$	0.5^{0}_{3}	$0.0054^{0.0053}_{0.0116}$
1331	25	$0.007^{0.001}_{0.014}$	$0.053^{0.019}_{0.053}$	4^{4}_{25}	$0.2558^{0.1056}_{0.2558}$

continued

VCC	Type-ID	Z_{gas}	SFR $[M_\odot/yr]$	τ [Gyr]	E(B-V) [mag]
[1]	[2]	[3]	[4]	[5]	[6]
1336	25	$0.001^{0.001}_{0.033}$	$0.013^{0.000}_{0.023}$	25^{2}_{25}	$0.0778^{0.0000}_{0.1094}$
1356	11	$0.001^{0.001}_{0.004}$	$0.073^{0.071}_{0.073}$	25^{15}_{25}	$0.0111^{0.0000}_{0.0112}$
1358	30	$0.001^{0.001}_{0.025}$	$0.173^{0.055}_{0.173}$	25^{6}_{25}	$0.2089^{0.0099}_{0.2090}$
1361	25	$0.001^{0.001}_{0.033}$	$0.036^{0.000}_{0.036}$	25^{0}_{25}	$0.3526^{0.0000}_{0.3526}$
1374	1	$0.001^{0.001}_{0.001}$	$0.131^{0.131}_{0.131}$	25^{25}_{25}	$0.0006^{0.0006}_{0.0006}$
1375	7	$0.001^{0.001}_{0.001}$	$2.108^{2.108}_{2.108}$	25^{25}_{25}	$0.0889^{0.0889}_{0.0889}$
1377	3	$0.007^{0.001}_{0.007}$	$0.145^{0.078}_{0.146}$	4^{4}_{25}	$0.0601^{0.0000}_{0.0601}$
1379	7	$0.001^{0.001}_{0.014}$	$1.567^{0.981}_{1.567}$	25^{8}_{25}	$0.1498^{0.0421}_{0.1498}$
1393	7	$0.001^{0.001}_{0.014}$	$0.763^{0.477}_{0.763}$	25^{8}_{25}	$0.1553^{0.0474}_{0.1553}$
1397	3	$0.001^{0.001}_{0.025}$	$0.008^{0.003}_{0.014}$	25^{4}_{25}	$0.1341^{0.0000}_{0.1820}$
1403	3	$0.007^{0.004}_{0.014}$	$0.071^{0.025}_{0.071}$	4^{4}_{15}	$0.2758^{0.1288}_{0.2758}$
1408	25	$0.007^{0.001}_{0.033}$	$0.042^{0.000}_{0.042}$	4^{3}_{25}	$0.3153^{0.0000}_{0.3154}$
1410	11	$0.001^{0.001}_{0.014}$	$0.249^{0.156}_{0.249}$	25^{8}_{25}	$0.1064^{0.0000}_{0.1064}$
1411	1	$0.001^{0.001}_{0.014}$	$0.101^{0.063}_{0.101}$	25^{8}_{25}	$0.1459^{0.0370}_{0.1792}$
1412	17	$0.033^{0.032}_{0.033}$	$0.007^{0.000}_{0.007}$	3^{0}_{3}	$0.0769^{0.0706}_{0.0769}$
1413	25	$0.007^{0.001}_{0.033}$	$0.046^{0.001}_{0.046}$	4^{4}_{25}	$0.3971^{0.0199}_{0.3971}$
1419	23	$0.030^{0.001}_{0.033}$	$0.211^{0.043}_{1.531}$	5^{4}_{25}	$0.0512^{0.0000}_{0.3285}$
1426	3	$0.007^{0.001}_{0.030}$	$0.363^{0.030}_{0.363}$	4^{4}_{25}	$0.3598^{0.0577}_{0.3598}$
1427	29	$0.001^{0.001}_{0.025}$	$0.134^{0.046}_{0.134}$	25^{6}_{25}	$0.1718^{0.0000}_{0.1718}$
1435	3	$0.001^{0.001}_{0.025}$	$0.470^{0.150}_{0.470}$	25^{6}_{25}	$0.2196^{0.0210}_{0.2197}$

continued

VCC	Type-ID	Z_{gas}	SFR [$M_\odot$/yr]	τ [Gyr]	E(B-V) [mag]
[1]	[2]	[3]	[4]	[5]	[6]
1437	1	$0.001^{0.001}_{0.025}$	$0.181^{0.060}_{0.181}$	25^{6}_{25}	$0.1824^{0.0000}_{0.2152}$
1442	9	$0.001^{0.001}_{0.014}$	$0.248^{0.155}_{0.248}$	25^{8}_{25}	$0.1251^{0.0174}_{0.1251}$
1448	25	$0.001^{0.001}_{0.014}$	$0.523^{0.328}_{0.523}$	25^{8}_{25}	$0.1540^{0.0464}_{0.1540}$
1450	7	$0.001^{0.001}_{0.009}$	$0.730^{0.581}_{0.730}$	25^{10}_{25}	$0.0650^{0.0009}_{0.0650}$
1455	3	$0.001^{0.001}_{0.014}$	$0.043^{0.027}_{0.043}$	25^{8}_{25}	$0.1636^{0.0538}_{0.1636}$
1459	1	$0.001^{0.001}_{0.025}$	$0.053^{0.017}_{0.094}$	25^{4}_{25}	$0.2226^{0.0235}_{0.3020}$
1465	3	$0.007^{0.001}_{0.033}$	$0.115^{0.000}_{0.115}$	4^{3}_{25}	$0.0000^{0.0000}_{0.0000}$
1468	3	$0.007^{0.001}_{0.007}$	$0.059^{0.037}_{0.059}$	4^{4}_{25}	$0.0088^{0.0000}_{0.0089}$
1507	11	$0.001^{0.001}_{0.025}$	$0.120^{0.041}_{0.120}$	25^{6}_{25}	$0.1790^{0.0000}_{0.1790}$
1508	7	$0.001^{0.001}_{0.001}$	$1.473^{1.473}_{1.473}$	25^{25}_{25}	$0.0697^{0.0696}_{0.0697}$
1515	3	$0.001^{0.001}_{0.033}$	$0.008^{0.000}_{0.012}$	25^{3}_{25}	$0.0000^{0.0000}_{0.0000}$
1516	7	$0.001^{0.001}_{0.025}$	$1.707^{0.543}_{1.707}$	25^{6}_{25}	$0.2188^{0.0201}_{0.2188}$
1524	9	$0.001^{0.001}_{0.007}$	$0.574^{0.541}_{1.019}$	25^{4}_{25}	$0.0283^{0.0068}_{0.0718}$
1529	9	$0.001^{0.001}_{0.014}$	$0.248^{0.156}_{0.248}$	25^{8}_{25}	$0.1498^{0.0418}_{0.1499}$
1532	7	$0.001^{0.001}_{0.014}$	$0.705^{0.441}_{0.705}$	25^{8}_{25}	$0.1572^{0.0496}_{0.1573}$
1540	5	$0.030^{0.001}_{0.033}$	$2.922^{0.011}_{21.110}$	5^{3}_{25}	$0.1770^{0.0632}_{0.4533}$
1552	17	$0.033^{0.032}_{0.033}$	$0.003^{0.000}_{0.003}$	3^{0}_{3}	$0.0000^{0.0000}_{0.0000}$
1554	11	$0.007^{0.001}_{0.007}$	$2.341^{1.359}_{2.341}$	4^{4}_{25}	$0.0339^{0.0000}_{0.0340}$
1555	7	$0.001^{0.001}_{0.025}$	$14.984^{4.770}_{14.986}$	25^{6}_{25}	$0.2150^{0.0165}_{0.2150}$
1557	7	$0.001^{0.001}_{0.025}$	$0.497^{0.158}_{0.497}$	25^{6}_{25}	$0.2121^{0.0135}_{0.2121}$

continued

VCC	Type-ID	Z_{gas}	SFR [$M_\odot$/yr]	τ [Gyr]	E(B-V) [mag]
[1]	[2]	[3]	[4]	[5]	[6]
1562	7	$0.001^{0.001}_{0.025}$	$11.318^{3.602}_{11.318}$	25^{6}_{25}	$0.2543^{0.0557}_{0.2543}$
1566	9	$0.007^{0.004}_{0.014}$	$0.290^{0.103}_{0.290}$	4^{4}_{15}	$0.2068^{0.0585}_{0.2068}$
1569	7	$0.001^{0.001}_{0.014}$	$0.093^{0.058}_{0.093}$	25^{8}_{25}	$0.1264^{0.0170}_{0.1264}$
1572	1	$0.010^{0.009}_{0.030}$	$0.042^{0.022}_{0.096}$	10^{6}_{10}	$0.2752^{0.0300}_{0.3366}$
1574	23	$0.014^{0.001}_{0.025}$	$0.020^{0.010}_{0.032}$	8^{6}_{25}	$0.1246^{0.0356}_{0.2347}$
1575	11	$0.030^{0.030}_{0.030}$	$0.149^{0.149}_{0.149}$	5^{5}_{5}	$0.0000^{0.0000}_{0.0000}$
1581	11	$0.001^{0.001}_{0.014}$	$0.252^{0.158}_{0.252}$	25^{8}_{25}	$0.1456^{0.0375}_{0.1456}$
1582	25	$0.001^{0.001}_{0.014}$	$0.034^{0.021}_{0.034}$	25^{8}_{25}	$0.1619^{0.0525}_{0.1619}$
1585	3	$0.004^{0.001}_{0.004}$	$0.080^{0.080}_{0.084}$	15^{15}_{25}	$0.0000^{0.0000}_{0.0175}$
1588	7	$0.030^{0.001}_{0.030}$	$0.458^{0.457}_{3.183}$	5^{5}_{25}	$0.0000^{0.0000}_{0.2634}$
1596	3	$0.001^{0.001}_{0.009}$	$0.008^{0.008}_{0.015}$	25^{4}_{25}	$0.0245^{0.0000}_{0.0687}$
1605	9	$0.001^{0.001}_{0.014}$	$0.016^{0.011}_{0.016}$	25^{8}_{25}	$0.0743^{0.0000}_{0.0744}$
1615	5	$0.033^{0.032}_{0.033}$	$0.013^{0.000}_{0.013}$	3^{0}_{3}	$0.0000^{0.0000}_{0.0000}$
1623	29	$0.001^{0.001}_{0.030}$	$0.034^{0.010}_{0.060}$	25^{4}_{25}	$0.1347^{0.0000}_{0.2166}$
1624	7	$0.030^{0.001}_{0.033}$	$0.187^{0.035}_{1.355}$	5^{4}_{25}	$0.0768^{0.0000}_{0.3543}$
1644	11	$0.001^{0.001}_{0.009}$	$0.013^{0.012}_{0.024}$	25^{4}_{25}	$0.0291^{0.0000}_{0.0765}$
1645	25	$0.014^{0.001}_{0.025}$	$0.006^{0.003}_{0.016}$	8^{4}_{25}	$0.0552^{0.0000}_{0.2092}$
1654	3	$0.001^{0.001}_{0.009}$	$0.046^{0.036}_{0.046}$	25^{10}_{25}	$0.0696^{0.0055}_{0.0696}$
1656	25	$0.025^{0.001}_{0.030}$	$0.015^{0.008}_{0.048}$	6^{5}_{25}	$0.0087^{0.0000}_{0.2084}$
1675	15	$0.025^{0.001}_{0.025}$	$0.114^{0.114}_{0.358}$	6^{6}_{25}	$0.0038^{0.0038}_{0.2023}$

continued

VCC	Type-ID	Z_{gas}	SFR $[M_\odot/yr]$	τ [Gyr]	E(B-V) [mag]
[1]	[2]	[3]	[4]	[5]	[6]
1678	9	$0.001^{0.001}_{0.004}$	$0.224^{0.212}_{0.224}$	25^{15}_{25}	$0.0190^{0.0000}_{0.0190}$
1685	9	$0.001^{0.001}_{0.007}$	$0.038^{0.038}_{0.067}$	25^{4}_{25}	$0.0000^{0.0000}_{0.0399}$
1686	11	$0.001^{0.001}_{0.009}$	$0.574^{0.510}_{0.574}$	25^{10}_{25}	$0.0287^{0.0000}_{0.0287}$
1690	17	$0.030^{0.001}_{0.030}$	$4.048^{4.048}_{29.374}$	5^{5}_{25}	$0.0223^{0.0223}_{0.3002}$
1696	7	$0.030^{0.001}_{0.030}$	$0.935^{0.935}_{6.791}$	5^{5}_{25}	$0.0048^{0.0048}_{0.2832}$
1699	11	$0.001^{0.001}_{0.004}$	$0.199^{0.188}_{0.199}$	25^{15}_{25}	$0.0275^{0.0058}_{0.0275}$
1713	29	$0.001^{0.001}_{0.010}$	$0.049^{0.033}_{0.049}$	25^{10}_{25}	$0.0632^{0.0000}_{0.1500}$
1725	11	$0.001^{0.001}_{0.001}$	$0.225^{0.225}_{0.225}$	25^{25}_{25}	$0.0730^{0.0730}_{0.0731}$
1726	9	$0.007^{0.007}_{0.007}$	$0.133^{0.133}_{0.133}$	4^{4}_{4}	$0.0161^{0.0160}_{0.0161}$
1727	17	$0.033^{0.033}_{0.033}$	$0.021^{0.000}_{1.058}$	3^{0}_{4}	$0.0000^{0.0000}_{0.0298}$
1728	3	$0.001^{0.001}_{0.025}$	$0.040^{0.014}_{0.040}$	25^{6}_{25}	$0.1563^{0.0000}_{0.1564}$
1730	7	$0.033^{0.032}_{0.033}$	$0.002^{0.000}_{0.003}$	3^{0}_{3}	$0.0000^{0.0000}_{0.0000}$
1744	1	$0.010^{0.001}_{0.030}$	$0.010^{0.005}_{0.025}$	10^{4}_{25}	$0.0000^{0.0000}_{0.0981}$
1756	25	$0.007^{0.004}_{0.014}$	$0.024^{0.008}_{0.024}$	4^{4}_{15}	$0.2444^{0.0921}_{0.2445}$
1757	17	$0.030^{0.001}_{0.033}$	$0.153^{0.034}_{1.108}$	5^{4}_{25}	$0.0168^{0.0000}_{0.2944}$
1758	7	$0.001^{0.001}_{0.025}$	$0.239^{0.079}_{0.239}$	25^{6}_{25}	$0.1847^{0.0000}_{0.1848}$
1760	17	$0.033^{0.032}_{0.033}$	$0.003^{0.000}_{0.003}$	3^{0}_{3}	$0.0518^{0.0452}_{0.0518}$
1776	25	$0.001^{0.001}_{0.033}$	$0.034^{0.000}_{0.060}$	25^{2}_{25}	$0.3112^{0.0000}_{0.3464}$
1778	15	$0.001^{0.001}_{0.025}$	$0.406^{0.141}_{0.406}$	25^{6}_{25}	$0.1681^{0.0000}_{0.1681}$
1784	3	$0.033^{0.001}_{0.033}$	$0.002^{0.000}_{0.070}$	4^{0}_{25}	$0.0000^{0.0000}_{0.3248}$

continued

VCC	Type-ID	Z_{gas}	SFR [$M_{\odot}$/yr]	τ [Gyr]	E(B-V) [mag]
[1]	[2]	[3]	[4]	[5]	[6]
1789	3	$0.001^{0.001}_{0.025}$	$0.160^{0.053}_{0.160}$	25^{6}_{25}	$0.1831^{0.0000}_{0.1832}$
1791	11	$0.007^{0.007}_{0.007}$	$0.250^{0.250}_{0.250}$	4^{4}_{4}	$0.0000^{0.0000}_{0.0000}$
1804	29	$0.001^{0.001}_{0.025}$	$0.116^{0.037}_{0.116}$	25^{6}_{25}	$0.2347^{0.0358}_{0.2347}$
1811	7	$0.001^{0.001}_{0.014}$	$1.170^{0.732}_{1.170}$	25^{8}_{25}	$0.1200^{0.0122}_{0.1200}$
1813	17	$0.033^{0.032}_{0.033}$	$0.012^{0.000}_{0.012}$	3^{0}_{3}	$0.0619^{0.0554}_{0.0619}$
1816	3	$0.001^{0.001}_{0.014}$	$0.040^{0.035}_{0.074}$	25^{4}_{25}	$0.0118^{0.0000}_{0.0603}$
1821	11	$0.009^{0.001}_{0.014}$	$0.015^{0.012}_{0.019}$	10^{8}_{25}	$0.1206^{0.0774}_{0.1888}$
1822	3	$0.001^{0.001}_{0.014}$	$0.036^{0.023}_{0.036}$	25^{8}_{25}	$0.0922^{0.0000}_{0.0922}$
1825	25	$0.030^{0.001}_{0.033}$	$0.014^{0.003}_{0.100}$	5^{4}_{25}	$0.0000^{0.0000}_{0.2659}$
1834	19	$0.033^{0.030}_{0.033}$	$0.060^{0.000}_{0.323}$	4^{0}_{5}	$0.0000^{0.0000}_{0.0825}$
1837	25	$0.025^{0.001}_{0.025}$	$0.015^{0.015}_{0.046}$	6^{6}_{25}	$0.0206^{0.0206}_{0.2205}$
1855	19	$0.025^{0.001}_{0.025}$	$0.048^{0.048}_{0.152}$	6^{6}_{25}	$0.0283^{0.0283}_{0.2271}$
1859	17	$0.033^{0.001}_{0.033}$	$0.098^{0.000}_{3.528}$	4^{2}_{25}	$0.0000^{0.0000}_{0.3322}$
1860	25	$0.001^{0.001}_{0.033}$	$0.023^{0.000}_{0.043}$	25^{2}_{25}	$0.0907^{0.0000}_{0.1508}$
1868	7	$0.032^{0.032}_{0.033}$	$0.000^{0.000}_{0.049}$	0.5^{0}_{4}	$0.0028^{0.0027}_{0.0416}$
1873	11	$0.004^{0.001}_{0.007}$	$0.021^{0.021}_{0.039}$	15^{4}_{25}	$0.0373^{0.0373}_{0.1007}$
1883	19	$0.033^{0.032}_{0.033}$	$0.003^{0.000}_{0.003}$	3^{0}_{3}	$0.0000^{0.0000}_{0.0000}$
1884	25	$0.001^{0.001}_{0.033}$	$0.032^{0.000}_{0.050}$	25^{2}_{25}	$0.0000^{0.0000}_{0.0000}$
1885	3	$0.014^{0.004}_{0.014}$	$0.046^{0.046}_{0.131}$	8^{4}_{15}	$0.1338^{0.1338}_{0.2822}$
1898	25	$0.030^{0.001}_{0.030}$	$0.020^{0.020}_{0.147}$	5^{5}_{25}	$0.0205^{0.0205}_{0.2965}$

continued

VCC	Type-ID	Z_{gas}	SFR [$M_\odot$/yr]	τ [Gyr]	E(B-V) [mag]
[1]	[2]	[3]	[4]	[5]	[6]
1900	25	$0.001^{0.001}_{0.030}$	$0.072^{0.012}_{0.125}$	25^{4}_{25}	$0.2199^{0.0000}_{0.2555}$
1902	19	$0.033^{0.030}_{0.033}$	$0.051^{0.000}_{0.262}$	4^{0}_{5}	$0.0000^{0.0000}_{0.0657}$
1905	25	$0.007^{0.001}_{0.033}$	$0.071^{0.000}_{0.071}$	$4^{0.5}_{25}$	$0.4220^{0.0176}_{0.4220}$
1906	19	$0.033^{0.001}_{0.033}$	$0.004^{0.000}_{0.158}$	4^{0}_{25}	$0.0000^{0.0000}_{0.3273}$
1918	3	$0.001^{0.001}_{0.001}$	$0.021^{0.021}_{0.021}$	25^{25}_{25}	$0.0049^{0.0049}_{0.0050}$
1920	19	$0.030^{0.001}_{0.030}$	$0.025^{0.025}_{0.175}$	5^{5}_{25}	$0.0000^{0.0000}_{0.2700}$
1923	11	$0.025^{0.001}_{0.025}$	$0.522^{0.522}_{1.639}$	6^{6}_{25}	$0.0068^{0.0068}_{0.2052}$
1929	7	$0.001^{0.001}_{0.014}$	$0.671^{0.420}_{0.671}$	25^{8}_{25}	$0.1585^{0.0508}_{0.1585}$
1931	3	$0.001^{0.001}_{0.007}$	$0.056^{0.054}_{0.099}$	25^{4}_{25}	$0.0151^{0.0000}_{0.0572}$
1932	7	$0.030^{0.001}_{0.030}$	$0.279^{0.279}_{2.028}$	5^{5}_{25}	$0.0077^{0.0077}_{0.2860}$
1933	17	$0.001^{0.001}_{0.009}$	$0.027^{0.023}_{0.048}$	25^{4}_{25}	$0.0476^{0.0000}_{0.0919}$
1943	5	$0.030^{0.001}_{0.030}$	$0.585^{0.584}_{4.194}$	5^{5}_{25}	$0.0000^{0.0000}_{0.2741}$
1944	31	$0.033^{0.030}_{0.033}$	$0.002^{0.000}_{0.009}$	4^{0}_{5}	$0.0468^{0.0111}_{0.1220}$
1952	3	$0.007^{0.007}_{0.007}$	$0.051^{0.051}_{0.051}$	4^{4}_{4}	$0.0556^{0.0556}_{0.0557}$
1955	30	$0.001^{0.001}_{0.030}$	$0.925^{0.146}_{0.925}$	25^{5}_{25}	$0.2300^{0.0000}_{0.2300}$
1960	29	$0.001^{0.001}_{0.014}$	$0.009^{0.006}_{0.009}$	25^{8}_{25}	$0.1074^{0.0000}_{0.1074}$
1965	3	$0.001^{0.001}_{0.014}$	$0.043^{0.027}_{0.043}$	25^{8}_{25}	$0.1644^{0.0535}_{0.1645}$
1970	3	$1.000^{1.000}_{1.000}$	$0.000^{0.000}_{0.000}$	0^{0}_{0}	$0.0000^{0.0000}_{0.0000}$
1987	7	$0.001^{0.001}_{0.025}$	$9.113^{2.901}_{9.115}$	25^{6}_{25}	$0.2109^{0.0124}_{0.2110}$
1992	3	$0.001^{0.001}_{0.009}$	$0.044^{0.043}_{0.072}$	25^{4}_{25}	$0.0000^{0.0000}_{0.0206}$

continued

VCC	Type-ID	Z_{gas}	SFR $[M_\odot/yr]$	τ [Gyr]	E(B-V) [mag]
[1]	[2]	[3]	[4]	[5]	[6]
1994	25	$0.033^{0.001}_{0.033}$	$0.000^{0.000}_{0.072}$	3^{0}_{25}	$0.0990^{0.0921}_{0.4786}$
1999	17	$0.033^{0.032}_{0.033}$	$0.000^{0.000}_{0.002}$	2^{0}_{3}	$0.0182^{0.0147}_{0.0212}$
2006	9	$0.001^{0.001}_{0.025}$	$0.678^{0.215}_{0.678}$	25^{6}_{25}	$0.2240^{0.0250}_{0.2240}$
2007	29	$0.001^{0.001}_{0.014}$	$0.077^{0.048}_{0.077}$	25^{8}_{25}	$0.1532^{0.0449}_{0.1533}$
2015	1	$0.001^{0.001}_{0.014}$	$0.050^{0.032}_{0.050}$	25^{8}_{25}	$0.1258^{0.0173}_{0.1258}$
2023	7	$0.001^{0.001}_{0.014}$	$0.357^{0.232}_{0.358}$	25^{8}_{25}	$0.0965^{0.0000}_{0.0965}$
2033	1	$0.001^{0.001}_{0.014}$	$0.133^{0.083}_{0.133}$	25^{8}_{25}	$0.1297^{0.0219}_{0.1632}$
2034	3	$0.001^{0.001}_{0.014}$	$0.079^{0.050}_{0.079}$	25^{8}_{25}	$0.1247^{0.0161}_{0.1248}$
2037	3	$0.001^{0.001}_{0.025}$	$0.093^{0.039}_{0.168}$	25^{4}_{25}	$0.1069^{0.0000}_{0.1522}$
2058	7	$0.030^{0.001}_{0.030}$	$1.188^{1.185}_{8.610}$	5^{5}_{25}	$0.0184^{0.0182}_{0.2964}$
2066	15	$0.030^{0.001}_{0.030}$	$0.597^{0.596}_{4.234}$	5^{5}_{25}	$0.0000^{0.0000}_{0.2706}$
2070	17	$0.033^{0.032}_{0.033}$	$0.009^{0.000}_{0.009}$	3^{0}_{3}	$0.0326^{0.0263}_{0.0326}$
2089	31	$0.033^{0.032}_{0.033}$	$0.000^{0.000}_{0.000}$	2^{0}_{3}	$0.1639^{0.1604}_{0.1669}$
2090	25	$0.001^{0.001}_{0.025}$	$0.109^{0.035}_{0.109}$	25^{6}_{25}	$0.1955^{0.0000}_{0.1955}$
2094	3	$0.007^{0.001}_{0.014}$	$0.018^{0.006}_{0.018}$	4^{4}_{25}	$0.2334^{0.0827}_{0.2334}$

Results from GALEV/GAZELLE runs (Part II).

6.4 Results of the GAZELLE surface brightness profiles

In Chapter 4 the time evolution of the SBPs was analysed, using the GALEV/GAZELLE-models. The following Tab. 6.6 shows the derived parameters from this analysis for the different evolutionary assumptions: galaxy today (t=0); undisturbed evolution in 2 Gyr (t=2) and truncated evolution in 2 Gyr (t=2, tru).

Table 6.6: Derived parameters of the fits to the SBPs for different evolutionary scenarios.

VCC [1]	μ_0 (t = 0) [2]	$\mu_{\rm eff}$ (t = 0) [3]	α (t = 0) [4]	$R_{\rm eff}$ [″] (t = 0) [5]	μ_0 (t = 2) [6]	$\mu_{\rm eff}$ (t = 2) [7]	α (t = 2) [8]	$R_{\rm eff}$ [″] (t = 2) [9]	μ_0 (t = 2, tru) [10]	$\mu_{\rm eff}$ (t = 2, tru) [11]	α (t = 2, tru) [12]	$R_{\rm eff}$ [″] (t = 2, tru) [13]
0001	19.070	20.187	5.338	8.956	19.326	20.443	5.354	8.985	19.428	20.544	5.410	9.079
0004	22.016	23.132	6.154	10.326	21.709	22.826	5.956	9.994	22.948	24.065	6.503	10.912
0010	19.343	20.459	4.476	7.511	19.509	20.625	4.778	8.018	19.762	20.878	4.742	7.958
0015	21.562	22.678	10.692	17.941	21.405	22.522	10.410	17.468	21.700	22.816	10.652	17.874
0017	22.074	23.191	10.348	17.363	21.918	23.034	10.692	17.942	23.052	24.168	11.535	19.356
0020	22.238	23.354	3.975	6.670	22.178	23.294	4.316	7.243	22.869	23.985	5.123	8.597
0022	20.285	21.401	3.695	6.200	20.193	21.310	3.592	6.027	21.030	22.147	4.456	7.477
0024	19.291	20.407	3.815	6.401	19.227	20.344	3.823	6.415	19.840	20.957	4.248	7.129
0025	18.725	19.841	9.506	15.951	18.922	20.038	10.809	18.137	18.970	20.086	8.122	13.628
0026	22.251	23.367	4.333	7.270	22.040	23.156	4.325	7.258	24.223	25.340	14.201	23.829
0030	22.544	23.660	9.589	16.091	22.579	23.696	10.492	17.606	23.414	24.531	11.233	18.850
0031	19.277	20.393	3.557	5.968	19.147	20.263	3.557	5.968	19.653	20.769	3.465	5.814
0034	20.963	22.079	10.228	17.163	20.833	21.949	10.229	17.163	21.512	22.628	10.097	16.943
0041	23.172	24.288	9.636	16.169	23.110	24.226	10.082	16.917	23.462	24.578	9.667	16.221
0048	21.784	22.900	15.178	25.469	21.722	22.838	15.845	26.587	22.285	23.401	14.004	23.498
0052	22.537	23.653	5.500	9.229	22.503	23.619	5.692	9.551	23.089	24.206	5.306	8.904

continued

VCC	μ_0 (t = 0)	$\mu_{\rm eff}$ (t = 0)	α (t = 0)	$R_{\rm eff}$ [″] (t = 0)	μ_0 (t = 2)	$\mu_{\rm eff}$ (t = 2)	α (t = 2)	$R_{\rm eff}$ [″] (t = 2)	μ_0 (t = 2, tru)	$\mu_{\rm eff}$ (t = 2, tru)	α (t = 2, tru)	$R_{\rm eff}$ [″] (t = 2, tru)
[1]	[2]	[3]	[4]	[5]	[6]	[7]	[8]	[9]	[10]	[11]	[12]	[13]
0058	20.367	21.483	20.407	34.243	20.471	21.588	21.594	36.234	20.645	21.761	20.438	34.294
0066	19.946	21.063	40.426	67.834	19.908	21.024	42.608	71.496	20.031	21.147	35.175	59.023
0067	21.020	22.136	20.850	34.987	20.813	21.929	19.887	33.370	21.649	22.766	22.062	37.021
0073	18.014	19.130	9.325	15.647	18.247	19.364	9.269	15.554	17.811	18.927	8.545	14.339
0074	21.224	22.341	8.438	14.159	21.029	22.145	7.737	12.982	21.522	22.639	8.640	14.498
0081	21.995	23.112	13.654	22.912	22.021	23.137	14.491	24.316	22.404	23.521	12.151	20.389
0083	21.134	22.250	7.637	12.814	20.927	22.043	7.305	12.258	21.745	22.862	8.630	14.481
0085	23.671	24.787	9.304	15.613	23.500	24.616	9.186	15.415	24.145	25.262	9.189	15.419
0087	20.997	22.113	12.360	20.741	20.935	22.051	12.951	21.731	21.850	22.966	13.348	22.398
0089	19.541	20.657	17.679	29.665	19.582	20.698	17.943	30.108	19.699	20.815	17.251	28.947
0092	19.104	20.220	56.265	94.413	19.289	20.406	55.254	92.717	18.880	19.997	49.734	83.454
0097	19.198	20.314	16.073	26.971	19.491	20.607	17.618	29.563	19.367	20.483	16.485	27.662
0099	19.918	21.034	8.715	14.624	20.216	21.333	8.907	14.947	20.218	21.334	9.443	15.845
0104	24.335	25.452	13.015	21.840	24.257	25.373	12.839	21.544	24.998	26.114	13.727	23.034
0105	21.515	22.632	19.575	32.846	21.427	22.543	19.787	33.202	21.841	22.958	19.903	33.397
0113	22.513	23.630	8.345	14.002	22.119	23.235	8.005	13.432	23.680	24.796	11.296	18.954
0114	23.055	24.172	10.937	18.352	22.836	23.952	10.558	17.716	23.748	24.865	13.984	23.465
0117	21.412	22.528	5.236	8.786	21.320	22.437	5.627	9.441	22.010	23.126	4.706	7.896
0119	21.586	22.703	14.925	25.044	21.548	22.665	15.853	26.601	22.163	23.279	13.626	22.864
0120	19.585	20.701	19.749	33.139	19.682	20.798	21.047	35.317	19.924	21.041	18.671	31.330

continued

VCC [1]	μ_0 (t = 0) [2]	$\mu_{\rm eff}$ (t = 0) [3]	α (t = 0) [4]	$R_{\rm eff}$ [″] (t = 0) [5]	μ_0 (t = 2) [6]	$\mu_{\rm eff}$ (t = 2) [7]	α (t = 2) [8]	$R_{\rm eff}$ [″] (t = 2) [9]	μ_0 (t = 2, tru) [10]	$\mu_{\rm eff}$ (t = 2, tru) [11]	α (t = 2, tru) [12]	$R_{\rm eff}$ [″] (t = 2, tru) [13]
0126	21.910	23.026	17.858	29.965	21.878	22.995	18.916	31.742	22.130	23.247	16.455	27.612
0130	20.751	21.867	3.751	6.294	20.627	21.743	3.725	6.251	21.596	22.712	3.946	6.621
0131	19.510	20.626	15.018	25.200	19.782	20.898	16.683	27.994	19.420	20.536	14.037	23.555
0132	23.015	24.131	10.599	17.785	22.976	24.092	11.305	18.969	24.116	25.232	14.052	23.579
0137	21.443	22.560	5.356	8.988	21.840	22.956	6.012	10.088	21.850	22.966	5.684	9.539
0143	20.436	21.552	8.376	14.055	20.199	21.315	7.519	12.616	20.603	21.720	8.140	13.658
0144	18.233	19.350	2.421	4.063	19.513	20.630	3.214	5.392	20.132	21.248	3.173	5.324
0145	19.844	20.960	36.347	60.990	20.088	21.205	40.001	67.121	20.067	21.183	34.726	58.271
0152	18.959	20.075	11.577	19.427	19.162	20.278	11.438	19.192	18.624	19.741	9.988	16.760
0157	18.845	19.961	20.671	34.685	18.842	19.959	19.794	33.214	18.865	19.981	19.678	33.019
0159	21.470	22.586	8.131	13.644	21.262	22.378	8.378	14.058	22.369	23.485	8.416	14.123
0162	20.677	21.793	21.024	35.279	20.420	21.537	19.332	32.438	21.227	22.343	20.748	34.815
0168	22.477	23.594	8.295	13.918	22.421	23.537	8.645	14.507	23.227	24.344	12.905	21.655
0169	24.464	25.581	19.009	31.898	24.130	25.246	18.328	30.754	25.709	26.825	29.418	49.363
0172	20.401	21.518	9.072	15.223	20.266	21.382	8.983	15.073	21.313	22.430	10.155	17.040
0187	20.088	21.204	24.266	40.718	19.904	21.020	23.571	39.552	19.882	20.998	22.872	38.379
0199	18.886	20.003	18.644	31.284	19.065	20.181	18.864	31.654	18.463	19.580	16.592	27.842
0207	17.147	18.263	0.799	1.340	18.431	19.547	0.894	1.500	19.205	20.321	0.926	1.553
0213	19.001	20.118	5.072	8.510	18.967	20.084	4.886	8.198	19.240	20.356	5.047	8.470
0217	23.509	24.625	18.516	31.070	23.504	24.621	19.978	33.524	24.136	25.252	17.936	30.097

continued

VCC	μ_0 (t = 0)	μ_{eff} (t = 0)	α (t = 0)	R_{eff} [″] (t = 0)	μ_0 (t = 2)	μ_{eff} (t = 2)	α (t = 2)	R_{eff} [″] (t = 2)	μ_0 (t = 2, tru)	μ_{eff} (t = 2, tru)	α (t = 2, tru)	R_{eff} [″] (t = 2, tru)
[1]	[2]	[3]	[4]	[5]	[6]	[7]	[8]	[9]	[10]	[11]	[12]	[13]
0221	19.838	20.954	11.920	20.002	19.682	20.798	11.195	18.785	20.439	21.555	13.405	22.494
0222	18.712	19.829	22.792	38.245	18.889	20.005	22.980	38.560	18.346	19.463	20.590	34.550
0223	20.014	21.130	3.233	5.424	20.237	21.354	3.463	5.811	20.821	21.937	3.885	6.519
0226	18.796	19.912	15.406	25.851	19.069	20.185	15.628	26.224	18.901	20.017	14.974	25.126
0234	19.615	20.731	21.877	36.709	19.762	20.878	21.569	36.194	19.450	20.566	20.055	33.653
0237	22.223	23.340	6.265	10.513	21.781	22.898	5.925	9.942	23.587	24.703	8.957	15.029
0241	21.138	22.255	17.279	28.994	20.747	21.863	17.278	28.993	22.233	23.350	17.715	29.726
0247	23.273	24.390	6.948	11.659	23.235	24.352	7.418	12.448	24.403	25.520	11.799	19.799
0260	22.595	23.712	8.407	14.108	22.504	23.620	7.982	13.393	22.907	24.023	7.831	13.141
0267	21.067	22.183	18.162	30.475	20.986	22.102	18.515	31.068	21.581	22.697	19.004	31.888
0274	19.273	20.389	2.447	4.106	19.453	20.570	2.499	4.193	20.223	21.339	2.585	4.337
0286	20.855	21.972	4.813	8.077	20.672	21.789	4.558	7.648	21.311	22.428	4.822	8.091
0289	19.776	20.892	10.380	17.418	19.646	20.762	10.380	17.418	20.187	21.303	9.887	16.590
0307	18.944	20.060	36.430	61.130	18.814	19.930	36.431	61.131	18.959	20.075	32.428	54.413
0309	22.446	23.562	9.310	15.622	22.308	23.425	9.237	15.499	23.307	24.423	9.727	16.322
0318	20.919	22.035	14.016	23.518	20.859	21.976	14.935	25.061	21.662	22.779	14.133	23.715
0320	22.866	23.982	9.709	16.291	22.628	23.745	9.323	15.644	24.390	25.507	24.994	41.941
0322	22.068	23.184	23.926	40.148	22.029	23.145	25.937	43.522	22.607	23.723	26.328	44.178
0323	18.808	19.924	8.260	13.861	19.068	20.185	8.667	14.544	18.840	19.957	8.350	14.012
0324	16.611	17.727	2.640	4.430	16.777	17.893	2.680	4.497	17.773	18.889	2.855	4.790

continued

VCC [1]	μ_0 (t = 0) [2]	$\mu_{\rm eff}$ (t = 0) [3]	α (t = 0) [4]	$R_{\rm eff}$ [″] (t = 0) [5]	μ_0 (t = 2) [6]	$\mu_{\rm eff}$ (t = 2) [7]	α (t = 2) [8]	$R_{\rm eff}$ [″] (t = 2) [9]	μ_0 (t = 2, tru) [10]	$\mu_{\rm eff}$ (t = 2, tru) [11]	α (t = 2, tru) [12]	$R_{\rm eff}$ [″] (t = 2, tru) [13]
0329	22.624	23.740	4.542	7.621	22.564	23.681	4.887	8.201	23.575	24.691	4.803	8.060
0334	20.026	21.142	3.977	6.674	20.447	21.563	4.348	7.295	21.204	22.320	5.223	8.764
0340	19.335	20.451	5.743	9.637	18.912	20.028	4.830	8.104	20.119	21.235	6.642	11.145
0341	18.960	20.077	20.924	35.110	19.137	20.253	21.087	35.385	18.734	19.850	19.776	33.184
0343	21.182	22.299	8.270	13.877	21.052	22.169	8.270	13.877	21.357	22.473	7.769	13.037
0350	23.556	24.673	13.703	22.994	23.336	24.452	13.032	21.868	24.421	25.538	15.135	25.396
0358	18.636	19.752	6.752	11.330	18.809	19.926	6.787	11.388	18.649	19.765	6.792	11.396
0364	23.252	24.368	12.273	20.594	23.244	24.360	13.743	23.061	23.381	24.497	12.740	21.378
0367	24.494	25.610	34.828	58.442	23.992	25.108	31.910	53.546	24.576	25.692	45.209	75.860
0381	24.156	25.273	16.287	27.330	23.608	24.724	14.088	23.640	25.622	26.739	33.604	56.388
0382	18.804	19.921	14.093	23.648	18.849	19.965	14.770	24.785	19.236	20.353	14.150	23.744
0386	19.900	21.016	10.148	17.028	20.040	21.156	10.024	16.820	19.880	20.997	9.878	16.576
0393	20.160	21.276	13.459	22.584	19.917	21.033	12.490	20.957	20.310	21.426	13.063	21.920
0404	19.943	21.059	15.112	25.357	19.945	21.061	15.112	25.358	19.370	20.486	12.815	21.503
0410	20.810	21.926	2.762	4.634	21.740	22.856	3.390	5.689	22.372	23.488	3.240	5.437
0413	21.986	23.102	6.074	10.192	21.909	23.025	6.051	10.153	22.689	23.806	7.450	12.501
0414	22.277	23.393	6.381	10.708	22.423	23.540	6.656	11.169	22.658	23.775	7.464	12.525
0415	21.273	22.390	11.655	19.557	21.090	22.206	11.403	19.134	21.622	22.738	12.301	20.640
0423	25.051	26.167	38.178	64.062	24.990	26.107	38.905	65.283	25.088	26.204	38.828	65.154
0425	24.034	25.150	11.999	20.134	24.048	25.165	12.671	21.262	24.551	25.667	13.553	22.742

continued

VCC [1]	μ_0 (t = 0) [2]	μ_{eff} (t = 0) [3]	α (t = 0) [4]	R_{eff} [″] (t = 0) [5]	μ_0 (t = 2) [6]	μ_{eff} (t = 2) [7]	α (t = 2) [8]	R_{eff} [″] (t = 2) [9]	μ_0 (t = 2, tru) [10]	μ_{eff} (t = 2, tru) [11]	α (t = 2, tru) [12]	R_{eff} [″] (t = 2, tru) [13]
0428	21.501	22.617	5.401	9.063	22.621	23.737	6.139	10.301	23.256	24.372	6.167	10.349
0429	22.057	23.174	9.040	15.168	21.742	22.858	8.322	13.964	23.027	24.144	13.914	23.348
0446	21.546	22.663	9.855	16.537	21.707	22.823	10.926	18.334	22.087	23.203	10.539	17.684
0448	21.298	22.414	4.082	6.849	21.114	22.231	3.984	6.684	22.304	23.421	4.943	8.295
0449	19.654	20.770	12.220	20.505	19.846	20.963	13.860	23.257	18.796	19.912	10.151	17.033
0453	20.664	21.781	6.358	10.668	20.534	21.651	6.357	10.668	20.921	22.038	6.563	11.013
0459	19.453	20.569	5.226	8.769	19.335	20.452	4.907	8.235	20.377	21.493	5.681	9.532
0460	19.376	20.492	43.058	72.252	19.682	20.798	46.606	78.206	19.445	20.561	43.865	73.606
0465	19.465	20.582	21.674	36.370	19.458	20.574	22.359	37.519	20.428	21.544	25.241	42.355
0472	22.865	23.981	11.038	18.521	23.255	24.371	12.899	21.644	23.808	24.924	21.181	35.541
0476	23.101	24.218	6.756	11.336	23.079	24.195	6.656	11.169	23.582	24.699	6.662	11.179
0477	23.678	24.794	12.911	21.664	23.495	24.611	13.009	21.829	23.939	25.055	11.617	19.493
0479	22.473	23.589	12.943	21.718	22.319	23.435	12.569	21.090	23.521	24.637	19.999	33.559
0488	22.542	23.659	9.686	16.253	22.319	23.436	8.678	14.562	23.119	24.235	11.037	18.521
0491	19.988	21.104	14.174	23.784	19.526	20.642	13.174	22.106	21.378	22.494	19.530	32.771
0509	21.597	22.714	13.639	22.887	21.566	22.683	14.387	24.141	22.064	23.180	13.096	21.975
0512	22.131	23.247	15.909	26.695	22.001	23.117	15.908	26.694	22.786	23.902	17.375	29.156
0513	19.142	20.258	3.152	5.288	19.306	20.423	3.202	5.372	19.346	20.462	3.076	5.162
0514	21.803	22.919	14.270	23.946	21.980	23.096	15.806	26.523	22.011	23.127	12.880	21.613
0520	23.062	24.178	6.961	11.681	22.708	23.824	6.460	10.840	24.946	26.062	21.108	35.419

continued

VCC	μ_0 (t = 0)	μ_{eff} (t = 0)	α (t = 0)	R_{eff} [″] (t = 0)	μ_0 (t = 2)	μ_{eff} (t = 2)	α (t = 2)	R_{eff} [″] (t = 2)	μ_0 (t = 2, tru)	μ_{eff} (t = 2, tru)	α (t = 2, tru)	R_{eff} [″] (t = 2, tru)
[1]	[2]	[3]	[4]	[5]	[6]	[7]	[8]	[9]	[10]	[11]	[12]	[13]
0522	19.960	21.077	19.888	33.373	20.153	21.269	19.704	33.064	20.138	21.255	19.430	32.603
0524	18.977	20.093	25.603	42.962	19.118	20.235	25.393	42.610	18.520	19.637	22.250	37.336
0530	23.445	24.561	23.313	39.119	23.263	24.379	23.316	39.125	24.639	25.755	41.716	70.000
0534	19.885	21.002	17.186	28.838	20.011	21.128	16.775	28.148	19.815	20.932	15.956	26.774
0559	19.452	20.568	30.653	51.436	19.669	20.785	30.291	50.828	19.444	20.560	28.154	47.243
0562	18.170	19.286	2.020	3.390	18.670	19.786	2.111	3.542	19.645	20.761	2.273	3.813
0566	21.198	22.314	5.696	9.557	20.893	22.010	5.695	9.557	22.188	23.304	5.681	9.533
0567	20.438	21.554	16.850	28.274	20.182	21.298	15.480	25.975	20.496	21.612	16.004	26.855
0570	19.378	20.494	22.533	37.811	19.543	20.659	22.533	37.810	19.298	20.414	21.586	36.221
0574	23.481	24.598	11.322	18.998	23.793	24.910	12.608	21.156	24.255	25.371	18.924	31.754
0576	19.034	20.150	16.015	26.873	19.374	20.490	16.949	28.441	18.573	19.689	14.150	23.744
0583	22.786	23.902	20.885	35.045	22.625	23.741	20.182	33.865	22.887	24.003	21.358	35.839
0585	23.897	25.013	11.434	19.186	23.762	24.878	11.877	19.930	24.679	25.795	12.999	21.812
0593	20.282	21.399	10.681	17.923	20.049	21.165	10.030	16.831	20.617	21.733	11.087	18.605
0596	19.780	20.896	58.983	98.974	19.999	21.116	66.535	111.645	19.975	21.091	59.721	100.212
0618	22.178	23.294	8.464	14.203	21.960	23.077	8.462	14.200	23.258	24.374	9.636	16.168
0620	20.834	21.950	7.997	13.419	20.745	21.862	8.106	13.601	21.616	22.732	8.937	14.996
0630	20.186	21.302	41.675	69.931	20.342	21.458	42.562	71.420	20.173	21.289	39.516	66.308
0641	20.431	21.547	4.407	7.395	20.015	21.131	3.725	6.250	20.827	21.944	4.019	6.744
0654	19.210	20.327	21.493	36.065	19.376	20.492	21.494	36.066	19.144	20.260	22.404	37.594

continued

VCC	μ_0 (t = 0)	μ_{eff} (t = 0)	α (t = 0)	R_{eff} [″] (t = 0)	μ_0 (t = 2)	μ_{eff} (t = 2)	α (t = 2)	R_{eff} [″] (t = 2)	μ_0 (t = 2, tru)	μ_{eff} (t = 2, tru)	α (t = 2, tru)	R_{eff} [″] (t = 2, tru)
[1]	[2]	[3]	[4]	[5]	[6]	[7]	[8]	[9]	[10]	[11]	[12]	[13]
0656	18.699	19.815	10.983	18.430	18.881	19.997	10.910	18.307	18.244	19.360	9.481	15.909
0664	21.296	22.412	21.712	36.433	20.968	22.084	21.106	35.416	22.552	23.668	28.128	47.198
0666	22.931	24.047	10.903	18.295	22.893	24.009	11.655	19.558	22.783	23.900	9.432	15.826
0667	20.616	21.732	17.245	28.936	20.790	21.906	17.197	28.856	20.865	21.982	17.444	29.270
0679	21.420	22.536	10.412	17.471	21.290	22.406	10.412	17.471	21.584	22.701	9.854	16.534
0688	19.624	20.740	9.321	15.640	19.760	20.877	9.778	16.407	19.851	20.968	10.099	16.947
0692	20.354	21.470	19.605	32.896	20.224	21.340	19.605	32.896	20.923	22.039	21.866	36.690
0697	20.829	21.945	14.281	23.964	20.962	22.078	15.088	25.319	21.004	22.120	14.230	23.879
0699	19.787	20.903	9.051	15.187	19.546	20.663	8.800	14.767	20.905	22.021	12.408	20.820
0703	22.258	23.374	5.818	9.762	22.129	23.246	5.934	9.957	23.180	24.296	6.913	11.600
0713	19.940	21.057	28.930	48.545	20.106	21.223	28.400	47.655	19.706	20.822	25.777	43.254
0739	21.438	22.554	16.272	27.304	21.308	22.424	16.272	27.304	22.100	23.216	15.658	26.275
0740	21.298	22.415	7.917	13.284	21.168	22.285	7.917	13.284	21.851	22.967	7.950	13.340
0768	20.152	21.269	10.370	17.401	19.919	21.035	9.739	16.343	20.796	21.912	11.647	19.544
0792	19.824	20.940	29.298	49.161	19.977	21.093	28.932	48.548	19.976	21.092	29.706	49.847
0801	18.160	19.277	9.109	15.284	18.000	19.116	8.976	15.062	18.940	20.056	11.131	18.677
0802	22.064	23.180	10.017	16.809	22.250	23.366	10.495	17.610	22.838	23.955	11.422	19.166
0809	20.308	21.424	18.315	30.732	20.464	21.580	18.070	30.322	20.596	21.712	17.775	29.827
0825	22.049	23.166	8.515	14.288	21.984	23.101	8.324	13.967	22.358	23.474	8.412	14.115
0826	22.617	23.734	16.737	28.085	22.507	23.624	16.782	28.160	23.357	24.473	16.952	28.446

continued

VCC [1]	μ_0 (t = 0) [2]	μ_{eff} (t = 0) [3]	α (t = 0) [4]	$\mathrm{R_{eff}}$ [″] (t = 0) [5]	μ_0 (t = 2) [6]	μ_{eff} (t = 2) [7]	α (t = 2) [8]	$\mathrm{R_{eff}}$ [″] (t = 2) [9]	μ_0 (t = 2, tru) [10]	μ_{eff} (t = 2, tru) [11]	α (t = 2, tru) [12]	$\mathrm{R_{eff}}$ [″] (t = 2, tru) [13]
0827	19.825	20.941	25.069	42.066	20.053	21.170	27.146	45.551	19.675	20.792	23.332	39.151
0836	19.064	20.180	33.392	56.033	19.300	20.417	33.162	55.646	19.107	20.223	30.846	51.760
0841	21.126	22.243	11.232	18.848	21.126	22.242	10.691	17.939	21.620	22.737	12.669	21.259
0849	20.037	21.154	14.062	23.597	19.907	21.024	14.062	23.597	20.512	21.628	14.467	24.276
0851	20.160	21.277	21.933	36.803	20.312	21.428	21.590	36.228	20.218	21.335	20.600	34.567
0857	19.638	20.755	27.475	46.102	19.945	21.061	29.684	49.810	19.960	21.077	30.927	51.895
0859	20.515	21.632	16.768	28.136	20.764	21.880	16.886	28.334	20.038	21.154	14.284	23.968
0865	20.710	21.826	36.982	62.055	20.847	21.963	43.114	72.346	21.327	22.443	35.893	60.228
0869	22.758	23.874	17.940	30.103	22.883	24.000	18.754	31.470	22.767	23.883	16.586	27.832
0874	19.025	20.141	12.181	20.440	19.289	20.406	12.181	20.439	19.261	20.377	12.022	20.172
0888	21.548	22.665	12.827	21.523	21.534	22.650	13.629	22.870	22.046	23.163	12.710	21.328
0890	20.367	21.484	3.041	5.103	20.887	22.003	3.327	5.583	21.617	22.733	4.167	6.992
0905	21.207	22.323	20.291	34.049	21.145	22.261	21.142	35.477	21.609	22.725	20.221	33.931
0912	19.991	21.108	20.350	34.147	19.854	20.970	18.387	30.854	20.016	21.132	19.224	32.258
0938	20.053	21.169	15.267	25.618	20.265	21.381	17.314	29.054	20.253	21.369	14.400	24.164
0939	20.921	22.037	22.282	37.389	20.755	21.872	21.584	36.219	21.304	22.420	22.580	37.889
0945	21.608	22.724	12.272	20.592	21.089	22.205	11.256	18.888	22.916	24.033	15.073	25.293
0950	23.059	24.176	21.339	35.807	22.823	23.940	22.334	37.476	24.152	25.268	24.740	41.514
0957	18.795	19.911	12.928	21.693	18.841	19.958	13.370	22.434	19.130	20.246	12.335	20.698
0958	17.764	18.880	17.210	28.878	17.947	19.063	17.209	28.877	17.425	18.542	15.291	25.659

continued

VCC	μ_0 (t = 0)	$\mu_{\rm eff}$ (t = 0)	α (t = 0)	$R_{\rm eff}$ [″] (t = 0)	μ_0 (t = 2)	$\mu_{\rm eff}$ (t = 2)	α (t = 2)	$R_{\rm eff}$ [″] (t = 2)	μ_0 (t = 2, tru)	$\mu_{\rm eff}$ (t = 2, tru)	α (t = 2, tru)	$R_{\rm eff}$ [″] (t = 2, tru)
[1]	[2]	[3]	[4]	[5]	[6]	[7]	[8]	[9]	[10]	[11]	[12]	[13]
0963	22.623	23.740	8.523	14.302	22.610	23.727	9.437	15.836	23.595	24.711	12.644	21.217
0979	19.798	20.914	27.931	46.869	20.002	21.118	30.489	51.160	20.056	21.173	31.887	53.506
0980	21.200	22.317	19.453	32.643	21.028	22.144	19.769	33.172	22.105	23.221	19.830	33.275
0984	18.560	19.676	16.594	27.845	18.709	19.825	16.459	27.619	18.494	19.610	15.630	26.227
0989	22.022	23.138	6.149	10.319	21.700	22.816	5.743	9.636	22.961	24.077	6.949	11.660
0995	20.217	21.333	9.932	16.666	20.087	21.203	9.932	16.666	20.802	21.918	9.302	15.608
1001	22.248	23.364	6.732	11.296	22.230	23.346	6.863	11.516	23.352	24.468	10.000	16.779
1011	21.188	22.305	12.798	21.476	21.100	22.216	12.963	21.753	21.464	22.580	13.190	22.133
1013	22.334	23.450	8.408	14.109	22.178	23.295	7.873	13.212	22.998	24.114	9.401	15.775
1017	23.255	24.371	26.205	43.972	23.393	24.509	28.175	47.277	23.423	24.540	25.683	43.095
1020	22.086	23.202	7.801	13.090	22.337	23.453	7.811	13.107	22.470	23.586	8.290	13.910
1021	21.785	22.901	14.179	23.792	21.658	22.774	14.694	24.657	21.791	22.907	12.987	21.791
1047	18.703	19.819	11.225	18.836	18.860	19.977	11.213	18.816	18.614	19.731	10.980	18.425
1060	21.340	22.456	8.522	14.300	21.191	22.307	8.810	14.784	22.429	23.546	9.732	16.330
1086	19.207	20.324	18.116	30.399	19.436	20.553	18.036	30.265	19.066	20.182	16.574	27.812
1091	19.546	20.663	8.857	14.862	19.329	20.446	8.857	14.862	20.299	21.416	8.486	14.239
1098	25.427	26.543	28.277	47.449	25.134	26.250	26.498	44.464	25.833	26.949	26.913	45.160
1102	21.907	23.024	6.067	10.181	21.647	22.764	5.513	9.252	22.663	23.779	6.669	11.191
1106	22.858	23.974	8.735	14.657	23.199	24.315	9.447	15.852	23.350	24.466	9.786	16.421
1110	19.121	20.237	37.754	63.351	19.228	20.345	36.523	61.285	19.056	20.172	35.681	59.872

continued

VCC	μ_0 (t = 0)	μ_{eff} (t = 0)	α (t = 0)	R_{eff} [″] (t = 0)	μ_0 (t = 2)	μ_{eff} (t = 2)	α (t = 2)	R_{eff} [″] (t = 2)	μ_0 (t = 2, tru)	μ_{eff} (t = 2, tru)	α (t = 2, tru)	R_{eff} [″] (t = 2, tru)
[1]	[2]	[3]	[4]	[5]	[6]	[7]	[8]	[9]	[10]	[11]	[12]	[13]
1114	21.996	23.112	22.779	38.223	21.785	22.902	21.284	35.715	22.189	23.305	21.764	36.520
1118	18.935	20.051	10.065	16.890	18.922	20.038	9.317	15.633	19.085	20.202	9.678	16.240
1121	23.212	24.328	10.041	16.849	23.194	24.310	10.147	17.027	23.616	24.732	12.645	21.218
1126	19.406	20.522	18.989	31.863	19.639	20.756	18.988	31.862	19.482	20.598	18.161	30.474
1128	23.040	24.156	10.340	17.350	22.979	24.095	11.095	18.617	23.945	25.061	14.846	24.911
1141	20.115	21.232	3.436	5.766	19.953	21.069	3.218	5.400	20.511	21.627	3.561	5.975
1145	17.864	18.980	13.524	22.693	18.053	19.170	13.656	22.915	17.945	19.061	13.338	22.381
1156	21.545	22.662	17.991	30.189	21.483	22.600	18.597	31.206	22.125	23.241	17.566	29.476
1158	18.046	19.163	12.528	21.023	18.199	19.316	12.592	21.130	17.826	18.943	12.341	20.707
1165	23.599	24.715	9.552	16.029	23.878	24.994	11.129	18.674	24.203	25.320	10.743	18.028
1166	23.189	24.305	10.915	18.315	23.251	24.367	11.224	18.833	23.773	24.889	13.623	22.859
1168	21.856	22.972	5.472	9.182	21.816	22.932	5.902	9.903	22.968	24.085	11.105	18.635
1169	21.974	23.090	3.924	6.584	21.736	22.853	3.843	6.448	23.745	24.862	9.021	15.137
1179	21.459	22.576	15.044	25.244	21.142	22.259	13.817	23.185	22.238	23.354	18.042	30.274
1186	23.051	24.167	6.602	11.078	22.817	23.933	6.873	11.533	22.988	24.104	5.864	9.839
1188	19.002	20.119	10.233	17.171	19.255	20.371	10.216	17.143	19.268	20.385	10.145	17.024
1189	20.590	21.706	14.973	25.124	20.649	21.765	16.189	27.165	21.965	23.081	32.134	53.921
1190	18.815	19.931	25.156	42.211	18.980	20.096	25.155	42.211	18.470	19.586	22.722	38.128
1193	19.843	20.959	13.218	22.179	19.702	20.818	12.284	20.612	20.106	21.222	13.013	21.836
1200	21.596	22.712	11.485	19.272	21.468	22.584	11.912	19.989	22.460	23.576	11.330	19.011

continued

VCC [1]	μ_0 (t = 0) [2]	μ_{eff} (t = 0) [3]	α (t = 0) [4]	R_{eff} [″] (t = 0) [5]	μ_0 (t = 2) [6]	μ_{eff} (t = 2) [7]	α (t = 2) [8]	R_{eff} [″] (t = 2) [9]	μ_0 (t = 2, tru) [10]	μ_{eff} (t = 2, tru) [11]	α (t = 2, tru) [12]	R_{eff} [″] (t = 2, tru) [13]
1205	19.072	20.188	10.808	18.136	19.101	20.217	10.849	18.205	19.794	20.911	12.462	20.911
1208	20.323	21.440	4.614	7.742	20.193	21.310	4.614	7.742	20.835	21.952	4.358	7.313
1217	22.632	23.748	23.831	39.988	22.568	23.684	24.210	40.625	23.037	24.153	22.300	37.420
1227	24.686	25.802	18.928	31.761	25.073	26.189	23.058	38.691	24.644	25.761	17.299	29.027
1237	20.926	22.042	6.184	10.376	20.864	21.981	6.473	10.862	21.251	22.367	6.199	10.402
1257	22.033	23.150	12.557	21.071	21.840	22.956	12.874	21.602	23.056	24.172	15.190	25.489
1266	21.607	22.723	9.376	15.733	21.482	22.598	10.002	16.783	22.313	23.429	8.642	14.501
1273	20.962	22.079	10.002	16.783	21.096	22.212	10.002	16.783	21.196	22.312	9.916	16.639
1290	19.186	20.302	12.523	21.014	19.263	20.379	13.096	21.975	19.424	20.540	12.235	20.529
1313	19.912	21.028	2.043	3.429	21.053	22.169	2.245	3.767	21.725	22.841	2.272	3.812
1326	19.475	20.592	15.262	25.610	19.721	20.837	15.382	25.810	19.786	20.903	15.639	26.243
1330	20.242	21.358	25.060	42.051	20.359	21.476	24.802	41.618	20.237	21.353	24.038	40.336
1331	23.851	24.968	12.654	21.234	23.803	24.920	13.624	22.861	24.507	25.623	15.845	26.588
1356	20.016	21.132	5.848	9.812	19.730	20.847	5.599	9.395	21.029	22.146	6.710	11.260
1374	20.293	21.409	11.768	19.746	20.847	21.963	14.243	23.901	21.690	22.806	16.580	27.821
1375	20.367	21.483	26.646	44.712	20.209	21.325	26.171	43.915	20.771	21.887	25.376	42.581
1377	22.915	24.031	20.849	34.984	22.766	23.882	21.648	36.326	23.390	24.506	19.088	32.031
1379	19.907	21.024	22.283	37.391	19.777	20.894	22.283	37.391	20.231	21.347	22.442	37.657
1393	20.413	21.529	16.587	27.833	20.247	21.363	15.923	26.719	20.933	22.049	18.605	31.219
1397	21.889	23.005	3.173	5.324	21.806	22.922	3.311	5.556	22.228	23.345	2.813	4.720

continued

VCC [1]	μ_0 (t = 0) [2]	$\mu_{\rm eff}$ (t = 0) [3]	α (t = 0) [4]	$R_{\rm eff}$ [″] (t = 0) [5]	μ_0 (t = 2) [6]	$\mu_{\rm eff}$ (t = 2) [7]	α (t = 2) [8]	$R_{\rm eff}$ [″] (t = 2) [9]	μ_0 (t = 2, tru) [10]	$\mu_{\rm eff}$ (t = 2, tru) [11]	α (t = 2, tru) [12]	$R_{\rm eff}$ [″] (t = 2, tru) [13]
1403	23.141	24.257	11.092	18.612	23.582	24.699	13.501	22.654	23.716	24.832	13.517	22.682
1408	23.364	24.481	8.700	14.599	23.542	24.658	9.615	16.134	23.560	24.676	9.485	15.915
1410	19.924	21.041	8.983	15.074	19.794	20.911	8.983	15.074	20.259	21.375	8.650	14.515
1411	18.176	19.292	2.977	4.995	18.042	19.159	2.952	4.954	18.921	20.037	3.169	5.317
1412	18.323	19.440	18.928	31.762	18.455	19.572	18.592	31.197	18.091	19.208	18.141	30.440
1413	23.324	24.440	8.557	14.358	23.265	24.381	8.498	14.259	24.432	25.548	26.908	45.151
1419	20.136	21.252	15.146	25.416	20.473	21.589	16.189	27.166	20.438	21.554	15.950	26.764
1426	22.346	23.462	13.533	22.708	22.623	23.739	16.302	27.354	22.662	23.778	15.284	25.647
1427	20.984	22.100	9.586	16.086	20.763	21.879	8.681	14.567	21.433	22.550	10.040	16.847
1435	21.841	22.957	21.964	36.856	21.640	22.756	20.354	34.155	21.782	22.899	20.015	33.586
1437	18.878	19.995	3.589	6.023	18.760	19.877	3.436	5.765	19.279	20.395	3.886	6.521
1442	20.664	21.780	20.256	33.989	20.430	21.547	19.125	32.092	21.122	22.239	20.878	35.034
1448	22.159	23.276	28.591	47.976	22.332	23.449	31.965	53.638	22.123	23.239	23.930	40.154
1450	20.376	21.493	18.439	30.940	20.293	21.410	18.675	31.337	21.299	22.416	21.816	36.608
1455	21.875	22.991	8.703	14.603	21.665	22.781	7.964	13.364	22.556	23.672	10.440	17.518
1459	21.531	22.647	6.944	11.652	21.384	22.500	6.239	10.469	21.675	22.791	6.861	11.512
1465	22.717	23.834	16.592	27.842	22.326	23.443	16.593	27.843	23.792	24.908	16.595	27.846
1468	22.252	23.368	12.029	20.185	22.061	23.177	12.295	20.631	23.170	24.287	11.950	20.052
1507	21.615	22.731	12.181	20.440	21.388	22.504	11.459	19.228	21.839	22.955	12.374	20.764
1508	19.816	20.932	18.906	31.725	19.747	20.863	19.450	32.637	20.204	21.320	17.656	29.626

continued

VCC	μ_0 (t = 0)	μ_{eff} (t = 0)	α (t = 0)	R_{eff} [″] (t = 0)	μ_0 (t = 2)	μ_{eff} (t = 2)	α (t = 2)	R_{eff} [″] (t = 2)	μ_0 (t = 2, tru)	μ_{eff} (t = 2, tru)	α (t = 2, tru)	R_{eff} [″] (t = 2, tru)
[1]	[2]	[3]	[4]	[5]	[6]	[7]	[8]	[9]	[10]	[11]	[12]	[13]
1515	22.538	23.655	5.037	8.453	22.353	23.469	4.831	8.106	23.946	25.062	9.581	16.076
1516	19.967	21.083	30.404	51.017	19.959	21.076	31.366	52.632	20.062	21.179	30.415	51.036
1524	21.489	22.606	24.958	41.880	21.430	22.547	26.770	44.920	22.229	23.346	24.605	41.287
1529	21.700	22.816	15.284	25.647	21.492	22.609	14.560	24.431	22.259	23.376	17.672	29.653
1532	20.628	21.744	16.891	28.343	20.752	21.869	17.465	29.305	21.080	22.197	16.992	28.512
1540	18.830	19.947	39.122	65.647	19.079	20.195	39.119	65.642	18.244	19.361	33.214	55.733
1552	19.632	20.749	23.021	38.630	19.766	20.882	22.721	38.125	19.762	20.878	22.669	38.038
1554	19.099	20.215	17.874	29.993	18.637	19.754	16.659	27.954	20.195	21.312	20.384	34.204
1555	20.023	21.139	54.960	92.222	20.100	21.216	57.789	96.969	20.056	21.172	50.378	84.535
1557	20.135	21.251	17.878	30.000	20.005	21.121	17.878	29.999	20.455	21.571	20.139	33.794
1562	19.758	20.874	53.957	90.540	19.862	20.979	57.379	96.282	19.590	20.706	48.079	80.677
1566	21.678	22.795	14.151	23.745	21.672	22.788	15.559	26.108	22.342	23.458	17.383	29.169
1569	21.907	23.023	12.823	21.517	21.681	22.797	11.929	20.017	22.688	23.804	15.671	26.296
1572	21.637	22.754	9.601	16.110	21.598	22.714	9.127	15.316	22.027	23.143	9.808	16.458
1574	20.930	22.046	3.430	5.755	21.073	22.190	3.642	6.112	20.905	22.021	3.254	5.461
1575	20.260	21.376	14.429	24.212	20.545	21.661	14.796	24.827	20.698	21.815	15.504	26.015
1581	22.149	23.265	19.841	33.293	22.110	23.226	21.416	35.935	22.481	23.598	19.695	33.049
1582	23.314	24.431	11.039	18.524	23.190	24.307	10.929	18.338	23.792	24.908	11.406	19.139
1585	21.804	22.920	14.821	24.870	21.655	22.772	15.423	25.879	22.540	23.656	14.383	24.134
1588	19.720	20.836	18.646	31.288	19.582	20.699	16.848	28.271	19.705	20.821	17.162	28.797

continued

VCC	μ_0 (t = 0)	μ_{eff} (t = 0)	α (t = 0)	R_{eff} [″] (t = 0)	μ_0 (t = 2)	μ_{eff} (t = 2)	α (t = 2)	R_{eff} [″] (t = 2)	μ_0 (t = 2, tru)	μ_{eff} (t = 2, tru)	α (t = 2, tru)	R_{eff} [″] (t = 2, tru)
[1]	[2]	[3]	[4]	[5]	[6]	[7]	[8]	[9]	[10]	[11]	[12]	[13]
1596	22.290	23.406	6.137	10.298	21.829	22.946	5.503	9.235	24.011	25.127	15.231	25.558
1605	22.084	23.200	10.176	17.076	21.977	23.093	10.447	17.530	22.561	23.678	10.114	16.971
1615	19.555	20.671	41.796	70.133	19.688	20.804	40.798	68.458	19.472	20.588	38.910	65.292
1623	21.427	22.544	6.135	10.295	21.365	22.482	6.418	10.770	21.871	22.987	6.254	10.494
1624	19.432	20.549	13.906	23.335	19.677	20.793	13.843	23.229	19.365	20.482	12.740	21.378
1644	21.857	22.973	7.813	13.110	21.773	22.890	8.244	13.834	22.676	23.792	8.201	13.761
1654	21.472	22.588	10.045	16.856	21.365	22.482	10.315	17.308	22.377	23.493	12.085	20.279
1656	22.884	24.001	11.990	20.119	23.269	24.385	13.393	22.474	23.125	24.241	11.243	18.866
1675	21.387	22.504	17.205	28.869	21.299	22.415	17.478	29.329	21.675	22.792	18.687	31.356
1678	21.790	22.906	19.000	31.882	21.535	22.651	18.103	30.377	22.520	23.636	19.086	32.026
1685	21.879	22.995	15.856	26.607	21.749	22.865	15.856	26.607	22.704	23.820	15.822	26.549
1686	21.032	22.148	26.213	43.986	20.902	22.018	26.213	43.985	21.752	22.868	26.563	44.572
1690	19.127	20.243	57.660	96.753	19.479	20.595	64.098	107.556	19.152	20.269	54.846	92.031
1696	20.162	21.278	31.657	53.121	20.438	21.555	34.070	57.170	20.397	21.513	32.118	53.895
1699	20.829	21.945	13.771	23.108	20.588	21.705	13.376	22.445	21.777	22.893	16.497	27.682
1713	21.553	22.670	8.511	14.281	21.188	22.304	7.792	13.075	22.534	23.650	10.580	17.753
1725	21.490	22.606	16.776	28.150	20.981	22.097	14.298	23.991	22.676	23.793	23.234	38.987
1726	22.188	23.304	14.686	24.643	21.600	22.717	13.019	21.847	23.556	24.673	18.608	31.224
1727	18.839	19.956	38.366	64.378	18.991	20.108	37.644	63.166	18.814	19.931	36.242	60.814
1728	22.400	23.517	8.709	14.613	22.169	23.286	7.982	13.393	23.219	24.335	10.535	17.677

continued

VCC	μ_0 (t = 0)	$\mu_{\rm eff}$ (t = 0)	α (t = 0)	$R_{\rm eff}$ [″] (t = 0)	μ_0 (t = 2)	$\mu_{\rm eff}$ (t = 2)	α (t = 2)	$R_{\rm eff}$ [″] (t = 2)	μ_0 (t = 2, tru)	$\mu_{\rm eff}$ (t = 2, tru)	α (t = 2, tru)	$R_{\rm eff}$ [″] (t = 2, tru)
[1]	[2]	[3]	[4]	[5]	[6]	[7]	[8]	[9]	[10]	[11]	[12]	[13]
1730	19.379	20.495	17.712	29.721	19.591	20.707	17.998	30.201	19.487	20.603	17.673	29.656
1744	21.741	22.857	6.419	10.771	22.654	23.770	9.034	15.159	23.504	24.620	12.172	20.425
1756	22.780	23.896	6.619	11.106	22.746	23.862	6.927	11.623	22.616	23.732	6.001	10.069
1757	20.010	21.126	13.479	22.617	20.296	21.413	13.724	23.029	20.363	21.479	13.962	23.428
1758	20.232	21.348	18.967	31.826	20.102	21.218	18.967	31.826	20.421	21.537	18.772	31.499
1760	19.431	20.548	21.219	35.606	19.587	20.703	21.155	35.498	19.196	20.312	19.297	32.380
1776	24.639	25.755	16.550	27.771	24.857	25.973	19.786	33.201	24.409	25.525	13.565	22.762
1778	20.362	21.478	13.462	22.590	20.232	21.348	13.462	22.590	20.863	21.980	15.311	25.692
1784	23.598	24.714	16.578	27.818	23.540	24.656	16.593	27.843	24.057	25.173	17.715	29.726
1789	20.868	21.985	9.408	15.786	20.806	21.922	9.827	16.490	21.139	22.255	9.924	16.652
1791	21.183	22.299	15.155	25.431	20.789	21.905	14.659	24.598	22.404	23.521	17.738	29.764
1804	21.568	22.685	11.327	19.006	21.572	22.689	11.484	19.270	21.978	23.094	12.682	21.280
1811	19.363	20.479	13.298	22.314	19.233	20.349	13.298	22.314	19.820	20.937	13.756	23.082
1813	19.185	20.302	29.944	50.246	19.351	20.467	29.943	50.245	19.000	20.116	28.613	48.014
1816	22.985	24.102	15.513	26.031	22.755	23.872	14.527	24.376	24.041	25.157	18.706	31.389
1821	21.597	22.714	4.584	7.691	21.534	22.651	4.768	8.000	22.426	23.542	7.210	12.099
1822	22.097	23.213	9.642	16.179	21.872	22.988	8.955	15.026	22.980	24.096	11.550	19.382
1825	21.947	23.064	8.901	14.935	22.143	23.259	8.973	15.056	22.212	23.329	8.700	14.599
1837	22.453	23.569	10.959	18.388	22.705	23.821	12.563	21.080	22.456	23.573	9.605	16.118
1859	19.509	20.626	21.029	35.287	19.743	20.859	21.029	35.286	19.730	20.847	20.934	35.128

continued

VCC	μ_0 (t = 0)	μ_{eff} (t = 0)	α (t = 0)	R_{eff} [″] (t = 0)	μ_0 (t = 2)	μ_{eff} (t = 2)	α (t = 2)	R_{eff} [″] (t = 2)	μ_0 (t = 2, tru)	μ_{eff} (t = 2, tru)	α (t = 2, tru)	R_{eff} [″] (t = 2, tru)
[1]	[2]	[3]	[4]	[5]	[6]	[7]	[8]	[9]	[10]	[11]	[12]	[13]
1868	19.912	21.028	25.320	42.487	19.957	21.074	24.033	40.327	19.195	20.311	20.074	33.684
1873	21.697	22.813	7.396	12.410	21.499	22.615	7.334	12.307	22.760	23.877	9.042	15.172
1883	18.392	19.509	12.532	21.028	18.539	19.655	12.361	20.742	18.485	19.601	12.178	20.434
1884	24.116	25.232	18.953	31.802	24.291	25.407	21.466	36.020	24.524	25.640	19.840	33.292
1885	22.826	23.942	15.864	26.620	22.864	23.981	15.734	26.402	22.951	24.067	15.759	26.443
1898	21.651	22.767	9.816	16.471	21.886	23.003	9.745	16.352	21.894	23.010	9.616	16.135
1900	23.021	24.137	13.774	23.112	22.952	24.068	13.692	22.975	23.305	24.421	14.304	24.002
1905	25.731	26.848	25.584	42.930	25.719	26.836	24.383	40.915	26.723	27.840	135.524	227.409
1918	21.986	23.102	7.760	13.021	21.879	22.996	7.964	13.364	22.892	24.008	8.325	13.970
1923	19.803	20.920	15.871	26.631	19.848	20.965	16.704	28.030	20.219	21.336	18.158	30.469
1929	20.527	21.643	20.820	34.936	20.433	21.549	19.807	33.237	21.012	22.129	21.913	36.770
1931	21.976	23.093	10.731	18.006	21.580	22.697	10.000	16.779	22.968	24.085	11.989	20.118
1932	19.296	20.413	25.333	42.508	19.180	20.296	25.247	42.364	19.107	20.223	23.610	39.617
1933	21.995	23.111	6.392	10.726	21.798	22.915	6.084	10.209	23.622	24.738	11.868	19.914
1943	18.785	19.901	13.682	22.958	18.998	20.114	14.842	24.906	18.770	19.887	12.649	21.225
1944	20.394	21.511	2.714	4.554	20.678	21.794	2.791	4.683	20.237	21.354	2.671	4.481
1952	22.139	23.256	9.775	16.402	21.946	23.062	10.015	16.805	23.078	24.194	10.370	17.401
1960	21.305	22.421	3.064	5.141	21.090	22.206	2.987	5.013	22.738	23.854	6.175	10.361
1965	21.895	23.011	7.842	13.159	21.788	22.905	7.255	12.175	22.333	23.450	7.918	13.286
1987	19.444	20.561	34.531	57.942	19.549	20.666	36.608	61.429	19.657	20.774	34.593	58.046

continued

VCC	μ_0 (t = 0)	μ_{eff} (t = 0)	α (t = 0)	$\mathrm{R_{eff}}$ [″] (t = 0)	μ_0 (t = 2)	μ_{eff} (t = 2)	α (t = 2)	$\mathrm{R_{eff}}$ [″] (t = 2)	μ_0 (t = 2, tru)	μ_{eff} (t = 2, tru)	α (t = 2, tru)	$\mathrm{R_{eff}}$ [″] (t = 2, tru)
[1]	[2]	[3]	[4]	[5]	[6]	[7]	[8]	[9]	[10]	[11]	[12]	[13]
1992	22.347	23.463	13.099	21.981	22.029	23.145	12.320	20.674	23.395	24.511	14.546	24.409
1994	22.958	24.074	8.394	14.085	23.393	24.509	10.432	17.505	24.074	25.191	19.962	33.496
1999	18.816	19.932	10.947	18.368	18.982	20.098	11.039	18.524	19.022	20.139	11.571	19.416
2006	20.634	21.750	23.173	38.884	20.535	21.652	22.874	38.383	20.808	21.925	23.890	40.088
2007	20.944	22.060	6.164	10.344	20.814	21.930	6.164	10.344	21.424	22.540	6.574	11.030
2015	21.282	22.399	6.786	11.386	21.569	22.686	7.437	12.479	22.285	23.401	9.119	15.302
2023	20.432	21.548	15.358	25.772	20.163	21.279	14.100	23.660	21.089	22.205	16.254	27.274
2033	20.243	21.359	5.829	9.780	20.529	21.646	6.353	10.660	21.162	22.279	7.584	12.726
2034	21.962	23.079	10.522	17.656	21.755	22.872	10.031	16.832	22.385	23.501	10.516	17.646
2037	22.731	23.848	24.428	40.990	22.601	23.718	24.427	40.989	23.398	24.514	26.513	44.488
2058	20.318	21.434	39.745	66.691	20.645	21.762	45.935	77.079	20.729	21.845	47.431	79.589
2066	19.080	20.196	20.078	33.691	19.110	20.226	18.785	31.521	19.250	20.366	19.252	32.304
2070	18.764	19.880	22.826	38.303	19.002	20.118	23.702	39.772	18.728	19.845	23.363	39.203
2089	19.271	20.388	2.891	4.852	19.413	20.529	2.884	4.840	18.766	19.882	2.768	4.645
2094	23.474	24.590	6.102	10.239	23.849	24.965	7.341	12.318	23.457	24.574	5.432	9.116

Derived parameters of the fits to the SBPs for different evolutionary scenarios.